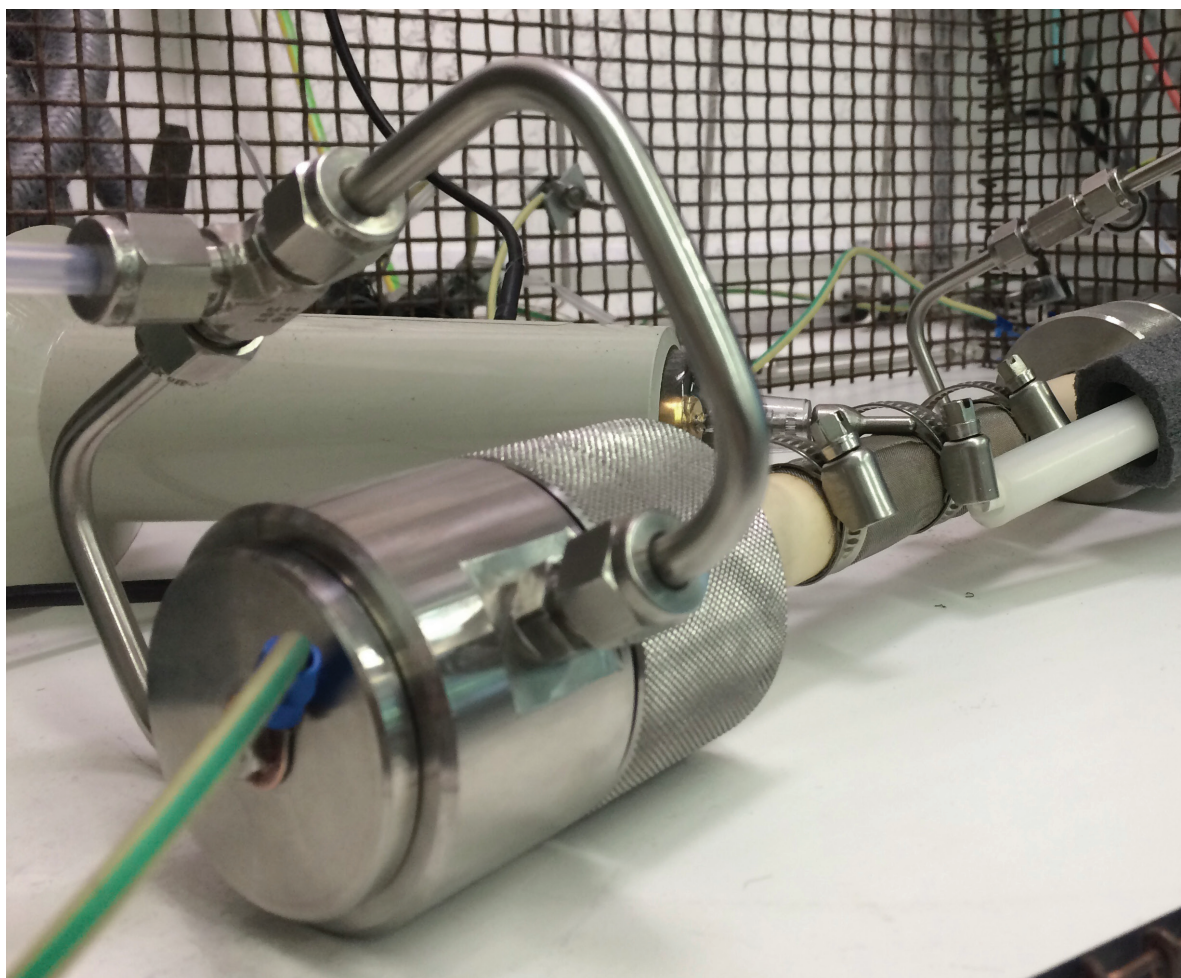


# Tuning the performance of a DBD plasma reactor for CO<sub>2</sub> reforming

Yannick Uytendhouwen



Promotoren **prof. dr. Annemie Bogaerts** | **prof. dr. Pegie Cool**

Proefschrift voorgedragen tot het behalen van de graad van doctor in de wetenschappen  
Faculteit Wetenschappen - Departement Chemie - PLASMANT / LADCA | Antwerpen 2020





Universiteit  
Antwerpen

Faculteit Wetenschappen  
Departement Chemie

# Tuning the performance of a DBD plasma reactor for CO<sub>2</sub> reforming

Proefschrift voorgelegd tot het behalen van de graad  
**Doctor in de wetenschappen**  
aan de Universiteit Antwerpen  
te verdedigen door

**Ing. Yannick Uytendhouwen**

Promotoren:  
Prof. dr. A. Bogaerts  
Prof. dr. P. Cool

Antwerpen, 2020

## **Jury**

### **Voorzitter**

Prof. dr. K. Verhulst, Universiteit Antwerpen, België

### **Promotoren**

Prof. dr. A. Bogaerts, Universiteit Antwerpen, België

Prof. dr. P. Cool, Universiteit Antwerpen, België

### **Leden**

Prof. dr. V. Meynen, Universiteit Antwerpen, België

Prof. dr. F. Reniers, Université Libre de Bruxelles, België

Prof. dr. R. Engeln, Technische Universiteit Eindhoven, Nederland

Prof. dr. J. Thybaut, Universiteit Gent, België

## **Universiteit Antwerpen**

Faculteit Wetenschappen

Universiteitsplein 1, 2610 Antwerpen, België

### **Onderzoeksgroep PLASMANT**

Plasma Lab for Applications in Sustainability and Medicine - ANTwerp

### **Onderzoeksgroep LADCA**

Laboratory of Adsorption & Catalysis

© 2020 Yannick Uytendhouwen

Alle rechten voorbehouden.

*Voor mijn kleine prinses*



# Table of contents

Table of contents	v
List of figures	x
List of tables	xii
List of abbreviations	xii
Nomenclature	xiv
Acknowledgements	xvii
Summary	xxi
Samenvatting	xxvii
<b>1 Introduction</b>	<b>1</b>
1.1 General setting . . . . .	3
1.1.1 CO <sub>2</sub> : The end of the world, or the future of green fuels? . .	3
1.1.2 Renewable energy: The future of energy, but not perfect either... . . . . .	10
1.1.3 Energy storage through chemical energy . . . . .	13
1.2 Plasma: Something ... different . . . . .	15
1.2.1 Plasma basics . . . . .	15
1.2.2 Plasma chemistry . . . . .	17
1.2.3 Plasma generation . . . . .	19
1.2.4 Plasma reactors . . . . .	22
1.3 Dielectric barrier discharge (DBD) reactor . . . . .	29
1.3.1 General structure . . . . .	29
1.3.2 Motivation and limitations of a DBD reactor . . . . .	32
1.3.3 Opportunities for performance enhancement . . . . .	34
1.4 Aim of this PhD work . . . . .	43
<b>2 A packed-bed DBD micro plasma reactor for CO<sub>2</sub> dissociation.</b>	<b>45</b>
2.1 Introduction . . . . .	49

2.2	Materials and methods . . . . .	51
2.2.1	Experimental set-up . . . . .	51
2.2.2	Performance characterisation: conversion and efficiency . .	53
2.2.3	Electrical characterisation . . . . .	54
2.2.4	Experimental method . . . . .	55
2.3	Results and discussion . . . . .	56
2.3.1	Empty reactor . . . . .	56
2.3.2	Packed reactor . . . . .	65
2.4	Conclusion . . . . .	75
<b>3</b>	<b>The potential use of core-shell structured spheres</b>	<b>77</b>
3.1	Introduction . . . . .	79
3.2	Materials and methods . . . . .	81
3.2.1	Core-shell spheres . . . . .	81
3.2.2	Experimental set-up . . . . .	82
3.2.3	Experimental method . . . . .	83
3.3	Results . . . . .	83
3.3.1	Benchmark measurements for the empty reactor and the reactor packed with pure spheres . . . . .	83
3.3.2	Core-shell spheres . . . . .	85
3.4	Discussion . . . . .	89
3.5	Conclusion . . . . .	92
<b>4</b>	<b>How process parameters and packing materials tune the kinetics</b>	<b>93</b>
4.1	Introduction . . . . .	95
4.2	Methods and theory . . . . .	97
4.2.1	Experimental set-up . . . . .	97
4.2.2	Experimental method . . . . .	98
4.2.3	Partial chemical equilibrium . . . . .	99
4.3	Results and discussion . . . . .	101
4.3.1	CO <sub>2</sub> splitting can reach a partial chemical equilibrium . . .	101
4.3.2	Tuning equilibrium and kinetics in plasma-based gas conversion . . . . .	104
4.3.3	Distinguishing catalytic effects from plasma chemistry . . .	109
4.3.4	A common underlying connection, or a more complicated story? . . . . .	114
4.3.5	Future potential of PCE studies . . . . .	118
4.4	Conclusion . . . . .	119
<b>5</b>	<b>On the kinetics and equilibria of plasma-based dry reforming of methane</b>	<b>123</b>
5.1	Introduction . . . . .	125



---

5.2	Methods and theory . . . . .	126
5.2.1	Experimental set-up . . . . .	126
5.2.2	Experimental method . . . . .	128
5.2.3	Partial chemical equilibrium (PCE) . . . . .	128
5.3	Results and discussion . . . . .	130
5.3.1	The benchmark: Separate CO <sub>2</sub> and CH <sub>4</sub> conversion . . . . .	130
5.3.2	DRM: The best of both worlds . . . . .	132
5.3.3	Tuning the kinetics by packing material . . . . .	133
5.3.4	Tuning the kinetics by mixing ratio . . . . .	135
5.3.5	How residence time and gas mixture tune product composition . . . . .	138
5.3.6	Further considerations . . . . .	143
5.4	Conclusion . . . . .	146
<b>6</b>	<b>How gas flow design influences the conversion of DRM in a DBD reactor</b>	<b>149</b>
6.1	Introduction . . . . .	151
6.2	Methods and theory . . . . .	152
6.2.1	Novel multi-purpose DBD reactor . . . . .	152
6.2.2	Reactor configurations . . . . .	153
6.2.3	Experimental set-up . . . . .	156
6.3	Results . . . . .	157
6.3.1	One inlet – one outlet . . . . .	157
6.3.2	Multiple inlets and outlets . . . . .	164
6.4	Discussion . . . . .	171
6.5	Conclusion . . . . .	174
<b>7</b>	<b>How gas flow design influences the ammonia yield in a DBD reactor</b>	<b>177</b>
7.1	Introduction . . . . .	178
7.2	Methods and theory . . . . .	178
7.3	Results . . . . .	178
7.3.1	One inlet – one outlet . . . . .	179
7.3.2	Multiple inlets and outlets . . . . .	183
7.3.3	Discussion . . . . .	186
7.4	Conclusion . . . . .	187
<b>8</b>	<b>Future outlook</b>	<b>189</b>
	<b>List of publications</b>	<b>193</b>
	<b>List of presentations</b>	<b>195</b>

---

<b>A</b>	<b>Appendix of Chapter 2: Micro gap</b>	<b>197</b>
A.1	Electrical characterisation: Theory . . . . .	197
A.2	Electrical characterisation: Results of the packed reactor . . . . .	201
A.3	MATLAB code for electrical characterisation . . . . .	209
A.3.1	Empty reactor . . . . .	209
A.3.2	Packed reactor . . . . .	216
<b>B</b>	<b>Appendix of Chapter 3: Core-shell</b>	<b>219</b>
B.1	Schematic representation of the spray coating set-up used . . . . .	219
B.2	Example of four layer thicknesses of BaTiO <sub>3</sub> @SiO <sub>2</sub> core-shell spheres	221
B.3	Raw data of figure 3.1 and figure 3.2 . . . . .	223
<b>C</b>	<b>Appendix of Chapter 4: CO<sub>2</sub> kinetics</b>	<b>225</b>
C.1	Calculation of the packing efficiency in a coaxial DBD (micro) plasma reactor . . . . .	225
C.1.1	Description . . . . .	225
C.1.2	MATLAB code . . . . .	228
C.1.3	Results for different gap and sphere sizes . . . . .	233
C.2	Fit equation . . . . .	234
C.2.1	Derivation of general operational fit equation . . . . .	234
C.2.2	Dissociation reaction . . . . .	234
C.2.3	Oxidation reaction . . . . .	236
C.2.4	General reaction . . . . .	237
C.2.5	MATLAB code for kinetic data fitting . . . . .	239
C.3	Extra version of figure 4.4 . . . . .	240
<b>D</b>	<b>Appendix of Chapter 5: DRM kinetics</b>	<b>241</b>
D.1	Derivation of the generalised reaction fit equation. . . . .	241
D.2	Raw conversion and energy cost data of figures 5.1 and 5.2 . . . . .	244
D.3	Overview of measured components . . . . .	245
D.4	How residence time and gas mixture tune product composition. . . . .	246
D.4.1	CO <sub>2</sub> dissociation . . . . .	246
D.4.2	CH <sub>4</sub> reforming . . . . .	246
D.4.3	Dry reforming of methane . . . . .	247
D.5	Raw product composition data of all experiments . . . . .	250
D.6	Atom balances of all experiments . . . . .	262
D.7	Applied voltage vs. different gas mixing ratios and packing material.	263
<b>E</b>	<b>Appendix of Chapter 6: Gas flow DRM</b>	<b>265</b>
E.1	Residence time distribution (RTD) simulations and measurements	265
E.1.1	Principle . . . . .	265
E.1.2	Highlights of the simulations . . . . .	266

E.1.3	Results of the RTD study . . . . .	270
E.1.4	Summary of the obtained RTD data . . . . .	273
E.2	Raw data of figures 6.3 to 6.7 . . . . .	275
<b>F</b>	<b>Appendix of Chapter 7: Gas flow NH<sub>3</sub></b>	<b>283</b>
F.1	Raw data of figure 7.1 to figure 7.5 . . . . .	283
	<b>Bibliography</b>	<b>285</b>



# List of Figures

1.1	(a) CO <sub>2</sub> concentration in the atmosphere. (b) Cumulative CO <sub>2</sub> emissions by world region. . . . .	4
1.2	CO <sub>2</sub> emissions worldwide by sector or source from 1960 to 2014. . . . .	5
1.3	Theoretical thermal conversion and energy efficiency as a function of temperature for the three main CO <sub>2</sub> conversion reactions. . . . .	8
1.4	Renewable energy generation worldwide from 1956 to 2018. . . . .	11
1.5	Hourly production of energy by different renewable energy sources. . . . .	12
1.6	An example of the “Duck curve”. . . . .	13
1.7	Schematic representation of energy storage in chemical energy via plasma-based CO <sub>2</sub> conversion. . . . .	14
1.8	Examples of natural and manmade plasmas. . . . .	16
1.9	Breakdown voltage as a function of the pressure—discharge gap product, i.e. the Paschen curve, for parallel-plate electrodes at 20°C for (a) noble gases and (b) molecular gases. . . . .	22
1.10	Generalised current-voltage characteristic of DC discharges and a schematic representation of the different discharge modes. . . . .	25
1.11	Schematic representation of the (a) traditional divergent-electrode gliding arc reactor, and (b) gliding arc plasmatron. . . . .	25
1.12	Schematic representation of a (a) glow discharge reactor, and (b) corona discharge reactor. . . . .	26
1.13	Schematic representation of a microwave plasma reactor. . . . .	28
1.14	Schematic representation of the different stages in the DBD micro discharge formation. . . . .	30
1.15	Schematic representation of some of the typical configurations used for a DBD reactor. . . . .	31
1.16	Schematic representation of a (a) glow discharge reactor, and (b) corona discharge reactor. . . . .	32
1.17	Example of a commercial DBD ozone generator. . . . .	33
1.18	Schematic representation of (a) an empty DBD reactor, (b) a packed-bed DBD reactor, and (c) catalytic packed-bed DBD reactor. . . . .	36
1.19	Schematic representation of (a) a pure sphere, (b) a core shell sphere, and (c) a catalytically activated core-shell sphere. . . . .	37
1.20	Examples of novel DBD reactor designs. . . . .	39
2.1	Packed bed DBD reactor used in this work with analytical equipment. . . . .	52

2.2	Acquired data from digital oscilloscope and simplified Lissajous figured annotated with typical values. . . . .	55
2.3	Conversion as a function of gap size for an empty reactor. . . . .	57
2.4	Raw Lissajous plots for different empty discharge gap sizes and associated slopes calculated by the MATLAB script. . . . .	59
2.5	Current profiles for a 30 W DBD reactor at different discharge gaps.	61
2.6	Efficiency of the empty reactor as a function of gap size. . . . .	62
2.7	Conversion and efficiency as a function of residence time and flow rate for an empty reactor. . . . .	64
2.8	Conversion in packed-bed DBD reactors for different sphere and gap sizes. . . . .	66
2.9	Conversion for different materials and sphere sizes, as a function of gap size, throughout the micro gap size range. . . . .	70
2.10	Raw Lissajous plots for different packed discharge gap sizes and associated slopes calculated by the MATLAB script. . . . .	71
2.11	Energy efficiency in packed-bed DBD reactors for different sphere and gap sizes. . . . .	73
3.1	Overview graph of the conversion and energy efficiency of the benchmark results and all core-shell samples. . . . .	84
3.2	Influence of the core and shell material tested by 50 $\mu\text{m}$ thick shells applied on different core materials. . . . .	87
4.1	$\text{CO}_2$ conversion and total $\text{CO} + \text{O}_2$ conversion in a 455 $\mu\text{m}$ gap size, plotted as a function of residence time. . . . .	103
4.2	$\text{CO}_2$ conversion plotted for different powers, pressures, and gap sizes, as a function of residence time. . . . .	105
4.3	$\text{CO}_2$ conversion plotted for different packing materials in the 455 and 4705 $\mu\text{m}$ gap size, as a function of residence time and SEI. . .	110
4.4	Combined graph of the equilibrium constants and reaction rate coefficients, plotted as a function of the estimated reduced electric field ( $E/N$ ). . . . .	115
5.1	Conversion of $\text{CO}_2$ , $\text{CH}_4$ , and DRM, plotted as a function of residence time for both the empty and $\text{SiO}_2$ -packed reactor. . . . .	131
5.2	Total conversion of DRM with a $\text{CO}_2:\text{CH}_4$ ratio of 3:1, 1:1, and 1:3; plotted as a function of residence time in an empty reactor. . . . .	136
5.3	Measured concentration of different calibrated components after $\text{CO}_2$ dissociation and $\text{CH}_4$ reforming for the empty reactor and $\text{SiO}_2$ -packed reactor, plotted as a function of residence time. . . . .	139

---

5.4	Measured concentration of different calibrated components for DRM, plotted as a function of residence time, for the empty and SiO <sub>2</sub> -packed reactor for different ratios. . . . .	141
6.1	Expanded view and assembled views of the novel parallel plate DBD reactor design used in this work. . . . .	153
6.2	DBD plasma reactor set-up used in this work with analytical equipment. . . . .	156
6.3	Conversion, product composition, peak areas of the uncalibrated gas components, and energy cost of 1:1 DRM, plotted for different reactor geometries. . . . .	158
6.4	Conversion, product composition, peak areas of the uncalibrated gas components, and energy cost for 1:1 DRM, plotted as a function of residence time in the benchmark 'L' reactor. . . . .	161
6.5	Conversion, product composition, peak areas of the uncalibrated gas components, and energy cost, plotted for different CO <sub>2</sub> :CH <sub>4</sub> , in the benchmark 'L' reactor. . . . .	164
6.6	Conversion, product composition, peak areas of the uncalibrated gas components, and energy cost of different gradual/side addition reactor configurations. . . . .	166
6.7	Conversion, product composition, peak areas of the uncalibrated gas components, and energy cost of pre-activation reactor configurations. . . . .	170
7.1	Ammonia yield of stoichiometric ammonia synthesis and conversion of 1:1 DRM plotted for different reactor geometry cases.	179
7.2	Ammonia yield for stoichiometric ammonia synthesis plotted as a function of residence time in the benchmark straight 'L' reactor. . . . .	182
7.3	Ammonia yield plotted for different N <sub>2</sub> :H <sub>2</sub> ratios. . . . .	183
7.4	Ammonia yield of stoichiometric ammonia synthesis and conversion of 1:1 DRM plotted for different gradual addition cases.	185
7.5	Ammonia yield of stoichiometric ammonia synthesis and conversion of 1:1 DRM plotted for different reactor separate addition cases. . . . .	186
A.1	Simplified and extended electrical model for a DBD reactor incorporating partial discharging. . . . .	198
A.2	Peak-to-peak voltage of packed bed DBD (micro) reactors for different sphere and gap sizes. . . . .	202
A.3	Average current flow (RMS) of packed bed DBD (micro) reactors for different sphere and gap sizes. . . . .	203

A.4	Effective capacitance of packed bed DBD (micro) reactors for different sphere and gap sizes. . . . .	204
A.5	Partial discharging of packed bed DBD (micro) reactors for different sphere and gap sizes. . . . .	205
A.6	Burning voltage of packed bed DBD (micro) reactors for different sphere and gap sizes. . . . .	206
A.7	Number of micro discharges in packed bed DBD (micro) reactors for different sphere and gap sizes. . . . .	207
A.8	Average displaced charge per micro discharge in packed bed DBD (micro) reactors for different sphere and gap sizes. . . . .	208
B.1	Schematic representation of the spray coating set-up used in this work. . . . .	220
C.1	Schematic representation of the MATLAB code used to calculate the packing efficiency of the spherical packing materials in a coaxial DBD (micro) reactor. . . . .	227
C.2	Examples of different generated packings by the MATLAB code. . . . .	228
C.3	Extra version of figure 4.4 from chapter 4 with the data of the 4705 $\mu\text{m}$ gap added. . . . .	240
D.1	GC peak areas of different uncalibrated components after $\text{CH}_4$ reforming as a function of residence time. . . . .	247
D.2	GC peak areas of different uncalibrated components for DRM, plotted as a function of residence time, for the empty and $\text{SiO}_2$ -packed reactor for different ratios. . . . .	248
D.3	Product shares based on the total mole equivalent FID peak area are shown for the empty and $\text{SiO}_2$ -packed reactor. . . . .	253
D.4	Product shares based on the total mole equivalent FID peak area for DRM for the empty and $\text{SiO}_2$ -packed reactor. . . . .	260
E.1	Velocity profile and example of a concentration profile. . . . .	267
E.2	Calculated RTD of $\text{CO}_2$ and $\text{CH}_4$ in the gradual addition configurations. . . . .	270
E.3	Calculated RTD of $\text{CO}_2$ and $\text{CH}_4$ in the separate addition configurations. . . . .	271
E.4	Experimental RTD of the added gas in the separate addition configurations. . . . .	272
E.5	Calculated RTD of $\text{CO}_2$ and $\text{CH}_4$ in the pre-activation configurations. . . . .	272



# List of Tables

1.1	Overview of typical reactions in a plasma. . . . .	18
1.2	Comparison of different properties for spherical packing materials of SiO <sub>2</sub> , Al <sub>2</sub> O <sub>3</sub> , ZrO <sub>2</sub> , and BaTiO <sub>3</sub> . . . . .	37
2.1	Corrected packing efficiencies for the gap and sphere size combinations used in chapter 2. . . . .	48
2.2	Measured data from the input signals of the oscilloscope. . . . .	60
2.3	Calculated data from the raw data from table 2.2 . . . . .	60
4.1	Fitted kinetic and equilibrium data for the CO <sub>2</sub> splitting reaction, at different plasma powers. . . . .	106
4.2	Fitted kinetic and equilibrium data for the CO <sub>2</sub> splitting reaction, at different gas pressures. . . . .	107
4.3	Fitted kinetic and equilibrium data for the CO <sub>2</sub> splitting reaction, at different gap sizes. . . . .	109
4.4	Fitted kinetic and equilibrium data for the packed CO <sub>2</sub> splitting reaction, at different gap sizes. . . . .	111
5.1	Fitted kinetic and partial chemical equilibrium data for CO <sub>2</sub> dissociation, CH <sub>4</sub> reforming, and DRM. . . . .	131
5.2	Fitted kinetic and equilibrium data for DRM at different CO <sub>2</sub> :CH <sub>4</sub> ratios in an empty reactor. . . . .	136
6.1	Different configurations used in this work. . . . .	154
6.2	Conditions used when varying the electrode length in DRM. . . . .	160
7.1	Conditions used when varying the electrode length in NH <sub>3</sub> synthesis. . . . .	181
B.1	Example of four layer thicknesses of BaTiO <sub>3</sub> @SiO <sub>2</sub> core-shell spheres. . . . .	222
B.2	Conversion and energy efficiency of the empty DBD reactor and of all samples used in this work. . . . .	223
C.1	Calculated packing efficiencies for the gap and sphere size combinations used in this work. . . . .	233

D.1 Conversion (X) and Energy cost (EC) as a function of residence time, for all gas mixtures and for both empty and SiO<sub>2</sub>-packed reactorss. . . . . 244

D.2 Overview of the components measured by the GC used in this work.245

D.3 Measured concentration of different calibrated components for CO<sub>2</sub> dissociation and CH<sub>4</sub> reforming. . . . . 250

D.4 GC peak areas for different uncalibrated components for CH<sub>4</sub> reforming, as a function of residence time. . . . . 251

D.5 Total mole equivalent of the FID peak areas and the individual shares of each component for CH<sub>4</sub> reforming, for the empty and SiO<sub>2</sub>-packed reactor. . . . . 252

D.6 Measured concentration of different calibrated components for DRM.255

D.7 GC peak areas for different uncalibrated components for DRM. . . 256

D.8 Total mole equivalent of the FID peak areas and the individual shares of each component for the components formed during DRM for the empty and SiO<sub>2</sub>-packed reactor. . . . . 258

D.9 Atom balances for all gas mixtures and for both empty and SiO<sub>2</sub>-packed reactors (if applicable). . . . . 262

D.10 Comparison of the applied peak-to-peak voltage (a measure of the reduced electric field E/N and subsequent the electron temperature) versus the overall rate coefficients and PCE. . . . . 263

E.1 Snapshots at different time steps of an example RTD CFD simulation.268

E.2 Calculated average residence times of the CFD simulations and experiments. . . . . 273

E.3 Energy cost, i.e. the energy needed to convert one mole of reactant mixture, shown for all configurations. . . . . 276

E.4 Measured concentration of different calibrated components after the DRM reaction. . . . . 277

E.5 GC peak areas for different uncalibrated components for DRM. . . 278

E.6 Total mole equivalent of the FID peak areas and the individual shares of each component for the components formed during DRM for all configurations. . . . . 280

F.1 Ammonia yield and energy cost, i.e. the energy needed to convert one mole of reactant mixture, shown for all configurations. . . . . 284

# List of abbreviations

AC	Alternating current
APGD	Atmospheric pressure glow discharge
CFC	Chlorofluorocarbon
CFD	Computational fluid dynamics
DBD	Dielectric barrier discharge
DC	Direct current
DRIFTS	Diffuse reflectance infrared Fourier transform spectroscopy
DRM	Dry reforming of methane
EC	Energy cost
FID	Flame ionization detector
GC	Gas chromatograph
GC-MS	Gas chromatograph coupled to mass spectrometer
GHSV	Gas hourly space velocity
HV	High voltage
iCCD	Intensified charge coupled device
IR	Infrared
L	Long reactor configuration
LGA	Long with gradual addition reactor configuration
LSA	Long with separate addition and narrow side outlets reactor configuration
LSW	Long with separate addition and wide side outlets reactor configuration

## List of abbreviations

---

MFC	Mass Flow Controller
MS	Mass spectroscopy
NOx	Nitrogen oxide species
PCE	Partial chemical equilibrium
PMMA	Poly(methyl methacrylate)
POM	Polyoxymethylene
PSD	Power surface density
PV	Photovoltaic
RT	Residence time
S	Short reactor configuration
SEI	Specific energy input
SGA	Short with gradual addition reactor configuration
SOEC	Solid oxide electrolyser cell
SS	Stainless steel
SSN	Short with separate addition and narrow side outlets reactor configuration
SSW	Short with separate addition and wide side outlets reactor configuration
TCD	Thermal conductivity detector
UV	Ultraviolet
VITO	Flemish Institute for Technological Research
VOC	Volatile organic compounds
XAFS	X-ray absorption fine structure
YSZ	Yttria-stabilized zirconia

# Nomenclature

$A_{FID}$	FID peak area
$C_a$	Concentration of species A
$C_{cell}$	Capacitance of the reactor without the presence of plasma
$C_{diel}$	Capacitance of the reactor (dielectric layer) after full plasma discharge
$C_{gap}$	Capacitance of the gas filled gap
$E/N$	Reduced electric field
$E_y$	Energy yield
$I$	Current
$I_{RMS}$	Root-mean-square current
$K$	Equilibrium constant
$K_T$	Thermal equilibrium constant
$P$	Plasma power
$PI$	Probability interval
$Q$	Charge
$Q_{disp}$	Displaced charge
$S_n$	Sample standard deviation of the measurements
$T$	Period length
$T_s$	The two-tailed inverse of the Student t-distribution for sample size $n_s$ and probability PI set at 95%
$U$	Voltage
$U_{bur}$	Burning voltage
$U_{pp}$	Peak-to-peak voltage
$V_m$	Molar gas volume
$X$	Conversion
$X_e$	Equilibrium conversion
$X_i$	Actual conversion of $i$ based on $X_{GC}$ corrected for gas expansion
$X_{GC}$	Conversion calculated based on GC data
$X_{Total}$	Total conversion based on product composition
$\Delta G^0$	Gibbs free energy of formation
$\Delta H_{298K}^0$	Standard reaction enthalpy

## Nomenclature

---

$\Delta H_R$	Reaction enthalpy
$\Delta U$	Voltage difference between DA and BC in the Lissajous figure at Q equal to 0
$\alpha$	Partial discharged fraction of the reactor
$\beta$	Partial undischarged fraction of the reactor
$\dot{C}O_{2,in}$	Molar flow rate of CO <sub>2</sub> measured by GC without plasma treatment
$\dot{C}O_{2,out}$	Molar flow rate of CO <sub>2</sub> measured by GC after plasma treatment
$\dot{V}$	Volumetric flow rate
$\dot{y}$	Molar flow rate of component y
$\epsilon$	Dielectric constant / relative permittivity
$\eta$	Energy efficiency
$\theta$	Derivative
$\zeta_{diel}$	Effective capacitance of the reactor at partial plasma discharge
$f$	Fraction of the gas mixture with the right reactivity
$k$	Apparent rate coefficient
$n$	Number of consecutive periods
$n_s$	Sample size
$p$	Partial pressure
$r_A$	Rate of formation or loss of molecule A
$r_d$	Dissociation rate
$t_e$	Time to equilibrium
$x$	Mole fraction
$x_e$	Equilibrium mole fraction
$x_i$	Initial mole fraction
$x_{e,T}$	Thermal equilibrium fraction
$z$	Length of the reactor

# Acknowledgements

Eight years... That is how long ago this plasma adventure began. By a coincidental distribution of Bachelor thesis topics, three completely inexperienced students were told that they were going to “play with the power of lightning” as I cite Serge Tavernier. Tasked with designing and constructing a plasma reactor from scratch, we failed miserably, but the interest in this ‘special machine’ was sparked. The subsequent master thesis, under supervision of Kristof Verhulst and Marieke Wouters in collaboration with Annemie and the PLASMANT research group, did result in the successful operation and experimental results of a DBD plasma reactor and the road towards a more extensive PhD research was laid. It is therefore only logical to start these acknowledgements by thanking all the people who made my engineering undergraduate years possible, especially those mentioned above, and classmates/friends Glenn, Dorien, Thomas, Ellen, Sanja, Lars, Raf, and Mitch for all the fun we had back then and afterwards.

Of course, the PhD research part of this story could not be possible without my two promotors Annemie and Pegie. Thank you very much for giving me the opportunity to do a PhD in the PLASMANT and LADCA research groups. This PhD certainly was one of the most difficult things I have done in my life, but I can imagine that supervising me as a PhD student wasn’t the easiest thing either. Thank you very much for all the guidance and effort during this work, for letting me steer this research away from the original plan and towards the things I found interesting, for all the patience you had with me, for coping with my stubbornness in doing things my way and my very-sluggish-paper-writing, and for believing in the fulfilment of this work despite the extra time it took. Also thank you to Vera for being my ‘unofficial extra’ promotor, for all the scientific conversations, and especially for the non-scientific conversations that aided me towards my first-aid activities in the Flemish Red Cross and job opportunities.

B2.28... Legends will be told of that room until the end of time. Almost six years ago I first stepped foot into that office inhabited by an omniscient, talking-to-himself Kristof, a bodypumping, table-smashing, foul-mouthing Stijn, and a one-year-later-joining, cycling-race-watching, overly active Jonas. Little did I know that these men would be the very best colleagues you could ever wish for to fill your days with general loud talking and laughter, the weirdest conversations nobody should ever join midway, hardstyle dance parties, and other things that maybe I should not mention here. Thank you guys for these amazing moments.

The coffee room is only a close second to being crowned “The most important room at work”. Antonin, Georgi, Inne, and Vincent, ‘the OG coffee break group’. We kept it a thing throughout the years despite all the complaints (sorry Annemie). Thank you for all the wonderful moments here and of course all the other memorable activities we did. Viva la revolution!

You are all true friends, always ready for heart-to-heart talks, and sometimes a scientific discussion. Thank you again!

Next, I want to thank all the other people I had the pleasure to work, talk, and have fun with during this PhD within PLASMANT and LADCA, and beyond. Especially the afterwork activities and conferences were a blast. Thank you Qi, Sanne, Jeroen, Stefano, Radu, Annelore, Monika, Tim, Rana, Nick, Jasper, Sander, Jasper, Judith, Nick, Inge, Karen, Glenn, Saskia, Annick, Erik, Karel, Luc, Stijn, Marleen, Ramses, Chris, Maryam, Igor, Amin, Neda, Alp, Koen, Stefan, Claudia, Elise, Eline, Senne, Yannick, Charlotte, Joachim, Björn, Emilie, Fanny, Charlotta, Fatme, Kevin, Patrick, Parissa, Maksud, Jamol, Yrui, Angela, Abraham, Tom, Matthew, Fabiana, Nelly, Ingrid, Tom, Jonas, Bart, Bart, Thomas, Chris, and possibly many more for these moments.

I would also like to thank all those I have got to know over the years, the colleagues in the flemish Red Cross, colleagues from the Stuivenberg ambulance, and friends from climbing, for showing interest in the work I have done. A special thanks here to Kevin for his great support, pool/snooker sessions, numerous first-aid activities, and almost convincing me to stop my PhD and go into nursing; and Sam as my partner in crime for drinks and board games, and with whom I made the streets of Antwerp unsafe with our yellow-blue-lighted-van to drag countless



drunks from the sidewalks, attend various bleeds and broken body parts, and even deliver a baby!

Thank you to my family, especially my parents, sisters, grandparents, and family-in-law for supporting me through the years and always being interested in what I was doing with those “bollekes” in my reactor, even though it wasn’t always that clear to you. Thank you for your advise on more practical stuff during my various ‘construction projects’ during this PhD and discussions to offer another point of view on the subjects.

And finally, the biggest of thank-you’s for Winke. There are no words to describe how thankful I am to have you during these past 3.5 years. You stood by my side during my highs and so many lows, always encouraging me to go on, listening to my theories, really understanding it all, and giving on-point advise. Thank you for coping with my weirdness, procrastination, insecurities, and crazy work trajectory. I love you so much! I can’t wait for April to come... 🍷

This work was financially supported by the European Fund for Regional Development through the cross-border collaborative Interreg V program Flanders-the Netherlands (project EnOp), the Fund for Scientific Research (FWO; grant number: G.0254.14N), and both a TOP-BOF and IOF-SBO (SynCO2Chem) project from the University of Antwerp.



# Summary

Combatting the ever rising concentrations of greenhouse gases in the atmosphere, in particular CO<sub>2</sub> and CH<sub>4</sub>, is one of the biggest challenges of peoplekind in this century. Reducing emissions and developing innovative solutions for capturing and reusing the gases that are inevitably produced, are the tasks at hand for the next decades. However, novel technologies are required in order to convert these greenhouse gases in a sustainable and efficient way. Plasma technology could offer a viable solution, by directly targeting the molecules in reacting into value-added chemicals. Their quick on-and-off-switching capabilities by electrical energy, in combination with intermittent renewable energy sources, makes them a promising technology to directly convert CO<sub>2</sub> and CH<sub>4</sub> in a sustainable way.

Therefore, in this work, we studied the potential use of the DBD reactor for sustainable CO<sub>2</sub> and CH<sub>4</sub> conversion. We aimed to improve the reactor performance via different methods, and to develop a technique to gain more fundamental insight on how the kinetics in the reactor change on the macro scale when optimising the performance.

In chapter 2, we investigated the effect of gap size, as well as packing material and sphere size, on the CO<sub>2</sub> conversion and corresponding energy efficiency. This was done in both empty and packed-bed DBD reactors. We focused especially on micro gap size reactors (268-1230 μm), but also made the comparison with a regular sized reactor of 4705 μm. Reducing the gap size significantly enhances the conversion, compared to a regular size DBD reactor, both in an empty reactor and packed-bed reactor. Thorough analysis of the Lissajous figures reveals underlying electrical trends that can be used to explain the changes in reactor performance due to the gap size reduction. The influence of adding a packing material is greatly dependent on the type of material being used, the corresponding size and the discharge gap. Silica and glass wool give

the best improvements in conversion, next to alumina. Furthermore, the effect of size of the packing material is greatly dictated by the material being used. Silica and alumina show better results with decreasing sphere size for a given gap size, while zirconia shows the opposite trend. Electrical analysis of the Lissajous figures shows that several known and unknown parameters might play a role in determining the conversion. While the conversion significantly increases upon decreasing gap size and upon adding a packing in the reactor, the corresponding efficiency shows less impressive results. In general, the efficiency is found to be better in the larger gap sizes, when comparing at the same residence time, which is logical as larger gap sizes yield a (significantly) higher flow rate for the same residence time, and the energy efficiency is proportional to both conversion and flow rate. When the reactor is packed with different materials, some 'material-size-gap' combinations yielded higher efficiency compared to the same flow rate in the empty reactor, but when compared at the same residence time, the energy efficiency was always lower than in the empty reactor.

In chapter 3 we examined the potential of core-shell structured spheres as packing materials in a DBD reactor for CO<sub>2</sub> conversion. Core-shell spheres have the potential to be tailored to a specific reaction, requiring weak/strong bulk/surface effects, potentially in combination with a catalytically active material for optimal performance. We find strong core-shell interactions that could both improve or reduce the reactor performance. Al<sub>2</sub>O<sub>3</sub> is found to be the best core material, followed by BaTiO<sub>3</sub> and SiO<sub>2</sub>, in agreement with the behaviour of the pure spheres. It is also found that all three shell materials perform equally in low amounts (thin shell), with the exception of Al<sub>2</sub>O<sub>3</sub>@Al<sub>2</sub>O<sub>3</sub>, and that they are not able to provide any significant improvement. A strong mixing behaviour is seen where more active shell materials can improve weak core materials, but will have to compete against strong core materials to show their effect on the performance. Our results show that surface and bulk effects can have different influences on the performance of the spheres in a plasma reactor. A strong core material is not necessarily also a strong shell material, and vice versa, due to the different (surface and bulk) properties that seem to play a role; as shown by the Al<sub>2</sub>O<sub>3</sub>@Al<sub>2</sub>O<sub>3</sub> sample. This illustrates a great potential, as using core-shell spheres can provide us with the possibility of tuning the packing properties more closely to the application.

In chapters 4 and 5 we developed an apparent first-order reversible reaction fit equation to describe the operational behaviour of the DBD reactor. By performing experiments within an extended range of residence times and fitting the experimental data with the fit equation, we can retrieve essential kinetics and thermodynamics data, i.e. the equilibrium conversion and apparent reaction rate coefficients.

In chapter 4 we performed this investigation for CO<sub>2</sub> conversion and showed that a partial chemical equilibrium does exist in a DBD (micro) plasma reactor. Analysis of the effect of different process parameters (i.e. power, pressure, and gap size) on the equilibrium and rate coefficient, shows that a higher power shifts the equilibrium in the forward direction and enhances the rate. The pressure shows a different effect, with a drop for the equilibrium conversion and a rise for the rate coefficient, upon increasing pressure. Decreasing the gap size has a general positive effect, drastically enhancing the equilibrium conversion and the rate coefficient. When inserting a packing (SiO<sub>2</sub> and ZrO<sub>2</sub> spheres), a clear gap/material effect becomes apparent. In general, both packing materials do not positively affect the rate coefficients compared to the empty reactors in both gap sizes, while either increasing or decreasing the equilibrium conversion, and thus enhancing or inhibiting some plasma properties. Interestingly, ZrO<sub>2</sub> performs better than SiO<sub>2</sub> in the larger gap, indicating important material-gap-interactions on the kinetics.

In chapter 5 we extended this study to CH<sub>4</sub> reforming, and both CO<sub>2</sub> and CH<sub>4</sub> combined in DRM. We determined how both gases differ in kinetics and influence each other in DRM. CO<sub>2</sub> dissociation exhibits a higher apparent rate coefficient than CH<sub>4</sub> reforming, but CH<sub>4</sub> reforming has a higher equilibrium conversion than CO<sub>2</sub> dissociation. These differences could be attributed to the main reactions by the aid of 0D modelling done by other researchers in our group. Mixing both gases in a 1:1 ratio combines the best of both worlds, i.e. the higher equilibrium conversion of CH<sub>4</sub> reforming and the higher rate coefficient of CO<sub>2</sub> dissociation. These results point to additional interactions of the two gases, which open new pathways by the individual gas products. Adding the same SiO<sub>2</sub> packing material from previous chapters to the reactor, shifts the equilibrium further upwards, at the cost of slightly reducing the overall conversion rate, whereas for CH<sub>4</sub> reforming the equilibrium conversion stays about the same and the apparent rate

coefficient increases. Mixing the gases results in an increase of both equilibrium and rate coefficient in 1:1 DRM. Finally, comparing different CO<sub>2</sub>:CH<sub>4</sub> ratios revealed the delicate balance of the combined chemistry. CO<sub>2</sub> drives the loss reactions in DRM, resulting in higher reaction rate coefficients when present in higher fractions; the presence of CH<sub>4</sub> in the mixture suppresses back reactions, resulting in higher equilibrium conversions when it is more abundant.

Finally, in chapters 6 and 7 we studied whether the shape and length of the reaction zone, gradual gas addition, and the method of mixing gases can influence the conversion, energy cost, and product composition (in case of DRM). By designing a novel multi-inlet/outlet parallel plate DBD plasma reactor, we could achieve different gas flow and mixing patterns, and quickly change the geometry of the reaction volume. A traditional long rectangular shaped volume, similar to the shape of a traditional co-axial DBD reactor, acted as the benchmark.

Chapter 6 showed the results for DRM. Using the same reactor dimensions but in the short orientation can slightly improve the conversion, which is attributed to the lower gas velocities (allowing more reaction of the plasma components) as a result of the wider cross-section. Modifying the length of the rectangular reaction volume and varying the operating parameters (total gas flow rate and power), resulting in various parameters being kept constant or varied, i.e. residence time, specific energy input, and power surface density, shows no further improvements but reveals some interesting effects. Additionally, our results show that gradual addition of one of the gases, i.e. via 14 side inlets along the length of the reactor, improves the conversion, but the extent of the improvement highly depends on which gas is used as main gas and added gas (generally higher with CH<sub>4</sub> as main gas), as well as on the orientation of the reactor (effect by CO<sub>2</sub> as main gas). Pre-activation of the main gas, by delaying a separate side addition of the other gas via one pair of side inlets, shows improvements when CH<sub>4</sub> was used as the main gas, although we do not see a significant influence of the position of the inlet. Finally, pre-activation of the separate gases by using inlets from opposite sides in the reactor, with last-minute mixing of the products, is evaluated and shows small improvements on the reactor performance.

Chapter 7 showed the results for NH<sub>3</sub> synthesis from N<sub>2</sub> and H<sub>2</sub> as a

comparative study to identify reaction specific effects. Both  $N_2$  and  $H_2$  are unable to pre-react into intermediary products, whereas  $CO_2$  and  $CH_4$  can in DRM. It is shown that all observed trends regarding the benchmark design also hold for ammonia synthesis. The change in reaction does show deviant trends when the input of both gasses got separated, as expected. No additional benefits can be found from gradual addition nor gas pre-reaction. Gradual addition shows equal performance with  $N_2$  as the main gas but decreased yields with  $H_2$  as the main gas, suggesting  $N_2$  dissociation as the rate determining step. Separate addition also shows either equal yield due to enough diffusion or lower due to not enough residence time of one of the reactants.





# Samenvatting

De strijd tegen de almaar stijgende concentraties aan broeikasgassen, met name CO<sub>2</sub> en CH<sub>4</sub>, is één van de grootste uitdagingen van de mensheid in deze eeuw. Het verlagen van emissies, en het ontwikkelen van innovatieve oplossingen om de gasen die toch nog onvermijdelijk geproduceerd worden op te vangen en te hergebruiken, zijn nodig in de komende tientallen jaren. Hiervoor zijn echter vernieuwende technieken nodig om deze broeikasgassen om te zetten op een duurzame en efficiënte manier. Plasmatechnologie kan een interessante oplossing zijn doordat het direct de gasmoleculen kan stimuleren tot conversie in waardevollere chemicaliën. Ook de mogelijkheid om snel aan-en-uit geschakeld te worden via elektrische energie, in combinatie met de onderbroken hernieuwbare energiebronnen, maakt plasmatechnologie een veelbelovende techniek om CO<sub>2</sub> en CH<sub>4</sub> direct te converteren op een duurzame wijze.

Daarom hebben we in dit werk het potentieel bestudeerd van de DBD reactor voor duurzame CO<sub>2</sub> en CH<sub>4</sub> conversie. Het doel was om de prestatie van de reactor te verbeteren via verschillende methoden, en om een techniek te ontwikkelen om meer fundamenteel inzicht te verwerven in de kinetiek van de reactor en hoe deze verandert op een macroscopische schaal wanneer verscheidene optimalisaties uitgevoerd worden.

In hoofdstuk 2 werd het effect van de ontladingsafstand onderzocht, alsook het effect van pakkingmaterialen en hun grootte, op de CO<sub>2</sub> conversie en overeenkomstige energie-efficiëntie. Dit werd zowel gedaan in lege als gepakte reactoren. We hebben ons vooral gefocust op de micro reactoren (ontladingsafstanden van 268–1230 μm), maar hebben deze ook vergeleken met een reactor met traditionelere afmeting van 4705 μm. Het verkleinen van de ontladingsafstand blijkt de conversie aanzienlijk te verbeteren, vergeleken met een DBD reactor van normale grootte, zowel in een lege reactor als

in een gepakte reactor. Grondige analyse van de Lissajous-figures brengt onderliggende elektrische trends aan het licht die gebruikt kunnen worden om de veranderingen in reactorprestaties te verklaren als gevolg van het verkleinen van de ontladingsafstand. De invloed van het toevoegen van een pakkingmateriaal is sterk afhankelijk van het soort materiaal dat wordt gebruikt, de bijbehorende grootte, en de ontladingsafstand. Silica en glaswol geven de beste verbeteringen in omzetting, naast aluminiumoxide. Bovendien wordt het effect van de grootte van het pakkingsmateriaal sterk bepaald door het gebruikte materiaal. Silica en alumina laten betere resultaten zien met afnemende sfeergrootte voor een gegeven ontladingsafstand, terwijl zirkonia de tegenovergestelde trend vertoont. Elektrische analyse van de Lissajous-figures toont aan dat verschillende bekende en onbekende parameters een rol kunnen spelen bij het bepalen van de conversie. Hoewel de conversie aanzienlijk toeneemt bij het verkleinen van de ontladingsafstand en bij het toevoegen van een pakking in de reactor, toont de overeenkomstige energie-efficiëntie minder indrukwekkende resultaten. Over het algemeen blijkt de energie-efficiëntie beter te zijn in de grotere ontladingsafstand, bij vergelijking op dezelfde residentietijd, wat logisch is aangezien grotere ontladingsafstanden een (significant) hoger debiet opleveren voor dezelfde residentietijd, en de energie-efficiëntie evenredig is met zowel de conversie als het debiet. Wanneer de reactor gevuld wordt met verschillende materialen, leveren sommige ‘materiaal-afmeting-ontladingsafstand’-combinaties een hogere energie-efficiëntie op in vergelijking met hetzelfde debiet in de lege reactor, maar vergeleken met dezelfde residentietijd is de energie-efficiëntie altijd lager dan in de lege reactor.

In hoofdstuk 3 werd het potentieel van kern-schil gestructureerde bolletjes onderzocht als pakkingmateriaal in een DBD-reactor voor CO<sub>2</sub> conversie. Kern-schilbolletjes hebben het potentieel om op maat gemaakt te worden voor een specifieke reactie, waarbij zwakke/sterke bulk/oppervlakte-effecten vereist zijn, eventueel in combinatie met een katalytisch actief materiaal voor optimale prestaties. We vonden sterke interacties tussen kern en schil die de prestaties van de reactor zowel konden verbeteren als verminderen. Al<sub>2</sub>O<sub>3</sub> bleek het beste kernmateriaal te zijn, gevolgd door BaTiO<sub>3</sub> en SiO<sub>2</sub>, in overeenstemming met het gedrag van de pure bolletjes. Er werd ook gevonden dat alledrie de schilmaterialen in lage hoeveelheden (dunne schil) evenwaardig presteren, met

uitzondering van  $\text{Al}_2\text{O}_3@/\text{Al}_2\text{O}_3$ , en dat ze geen significante verbetering kunnen bieden. Een sterk menggedrag wordt gezien waar actievere schilmaterialen zwakke kernmaterialen kunnen verbeteren, maar zullen moeten concurreren met sterke kernmaterialen om hun effect op de prestaties te kunnen uiten. Onze resultaten laten zien dat oppervlakte- en bulkeffecten verschillende invloeden kunnen hebben op de prestatie van de bolletjes in een plasmareactor. Een sterk kernmateriaal is niet per se ook een sterk schilmateriaal, en vice versa, vanwege de verschillende (oppervlakte- en bulk) eigenschappen die een rol lijken te spelen; zoals getoond door het  $\text{Al}_2\text{O}_3@/\text{Al}_2\text{O}_3$  staal. Deze bevindingen tonen het potentieel aan van kern-schil gestructureerde bolletjes, aangezien ze ons de mogelijkheid bieden om de pakking beter af te stemmen op de toepassing.

In de hoofdstukken 4 en 5 werd een schijnbaar omkeerbare reactie-fitvergelijking van de eerste orde ontwikkeld om het operationele gedrag van de DBD reactor te beschrijven. Door experimenten uit te voeren over een uitgebreid bereik van reactorresidentietijden en de experimentele gegevens af te stemmen aan de fit-vergelijking, kunnen we essentiële kinetische en thermodynamische gegevens ophalen, zijnde de evenwichtsconversie en schijnbare reactiesnelheidscoëfficiënten.

In hoofdstuk 4 werd deze analyse uitgevoerd voor  $\text{CO}_2$  conversie en werd aangetoond dat er een gedeeltelijk chemisch evenwicht bestaat in een (micro) DBD-plasmareactor. Onderzoek van het effect van verschillende procesparameters (zijnde vermogen, druk, en ontladingsafstand) op het evenwicht en de snelheidscoëfficiënt, toont aan dat een hoger vermogen het evenwicht in voorwaartse richting verschuift en de snelheid verhoogt. De druk vertoonde een ander effect, met een daling voor de evenwichtsconversie en een stijging van de snelheidscoëfficiënt bij toenemende druk. Het verkleinen van de ontladingsafstand heeft een algemeen positief effect, waardoor de evenwichtsconversie en de snelheidscoëfficiënt drastisch worden verbeterd. Bij het plaatsen van een pakking ( $\text{SiO}_2$  en  $\text{ZrO}_2$  bolletjes) wordt een opvallend ontladingsafstand-materiaal-effect duidelijk. In het algemeen hebben beide pakkingmaterialen geen positieve invloed op de snelheidscoëfficiënten in vergelijking met de lege reactoren in beide ontladingsafstanden, terwijl ze de evenwichtsconversie ofwel verhoogden ofwel verminderden, en dus sommige plasma-eigenschappen verbeterde of remmen. Interessant genoeg presteerde

ZrO<sub>2</sub> beter dan SiO<sub>2</sub> in de grotere ontladingsafstand, wat wijst op belangrijke materiaal-ontladingsafstand-interacties op de kinetiek.

In hoofdstuk 5 werd deze studie uitgebreid naar CH<sub>4</sub> omzetting, en zowel CO<sub>2</sub> als CH<sub>4</sub> gecombineerd in DRM. We hebben bepaald hoe beide gassen verschillen in kinetiek en elkaar beïnvloeden in DRM. CO<sub>2</sub> dissociatie vertoont een hogere schijnbare snelheidscoëfficiënt dan CH<sub>4</sub> omzetting, maar CH<sub>4</sub> omzetting heeft een hogere evenwichtsconversie dan CO<sub>2</sub> dissociatie. Deze verschillen konden worden toegeschreven aan de belangrijkste reacties met behulp van OD-modellering uitgevoerd door andere onderzoekers in onze groep. Het mengen van beide gassen in een 1:1 verhouding combineert het beste van twee gassen, namelijk de hogere evenwichtsconversie van CH<sub>4</sub> omzetting en de hogere snelheidscoëfficiënt van CO<sub>2</sub> dissociatie. Deze resultaten wijzen op aanvullende interacties van de twee gassen, die nieuwe wegen openen door de individuele producten die zij vormen. Door hetzelfde SiO<sub>2</sub> pakkingmateriaal uit voorgaande hoofdstukken aan de reactor toe te voegen, wordt het evenwicht verder naar rechts verschoven ten koste van een lichte verlaging van de totale conversiesnelheid, terwijl voor CH<sub>4</sub> de evenwichtsconversie ongeveer hetzelfde blijft en de schijnbare snelheidscoëfficiënt toeneemt. Het mengen van de gassen in 1:1 DRM resulteert in een toename van zowel het evenwicht als de snelheidscoëfficiënt. Ten slotte onthulde het vergelijken van verschillende CO<sub>2</sub>:CH<sub>4</sub> verhoudingen het delicate evenwicht van de gecombineerde chemie. CO<sub>2</sub>, indien aanwezig in hogere fracties, stimuleert de verliesreacties van DRM, wat resulteert in hogere reactiesnelheidscoëfficiënten; de aanwezigheid van CH<sub>4</sub> in het mengsel onderdrukt terugreacties, wat resulteert in hogere evenwichtsconversies wanneer het meer aanwezig is.

Ten slotte werd in de hoofdstukken 6 en 7 onderzocht of de vorm en lengte van de reactiezone, geleidelijke gastoevoeging, en de methode van het mengen van gassen, de conversie, energiekosten, en productsamenstelling (in het geval van DRM) kunnen beïnvloeden. Door een nieuwe, parallelle DBD-plasmareactor met meerdere in- en uitlaten te ontwerpen, konden we verschillende gasstroom- en mengpatronen behalen, en de geometrie van het reactievolume snel veranderen. Een traditioneel lang rechthoekig volume, vergelijkbaar met de vorm van een traditionele coaxiale DBD-reactor, fungeert als standaardontwerp.

Hoofdstuk 6 toonde de resultaten voor DRM. Het gebruik van dezelfde

reactorafmetingen maar in de korte oriëntatie kan de conversie enigszins verbeteren, wat wordt toegeschreven aan de lagere gassnelheden (waardoor meer reactie van de plasmacomponenten mogelijk is) als gevolg van de grotere doorsnede. Het wijzigen van de lengte van het rechthoekige reactievolume en het variëren van de werkingsparameters (totale gasstroomsnelheid en vermogen), waardoor verschillende parameters constant werden gehouden of gevarieerd werden, zijnde residentietijd, specifieke energie-input en vermogensoppervlaktedichtheid, vertoonden geen verdere verbeteringen, maar onthulden enkele interessante effecten. Bovendien laten onze resultaten zien dat de geleidelijke toevoeging van één van de gassen, namelijk via veertien zij-inlaten langs de lengte van de reactor, de conversie verbetert, maar de mate van verbetering hangt sterk af van welk gas wordt gebruikt als hoofdgas en welk als toegevoegd gas (meestal hoger met CH<sub>4</sub> als hoofdgas), alsook op de oriëntatie van de reactor (effect van CO<sub>2</sub> als hoofdgas). Pre-activatie van het hoofdgas, door het andere gas via een paar zij-inlaten later toe te voegen, vertoont verbetering wanneer CH<sub>4</sub> als hoofdgas wordt gebruikt, hoewel we geen significante invloed van de positie van de inlaat zien. Ten slotte wordt de pre-activatie van de afzonderlijke gassen, door gebruik te maken van inlaten van tegenoverliggende zijden in de reactor met op het laatste moment mengen van de producten, geëvalueerd en vertoont dit kleine verbeteringen in de prestatie van de reactor.

Hoofdstuk 7 toonde de resultaten voor NH<sub>3</sub>-synthese vanuit N<sub>2</sub> en H<sub>2</sub> als een vergelijkende studie om reactie-specifieke effecten te identificeren. Zowel N<sub>2</sub> als H<sub>2</sub> kunnen niet reageren op zichzelf tot stabiele tussenproducten, terwijl CO<sub>2</sub> en CH<sub>4</sub> dat wel kunnen in DRM. Er wordt aangetoond dat alle waargenomen trends met betrekking tot het standaardontwerp ook gelden voor ammoniaksynthese. De reactieverandering vertoonde afwijkende trends wanneer de input van beide gassen, zoals verwacht, worden gescheiden. Er kunnen geen extra voordelen worden gevonden door geleidelijke toevoeging of pre-reactie van één van de gassen. Geleidelijke toevoeging laat gelijke prestaties zien met N<sub>2</sub> als het hoofdgas, maar verminderde opbrengsten met H<sub>2</sub> als het hoofdgas, hetgeen duidt op N<sub>2</sub>-dissociatie als de snelheidsbepalende stap. Afzonderlijke toevoeging toont ook een gelijke opbrengst vanwege voldoende diffusie of lager vanwege onvoldoende residentietijd van een van de reactanten.



# **Chapter 1**

## **Introduction**

## **Abstract**

This chapter is a brief introduction into the general setting and the broader plasma chemistry, technology, and opportunities of this work. Each subsequent chapter in this thesis will discuss a different topic with a specific introduction to the research question at hand.



## 1.1 General setting

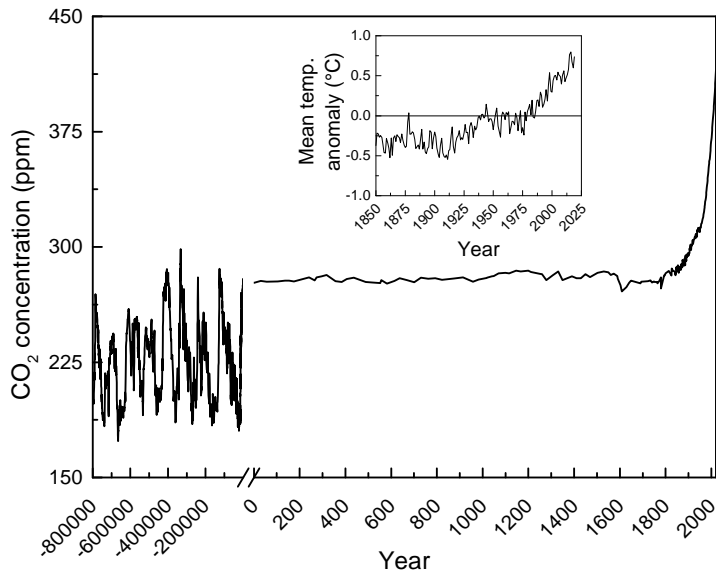
Climate change is upon us! Or to be more correct, we are already stuck up to our necks into it. What once could be described as the pinnacle of humankind, the industrial revolution, can now be seen as the moment that started it all. The giant leaps forward in production, technology, and demographic transition were associated with enormous increases in fossil fuel usage, waste production, new ‘wonder materials’, and a “laissez faire” mentality without thinking about, or any awareness of, the consequences. Only years later we see the outcome: increasing global temperatures, rising sea levels, seasons changing, harsher weather effects, and reformed landscapes are only a few of the signs that something went terribly wrong [1]. Some nations or people still in denial, but more and more realising that things must change, in an attempt to stop a giant boulder rolling downhill...

### 1.1.1 CO<sub>2</sub>: The end of the world, or the future of green fuels?

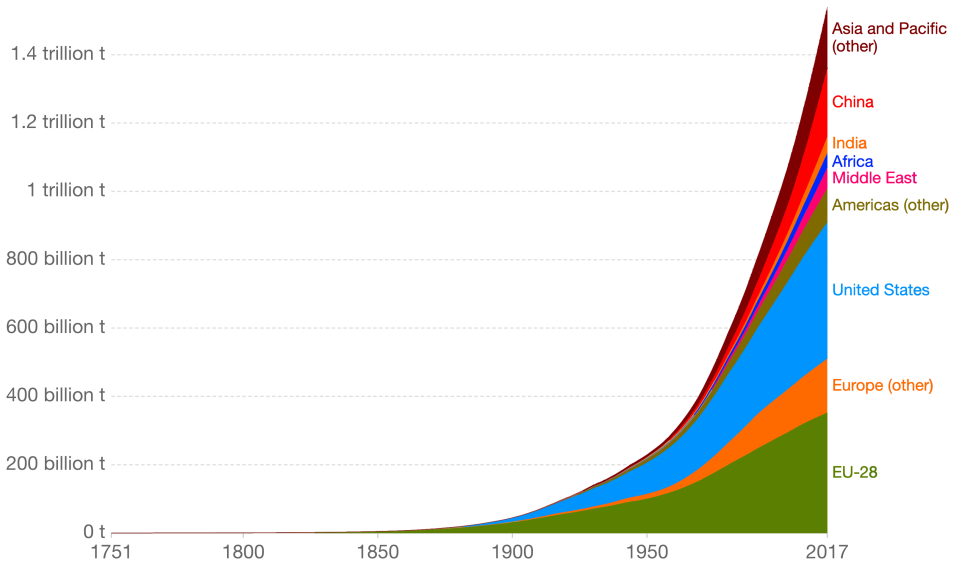
#### 1.1.1.1 The problem with CO<sub>2</sub>

One of the main attributing factors to the climate change is the increased concentrations of greenhouse gases in our atmosphere [1]. They are called this way because they absorb and trap heat, in the form of infra-red radiation, in our atmosphere. A greenhouse effect that is necessary for our life on earth, but too much, by the growing concentration of CO<sub>2</sub>, CH<sub>4</sub>, and CFC’s of different emission sources, and the delicate balance of nature is disrupted. Although a CO<sub>2</sub> molecule on its own has a fairly low greenhouse effect in comparison to the other greenhouse gases, the sheer amount of CO<sub>2</sub> present has major repercussions [2]. The CO<sub>2</sub> concentration in our atmosphere has nearly doubled the average level of the last million years from around 225 ppm to a staggering 415 ppm at the time of writing this thesis, resulting in an average temperature shift of 1°C, see figure 1.1a [3].

A large effort is needed from the public to reduce CO<sub>2</sub> emissions. Although their direct share is only about 9% of the global emissions, their behaviour has also indirect consequences in electricity and heat production (non-household) (~50%), transport (~20%), and industry and production (~20%) that account for the majority of the pollution, see figure 1.2 [3]. Despite the public having an influence on the ‘supply and demand’ part of the equation, even larger



(a)



(b)

**Figure 1.1:** (a) CO<sub>2</sub> concentration in the atmosphere, measured in parts per million (ppm), from historical preserved ice samples to now. Insert: Global average land-sea temperature anomaly relative to the 1961-1990 average temperature. (b) Cumulative CO<sub>2</sub> emissions by world region from 1751 to 2017. Data from NOAA and Hadley Centre, and adapted from [3].

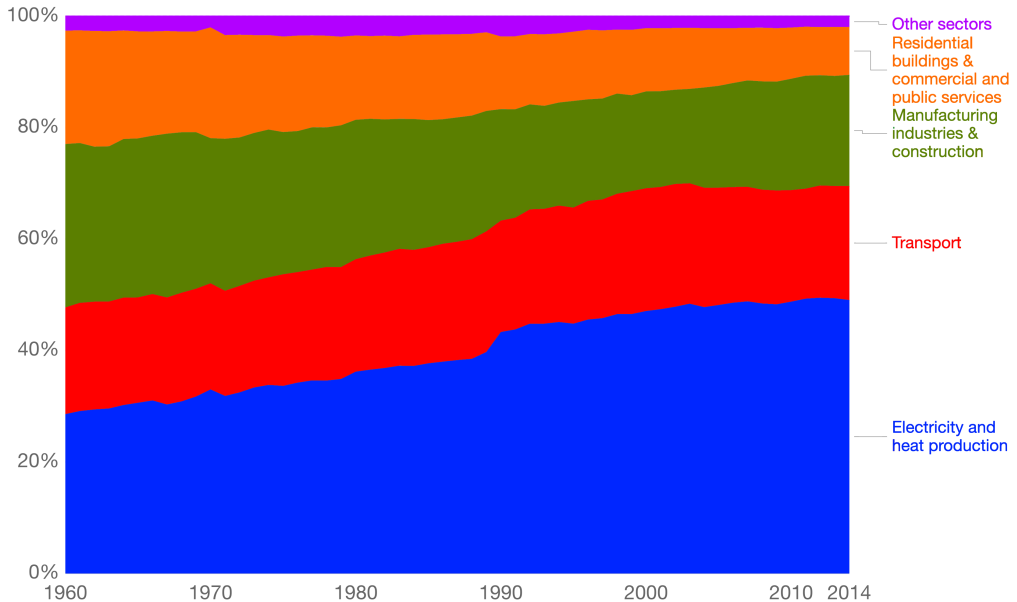


**Figure 1.2:** CO<sub>2</sub> emissions worldwide by sector or source from 1960 to 2014. Adapted from [3].

effort should be taken by the above mentioned sectors to reduce their CO<sub>2</sub> emissions. Looking for alternatives in production strategies, materials choices, transportation methods, etc., but also the transition towards greener energy, green chemistry, cradle-to-cradle products, etc. can have major effects on the global emissions due to their immense share. This is now the big focus for a lot of companies as they are rightfully being pressured in doing something about it [4]. It is clear that this is a worldwide problem that needs to be tackled by every nation, and especially the Western countries as, on a cumulative basis, European and North American countries have been responsible for almost 2/3 of the global CO<sub>2</sub> emissions since 1800, as shown in figure 1.1b [3]. We therefore have a lot to make up for and should be on the forefront of reducing CO<sub>2</sub> emissions and taking other nations on board, e.g. Asian countries like China with its explosively growing industry, that seem not to care as much.

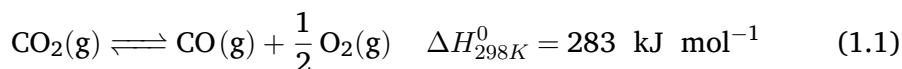
Lowering the emissions is one thing, complete reduction to zero is another one and is near impossible. Although a lot of measures can be taken to reduce it, there will always be some processes that need to be running, or transportation method without competitive alternatives. Examples are the synthesis of ammonia that is key in producing fertilisers and hundreds of chemical processes but is producing

up to five times as much CO<sub>2</sub> as it produces NH<sub>3</sub> [5], or the use of cargo ships as they are still the most “eco-friendly” way of transporting massive amounts of freight [6, 7]. There is, however, a big difference between CO<sub>2</sub> production and CO<sub>2</sub> emission; producing a pollutant is not necessarily bad, actually releasing it into the atmosphere is. Therefore, besides the reduction of CO<sub>2</sub> production, a lot of effort can and should be done in capturing CO<sub>2</sub> and doing something with it.

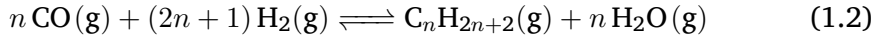
### 1.1.1.2 The potential of CO<sub>2</sub>

Chemistry is all about reactions and these are never perfect in converting all reagents into products. So, we usually end up with a balanced mixture of leftover reagents, the desired product, and perhaps some unwanted side products. This is known as the equilibrium state of the reaction. There is a problem however with CO<sub>2</sub>: the reactions where CO<sub>2</sub> is produced tend to be near perfect and the bonds holding the carbon and oxygen atoms together are so strong and stable that a lot of CO<sub>2</sub> is produced and that it does not want to react back into something else [8]. Therefore, the first idea that was brought up to get rid of CO<sub>2</sub> was called ‘Carbon Capture and Storage’; capturing the CO<sub>2</sub> and storing it longterm [9]. This was found to be possible with certain porous minerals being able to (permanently) bind the CO<sub>2</sub> into its structure, but the idea of storing it indefinitely is clearly not a permanent and suitable solution. The better solution would be to utilise it into something else, ‘Carbon Capture and Utilisation’, up-cycling the CO<sub>2</sub> into something of value via this way [9].

There are two major routes for converting CO<sub>2</sub> into more valuable chemicals via traditional thermal conversion processes [8]. The first route is simply splitting (or dissociating) the CO<sub>2</sub> molecule in two, producing CO and O (recombined with another O atom in O<sub>2</sub>) according to:



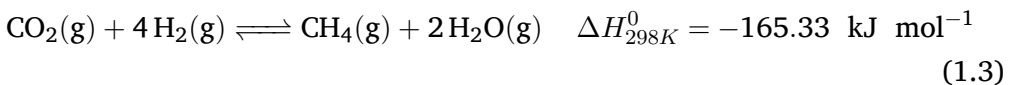
The produced CO combined with H<sub>2</sub> from another source forms a mixture that is known as synthesis gas, or syngas. Syngas is a crucial intermediate in the production of methanol and synthetic hydrocarbon fuels, the latter mainly via the Fischer-Tropsch process according to:



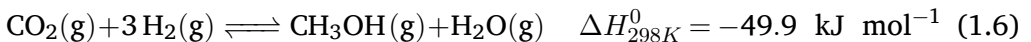
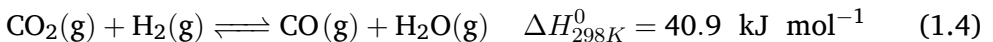
with the optimal H<sub>2</sub>:CO ratio around 2. CO<sub>2</sub> dissociation requires a lot of heat though for decent conversion levels, as shown in figure 1.3a, with the most energy efficient conversion at about 3200 K.

The second route is combining CO<sub>2</sub> with a co-reactant. Adding pure H<sub>2</sub> or co-producing H<sub>2</sub> from another chemical creates the potential of producing a syngas (intermediate) mixture that can be used similarly as the Fischer-Tropsch synthesis; either in a separate reactor (two-stage process), or within the same reactor (one-stage process) if the reactor conditions and chemistry allow for it (temperature, pressure, catalyst, size, etc.). This route can (directly) produce higher or oxygenated hydrocarbons, resulting in more valuable and energy dense chemicals. The three most potent co-reactants are either directly using pure H<sub>2</sub>, or using H<sub>2</sub>O or CH<sub>4</sub>.

Using pure H<sub>2</sub> opens the possibility to a few different reactions. The complete hydrogenation of CO<sub>2</sub>, according to equation 1.3, produces CH<sub>4</sub> and H<sub>2</sub>O that can be further used to produce syngas via the steam reforming reaction (CH<sub>4</sub>(g) + H<sub>2</sub>O(g)  $\rightleftharpoons$  CO(g) + 3 H<sub>2</sub>(g)), to be used in Fischer-Tropsch. This is, for starters, a really long route to obtain any valuable chemicals. Taking into account that H<sub>2</sub> is mainly produced from CH<sub>4</sub> via the same steam reforming reaction, making H<sub>2</sub> already a highly valuable gas, results in an unnecessary and costly loop of chemicals rendering this option highly unfeasible.



Alternatively, partial hydrogenation of CO<sub>2</sub> to methanol via a catalytic reaction is possible. Methanol can be formed in either a one-step or two-step reaction via equations 1.4-1.6, but the downside is the high co-production of H<sub>2</sub>O wasting a third of the valuable H<sub>2</sub>.



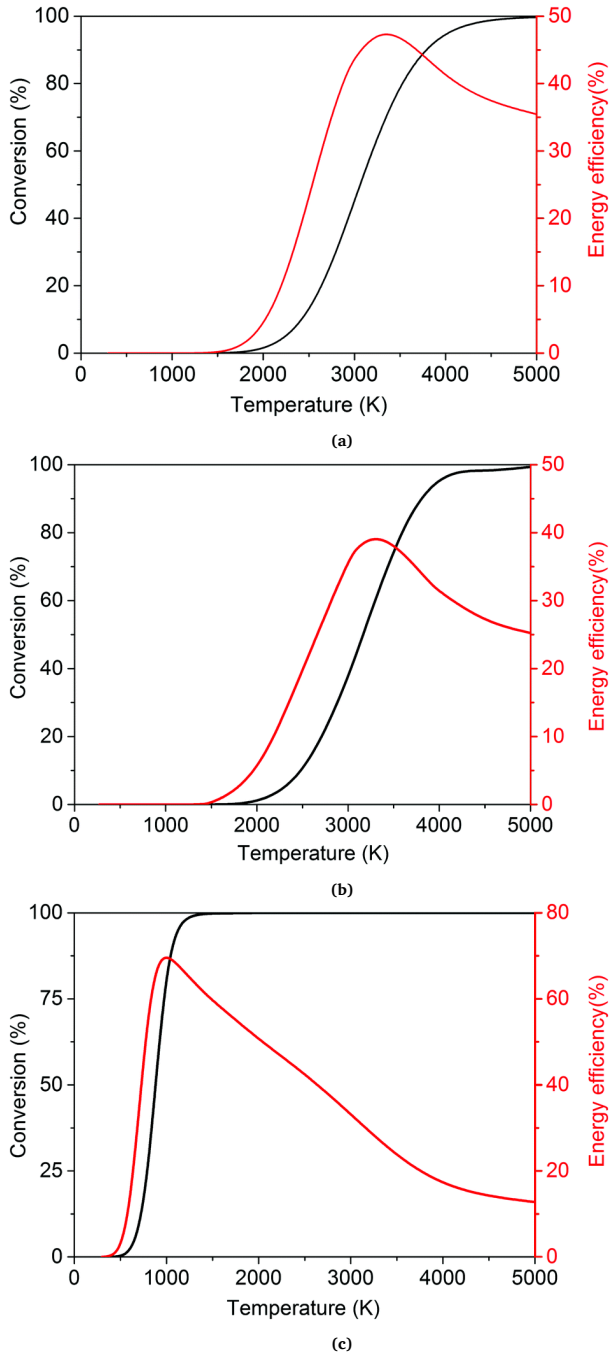
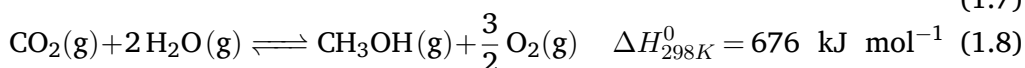
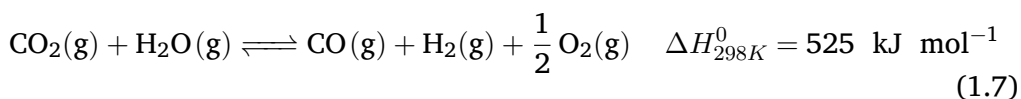
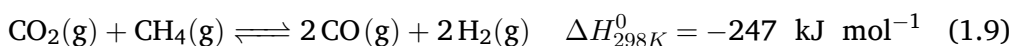


**Figure 1.3:** Theoretical thermal conversion and energy efficiency as a function of temperature for (a) CO<sub>2</sub> dissociation, (b) artificial photosynthesis, and (c) DRM. Adapted from [8].

The reaction of CO<sub>2</sub> with H<sub>2</sub>O, also dubbed artificial photosynthesis, is a first example to attempt co-producing H atoms or H<sub>2</sub> to produce syngas or directly produce (oxygenated) hydrocarbons, as shown by equations 1.7 and 1.8. Although not being used in traditional thermal processes, it has been attempted and modelled in plasma processes, but rendered not to be feasible due to prominent back reactions towards CO<sub>2</sub> with H<sub>2</sub>O.



The final, and one of the more desirable, reactions is the combination of CO<sub>2</sub> with CH<sub>4</sub>, also known as dry reforming of methane (DRM). It combines CO<sub>2</sub> with another dominant greenhouse gas and generates syngas according to:



The more optimised temperature dependency, read lower thermal energy needs, as shown in figure 1.3c, combined with subsequent reactions according to Fischer-Tropsch, or via alternative/direct pathways, gives us overall a simple reaction consuming lower cost greenhouse gases and producing high value (oxygenated) hydrocarbons.

The reactions discussed above are, however, only on a theoretical thermal-reaction-basis and have a few problems in real life. First of all, these reactions assume purified gases which are not always available, especially when talking about waste gas streams from (industrial) processes. These gases could be of low quality, for example being diluted in air, unreacted reagents, or containing nitrogen or sulphur compounds. It has to be taken into account that these waste gases need to be purified before use, requiring a higher cost, or the novel conversion process needs to be able to handle the impurities. Secondly, a large number of side reactions may occur, either desirable or undesirable, even within the pure mixtures, depending on the reactor type and conditions. There is high potential of producing multiple higher hydrocarbons or oxygenated hydrocarbons in one reactor, but the matrix of produced products should be limited in order to aid subsequent purifying steps. Also soot production that

deactivates catalyst materials and most of these reaction options require high temperatures due to the high activation energy of CO<sub>2</sub> in the reactions. Finally, the incompatibility of thermal processes with renewable energy sources is less ideal in order to have carbon neutral applications.

### **1.1.2 Renewable energy: The future of energy, but not perfect either...**

Renewable energy is one of the most important solutions in our society for reducing CO<sub>2</sub> emissions by moving from combustion-based energy production to more sustainable carbon neutral solutions [10]. Historical production of renewable energy has been dominated by traditional biomass, i.e. burning of wood, forestry materials, and agricultural waste biomass. Although technically carbon neutral in essence, due to the cyclic nature of carbon capture in the biomass and release by burning, it has not been until the small scale use of hydropower (water wheel) and wind energy (wind mills) that emission-less renewable energy sources started to be used. Hydropower stayed the main industrial method of renewable energy production (mainly via dams) until the early 1990s when large scale wind and solar energy began to develop, see figure 1.4. Hydropower still has the highest share, but the impressive advancements made in the last 30 years resulted in the increased used of wind energy, solar PV energy, bioenergy, geothermal, and wave and tidal energy.

The obvious advantages of modern renewable energy sources are their carbon neutral nature, reducing the CO<sub>2</sub> emissions for energy production, and their virtual endless supply of energy during their lifespan.

There are, however, also a few caveats. A first is that, while the production of renewable energy via these sources is carbon neutral, there are still CO<sub>2</sub> emissions during their entire lifespan. The production of steel for modern windmills, precious metals refining for solar PV cells, concrete pouring for water dams, etc. all require energy and cost intensive operations releasing CO<sub>2</sub> in the atmosphere [11]. Also recycling decommissioned renewable energy installations require energy and cost intensive processes that have to be taken into account. As a result, these “green” energy sources start and end with a large carbon debt. Therefore, we have to look at the CO<sub>2</sub> emissions saved during their operations, and as long as their carbon balance (CO<sub>2</sub> saved vs. CO<sub>2</sub> emitted) is positive, we



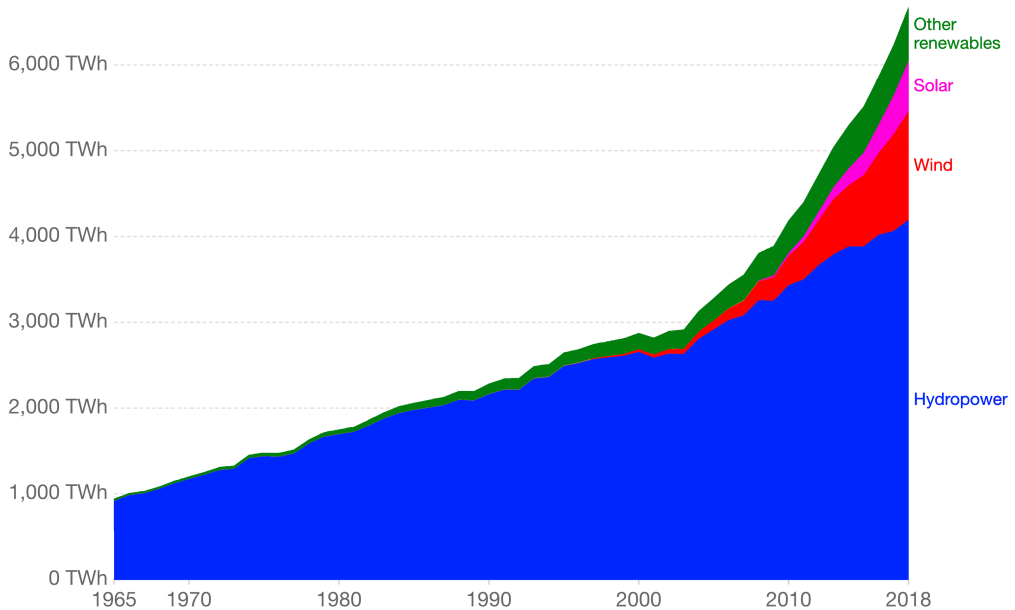


**Figure 1.4:** Renewable energy generation worldwide from 1956 to 2018. ‘Other renewables’ refers to renewable sources including geothermal, biomass, waste, wave, and tidal. Traditional biomass (i.e. wood, coal, and natural gas) is not included. Adapted from [10].

can talk about a carbon neutral technology.

Secondly, most of the renewable energy technologies require high surface areas, such as flooded grounds for hydropower or flat fields for solar energy [12]. These valuable areas need to be sacrificed for these projects. There are certainly areas of high potential, but these are usually far away from the consumption locations (sunny Sahara or far at sea vs. Europe). It is clear that a lot of investment, effort, and goodwill is still needed to further intensify the required boom in renewable energy.

A third major problem with renewable energy is their dependency on the elements [14]. Solar energy is obviously dependent on the availability of the sun during the day, with on average a gap of about twelve hours a day [15], see figure 1.5. Hydropower and wind energy depend on the always fluctuating flow of rain and wind, where both can also receive too much energy so that water needs to be bypassed or windmills be stopped for safe operation. This intermittent behaviour of renewable energy input results in even more intermittent energy output. The issue does not end there, power consumption by humans is not constant either during the day. Energy consumption for a power plant system

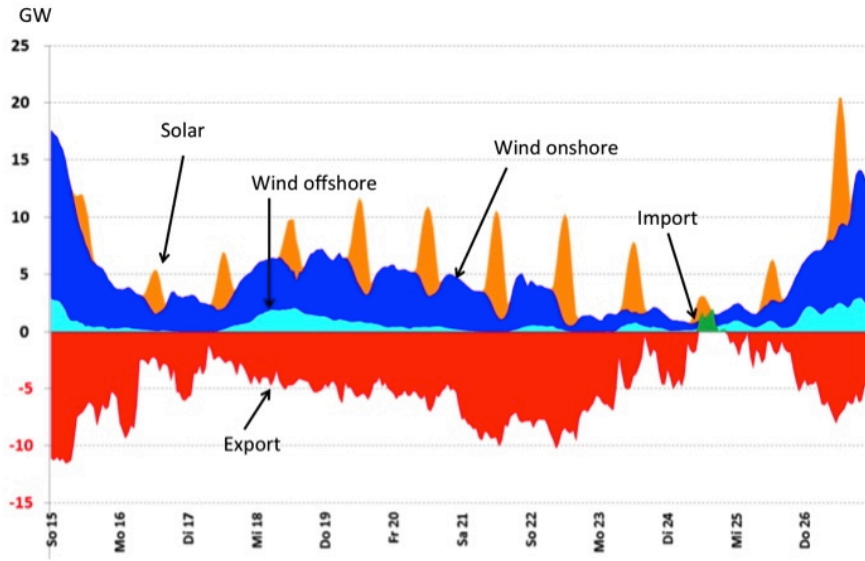


**Figure 1.5:** Hourly production of energy by different renewable energy sources during a dark and wind still period and compared to the electricity export for Germany (16-25 Januari 2017), taken from [13].

(connection of countrywide plants), has a minimum operating level that is mostly dependent on the industrial demand that stays pretty much constant during the day. However, in the morning as people wake up and start their day, the demand sees a sudden increase that settles and decreases a bit during the day at a steady work level. As the evening approaches, demand increases again rapidly when everyone returns home and levels back to normal as the night begins. Power companies have to continuously adapt their power production to this curve that fluctuates from day to day, month to month. This on its own is no problem, but adding renewable energy sources into the equation makes tuning the demand versus production a much harder job. Most power plants have to keep running 24/7 as shutting down and starting up can take days, they therefore have a minimum level at which they have to operate [16]. Regular or predictable fluctuations of energy production via renewable energy sources can be matched somewhat, and this results in an extra variable energy production rate where this trend is called the “Duck curve” as it resembles the shape of a duck, see figure 1.6. Over-production of energy renewables is the problem, when the curve dips below the minimal output level [17]. Energy companies can try to sell the energy to other close countries, but this is not always possible or feasible as they

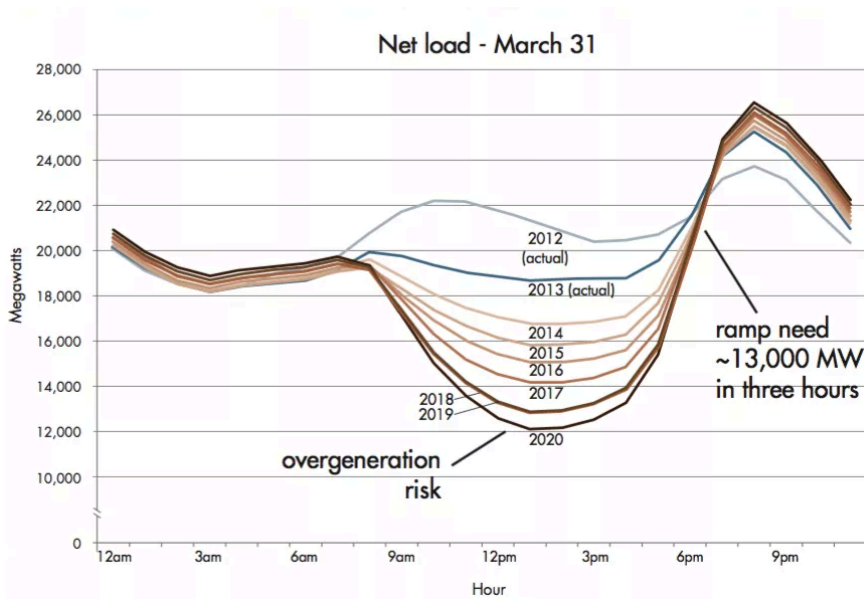


**Figure 1.6:** An example of the “Duck curve”, i.e. the changing typical load on traditional energy sources during the day under influence of the increasing renewable energy sources, taken from [16].

usually exhibit the same weather, resulting in negative consumer prices [18]. Removing traditional energy plants can resolve this, as more renewable sources are taking their place, but a stable and reliable minimum amount of energy is necessary to fill the gaps [17]. Energy storage is also a solution, this could be done in large batteries, but these are still too costly and big in size to use on a land-wide scale [19,20]. Energy storage in water reservoirs is an option already being used around the world, although with debatable efficiencies [20]. A more novel and energy efficient solution has to be found to temporary or permanently store/use the excess electrical energy at peak production moments.

### 1.1.3 Energy storage through chemical energy

Combining the opportunities of sections 1.1.1 and 1.1.2 could solve two problems in one, i.e. using the excess energy of renewable energy sources at peak moments to convert CO<sub>2</sub> into value added chemicals [21]. This way we can store the excess energy in the form of chemical energy so that it can be more efficiently used; while at the same time incorporating CO<sub>2</sub> back into a useful material loop and overall reducing CO<sub>2</sub> emissions, as schematically shown in figure 1.7.

This does, however, require a technology powered by electrical energy with

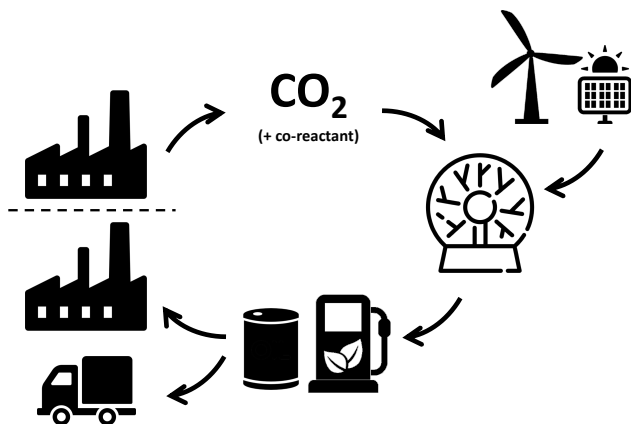


**Figure 1.7:** Schematic representation of energy storage in chemical energy via plasma-based CO<sub>2</sub> conversion.

quick on-off-switching capabilities. The former is to more efficiently use this high value energy type and not waste energy losses in converting it into a lower grade energy, such as heat energy. The latter is necessary to reduce lag and energy losses into the system. The complete worst example would be a typical big thermal reactor that, besides using heat via a direct burner or an indirect burner via steam heating, requires a lot of time and energy to heat up, because of the sheer mass of the reactor to reach decent conversion levels. A more suitable reactor would be smaller in size, though with high throughput if possible, but would be able to directly convert the applied electrical energy into chemical energy. The two main technologies responding to these criteria are electrochemical and plasma reactors. Despite the great potential of electrochemical reactors, we will focus our work on the promising plasma reactors and investigate how they might be a possible solution.

## 1.2 Plasma: Something ... different

### 1.2.1 Plasma basics

Plasma, although a well understood phenomenon, is all around us, but it is more often than not very poorly explained. And no wonder why that is, as it is truly something different, something special.

It is usually described as the fourth state of matter, an energetic gas, or more specified an ionised gas. But all of the above are not completely correct. Calling it a state of matter is possible, but it is not necessarily the fourth, as there are a lot different ways matter can exist, such as non-crystalline amorphous solids, liquid crystals, magnetically ordered states, superfluids, etc. Naming it the fourth is of course based on the theoretical order of phases, as heating up a solid turns it into a liquid, and further into a gas, and finally becoming a plasma as enough heat is added. But then states of matter and phases are used synonymously. Phases have well defined state variables (or temperature and pressure borders) where they exist, there are clear phase transitions, and they are chemically stable, with plasma not really fitting these descriptions. For example, turning solid  $\text{H}_2\text{O}$  into a gas and back will still chemically remain  $\text{H}_2\text{O}$ , unless going to extremes. Turning gaseous  $\text{H}_2\text{O}$  into a plasma, it will generate  $\text{H}_2$ ,  $\text{O}_2$ ,  $\text{H}_2\text{O}_2$ , and so on, and these new chemicals will stay upon returning to the gas phase, independent of the level of 'plasma activity'. Additionally, plasma can be generated without introducing any heat whatsoever via electric or magnetic fields, therefore calling it "the fourth" sounds a bit dull. Dubbing it an ionised gas is as well a really vague way of defining it, as it does not state the level of ionisation. Statistically speaking there will be some accidental ions existing in any gas due to (UV) radiation on the lower scale, making all gases a potential plasma, but a completely ionised gas on the other end of the scale is also rare. Additionally, a whole lot of different species can exist in a plasma, such as free electrons, ions, radicals, and both excited and neutral species.

So what is plasma then? Plasma is a "special" form in which matter can exist, that is quasi-neutral gas consisting of positively, negatively, and neutral charged species, which are subject to electric, magnetic, and other forces, exhibits collective behaviour, and can promote reactions between the different species. The plasma state is therefore loosely defined by three criteria [25].

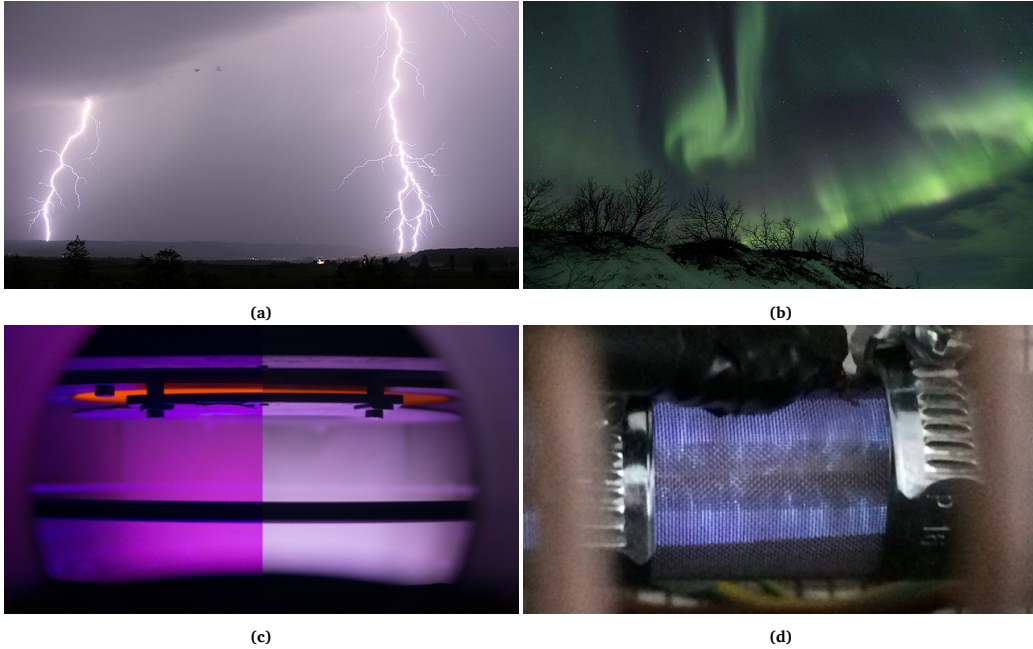


**Figure 1.8:** Examples of natural and manmade plasmas, i.e. (a) lightning (taken from [22]), (b) aurora borealis [23], (c) low pressure plasma for thin film deposition [24], and (d) micro discharges in dielectric barrier discharge reactor for chemical reactions.

The first is, as hinted above, the quasi-neutrality of a plasma. This means that under equilibrium conditions, in the absence of external disturbances such as an external force, a plasma is macroscopically neutral. There can exist deviations of the local charge on the ‘microscopic scale’, but in a volume of plasma sufficiently large containing enough charged species, the net electric charge must be zero.

The second criterion is the ‘plasma approximation’ stating that charged species must be close to each other, so that they influence many nearby charged species and not simply the closest one. This leads to an important plasma parameter, known as the Debye length, being the spherical distance over which the electrical field of an individual charged species can influence and be felt by other charged species. The Debye length  $\lambda_D$  is proportional to the temperature  $T$  and inversely proportional to the electron number density  $n_e$  according to:

$$\lambda_D = \left( \frac{\epsilon_0 k T}{n_e e^2} \right) \quad (1.10)$$

where  $\epsilon_0$  is the permittivity of free space ( $8.85 \times 10^{-12}$  F/m),  $k$  is the Boltzmann

constant ( $1.380 \times 10^{-23} \text{ J/K}$ ), and  $e$  is the electron charge. A necessary requirement for the existence of a volume of plasma is that the dimensions ought to be large compared to the Debye length. This means that interactions in the bulk of the plasma are more important than edge effects. That is because introducing a boundary surface to a plasma system will induce a disturbance in the local electrical neutrality of the plasma, with a layer thickness of a Debye length, called the plasma sheath.

The last criterion defines that the plasma frequency, i.e. the natural oscillation of the collective species motion when a plasma is disturbed, has to be large compared to the reactive collision frequency. This means that the electrostatic interactions between the charged species are dominant over the process of ordinary gas kinetics that can and will happen.

As long as a gas loosely follows the three criteria, it can be considered in the plasma state, and thus called a plasma. The plasma state can be characterised by a few major parameters, such as the ionisation degree, charged species densities, and bulk and electron temperature (measure for energy). Although plasmas can exist both at low and high temperatures, these last parameters are used to differentiate the plasma in thermal plasmas, where the temperature of the heavy species is equal to the electron temperature, and non-thermal plasmas, where the temperature of the heavy species is a lot lower compared to the electron temperature.

So, in the end, what is plasma then? Plasma is in essence just ... plasma, a state of its own with unique characteristics and more to offer than a gas. It consists of highly energetic electrons and reactive heavy species, that upon collision with each other can break and form chemical bonds; and that is where, practically speaking, the real magic happens.

### 1.2.2 Plasma chemistry

The consequence of the existence of highly energetic free electrons and reactive heavy species (ions and radicals) in a plasma is that at some moment they will collide into others, exchanging energy. These collisions happen all the time and can have many forms: going from a simple energy transfer to breaking or forming chemical bonds. An overview of typical reactions occurring in a plasma are shown in table 1.1 [26].

**Table 1.1:** Overview of typical reactions in a plasma. A and B are atoms, while M represents an arbitrary collision partner [26].

Type	Reaction
<b>Electron reactions</b>	
Non-dissociative ionisation	$AB + e^- \longrightarrow AB^+ + e^- + e^-$
Dissociative ionisation	$AB + e^- \longrightarrow A^+ + B + e^- + e^-$
Polar dissociation	$AB + e^- \longrightarrow A^- + B^+ + e^-$
Electron attachment	$AB + e^- \longrightarrow AB^-$
Dissociative electron attachment	$AB + e^- \longrightarrow (AB^-)^* \longrightarrow A^- + B$
Excitation	$AB + e^- \longrightarrow AB^* + e^-$
Dissociation	$AB + e^- \longrightarrow A + B + e^-$
Electron attachment	$A + B + e^- \longrightarrow A + B^-$
Step-wise ionisation	$A + e^- \longrightarrow A^* + e^- \longrightarrow A^+ + e^- + e^-$
Electron-ion recombination	$A^+ + e^- + e^- \longrightarrow A^* + e^-$
Electron-ion recombination	$AB^+ + e^- \longrightarrow AB$
Dissociative electron-ion recombination	$AB^+ + e^- \longrightarrow (AB^*) \longrightarrow A + B^*$
Radiative electron-ion recombination	$A^+ + e^- \longrightarrow A^* \longrightarrow A + h\nu$
Electron impact detachment	$AB^- + e^- \longrightarrow AB + e^- + e^-$
<b>Atomic reactions</b>	
Penning dissociation	$AB + M \longrightarrow A + B + M$
Penning ionisation	$AB + M^* \longrightarrow AB^+ + M + e^-$
Charge transfer	$A^+ + B \longrightarrow A + B^+$
Charge transfer	$A^- + B \longrightarrow A + B^-$
Ion-ion recombination	$A^- + B^+ \longrightarrow AB$
Ion-ion recombination	$A^- + B^+ + M \longrightarrow AB + M$
Neutral recombination	$A + B + M \longrightarrow AB + M$
Associative detachment	$A^- + B \longrightarrow (AB^-)^* \longrightarrow AB + e^-$
Detachment	$A^- + B^* \longrightarrow A + B + e^-$
<b>Decomposition reactions</b>	
Electron impact dissociation	$AB + e^- \longrightarrow A + B + e^-$
Energy transfer dissociation	$A^* + B_2 \longrightarrow AB + B$
<b>Synthesis reactions</b>	
Attachment	$A + B \longrightarrow AB$

There are also a lot of extra energy transfer pathways via translational and vibrational (excited) modes of the different molecules [26]. The natural vibrations in CO<sub>2</sub> for example have the opportunity to be excited through different levels until it reaches an energy level high enough to split the CO<sub>2</sub> spontaneously into CO and O [27]. The vibrational levels can also undergo many reactions with other species on their own. This makes for a tremendous number of possible reactions that can occur in a plasma, typically reaching hundreds for atomic gases and thousands for molecular gases [25,26]. They are, however, not all of them as likely as another to happen, with some reactions having a clear higher share. Certain types of plasma generators/reactors are more likely to



induce energy transfer via vibrational modes of molecules (microwave or gliding arc reactors), while others are more likely to induce energy transfer via electron impact electronic excitation or ionisation reactions (dielectric barrier discharge reactor) [28]. In the former case, the energy transferred into translational and vibrational modes is a significant pathway for energy dissipation into the system, effectively heating up the gas and losing the energy.

There is also a small side-effect that has little effect on the reaction chemistry, but is accountable for one of the most recognisable effects of a plasma: the radiative relaxation of excited species. Excited species can relax to a lower state releasing photons in the process, resulting in the typical light-emitting glow of a plasma. The colour is related to the gas specific relaxations happening in the plasma, making it also useful to perform diagnostics on plasma species densities.

### 1.2.3 Plasma generation

The plasma state is the most common state that matter can exist in, in fact more than 99% of matter in the universe is in the plasma state, most noticeably the stars activated by their high energy densities and interstellar voids weakly activated by solar radiation at low pressures [26]. Natural induced plasmas do occur on earth as well, but are limited to lightning (electrical discharge over a high potential electromagnetic field), some parts of a flame that can be described by the plasma state, and auroras where higher layers of the atmosphere at reduced pressures get ionised by solar winds (charged solar particles), see figures 1.8a and 1.8b.

Plasmas can, however, also be generated artificially by adding energy to a gas, so that the atoms and molecules split into free electrons, ions, radicals, and excited species, see examples in figures 1.8c and 1.8d [29]. This is usually accomplished by three main mechanisms, i.e. via heat, electromagnetic fields, and electromagnetic radiation. By adding energy in the form of heat to a gas, the atoms and molecules will gain kinetic energy and increase the energy exchanged upon collision, as defined by the thermal equilibrium, until it reaches a certain threshold that free electrons and charged species are formed besides neutral species. This requires temperatures of over 10000 K, that are far above any useful and efficient level.

A large portion of plasma generators use an external electromagnetic field to generate a plasma. An electromagnetic field generated by applying a potential

difference over two electrodes will induce a force on the accidental free electrons and ions present in a gas. If the electromagnetic field is sufficiently high and reaches a certain gas specific threshold (also known as the breakdown voltage), it can strip electrons from atoms or molecules, also producing positive ions. The available or stripped electrons will be accelerated towards the positive electrode and the available or produced positive ions will be accelerated towards the negative electrode, both gaining kinetic energy. These high energy generated charged species will collide into other (neutral) species, exchanging energy, leading to more charged species, and resulting in a chain reaction of generating high energy species. This phenomenon is called the Townsend discharge or Townsend avalanche. The gas is now “ignited” and as long as it is fed by the external electromagnetic field, the plasma state will exist. From this moment, the plasma state can undergo the multitude of possible reactions shown in section 1.2.2, until the field is lifted and the atoms and molecules present at that moment will regain their neutral ground state in a new chemical equilibrium. This type of plasma generation can be combined with an additional magnetic field, to shape or confine the plasma into a specific shape for optimal use.

The breakdown voltage is one of the most important parameters when designing the electric field based generators. It is important to understand how this parameter is affected and minimised for more practical usage, as the high voltage power source must be able to generate and maintain a high enough potential difference. Paschen’s law [30] describes the relation between the product of pressure  $p$  and discharge gap length  $d$ , and the breakdown voltage  $V_B$  for a specific gas at a certain temperature according to:

$$V_B = \frac{Bpd}{\ln(Apd) - \ln\left[\ln\left(1 + \frac{1}{\gamma_{sc}}\right)\right]} \quad (1.11)$$

where  $A$  and  $B$  are gas specific constants describing the saturation ionisation in the gas at a particular electric field/pressure proportion, and the excitation and ionisation energies, respectively.  $\gamma_{sc}$  is the secondary electron emission coefficient (the number of secondary electrons produced per incident positive ion). This equation results in the typical Paschen curve seen in figure 1.9, where the larger the pressure and/or gap distance, a higher breakdown voltage is required. On the other hand, lowering either or both of them too much results

as well in a rapid increase in breakdown voltage, as the mean free path nears the Debye length. Besides the pressure and gap distance, the breakdown voltage is mainly affected by the gas type (different  $A$  and  $B$  constants), resulting in different Paschen curves, and also the temperature, as this affects the required excitation and ionisation energies in constant  $B$  with higher temperatures lowering  $V_B$ . Be aware that the breakdown voltage is only the required potential difference to initiate a plasma, a lower potential difference, the burning voltage  $V_{Bur}$ , is necessary to maintain a plasma, similarly to the difference in static and kinetic friction forces when moving an object subjective to friction.

The last main method of plasma generation is by electromagnetic radiation [29]. Specific vibrational modes of a molecule can be targeted and amplified by directing and focussing electromagnetic radiation into a gas. Increasing the internal energy of the molecules above the breakdown threshold will result in the formation of the plasma state and induce the plasma chemistry. The most used electromagnetic radiation are radio frequency radiation or microwave radiation, with some specific applications using high power laser radiation.

These artificially generated plasmas can be used for a variety of cases, subdivided into three major categories, i.e. heat transfer, light generation, and reactions [29]. Plasmas can be used as a medium for high heat transfer such as in cutting or welding of metals. Although called a side-effect in section 1.2.2, the emission of light by plasma is one of the more civil used applications in e.g. fluorescent light bulbs and tubes, certain lasers, and television back-lighting (called the plasma TV). However, the category of most scientific interest is the capability of plasma for complex chemical reactions. There are applications that have been used for decades, such as ozone generation for water treatment, chemical vapour deposition, etching and modification of surfaces in e.g. chip development or surface modifications, and pollutant destruction. More recently, the possibilities of plasma for chemical synthesis of products have been explored more with examples being  $\text{CO}_2$  conversion and nitrogen fixation, but also medical applications in treatment of tissues, blood, micro-organisms, and cancers.

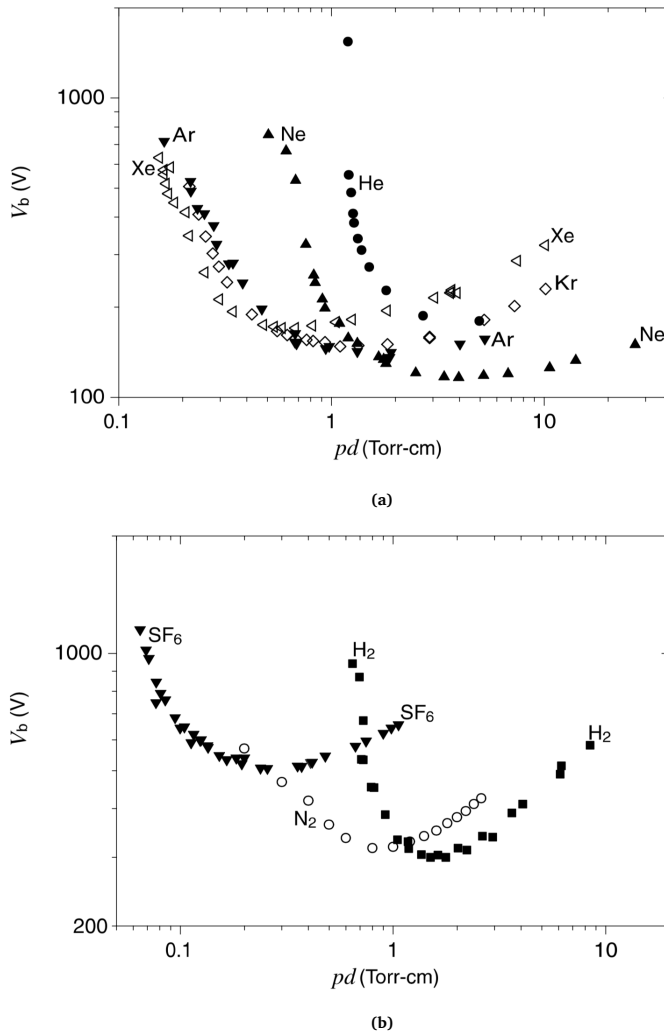


**Figure 1.9:** Breakdown voltage as a function of the pressure-discharge gap product, i.e. the Paschen curve, for parallel-plate electrodes at 20°C for a selection of (a) noble gases and (b) molecular gases. Adapted from [31].

### 1.2.4 Plasma reactors

A large number of different plasma devices can be designed based on the fundamental generation principles highlighted in section 1.2.3. A difference can be made between plasma generators and plasma reactors. Plasma generators generate a plasma for producing certain reactive, sometimes short-lived, species to use for specific treatments in a separate step, such as ozone for waste water or air treatment, or reactive oxygen and nitrogen species in the treatment

of cancers. Plasma reactors are used for the conversion of gases into other stable gases as a traditional reactor would do, such as VOC destruction, CO<sub>2</sub> conversion, or NH<sub>3</sub> synthesis.

Despite the extensive use of thermal reactors, i.e. reactors that operate completely according to the traditional thermodynamic equilibrium by regulating the temperature, plasma reactors offer a number of interesting opportunities. Due to the direct stimulation of the gas molecules via vibrational excitation or electron impact reactions, an overall net shift in the chemical composition can be induced without raising the entire gas temperature required according to the thermodynamic equilibrium [29]. The stimulation in a plasma reactor from a stable gas to a (partial) activated state, both at or near room temperature, is virtually without delay (hundreds of nanoseconds), as well as the return to the ground state. Therefore, a plasma reactor, and thus the conversion of gases, can be switched on and off instantaneously at command. Attempting the same in a traditional thermal reactor would require a lot of energy to not only heat up the reaction gas, but also the entire reactor body and catalytic bed if present, to perform any chemical reaction [32]. Shutting the reactor down will release all that latent energy, requiring additional techniques to attempt to recover the energy. Although thermal reactors are still the preferred type of reactor for industrial processes that run continuously, they are not useful for intermittent use, as proposed in this work, giving plasma reactors a high potential use.

As mentioned in section 1.2.2, plasmas suffer as well from heat losses, so the reactor body, and catalytic bed if present, will collect latent heat. These are usually highly limited due to low input energy or shielding effects under influence of reactor configuration. This does result in some thermal stabilisation of the reactor. As the plasma loses some energy into translational energy (and into the reactor body), the gas heats up, resulting in a lowered breakdown voltage, requiring adjustment of the reactor input parameters (e.g. lower voltage for a constant power). This process is still in the minutes range and is of minimal influence on the chemical product composition in comparison to its thermal counterpart.

Irrelevant of the application for which the plasma is used, a number of types of plasma reactors closely related to this work will be highlighted.

#### 1.2.4.1 Direct current (DC) discharges

One of the main categories of electromagnetic-field-based plasma reactors are all generated using essentially the most simple set-up, i.e. two electrodes separated by the gas that needs to be activated. Note that in certain cases, a physical second electrode is not required, as a nearby surface or even free gas can act as the “second electrode” [26]. By applying a sufficiently high DC voltage, the gas will start to ionise and will locally turn into the plasma state, resulting in a current flowing from one electrode to the other. This flow of energy can, however, happen in a few different ‘modes’ depending on the amount of current that is associated with it, see figure 1.10.

As seen in section 1.2.3, the first activation of the gas occurs via a Townsend discharge as the potential increases, resulting in a low current. As the discharge grows, the current can increase and can change in a mode called the corona discharge, where plasma streamers can become visible but are still characterised by low current. If the conditions are right, i.e. type of gas, pressure, temperature, and discharge gap, the discharge can “stabilise” in the glow regime, where a lower voltage is required to maintain the plasma state. Again, depending on the conditions, the current could increase, holding sufficient energy to physically bridge the entire discharge gap and form an arc discharge. A free path is now available for the potential energy, and current will increase dramatically. This state releases high amounts of energy in the gas, increasing the energy of both electrons and heavy species towards a thermal equilibrium plasma. Not only the plasma channel but also the neighbouring gas and reactor parts will heat up, leading to non-ideal situations, e.g. melting of reactor parts.

The shape and size of the different discharge modes in the graph depends on the gas. Tuning the discharge conditions by applied voltage and current, but also by pressure, temperature, and gas flow (also affects temperature) can alter the discharge mode that is desired.

***(Gliding) arc discharge*** Although being the most easy way of generating a plasma, only requiring two electrodes and enough power to form the arc, an arc discharge reactor usually needs a bit more design to embrace this type of plasma discharge in a useful way. Simply using two parallel electrodes would result in an arc formation at a random spot, or at a spot of contamination on

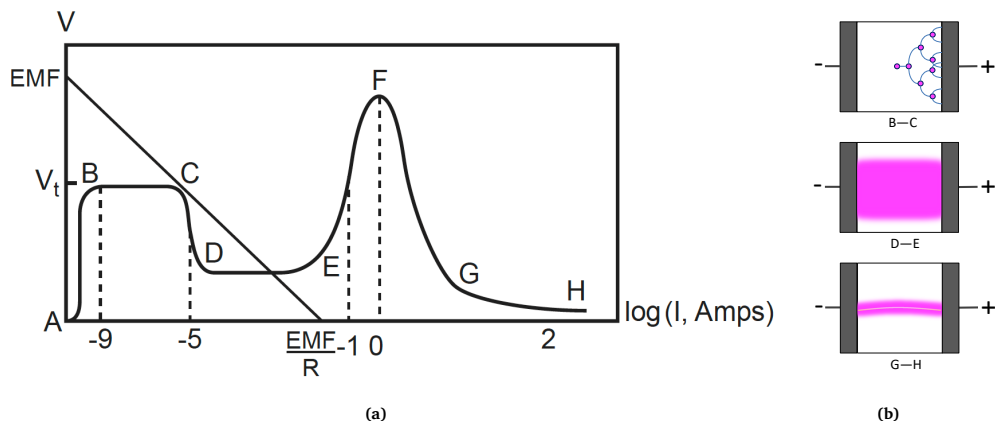


**Figure 1.10:** (a) Generalised current-voltage characteristic of DC discharges (adapted from [26]) and (b) a schematic representation of the different discharge modes.

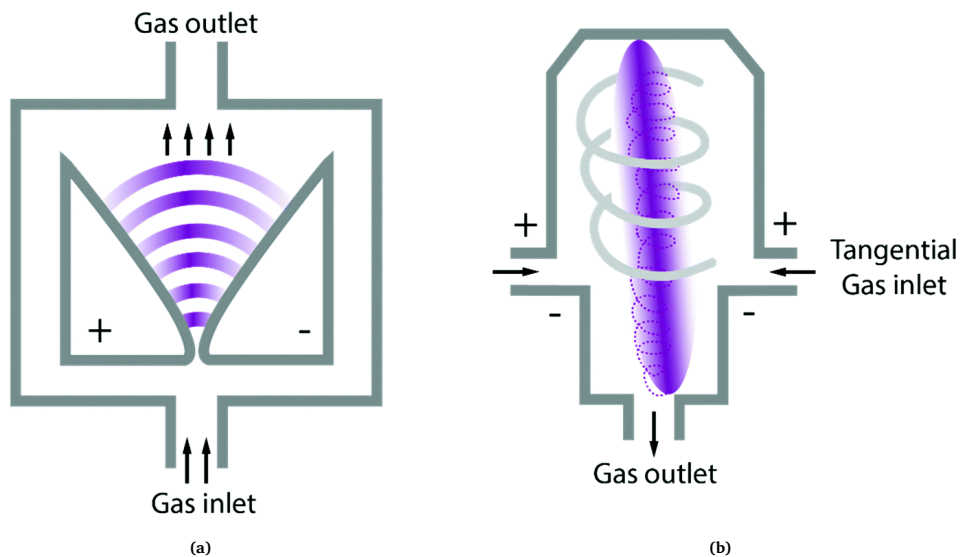


**Figure 1.11:** Schematic representation of the (a) traditional divergent-electrode gliding arc reactor, and (b) gliding arc plasmatron. Adapted from [8].

the electrode surface, and would generally stay there with the rest of the reactor unactivated.

Clever design using two divergent electrodes generates a dynamic arc discharge, see figure 1.11a. At the point where the electrodes are closest, the typical arc discharge will initiate. Helped by gas heating due to heat losses of the plasma, and directing the reagent gas flow through the device, the arc will expand towards the top of the arc ladder, converting gas on its path,

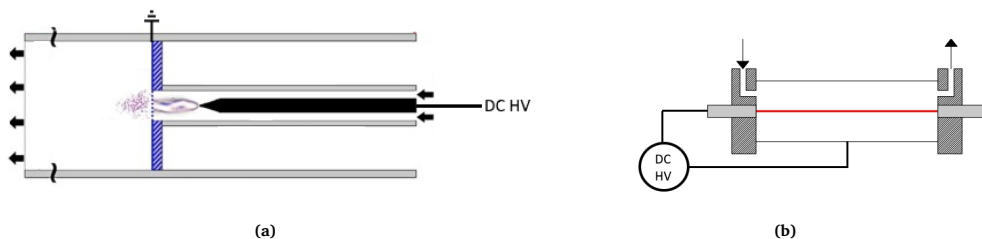


**Figure 1.12:** Schematic representation of a (a) glow discharge reactor, and (b) corona discharge reactor. Adapted from [35] and [36].

and extinguishing at the end. Although a significantly improved design, not all reagent gas is activated between the individual arc discharges [8]. Also, considerable heat losses result in electrode degradation and require additional gas to cool the reactor via bypasses, lowering the conversion even further.

Innovative adaptations to the classical 2D gliding arc reactor have successfully resolved this issue [33]. A cylindrical reactor with tangential gas inlets has led to a vortex flow gliding arc regime, stabilising the plasma arc in the centre of the cylinder, as shown in figure 1.11b. By limiting the size of the reactor outlet at the bottom of the reactor, the inflowing gas will first flow up the end of the reactor in an outer vortex, effectively shielding the discharge in the centre from the reactor walls, and then travelling via the centre downwards (reverse inner vortex) being reacted by the plasma discharge. This design, although more difficult in manufacturing and with a smaller operating window (voltage, current, flow rate, and gas mixtures), has gained a lot of interest due its promising results.

**(Atmospheric pressure) glow discharge** Glow discharge reactors, such as the atmospheric pressure glow discharge (APGD), try to operate in the more stable glow mode [34], as seen in figure 1.10. By typically using a sharp pin high voltage electrode facing a grounded plate, with the gas flowing parallel to the pin, a glow discharge can occur between the pin and plate that is both cooled and stabilised by the gas flow to not transition to the arc mode, see figure 1.12a. A continuous higher voltage and low current state is maintained ideal for plasma-based gas conversion, mostly promoting the molecule activation, and minimising relaxations and energy heat losses.

A major downside of this type of reactor is the axial gas flow with respect to the



discharge, resulting in only a partial treatment of the reaction volume, and still electrode overheating can be an issue [34]. The limited fraction of gas treated by the plasma could be successfully increased by confining the reaction volume, while the electrode overheating can be avoided by using a vortex flow, resulting in more gas mixing and cooling of the electrode.

**Corona discharge** The corona discharge reactor is usually operated by using a thin wire-to-surface or a pin-to-plate design, see figure 1.12b. In order to limit the discharge propagation at the corona mode, and not transition into glow or arc mode, a pulsed high voltage is used at short intervals (typically in the 1-100  $\mu$ s range) [36]. However, due to their lower energy density and low reaction volume treatment, these reactors are not used frequently in gas conversion processes, with a few exceptions in diluted waste gas treatment, but more so in surface treatment applications, such as surface charging in industrial printers.

### 1.2.4.2 Microwave discharge

Microwave plasma reactors make use of electromagnetic radiation, usually in the 300 MHz to 10 GHz range, to excite molecules and induce reactions. There are a number of different types of microwave reactors, with the most common one for CO<sub>2</sub> conversion applications being the surface wave discharge, see figure 1.13 [8]. In this configuration, the gas flows through a quartz tube with a perpendicular positioned microwave generator and waveguide intersection with the tube. At the tube—waveguide cross section, plasma is generated by microwave absorption, and reactions take place along the axis of the tube with part of the gas flow shielding the tube walls from the plasma.

There is a lot of interest in this type of plasma reactors, as they have the potential of more efficiently activating gases due to their more direct coupling with gas vibrational modes. In the case of CO<sub>2</sub> dissociation, they can induce (partial) vibrational ladder climbing for splitting reactions that require less net energy in comparison to electron impact dissociation.

There are, however, also some downsides to microwave plasma reactors. A first is poor performance at high pressures that are more desired in industrial applications, as vacuum pumps have high operating costs. At these higher pressures, the plasma tends to approach a thermal plasma state. Also, this

type of reactor is less suited to be combined with single-stage plasma catalysis (see section 1.3.3.4) due to high heat and possible microwave absorption by the packing material. Finally, they are generally more complex and bulkier in design.

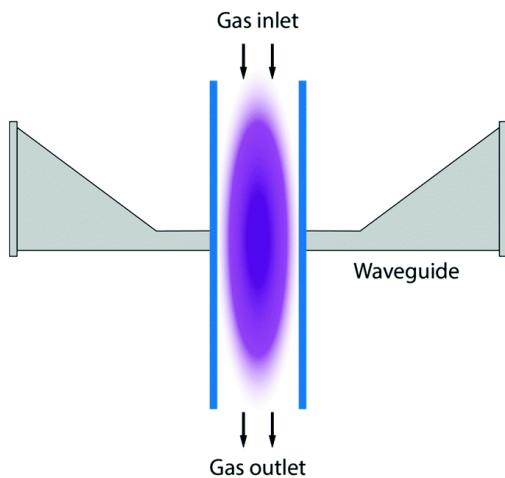


**Figure 1.13:** Schematic representation of a microwave plasma reactor. Adapted from [8].

## 1.3 Dielectric barrier discharge (DBD) reactor

Another type of plasma reactor that is often used for gas conversion applications, is the dielectric barrier discharge (DBD) reactor. It resolves a particular issue of some of the DC-based types mentioned in section 1.2.4, i.e. the high energy arc formation. It has already a long history with a number of industrial uses that might have potential in the conversion of CO<sub>2</sub> [37].

### 1.3.1 General structure

In order to resolve the arc formation that typically occurs in a DC discharge between two electrodes, a DBD reactor is constructed by adding, as the name implies, one (or two) dielectric barrier(s) between the electrodes [37], see figures 1.14 and 1.15. This evens out, or distributes, the electromagnetic field over the entire dielectric surface, but has one major consequence. As a discharge propagates between the electrodes via similar steps as the DC discharge explained in section 1.2.4.1, the dielectric surface gets locally charged at the place of impact and opposes the overall affecting electric field, extinguishing the discharge, as schematically shown in figure 1.14. As the main channel of energy flow is now shut off, but the overall electromagnetic field is still present, another arc forms and the cycle repeats over and over, until the entire dielectric surface has an opposing charge and no further arc can be formed. This is resolved by reversing the applied potential over the electrodes and thus using an alternating current (AC).

The DBD reactor can come in a number of different configurations, such as with one or two dielectrics, surface discharge or volume discharge, parallel plate or concentric design, etc. [37], see figure 1.15. Irrelevant of the specific case, it is always constructed by two electrodes, one grounded electrode and one connected to an AC high voltage source, separated by one or two dielectric layers. The reactor body provides the gas inlet and outlet and shapes the reactor gas volume. The free distance between the dielectric and one of the electrodes, or the two dielectrics, is called the discharge gap. In this thesis the two most used configurations will be studied, i.e. the single-dielectric, volume discharge type in both a parallel plate and concentric design. The volume discharge ensures maximum plasma distribution over the reactor volume, while the

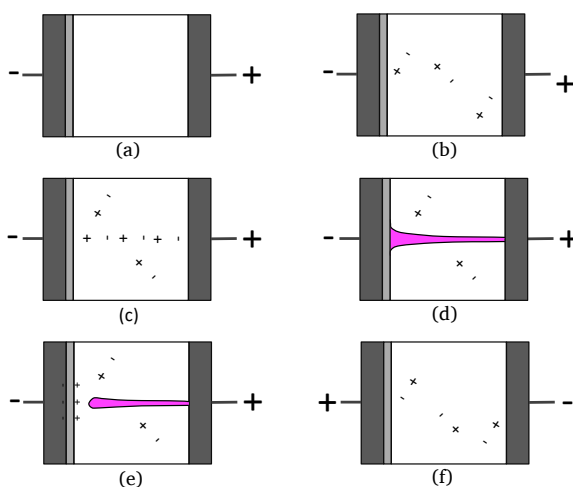


**Figure 1.14:** Schematic representation of the different stages in the DBD micro discharge formation, here displayed for a single discharge. (a) Start, (b) Townsend discharge, (c) channel of charged species, (d) micro discharge, (e) extinguishing of discharge due to polarisation of dielectric, and (f) applying reverse electric field for new discharge.

single dielectric simplifies the reactor design, if there is no need for double dielectrics when gas/plasma-electrode interactions might be of concern. The designs shown in figure 1.15 display their respective typical structure. The concentric design, as used in chapters 2 to 5, is preferred, because it is simpler to construct, as one electrode and the dielectric shape the reaction volume without any supplementary walls. This does, however, limit the options delivering and mixing the gases in the reactor. The parallel plate design, as used in chapters 6 and 7, is more flexible in design and use, but needs additional materials to contain and seal the reaction volume. Both designs will be discussed later in more detail.

The DBD reactor typically operates within a gap size range of 50  $\mu\text{m}$  to 5 mm, with pressures varying between partial vacuum and up to 6 bara, but usually staying within 1 and 1.5 bara [37]. The flow rate fed into the reactor can have a wide range, from millilitres to litres per minute, largely affecting the conversion and pressure in the reactor. The applied frequency can be varied from 50 to 50000 Hz and usually depends on the power source being used or the preference of the user. The frequency is believed to have an influence on the plasma discharge, but this is both supported and rejected by research and

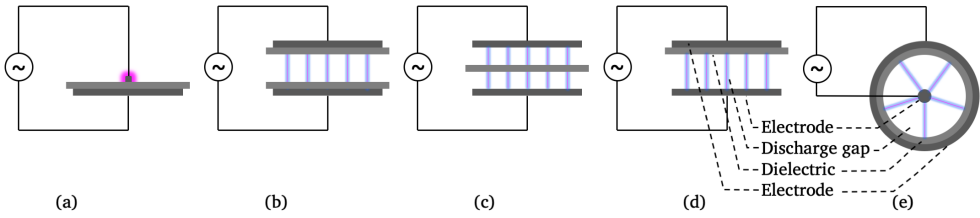


**Figure 1.15:** Schematic representation of some of the typical configurations used for a parallel-plate DBD reactor, i.e. (a) a surface discharge DBD, (b) dual-dielectric DBD, (c) centre-placed single-dielectric DBD, and (d) electrode-placed single-dielectric DBD. These configurations can also be used in a co-axial version. A co-axial version of (d) is shown in (e). Combinations of these structures are possible.

is probably dependent on a mixture of reactor geometry, gas parameters, and the possible interaction with a packing material [38, 39]. Finally, the applied voltage is completely dependent on most of the previous parameters, the type of gas being used, and the desired power level. A bigger gap, higher pressure, and lower frequency [39] require a higher applied voltage, with the type of gas influencing the Paschen curve, as seen in section 1.2.3.

As the applied electrical power is the plasma reactor equivalent of the thermal flux in a thermal reactor, precise monitoring of the electrical parameters is key in tuning the plasma reactor for a desired conversion level; more power results in more conversion. This can be done in two ways, with the first being the more traditional monitoring of the applied voltage  $U$  and resulting current  $I$  over a number  $n$  of consecutive periods  $T$ , see figure 1.16a, and calculating the power  $P$  according to:

$$P = \frac{1}{nT} \int_0^{nT} U(t)I(t)dt \quad (1.12)$$

The alternative is making use of the more fundamental displacement of charges in the reactor. By adding a monitoring capacitor in series with the reactor and measuring the voltage drop over the capacitor, we can measure this charge displacement  $Q$ . As proposed by Manley in 1943 [40], plotting a Lissajous curve (an X-Y plot of two time dependent parameters) of the applied voltage and the resulting charge for a DBD plasma reactor theoretically results in a parallelogram shaped curve, see figure 1.16b. This is due to the capacitive nature of the DBD reactor (basic capacitor construction) and having two distinct operating modes during one period half-cycle, i.e. a capacitive mode when

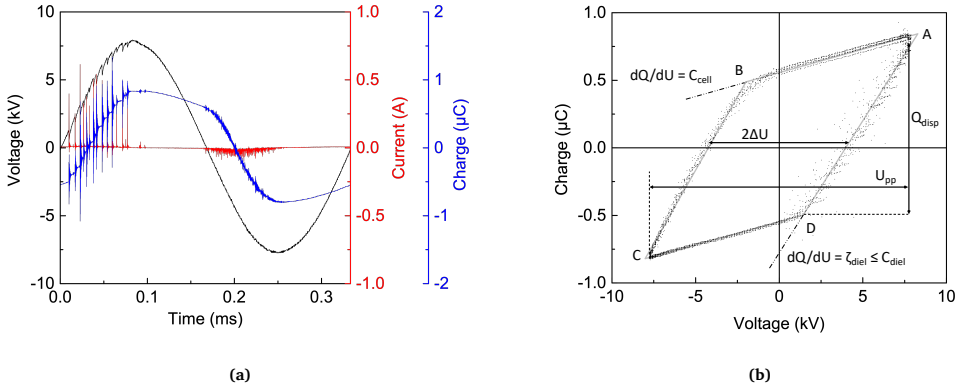


**Figure 1.16:** Example of a typical (a) oscilloscope displaying the applied voltage, and resulting current and displaced charge, and (b) a charge ( $Q$ ) – voltage ( $U$ ) Lissajous figure.

the potential reverses and a discharge mode when the potential difference is high enough, with two different capacitances. The area of the Lissajous curve, combined with the frequency (or inverse period  $T$ ), is a measure of the power according to:

$$P = \frac{1}{T} \oint U(Q)d(Q) \quad (1.13)$$

This convoluted way of calculating does have beneficial use over the traditional  $P = UI$  method in that it captures fundamental data on the reactor geometry and the quality of the plasma discharge itself, see figure 1.16b [41]. This is further discussed and used in chapter 2 and its appendix A.

### 1.3.2 Motivation and limitations of a DBD reactor

The DBD reactor saw its first use all the way back in 1857 [37]. Werner von Siemens experimentally investigated the generation of ozone from oxygen or air by using a co-axial double dielectric DBD reactor. Ozone generation for water treatment via chemical oxidation stayed the main research topic and industrial application, dubbing the DBD the “ozoniser discharge”, with more and more understanding of the DBD process and optimisations over the years. Figure 1.17 shows a modern day DBD ozone generator used by SUEZ – Water Technologies & Solutions. It wasn’t until about 30 years ago that additional applications emerged, such as surface modification, plasma chemical vapour deposition, pollution control, excitation of  $CO_2$  lasers and excimers, and large-area flat plasma display panels, known as the plasma television. In the last ten years, the

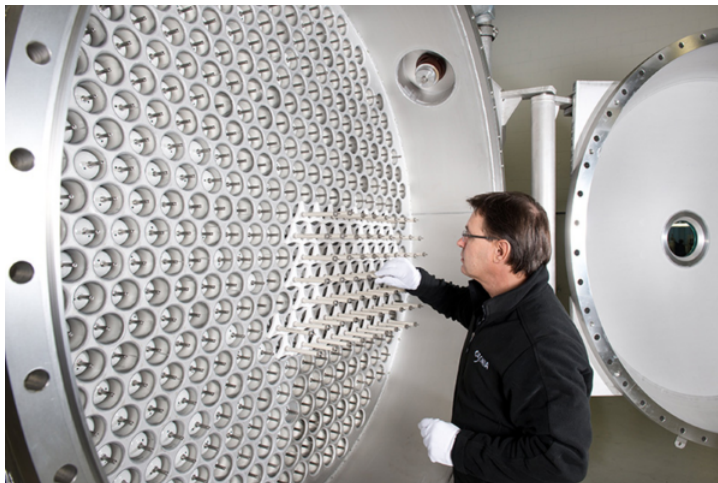


**Figure 1.17:** Example of a commercial DBD ozone generator. It displays an array of parallel co-axial DBD reactors to allow a high gas throughput. Courtesy of SUEZ – Water Technologies & Solutions [44].

use of the DBD reactor skyrocketed as a ‘novel solution from the past’ to combat the ever growing air pollution, CO<sub>2</sub>, and climate change. DBD reactors started to be used for VOC abatement with conversions near 100% [42], CO<sub>2</sub> conversion via several reaction schemes [8], and nitrogen fixation reactions (NO<sub>x</sub>, NH<sub>3</sub>, HNO<sub>3</sub>, etc.) to be used in the fertiliser industry [43].

Although different types of plasma reactors do exist, the DBD reactor was and still is one of the mostly used reactors for plasma-based gas conversions. Its simple and robust design that is easily up-scalable via parallelisation (as been done for ozone generation) [37], as well as miniaturisable and highly adaptable in design [45–53], results in its in a wide variety of applications [8, 42, 43]. It has little to no limitations about which (humid) gases are fed to it, and it can be used in a wide pressure range from low vacuum to several bars. This high pressure is especially important, as most industrial processes operate at elevated pressures, rendering a microwave plasma reactor less useful [54]. Also its feed rate is highly flexible from millilitres per minute up to litres per minute, depending on the design and desired conversion level, compared to other plasma reactor types (gliding arc, glow discharge, and microwave), requiring more limited ranges of flow rate of litres per minute, due to heat and plasma stability issues. Minimal wear and tear is seen in this type of reactor, as the arc energy is limited due to the dielectric barrier in comparison with the DC-based discharges where electrode erosion is a common problem.

There are, however, also a few drawbacks. Although a DBD reactor can operate in a glow discharge like mode (under very specific conditions), the filamentary discharge mode is a lot more common, resulting in the DBD micro discharges. This behaviour makes that only small portions of the reaction volume are being excited at a time, as the typical diameter of a micro discharge is about 100  $\mu\text{m}$  and lasts for a few hundred nanoseconds [37]. The DBD reactor does operate more like thousands of tiny batch plasma reactors, with all tiny sections having a certain chance to be discharged or not. A given volume of molecules will therefore experience a sequence of neutral gas, excited plasma, and return to neutral gas states as it travels from the reactor inlet to the outlet. This behaviour results in a somewhat less ideal method of plasma-based gas conversion in comparison to a stable glow plasma discharge, giving the DBD reactor a fairly low performance, especially for synthesis reactions and dissociation of stable molecules. Also, as the plasma discharges can initiate hundreds, up to thousands, of reactions, there is increased chance of back reactions or further reactions of the desired products. Finally, although the reactor is capable of reaching competitive conversions, these have to be accompanied by high energy input, resulting in low efficiencies.

In order to make the DBD reactor as a whole more competitive with its noticeable pros, a more efficient coupling between electrical energy, gas, and chemistry is needed.

### 1.3.3 Opportunities for performance enhancement

Despite the low base performance of the DBD reactor, there are a number of opportunities to explore in order to enhance its performance. First and foremost, a parameter optimisation is required to obtain the optimum result from any reactor. A lot of research has examined the obvious parameters of the typical DBD reactor, being the voltage/power, AC frequency, gap size in the millimetre range, flow rate, electrode material, dielectric material, and dielectric thickness, each with their specific effect on the reactor performance. In general, the conversion increases with higher power, lower frequency, smaller gap size, lower flow rate, and thicker dielectrics [38, 39, 55–57]. The reactor configuration aspects show interesting improvements, such as using the inner electrode as the high voltage electrode, and using tungsten or copper as the inner electrode could improve



conversion, but copper is more prone to corrosion [57], and an  $\text{Al}_2\text{O}_3$  dielectric improving the performance of a quartz dielectric [57, 58]. However, besides the parameter and reactor material optimisation of a given reactor, there is opportunity for more significant improvements.

### 1.3.3.1 Micro discharge gap

The discharge gap size is a very important parameter for DBD reactors [59, 60]. It defines the reaction volume within a reactor, when the other dimensions are fixed (length and width in parallel plate design, length and inner diameter of dielectric in the co-axial single dielectric design), resulting in altered residence times for given flow rates. In addition, it also has major effects on the electrical properties of the reactor and the plasma. First of all, the required voltage to initiate an electrical discharge in the reactor is dependent on the gap size according to the Paschen curve (see figure 1.9a), influencing the electric field and subsequently the plasma in the reactor. Shrinking the discharge gap from the millimetre to the micrometre range can have some beneficial effects by strengthening the electric field generated in the reactor, as it is inversely proportional to the distance between the electrodes for a fixed voltage. It is therefore speculated that decreasing this distance, and thus increasing the electric field, will result in a more powerful plasma for the same applied potential. It could increase the conversion and efficiency substantially and also potentially stabilise the plasma discharge even more [61].

### 1.3.3.2 Packing materials and the influence of their individual parameters

A popular method to improve the performance of the DBD reactor is adding a packing material to the reaction zone, see figure 1.18b. By adding a packing material to the reaction volume, the plasma behaviour and related chemistry will be altered. Adding a packing material to the reaction zone will induce both physical and chemical changes, resulting in a wide variety of outcomes [62, 63]. A packing material can lead to electric field enhancement [64] by polarisation and surface roughness of the particles, as well as changing the discharge type, from filamentary micro discharges to surface discharges [65], or forming micro-

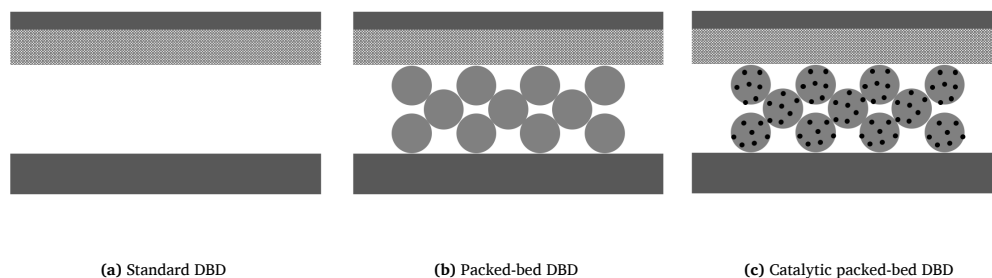


**Figure 1.18:** Schematic representation of (a) an empty DBD reactor, (b) a packed-bed DBD reactor filled with spheres for demonstrating purposes, and (c) a catalytically activated single-stage packed-bed DBD reactor.

plasmas in pores [66], altering the chemistry by (catalytic) surface reactions [62,67], changing the flow and mixing patterns, and reducing the residence time. Commonly, spheres or other shaped particles of different materials are applied [58, 68–74], but also wool-type materials, like glass wool for their high surface area, or ceramic foams for their rigid 3D structure [58, 68, 75, 76], are used. The drastic changes to the plasma discharge result in the high potential of packed-bed DBD reactors to show better performance than the traditional DBD reactor.

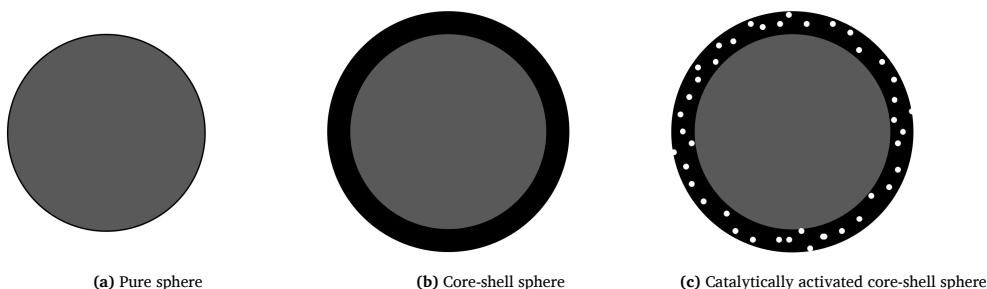
There is, however, a slight problem with this approach: each material has its fixed and specific properties that cannot be changed individually, such as size and shape, dielectric constant, (elemental) composition, surface roughness, thermal and electrical properties, porosity, etc., and these properties can influence the type of discharge, electron temperature and density, surface losses, etc. [60, 62, 77]. The plasma discharge is, as mentioned above, highly affected by these parameters.

In this work we will limit our investigations to spherical and fibrous packing materials with four compositions, i.e. spherical and fibrous  $\text{SiO}_2$ , spherical  $\text{Al}_2\text{O}_3$ , spherical  $\text{ZrO}_2$ , and spherical  $\text{BaTiO}_3$ . Each material has, as mentioned above, its specific properties with unique values that could potentially influence the reactor performance as summarised in table 1.2 for the spherical packing materials [78]. Note that these are only a handful of properties, others may have not been identified yet and could as well be of interest.

Finding the ‘most optimal’ packing material might require synthesising custom or hybrid materials to optimise all material properties to a specific reaction. A possible solution is the use of core-shell structured spheres. These materials

**Table 1.2:** Comparison of different properties for spherical packing materials of SiO<sub>2</sub>, Al<sub>2</sub>O<sub>3</sub>, ZrO<sub>2</sub>, and BaTiO<sub>3</sub>. Taken from [78].

Property	SiO <sub>2</sub>	Al <sub>2</sub> O <sub>3</sub>	ZrO <sub>2</sub>	BaTiO <sub>3</sub>
Molar mass (g/mol)	60.08	101.96	123.22	233.20
Density (g/cm <sup>3</sup> )	2.20	3.89	5.70	6.02
Thermal conductivity (W/mK)	1.38	28.0-35.0	1.7	2.85
Thermal expansion coefficient (10 <sup>-6</sup> /K)	0.550	5.8-8	12.2	11.4
Specific heat capacity (J/(gK))	0.99	0.798	0.456	0.406
Band gap (eV)	8.9	7.0	4.2	3.2
Dielectric constant	3.9	9	25	4000
Molar heat (J/(molK))	59.64	81.38	56.23	94.68
BET specific surface (m <sup>2</sup> /g)	0.5	0.08	0	0.8
Total open pore volume (mm <sup>3</sup> /g)	≈0	8.47	≈0	158.0
Pore size (μm)	≈0	0.080	≈0	0.87
Surface roughness (nm)	82 ± 3	150 ± 4	84 ± 1	590 ± 15

**Figure 1.19:** Schematic representation of (a) a pure sphere, (b) a core shell sphere, and (c) a catalytically activated core-shell sphere.

consist, as the name implies, out of core of a material A that is covered by a shell of material B (B can also be the same composition as A), as shown in figure 1.19a and 1.19b. The core will mainly determine the bulk effect of the entire sphere such as dielectric constant, thermal and electrical properties; while the shell, will determine mainly the surface effects such as porosity, adsorption, (electrical) surface properties, and surface chemistry, as well as some bulk effects, if the shell is made sufficiently thick, potentially shielding core effects. This way a custom, ‘most optimal’, packing material can be designed for optimal reaction performance. Additionally, only the porous shell could be catalytically activated to minimise the distance/time that activated plasma species have to travel to reach a catalyst spot, see figure 1.19c.

### 1.3.3.3 Reactor engineering

Reactor engineering, i.e. choosing the dimensions, the type of reactor, the method of feeding the reagent, etc., is a fundamental step in designing a reactor [79]. This is, however, a highly overlooked step in a lot of plasma-based gas conversion research. It is true that a lot of significant improvements have been or could be made by (and not limited to) the improvements mentioned in the sections above, i.e. parameter optimisation, packing materials, and catalysts, but large improvements could also be done by looking at the basic reactor engineering methods or other clever designs.

The DBD reactor (in either parallel plate or co-axial design, with or without packing) is virtually always used in a static ‘one inlet – one outlet’ design. While this might not really be an issue with a single-gas inlet stream, it is known from reaction engineering that such a design is rarely the best configuration for multi-gas inlet streams [79]. It can lead to reactor operation at non-ideal kinetic conditions, resulting in improper conversions of one or more of the reagents. This non-ideal behaviour of multi-gas reactions could be resolved by correct reactor design, such as the type of reactor (batch, perfect mixer, plug-flow, or combined “real” reactor), reactors in series and/or parallel, recycling, and/or separate addition of reactants [79]. Also the dimensions, and even shape, of a reaction zone, as well as the method of power delivery to the gas/plasma, might affect the reactor performance. Also active cooling of the reactor can promote shifting of the chemical equilibrium [80, 81].

There have been innovative solutions and alterations to the traditional DBD reactor design in an attempt to optimise its performance. Examples are a fluidised (catalytic) bed [46], forcing the gas flow through a thin-walled porous (catalytic) tube [47, 48], a sintered metal fibre (catalytic) electrode for product draining [49], a combined AC/DC DBD reactor for honeycomb structures [50], a DBD reactor combined with a solid oxide electrolyser cell (SOEC) [51], and a Y-shaped reactor, allowing separate addition of reagents [52, 53], see figure 1.20. Unfortunately, these attempts are very limited, with a lot of possible improvements still possible.

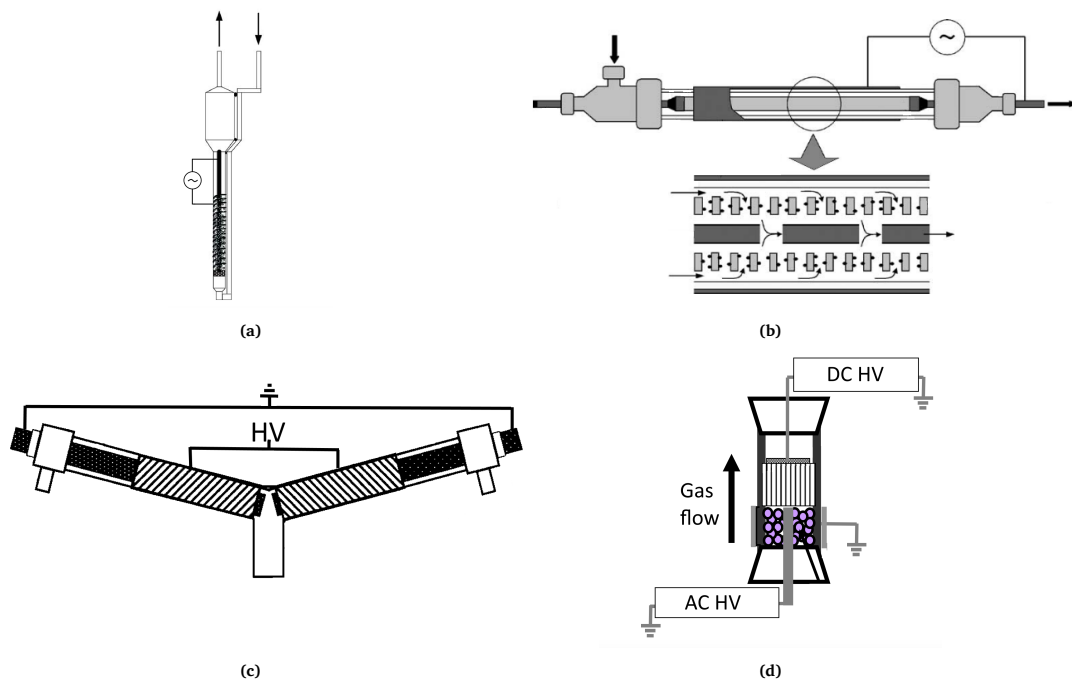


**Figure 1.20:** Examples of novel DBD reactor designs. (a) fluidised bed DBD reactor for DRM (adapted from [46]), (b) DBD reactor with an axially placed porous tube loaded with catalyst to force all gas flow via the catalyst (adapted from [47]), (c) Y-shaped dual DBD reactor for separate gas activation (adapted from [53]), and (d) combined AC/DC reactor where a DBD section is coupled to a DC field to stretch the plasma state through a honeycomb structure (adapted from [50]).

### 1.3.3.4 Plasma catalysis

Further improvement on section 1.3.3.2 can be done by adding a catalytically active element to the packing materials, see figure 1.18c [42, 67, 77, 82, 83]. Up to this point, all, or at least most, enhancements did influence either the physical aspects of the plasma (plasma properties) or the chemical equilibrium by changing the species concentrations by different mixing behaviours. The number one approach in traditional thermal reaction chemistry to enhance the reaction performance is the addition of a catalytic material [32]. A catalyst provides the reaction chemistry with an alternative pathway, increasing the reaction rate coefficient and/or improving the selectivity of the possible products. Also the plasma chemistry could benefit from both improvements, as higher rate coefficients could lead to higher conversions or even smaller reactors when operated below thermodynamic equilibrium. The enhanced selectivity might be the best reason to use a catalyst in a plasma reactor. It has been

shown that a plasma reactor can form a vast amount of species: for example tens of different (oxygenated) hydrocarbons when performing DRM [72, 84], different reactive nitrogen and oxygen species in humid air reactions [85], etc. There is, however, no method available to tune the plasma itself into selectively synthesising one molecule over the other. Add to this the relative higher instability of these desired products over the reagents, resulting in a fair amount of back reactions towards the reagents or smaller intermediate chemicals [77]. Enhanced selectivities by catalyst incorporation is therefore a highly anticipated effect when exploring, what can be called, plasma catalysis.

There are two main options, being single-stage or two-stage plasma catalysis [42, 82]. In single-stage catalysis, the catalyst is applied inside the plasma discharge zone; this can be either a catalytically active packing material or a catalyst deposited on the packing material support. It is suggested that the plasma discharge provides the initial dissociation and excitation/activation of the molecules, and that the catalyst can interact with these species and direct them into the desired chemistry [77]. This indirect activation of molecules can give plasma catalysis an edge over traditional catalysis, where the catalyst must be able to activate the molecules themselves [32]. The plasma-catalyst interaction can lead to the direct synthesis of the desired product on the catalyst surface, intermediate reagent synthesis aiding the product synthesis, or storing undesired species until later release (reactor swing use).

In two-stage plasma catalysis, the catalytic material is placed directly before or mostly behind the plasma reactor [42, 82]. The aim of this method is to generate long lived activated species in the plasma reactor and direct them on the catalytic bed for (thermal) catalysis. The lifetime of the activated species is, however, fairly short, i.e. 1-100 ns for vibrationally and electronically activated species [82], 100  $\mu$ s for positive ions, and even shorter for negative ions [86]. This route for plasma catalysis is therefore less suitable, and typically only of interest for plasma reactor types incompatible for the single-stage version, such as the gliding arc reactor, and with sufficiently high flow rates (and thus gas velocities) [87, 88]. Depending on the plasma reactor temperature, additional heating is required to have sufficient activity in the catalytic bed.

### 1.3.3.5 Alternative feed modes

The standard DBD reactor is usually operated in a continuous feed mode, i.e. the feed composition is stable during the entire operation. There are, however, reactions that are prone to depositing solids in a reactor, such as coking in DRM, clogging up parts of the reactor or poisoning catalyst material. These reactions could benefit from a swing feed mode between two feed compositions to maximise conversion. In the case of DRM, the CO<sub>2</sub>-CH<sub>4</sub> mixture producing coke can be switched to pure CO<sub>2</sub>, splitting it into CO and O<sub>2</sub> and using the latter to (partially) oxidise the coke in CO<sub>x</sub> [73].

Also clever use of ‘catalyst’ material and a swing feed mode can optimise conversion [78]. Capturing atoms/molecules on purpose on the catalyst surface during mode A can drive the reaction forward, while minimising unwanted side-products. During mode B the adsorbed species can be chemically released by a co-reactant to form a waste product, or preferably another valuable product. An example use is capturing oxygen atoms during DRM, to exclusively form hydrocarbons, followed by partial oxidation to CO.

This optimisation can be a valuable asset if the increased conversion rate benefits the decrease in original reactants feed rate. Parallelisation of two or more reactors in alternate modes can improve the overall efficiency.

### 1.3.3.6 Characterising the reactor kinetics and equilibrium

All adaptations to the standard DBD reactor proposed above will affect the reactor performance. Knowing how the performance changes by moving from one parameter/material/... to another is one thing, knowing why is another. This is especially a problem with plasma reactors, as changing one parameter can have an influence on many plasma or chemical parameters. Characterisation of a plasma reactor in a similar way as one does for a thermal reactor, by using an overall rate coefficient and thermodynamic equilibrium, would greatly reduce the tens of altered parameters down to only a handful.

The plasma in the DBD reactor is not in thermal equilibrium, which means that standard equilibrium thermodynamics is not applicable. However, as pointed out by Vepřek and co-workers [89–91], a kind of chemical equilibrium could still be reached in a plasma, where the total chemical flux (combined

consumption and production rate) of the reagent(s) is zero. Quantifying this partial chemical equilibrium (PCE) state can be used to uniquely characterise a plasma-based conversion process, because it directly depends on the plasma conditions. Furthermore, tracking how the plasma chemistry evolves from unreacted reagents towards the PCE can reveal an overall apparent rate coefficient. These new parameters, PCE and apparent rate coefficient, could be used to uniquely characterise a plasma-based conversion process and compare on a more fundamental level what ‘thermodynamically’ changes, despite the non-equilibrium nature of plasma.



## 1.4 Aim of this PhD work

The aim of this work is to explore the performance enhancement opportunities discussed in section 1.3.3. Although DRM is the targeted reaction in this thesis, also CO<sub>2</sub> dissociation and NH<sub>3</sub> synthesis will be used to analyse or isolate certain effects. The simpler chemistry of CO<sub>2</sub> dissociation allows us to ignore product selectivities when investigating the physical effects of packing materials, while NH<sub>3</sub> synthesis provides us with a different synthesis reaction to test if certain hypotheses for DRM are also valid for another reaction.

In chapter 2 we will investigate if it is possible to enhance the co-axial DBD reactor performance, in CO<sub>2</sub> dissociation, by using a micro discharge gap with or without the addition of non-porous spherical packing materials; referenced against a standard millimetre sized co-axial DBD reactor. Both the size of the gap and the spherical packing material will be examined, as well as the type of packing material, in terms of their effect on the reactor performance.

In chapter 3 we will dive a bit deeper into the material effect on the reactor performance. The concept of core-shell spheres will be explored to see whether the packing material composition can be tuned to the CO<sub>2</sub> dissociation reaction.

Chapters 4 and 5 will investigate if a partial chemical equilibrium exists in a DBD plasma reactor. We will test the CO<sub>2</sub> dissociation and dry reforming of methane (DRM) reaction for this behaviour, attempt to quantify it and link it back to different changes to the reactor parameters, such as power, gap size, packing material, and gas mixing ratios. Quantifying the partial chemical equilibria can reveal the origin of reactor performance changes under influence of these parameter changes.

Finally in chapters 6 and 7 we will explore whether the reactor performance with bi-component mixtures, such as DRM, can be optimised by changing how the gases are combined and mixed in a DBD reactor. This hypothesis is tested by using two different reactions, DRM in chapter 6 and ammonia synthesis in chapter 7, to reveal any differences between different reactions.



## Chapter 2

# A packed-bed DBD micro plasma reactor for CO<sub>2</sub> dissociation: Does size matter?

Published as:

Y. Uytendhouwen, S. Van Alphen, I. Michiels, V. Meynen, P. Cool, and A. Bogaerts, “A packed-bed DBD micro plasma reactor for CO<sub>2</sub> dissociation: Does size matter?,” *Chemical Engineering Journal*, vol. 348, pp. 557–568, 2018

## Abstract

DBD plasma reactors are of great interest for environmental and energy applications, such as CO<sub>2</sub> conversion, but they suffer from limited conversion and especially energy efficiency. The introduction of packing materials has been a popular subject of investigation in order to increase the reactor performance. Reducing the discharge gap of the reactor below one millimetre can enhance the plasma performance as well. In this work, we combine both effects and use a packed-bed DBD micro plasma reactor to investigate the influence of gap size reduction, in combination with a packing material, on the conversion and efficiency of CO<sub>2</sub> dissociation. Packing materials used in this work were SiO<sub>2</sub>, ZrO<sub>2</sub>, and Al<sub>2</sub>O<sub>3</sub> spheres as well as glass wool. The results are compared to a regular size reactor as a benchmark. Reducing the discharge gap can greatly increase the CO<sub>2</sub> conversion, although at a lower energy efficiency. Adding a packing material further increases the conversion when keeping a constant residence time, but is greatly dependent on the material composition, gap and sphere size used. Maximum conversions of 50-55% are obtained for very long residence times (30 s and higher) in an empty reactor or with certain packing material combinations, suggesting a balance in CO<sub>2</sub> dissociation and recombination reactions. The maximum energy efficiency achieved is 4.3%, but this is for the regular sized reactor at a short residence time (7.5 s). Electrical characterisation is performed to reveal some trends in the electrical behaviour of the plasma upon reduction of the discharge gap and addition of a packing material.

---

## Remarks

The study in this chapter was perceived and performed in 2015-2016 in which a comparative study between the empty reactor and packed reactor was done by testing both reactors at “the same residence time”. Different flow rates were used for the empty and packed reactor by making use of a packing efficiency equal to a close packing, i.e. 74.048%. A later study, shown in chapter 4, in 2017-2018, however, has shown that this value is far from true in the tubular reactors used in this thesis. By simulating dropped spheres in the different reactor geometries with MATLAB, more correct estimations of the packing efficiencies, for the gap and sphere size combinations we use, were found. These values are shown to be actually between 40.8% and 52.1%, see column 3 in table 2.1. As a result, the residence times of the packed reactors need to be corrected to values between 13.8 and 17.1 s (see column 6 in table 2.1; on average 15.1 s). As a result, all results of the packed reactors are actually not all performed at the exact same residence time, so the small changes between the different cases might overlap due to this error. The flow rates that should have been used are shown in column 7. The residence time, and thus the corresponding data, of the empty reactors is however still correct at 7.5 s and 29.8 s; only the direct comparison of the empty and packed reactor at ‘equal residence times’ is invalid. To be able to compare the packed reactors with the empty reactor, the new flow rates for the empty reactor in column 9 should be used.

This error in packing efficiency is resolved in all other packed-reactor chapters. The core-shell spheres in chapter 3 were already partially tested before resolving this issue, so a new standard was set by taking 38.98 mL/min for the 4.5 mm gap, resulting in a residence time of 14.07 s at a packing efficiency of 48.27%. New flow rates were calculated for the empty reactor and conversions were experimentally redetermined. Chapters 4 and 5 incorporated the more realistic estimated packing efficiencies from the start.

**Table 2.1:** Corrected packing efficiencies (column 3) for the gap and sphere size combinations used in chapter 2. The residence times and flow rates used for the packed reactor in the chapter (column 4-5) are compared to the actual residence times and the flow rate to be used for 7.5 s (columns 6-7). The chapter flow rates for 7.5 s and the flow rates required for a comparison of to the packed reactors based on modelled packing efficiency and actual residence time of around 15.1 s (column 8-9).

Gap size ( $\mu\text{m}$ )	Sphere size ( $\mu\text{m}$ )	Packing efficiency (%)	Packed reactor			Empty reactor		
			Chapter residence time (s)	Chapter flow rates (mL/min)	Actual residence time (s)	Flow rates for 7.5 s (mL/min)	Flow rates for actual comparison (mL/min)	
268	100-200	44.08 ± 0.04	7.5	2.99	16.17	6.45	11.52	5.35
	100-200	49.51 ± 0.02	7.5	5.03	14.60	9.79	19.35	9.96
	300-400	42.51 ± 0.02	7.5	5.03	16.62	11.15	19.35	8.75
705	100-200	50.55 ± 0.02	7.5	7.68	14.29	14.64	29.53	15.53
	300-400	47.57 ± 0.04	7.5	7.68	15.16	15.52	29.53	14.65
	100-200	52.10 ± 0.03	7.5	12.98	13.84	23.96	50.00	27.10
1230	300-400	49.14 ± 0.03	7.5	12.98	14.70	25.44	50.00	25.52
	800-900	40.16 ± 0.04	7.5	12.98	17.10	29.59	50.00	21.94
	1600-1800	48.27 ± 0.07	7.5	38.98	14.07	73.13	150.18	75.36
4705	2000-2240	46.51 ± 0.06	7.5	38.98	14.55	75.62	150.18	72.87

## 2.1 Introduction

The main drawbacks of the DBD reactor up till now are its poor conversion and energy efficiency. In the case of VOC decomposition, removal values of around 60-80% are obtained for benzene (up to 99% depending on the applied conditions), 20-70% for toluene, and even values of over 99% were reported for trichloroethylene [71]. This is, however, accompanied by a large energy demand, i.e. up to above thousands of J/L for the harder to remove compounds and low pollutant concentrations (100-1000 ppm). For the synthesis of value added chemicals from waste stocks, like greenhouse gas conversion, generally lower conversion values are reached. For instance, dry reforming of methane experiments performed by Tu and Whitehead reached only a maximum CH<sub>4</sub> conversion of 50% with a corresponding efficiency of only 0.10 mmol/kJ [72]. The highest efficiency they obtained was 0.19 mmol/kJ at a CH<sub>4</sub> conversion of only 15%.

The values obtained up to now in DBD reactors are not yet sufficient to implement them as a single technology in industrial applications without any further improvement. A first widely used approach for improvement is the implementation of a (catalytic) packing material in the reaction volume of the reactor, to create a so-called packed-bed reactor. By adding a packing material to the reaction volume, the plasma behaviour and related chemistry will be altered. A packing material can lead to electric field enhancement [64] by polarisation and surface roughness of the particles, as well as changing the discharge type, forming micro plasmas in pores [66], and altering the chemistry by (catalytic) surface reactions [62, 67]. Commonly, spheres or other shaped particles of different materials are applied [58, 68–74], due to their easy implementation in the reactor, possibility for catalytic activation, large number of contact points, and wide commercial availability for numerous materials. In addition, wool-type materials like glass wool for their high surface area, or ceramic foams for their rigid 3D structure [58, 68, 75, 76], have also been used. Numerous publications show that adding packing materials to the DBD reactor can indeed, depending on the applied material-set-up combination, enhance the conversion and efficiency [42, 70–72, 74, 77]. The decomposition of e.g. toluene found enhanced removal values of 40% to 96% and energy demands could be lowered to values of a few hundred J/L [71]. In the case of dry reforming of methane,

an increase of CH<sub>4</sub> conversion was found from 30.0% to 56.4% by adding 10%Ni/ $\gamma$ -Al<sub>2</sub>O<sub>3</sub> spheres to the reaction volume for the same conditions, and the efficiency rose from 0.14 mmol/kJ to 0.32 mmol/kJ [72]. A comprehensive overview of the state-of-the-art of DBD and other plasma reactor types, both packed and unpacked, for CO<sub>2</sub> conversion and dry reforming of methane, can be found in the review paper by Snoeckx and Bogaerts [8], presenting all results obtained up to 2017 in terms of conversion, energy efficiency and energy cost.

Another method of improving the performance of the reactor lies in the design itself. The distance between the reactor electrodes, either one or both covered by a dielectric material, not only defines the reaction volume; it has an important influence on the electrical behaviour of the reactor as well [45]. For a fixed potential applied over the electrodes, the electric field strength generated in the reactor is inversely proportional to the distance between the electrodes. It is therefore speculated that decreasing this distance, and thus increasing the electric field, will result in a more powerful plasma for the same applied potential. Also, confining plasmas at elevated pressures to sub-millimetre dimensions, yielding a so-called micro DBD reactor, is said to stabilise the plasma [61]. Bai *et al.* [59] suggested that decreasing the inter-electrode distance could increase the conversion and efficiency substantially for ammonia synthesis from methane and nitrogen mixtures. Sekiguchi *et al.* [93] reported that benzene hydroxylation increased by a factor of 4 when decreasing the inter-electrode distance.

Both of these improvements have been found successful and combining both approaches might even be better. The smaller gap can enhance the overall electric field, while the spheres can further enhance the local electric field between them. This in turn should provide us with a packed-bed micro DBD reactor that is expected to even further improve the performance of the original DBD reactor.

The targeted reaction in this work is CO<sub>2</sub> dissociation in CO and O<sub>2</sub>. This reaction is preferred for the purpose of this study over bi-component mixtures, like dry reforming of methane, because of its simple chemistry, to provide us with a more fundamental insight in the behaviour of the plasma in the DBD reactor with yet enough chemistry compared to a non-reactive gas, like helium or argon.

Following the hypotheses introduced above, the overall research question can



be summarised as: Does size matter? This question will be answered here, split up into three sub-questions:

- 1: What is the influence of gap size reduction in a DBD plasma reactor on the CO<sub>2</sub> conversion, and can the electrical parameters be linked?
- 2: What is the influence of the size and type of packing materials and can they even further improve the performance of the reactor? Is there a difference depending on the type of material?
- 3: Will these improvements also translate in higher energy efficiency?

## **2.2 Materials and methods**

The experimental set-up can be divided into three parts: (i) the DBD reactor forming the heart of the set-up, which is being controlled by (ii) the gas and (iii) electrical circuit, to steer and analyse the underlying chemistry and electrical behaviour. Analysis of the gas composition after the plasma reaction for calculating the conversion and analysis of the electrics for determining the power are straightforward and common operations, but we will go one step further in analysing the electric signals. Quantifying the discharge performance can show us more detailed information on the underlying behaviour of the plasma in the (packed) micro gaps.

### **2.2.1 Experimental set-up**

#### **2.2.1.1 Reactor**

The reactor in this work is a cylindrical DBD reactor as shown in figure 2.1. The concentric design has the advantage of providing a more uniform reaction volume, since there are no extra boundaries except for the dielectric wall and the electrode, and it is easier to use in both milli and micro gap configuration.

The reactor body is made of an alumina dielectric tube with 22 mm outer diameter and a precision-machined inner diameter of 17.41 mm. The live electrode is a stainless-steel mesh with a length of 100 mm that is tightly wound around the dielectric tube to form the outer electrode. A stainless-steel rod is placed in the centre of the tube to be used as the grounded inner electrode, to shape the reaction volume and alter the discharge gap. Five inner electrodes

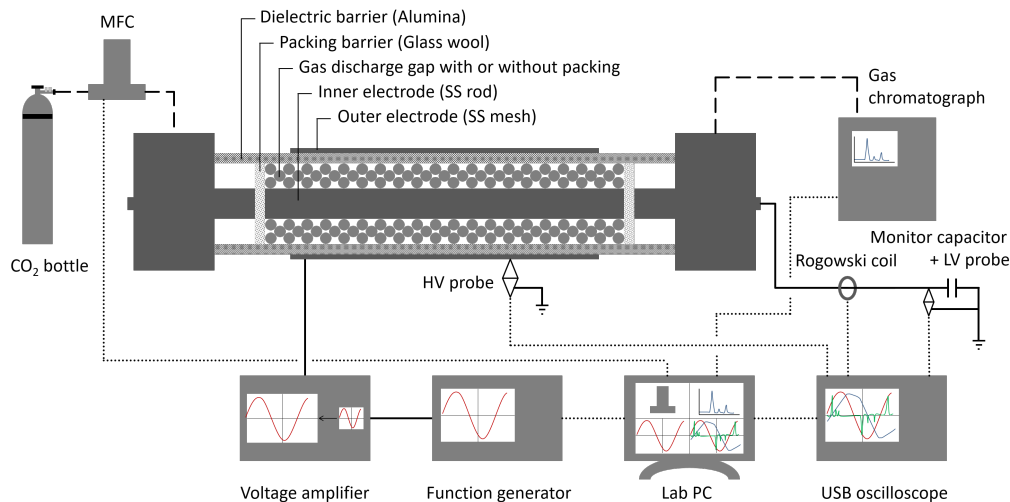


**Figure 2.1:** Packed bed DBD reactor used in this work with analytical equipment.

with different outer diameters were used in this research, resulting in discharge gap sizes of 268  $\mu\text{m}$ , 455  $\mu\text{m}$ , 705  $\mu\text{m}$ , 1230  $\mu\text{m}$ , and 4705  $\mu\text{m}$ . The first four gap sizes will be considered as micro gaps in this work and the last one as a milli gap; this is the benchmark that is also used in our other research [58]. Besides using the empty reactor as such, experiments were also performed with different packing materials. Spheres with different compositions made of SiO<sub>2</sub>, YSZ (yttria-stabilized zirconia) (both Sigmund Lindner), and  $\alpha\text{-Al}_2\text{O}_3$  (custom made at VITO) [94] were used in three size ranges: 100-200  $\mu\text{m}$ , 300-400  $\mu\text{m}$ , and 800-900  $\mu\text{m}$ . In addition, glass wool (superfine 8-50  $\mu\text{m}$ ) (Glaswarenfabrik Karl Hecht) was also used as a packing material.

### 2.2.1.2 Gas circuit

The reactor was fed with a pure CO<sub>2</sub> stream that is set and controlled by a mass flow controller (Bronkhorst EL-FLOW Select). Each reactor condition was tested with the same residence time of 7.5 s in order to isolate the influence of modifying the discharge gap size and adding a packing material in the reactor. Therefore, for an empty reactor, flow rates of 11.52 mL/min, 19.35 mL/min, 29.53 mL/min, 50.00 mL/min, and 150 mL/min were used for the 268  $\mu\text{m}$ , 455  $\mu\text{m}$ , 705  $\mu\text{m}$ , 1230  $\mu\text{m}$ , and 4705  $\mu\text{m}$  gap sizes, respectively. The available reaction volume decreases when adding a packing material, and assuming

a close spherical packing, this results in a 74.048% decrease in available reaction volume. Thus, adjusted lower flow rates were used to match the 7.5 s residence time: 2.99 mL/min, 5.03 mL/min, 7.68 mL/min, 12.98 mL/min, and 38.98 mL/min. These flow rates were also used for the glass wool filled reactor (i.e. a tightly wound long strip around the centre electrode filling the whole reaction volume), since it is not directly possible to estimate the volume loss of adding this non-uniformly shaped material.

The small flow rates do not have great industrial value but the focus in this work lies in exploring the “isolated” effect of the packing parameters. Furthermore, if higher throughputs are desirable, the influence of raising the flow rate within a specific reactor has been shown numerous times [39,58,59,95] (higher flow rate equals lower conversion); but solutions provided by using larger reaction volumes to get the same residence time, and/or placing multiple reactors in parallel are available [79].

### 2.2.2 Performance characterisation: conversion and efficiency

The gas stream leaving the reactor was analysed by a gas chromatograph (GC) (Trace GC 1310, Interscience). This GC has 12 pressureless sample loops for rapid sampling combined with both a flame ionisation detector (FID) and thermal conductivity detector (TCD) channel. Since the products formed in this reaction are CO, O<sub>2</sub>, and traces of O<sub>3</sub>, besides unreacted CO<sub>2</sub>, only the TCD channel was used. The CO<sub>2</sub> conversion derived from the GC data was defined as:

$$X_{GC} = \frac{C\dot{O}_{2in} - C\dot{O}_{2out}}{C\dot{O}_{2in}} \quad (2.1)$$

with  $C\dot{O}_2$  the molar flow rate of CO<sub>2</sub>. This value is, however, not correct in a pressureless sampling system (sampling at atmospheric pressure). As one mole of CO<sub>2</sub> is split into one mole of CO and half of a mole of O<sub>2</sub>, this gives rise to a gas expansion of a factor 1.5 in case of 100% conversion. Therefore, the pressure in the reactor, in the tubing leading to the GC, and eventually in the sample loops within the GC, will increase. When the GC samples, it will depressurise the sample loop to atmospheric pressure and thus loses a number of molecules to be detected. This will result in an apparent lower peak area and thus CO<sub>2</sub> concentration, leading to an overestimation of the CO<sub>2</sub> conversion. As

a consequence, the overestimated conversion has to be corrected based on the actual gas conversion and expansion. The actual CO<sub>2</sub> conversion ( $X_{CO_2}$ ) can be calculated by the following equation, shown by Pinhão *et al.* [96] and Snoeckx *et al.* [97]:

$$X_{GC} = 1 - \frac{1 - X_{CO_2}}{1 + \frac{X_{CO_2}}{2}} \Leftrightarrow X_{CO_2} = \frac{2X_{GC}}{3 - X_{GC}} \quad (2.2)$$

The energy efficiency of the conversion can be calculated based on the theoretical required and actual consumed energy. The energy efficiency is therefore defined as:

$$\eta = \frac{\Delta H_r X_{CO_2} \dot{V}}{P V_m} \quad (2.3)$$

with  $\Delta H_r$  the reaction enthalpy of CO<sub>2</sub> dissociation (279.8 kJ/mol),  $\dot{V}$  the volumetric flow rate,  $P$  the plasma power, and  $V_m$  the molar gas volume (22.4 L/mol). The ratio of the plasma power over the volumetric flow rate is also known as the specific energy input or SEI:

$$SEI = \frac{P}{\dot{V}} \quad (2.4)$$

### 2.2.3 Electrical characterisation

The outer electrode of the reactor was driven by a high voltage amplifier (TREK, Model 20/20C-HS) that amplifies an input signal by a factor 2000. This input signal was provided by a PC controlled function generator (Tektronix, AFG 2021) at a fixed frequency of 3000 Hz and an adjustable amplitude, depending on the reactor configuration, to load the reactor with a power of 30 W. The applied voltage was monitored by a high voltage probe (Tektronix, P6015A), the current pulses were measured by a current transformer (Pearson, Model 4100), and the dissipated charge was determined by using a monitor capacitor (10 nF) and a low voltage probe (Picotech, TA150). All signals were captured by a digital oscilloscope (Picotech, Picoscope 6402D) with which the plasma behaviour was tracked, and the power was continuously calculated to adjust the amplitude of the function generator. This way, a constant plasma power of 30 W was maintained.

Each experiment was evaluated by analysing the signals recorded by the digital oscilloscope: the applied voltage ( $U(t)$ ), the resulting current flow ( $I(t)$ ), and the dissipated charge ( $Q(t)$ ). The resulting oscillogram (cfr. figure 2.2(a)) yields the

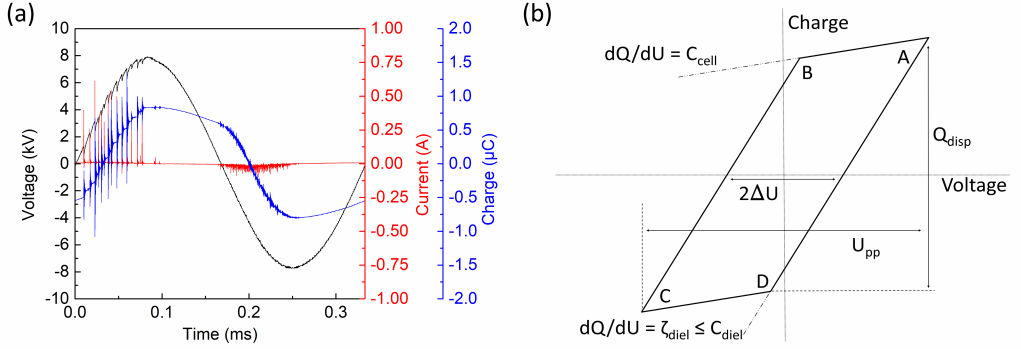


**Figure 2.2:** (a) Typical data acquired from the digital oscilloscope displayed for one period. (b) Simplified Lissajous figure generated by plotting charge as a function of applied voltage, annotated with typical measured values.

peak-to-peak voltage ( $U_{pp}$ ), the mean current ( $I_{RMS}$ ), and the plasma power ( $P$ ). The latter can be calculated during one or multiple period lengths ( $nT$ ):

$$P = \frac{1}{nT} \int_0^{nT} U(t)I(t)dt \quad (2.5)$$

Using the applied voltage and the dissipated charge, we can plot a Q-U graph, also known as a Lissajous figure, schematically illustrated in figure 2.2(b). Manley [40] has shown that the plasma power can also be determined from the area of the resulting graph:

$$P = \frac{1}{T} \oint U(Q)d(Q) \quad (2.6)$$

Further analysis of the oscillogram and resulting Lissajous figure is done to calculate the peak-to-peak voltage ( $U_{pp}$ ), root-mean-square current ( $I_{RMS}$ ), effective capacitance ( $\zeta_{diel}$ ), partial discharging fraction ( $\alpha$ ), burning voltage ( $U_{bur}$ ), displaced charge ( $Q_{disp}$ ), number of micro discharges per period, and displaced charge per micro discharge. Extra information about the extraction of these parameters and associated theory can be found in appendix A. Calculation of all the electrical parameters is done automatically by a MATLAB script.

### 2.2.4 Experimental method

A cooled-down (freshly packed) reactor was used for each experiment and operated for 40 min to achieve steady-state conversion, followed by the GC and Lissajous measurements. The input voltage was continuously adjusted to match

the desired plasma power of 30 W. Each experiment was performed three times with four GC and Lissajous analyses for statistical review. The error bars are subsequently defined as:

$$error = \pm S_n \frac{T_s(PI, n_s)}{\sqrt{n_s}} \quad (2.7)$$

with  $S_n$  the sample standard deviation of the measurements,  $n_s$  the sample size being 12, and  $T_s$  the two-tailed inverse of the Student t-distribution for sample size  $n_s$  and probability  $PI$  set at 95%.

## 2.3 Results and discussion

In order to answer the research questions listed in the introduction, the results will be judged both on gas analysis and electrical parameters. The results for the empty reactor will be shown first to partially answer the first question of this work. Subsequently, the results for the packed reactors will be presented to further supplement the former data and to investigate the second question. At the end of each sub-section, the efficiency will be discussed to provide answers to the third question.

### 2.3.1 Empty reactor

#### 2.3.1.1 Conversion

Figure 2.3 illustrates the influence of the gap size on the CO<sub>2</sub> conversion, for a plasma power of 30 W, both at a constant residence time of 7.5 s and 28.9 s (corresponding to the flow rate of the corresponding packed-bed reactors), for gaps typical of both a micro reactor and a regular sized reactor. The conversion increases remarkably by decreasing the gap size, up to 33.3% and 53.7% conversion at the smallest gap, for the residence time of 7.5 s and 28.9 s, respectively. This is an increase with a factor 2.6 and 1.8 compared to the largest micro gap of 1230 μm, and with a factor 7.8 and 4.9 with respect to the regular sized reactor. This trend is logical, because both the reduced electric field strength and the power density rise by reducing the discharge gap size (at constant applied voltage and power).

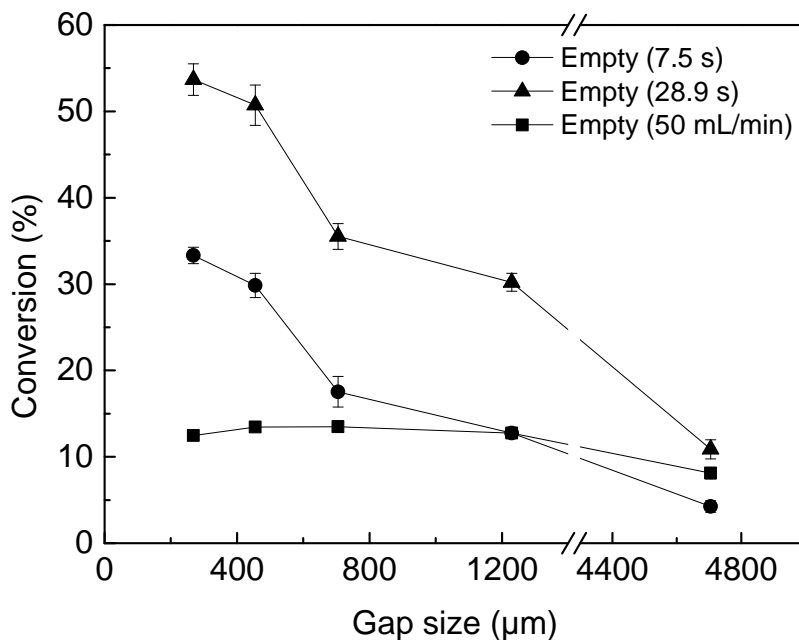


**Figure 2.3:** Conversion as a function of gap size for an empty reactor at a constant residence time of 7.5 s and 28.9 s, and at a constant flow rate of 50 mL/min at 30 W plasma power.

When reducing the gap size, the reduced electric field enhances proportionally, from 178 Td at 1230  $\mu\text{m}$  to 814 Td at 268  $\mu\text{m}$ , leading to a number of effects. First of all, a higher reduced electric field yields a higher electron temperature, resulting in more successful electron impact excitation and ionisation reactions, which are the most prominent reactions for  $\text{CO}_2$  dissociation in a DBD reactor [38]. In addition, the ionisation reactions cause a higher density of electrons and ions, resulting in an overall more reactive plasma [98], hence the higher conversion. Also, the critical value for the local reduced electric field is reached more often due to the overall higher electric field, resulting in a plasma that is easier to ignite, and this causes more micro discharges per period in the plasma (see section 2.3.1.2). The latter gives rise to a higher probability for gas molecules to be hit by a micro discharge and thus be converted upon collision in the plasma.

The specific energy input (SEI) increases as well when the discharge gap becomes smaller. This is because of the lower flow rate used to maintain the same residence time. In the case of 7.5 s residence time, the SEI increases from 36.0 kJ/L to 156.2 kJ/L with decreasing gap size, and at 28.9 s residence time, the SEI increases from 138.7 kJ/L to 602.0 kJ/L. This higher SEI also creates

a more reactive plasma, resulting in a higher conversion. It was not possible to compare the different gap sizes at both constant SEI and constant residence time, because the corresponding plasma powers could not be applied due to limitations of reactor and set-up. A constant power of 30 W was therefore used.

The effect of the micro gap is even more notable when the results are compared to the normal sized reactor of 4705  $\mu\text{m}$ . A conversion of only 4.1% and 10.9% is observed here due to the intrinsic lower reduced electric field of 70 Td, and the lower SEI of only 12.0 kJ/L and 46.2 kJ/L for the 7.5 s and 28.9 s residence times.

An attempt to isolate the influence of gap size from the SEI was done by performing the experiments at a constant flow rate of 50 mL/min. In this way, a constant SEI of 36 kJ/L is maintained and the results are displayed as well in figure 2.3. The results show that the conversion almost does not change from 1230  $\mu\text{m}$  to 268  $\mu\text{m}$ . Two effects occur here at the same time. On one hand, the reduced electric field enhances by decreasing the gap size, resulting in a higher conversion. However, since a constant flow rate was used in reactors with decreasing gap size, the residence time decreases significantly by a factor 4.4, i.e. from 7.5 s to 1.7 s. This shows that the reduction of the gap size can compensate for the reduced residence time and thus can enhance the performance of the reactor.

A side note has to be made here that SEI is not really a universal ‘input-parameter’, as shown by Aerts *et al.* [38]. Both power and flow rate have their distinct influences on the behaviour of the plasma, gas, and reactor behaviour. The power has a great influence on the magnitude of the applied voltage and resulting current, and thus on the reduced electric field, and subsequently on the number, and magnitude, of micro discharges. On the other hand, the flow rate has an influence on the general reactor residence time, but as well on the discharge filament residence time (i.e. the time that gas molecules spend in filaments) which is in fact the actual location of reaction. Nevertheless, the SEI can be used as a comparison tool, as long as enough of the set-up parameters are kept the same.



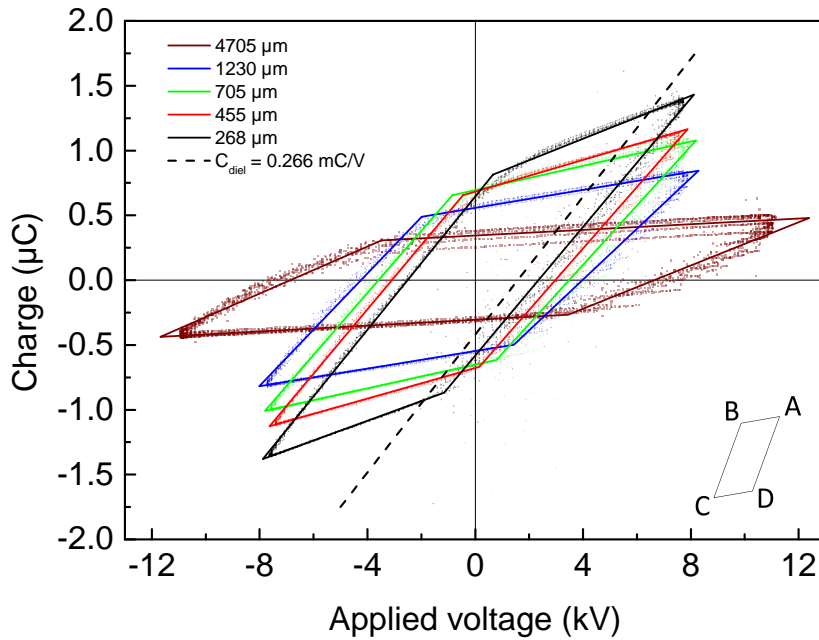


**Figure 2.4:** Raw Lissajous plots (dotted) for an empty reactor with different discharge gap sizes for a constant residence time of 7.5 s, as well as the slopes calculated by the MATLAB script (solid lines). Comparison is also made with the  $C_{diel}$  value of a completely discharged reactor (dashed line).

### 2.3.1.2 Electrical characterisation

Electrical characterisation of the experiments supports the trends above. Figure 2.4 shows the Lissajous figures of the different gap sizes for a residence time of 7.5 s. It reveals a significant change in electrical behaviour upon reducing the gap size, seen by the different slopes, heights, and widths of the different parts of the Lissajous figure.

First of all, there is a clear change in the slopes of the discharge phase BC and DA (cfr. figure 2.2 above). The slope, or capacitance, of this phase increases when the discharge gap gets smaller, to approach the capacitance value of a fully discharged reactor, marked by the dashed line. As seen in table 2.2, the effective capacitance  $\zeta_{diel}$  increases from 0.095 mC/V to 0.251 mC/V and thus it approaches the value of  $C_{diel}$ , i.e. 0.266 mC/V. This means that a smaller discharge gap tends to generate a more uniform (and fully discharged) plasma throughout the whole reaction volume. Indeed, the partial discharging value  $\alpha$  (see definition in appendix A) drops from 62% to 7.9% (see also table 2.3).

**Table 2.2:** Measured data from the input signals of the oscilloscope (voltage, current, and charge) and subsequently generated Lissajous figure for the empty reactors with varying gap size at a constant residence time of 7.5 s, calculated by the MATLAB script. The meaning of the parameters is explained in appendix A.

Gap size ( $\mu\text{m}$ )	$U_{pp}$ (kV)	$I_{RMS}$ (mA)	$C_{cell}$ (mC/V)	$\zeta_{diel}$ (mC/V)	Transferred charge ( $\mu\text{C}$ )	Conversion (%)
268	$15.49 \pm 0.03$	$27.9 \pm 0.2$	$0.078 \pm 0.001$	$0.251 \pm 0.001$	$2.2 \pm 0.1$	$33.3 \pm 0.9$
455	$15.25 \pm 0.05$	$28.2 \pm 0.5$	$0.065 \pm 0.002$	$0.246 \pm 0.002$	$1.6 \pm 0.2$	$30 \pm 1$
705	$15.3 \pm 0.1$	$27.8 \pm 0.3$	$0.048 \pm 0.001$	$0.236 \pm 0.001$	$1.57 \pm 0.06$	$18 \pm 2$
1230	$15.5 \pm 0.1$	$28 \pm 1$	$0.034 \pm 0.003$	$0.206 \pm 0.003$	$1.3 \pm 0.2$	$12.8 \pm 0.3$
4705	$23 \pm 2$	$15 \pm 2$	$0.012 \pm 0.003$	$0.095 \pm 0.003$	$0.59 \pm 0.06$	$4.3 \pm 0.7$

**Table 2.3:** Calculated data from the raw data from table 2.2 for the empty reactors with varying gap size at a constant residence time of 7.5 s, calculated by the MATLAB script. The meaning of the parameters is explained in appendix A.

Gap size ( $\mu\text{m}$ )	$\alpha$ value (%)	$U_{bur}$ (kV)	Number of micro dischargers (a.u./T)	Average filament charge (nC/disch.)	Conversion (%)
268	$7.9 \pm 0.4$	$2.605 \pm 0.001$	$49 \pm 2$	$45 \pm 2$	$33.3 \pm 0.9$
455	$10 \pm 1$	$3.21 \pm 0.08$	$29 \pm 3$	$55 \pm 3$	$30 \pm 1$
705	$13.5 \pm 0.6$	$3.737 \pm 0.001$	$26 \pm 1$	$59 \pm 2$	$18 \pm 2$
1230	$26 \pm 1$	$4.375 \pm 0.003$	$24 \pm 3$	$55 \pm 5$	$12.8 \pm 0.3$
4705	$62 \pm 2$	$7.25 \pm 0.08$	$21 \pm 2$	$28 \pm 3$	$4.3 \pm 0.7$

These results match the conversion results, and thus the fact that the more fully discharged reactor is one of the underlying reasons for the higher conversion upon decreasing discharge gap.

Secondly, there is a change visible in the voltage difference at  $Q = 0 \mu\text{C}$  (see figure 2.5), which is further used to calculate the burning voltage ( $U_{bur}$ ). The latter decreases from 7.25 kV to 2.605 kV upon decreasing discharge gap, as seen in table 2.3, making it easier to ignite and sustain the plasma with a lower minimum voltage. The actual applied peak-to-peak voltage to achieve the desired power of 30 W, however, stays about constant at around 15.4 kV, showing a small dip at 455  $\mu\text{m}$  and 705  $\mu\text{m}$ . This is significantly lower than the peak-to-peak voltage of 23 kV necessary to achieve a power of 30 W at a discharge gap of 4705  $\mu\text{m}$ . Despite the almost constant peak-to-peak voltage in the micro gaps, a change in the behaviour of the reactor is seen here by the capacitive phases AB and CD, which become shorter and steeper. The latter results from a smaller gap, giving a higher base reactor capacitance. The discharge phases BC and DA, on the other hand, become longer and more powerful. The displaced charge per period increases immensely from 0.59  $\mu\text{C}$  to 2.2  $\mu\text{C}$  when the discharge gap decreases

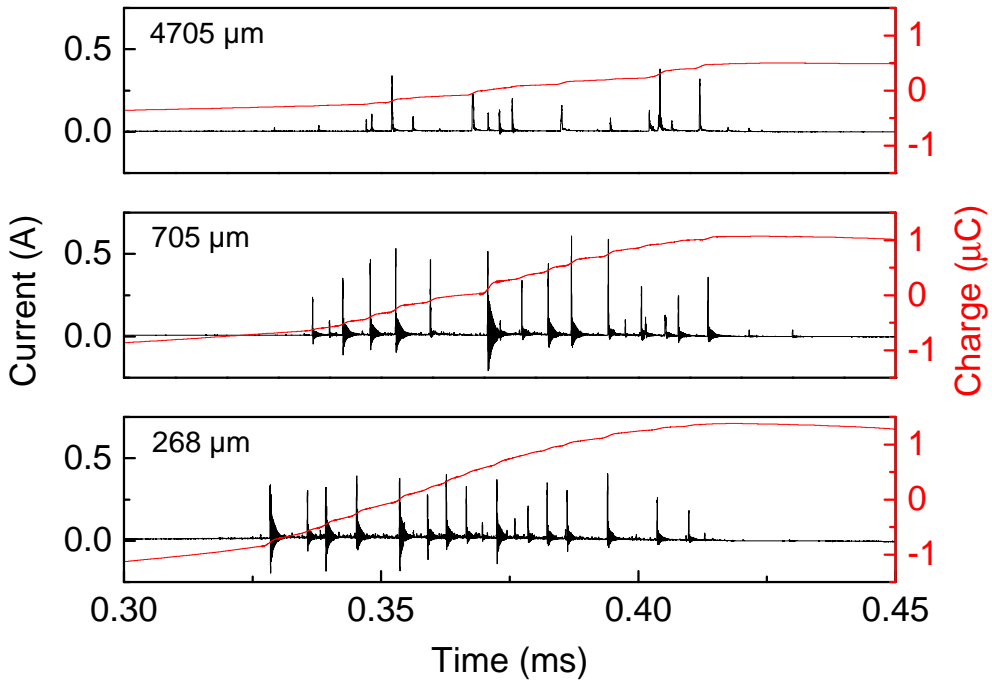


**Figure 2.5:** Detailed view of a positive half period of the current and charge profile of a 30 W DBD reactor operating at 4705, 705 and 268  $\mu\text{m}$  discharge gap with a residence time of 7.5 s.

from 4705  $\mu\text{m}$  to 268  $\mu\text{m}$  (see figure 2.5). This results in a greater part of the applied power that will be available in the plasma, providing a higher chance of high energy discharges and/or more individual discharges, as suggested in section 2.3.1.1.

Finally, closer examination of the current profile, as seen in figure 2.5, indicates a change in number of micro discharges per period. At a gap size of 4705  $\mu\text{m}$ , only 21 micro discharges on average were observed per period, while this number increases to 49 in the smallest gap size of 268  $\mu\text{m}$ . This is indeed consistent with the assumption that a higher reduced electric field leads to a higher chance of a discharge propagation in the reactor. The reduced higher electric field, however, does not mean that the micro discharges are more powerful as well. Dividing the number of discharges by the transferred charge shows that the most powerful discharges on average happen at a discharge gap of 705  $\mu\text{m}$ , with an average strength of 59 nC per discharge. The trend goes over a maximum, because the displaced charge during the discharge phase does

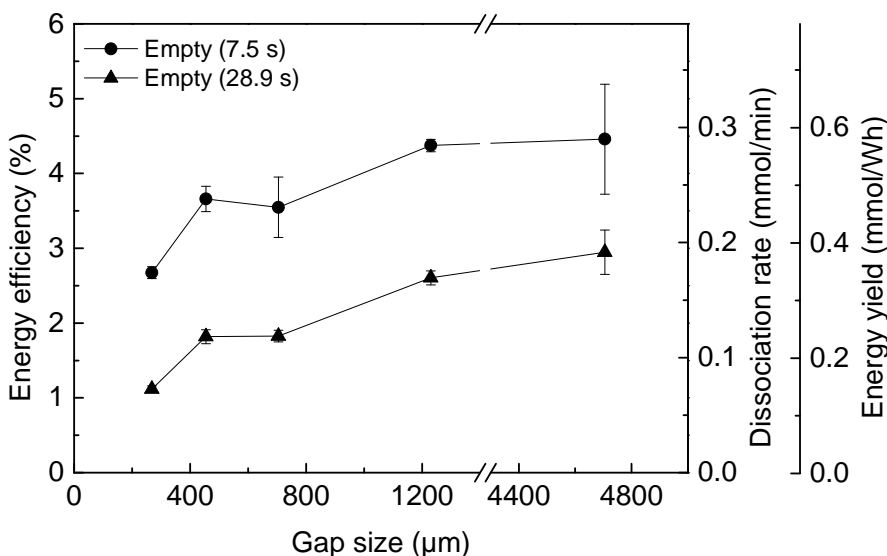


**Figure 2.6:** Efficiency as a function of gap size for an empty reactor at a constant residence time of both 7.5 s and 28.9 s. The efficiency is displayed as energy efficiency, as well as dissociation rate and energy yield.

not increase at the same rate as the number of micro discharges. This suggests that the higher plasma fraction in the discharge volume and the larger number of micro discharges per period have more effect on the CO<sub>2</sub> conversion than the transferred charge.

### 2.3.1.3 Efficiency

Although a great conversion is desired, it should be accompanied by a sufficient energy efficiency as well. Therefore, the efficiency will be discussed here, to judge if decreasing the discharge gap, while keeping a constant residence time, is really beneficial.

The energy efficiency, displayed in figure 2.6, shows the opposite trend from the conversion. Decreasing the discharge gap lowers the energy efficiency for both residence times. Although the conversion is higher at these smaller gap sizes, the energy efficiency also depends on the flow rate (see equation 2.3 in section 2.2.2 above), and the latter is lower in the smaller gap sizes to keep the residence time constant. This lower flow rate clearly has a larger overall impact than the enhanced conversion, explaining why the energy efficiency drops upon

decreasing gap size. The maximum value of 4.3% in these experiments was found at the shorter residence time, and thus lower SEI, in the 1230  $\mu\text{m}$  gap size.

The ideal process would have both high conversion and energy efficiency, but this is most of the time not achievable with the particular thermodynamics i.e. the highly endothermic reaction of  $\text{CO}_2$  dissociation, as the high thermodynamic stability (high negative Gibbs free energy of formation,  $\Delta G_0$ ) of  $\text{CO}_2$  drives the equilibrium strongly to the left. From these results it is evident that there is a trade-off between high conversion and high energy efficiency in this set-up when the discharge gap changes at the same residence time and power input. The quest of finding an optimum in both conversion and energy efficiency comes down to producing as much product per time or per amount of energy, to develop a competitive technology that can eventually be used in industry. The efficiency can therefore also be expressed as dissociation rate (mmol/min) and energy yield (mmol/Wh), which are related to the energy efficiency, except for a constant factor:

$$\begin{aligned}\eta &= \frac{\Delta H_r}{PV_m} X_{\text{CO}_2} \dot{V} \\ r_d &= \frac{1}{V_m} X_{\text{CO}_2} \dot{V} \\ E_y &= \frac{1}{PV_m} X_{\text{CO}_2} \dot{V}\end{aligned}\quad (2.8)$$

Plotting the results expressed as dissociation rate and energy yield thus shows the same trend as for the energy efficiency; see figure 2.6. The maximum values of 0.285 mmol/min and 0.57 mmol/Wh, respectively, are again reached at the shorter residence time at a discharge gap of 1230  $\mu\text{m}$ .

Comparing the results of these three efficiencies with the regular sized gap of 4705  $\mu\text{m}$  shows that increasing the discharge gap yields a somewhat higher efficiency for a residence time of 28.9 s, but the efficiency remains constant for a residence time of 7.5 s. The energy efficiency, dissociation rate and energy yield in the regular sized reactor, under the applied conditions here, are at maximum 4.3%, 0.28 mmol/min and 0.57 mmol/Wh, respectively.

To obtain maximum efficiency, the product of conversion and flow rate should be at maximum when the applied power is constant. Increasing the flow rate, however, will reduce the conversion, because of the shorter residence time. This

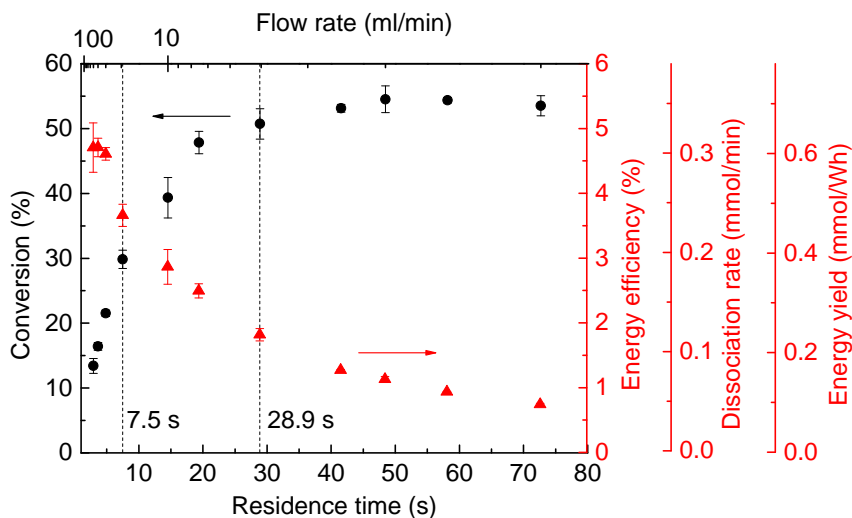


**Figure 2.7:** Conversion and efficiency as a function of residence time and flow rate for an empty reactor with a gap size of 455  $\mu\text{m}$ . The residence times of 7.5 s and 28.9 s are indicated with vertical dashed lines.

was checked in an empty reactor with 455  $\mu\text{m}$  discharge gap and fixed power of 30 W, by changing the flow rate from 50 ml/min to 2 ml/min, which results in residence times from 2.9 s to 72.7 s, as shown in figure 2.7.

First of all, the results show that, as expected, the steady-state conversion increases with residence times up to 30 s, and then stays more or less constant around 50-55%. These results demonstrate that a plasma with constant power will need a certain amount of time to convert as much CO<sub>2</sub> as possible. This is due to the filamentary behaviour of the DBD plasma, where a longer residence time means a higher chance of CO<sub>2</sub> molecules to be converted in a micro discharge, resulting in a higher “plasma residence time”. However, the probability for the back reaction will increase as well, and the CO<sub>2</sub> conversion will flatten and reach a plateau when both the forward and backward reactions cancel each other. Further increase in residence after 30 s will only result in further decrease in energy efficiency without any extra conversion. A new plasma-driven equilibrium is reached here, dependent on the reactor set-up conditions, that is different from the traditional thermal equilibrium.

Vice versa, the conversion drops upon higher flow rate, due to the shorter residence time, and this effect eventually is larger than the beneficial effect of higher flow rate on the efficiency. Thus, the product of flow rate and conversion

drops. Therefore, the energy efficiency increases with increasing flow rate (and decreasing residence time) up to 20 mL/min, but will then reach a plateau around 4.7%. The same trend is of course also seen in the dissociation rate and energy yield. Despite the lower conversion, more CO<sub>2</sub> is being dissociated into CO per time and per amount of energy at higher flow rates, reaching values up to 0.3 mmol/min and 0.6 mmol/Wh, respectively.

To further increase the product of conversion and efficiency, the conversion should be increased, without applying higher residence times or higher applied powers. This trade-off can only be surpassed with substantial changes to the reactor parameters, such as pulsed power, or changes to the reactor set-up such as using packing materials, different reactor geometry, discharge type, or CO separation. Improving the energy transfer from the electric field to chemical energy is key in optimising the overall efficiency of plasma reactors. The next section will discuss the possibility of using packing materials to enhance the performance of DBD (micro gap) reactors.

### **2.3.2 Packed reactor**

As mentioned in the introduction, implementing a packing material in the reaction zone can have multiple influences to enhance the CO<sub>2</sub> conversion in the plasma. Hence, the combination with a reduced gap size might even further improve the performance of the DBD reactor. Therefore, spheres of three different materials were selected in three different sizes, as well as glass wool. As in the previous section, a constant plasma power of 30 W was kept at 3000 Hz for a residence time of 7.5 s.

#### **2.3.2.1 Conversion**

The CO<sub>2</sub> conversion results of all these experiments are summarized in figure 2.8. Note that no data points could be recorded for 100-200 μm ZrO<sub>2</sub> and Al<sub>2</sub>O<sub>3</sub> spheres in the smallest gap reactor (268 μm), nor for 300-400 μm Al<sub>2</sub>O<sub>3</sub> spheres in the reactor with gap of 455 μm, due to failure of the reactor dielectric. Indeed, sphere-to-gap ratios near 1 are not favourable due to (heat) expansion of the spheres, putting too much stress on the reactor walls.

A number of interesting trends can be derived from this figure. First of all,

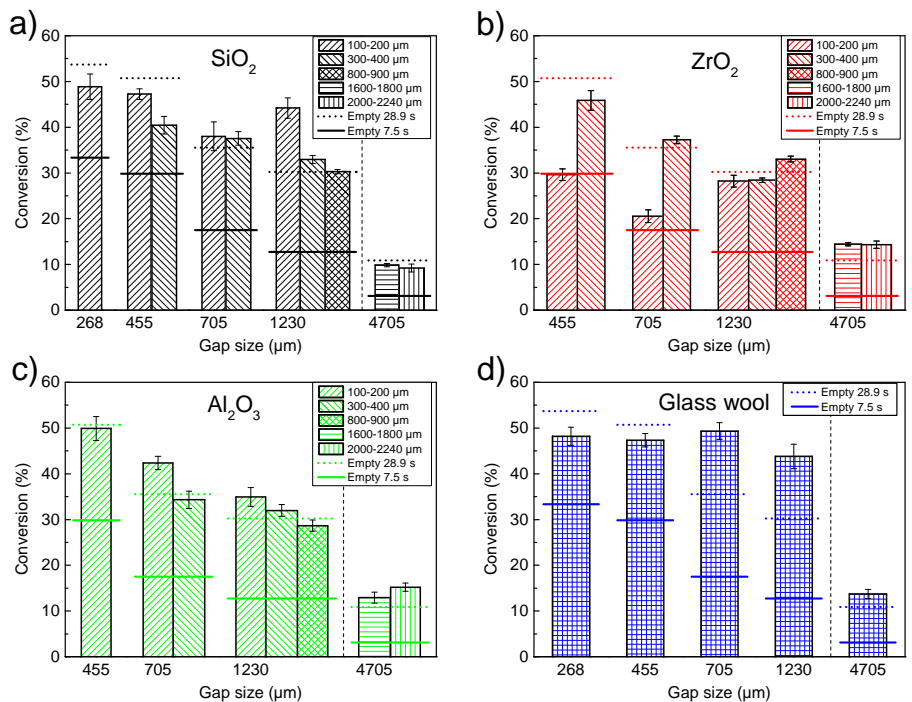


**Figure 2.8:** Conversion in packed-bed DBD (micro) reactors for a constant residence time of 7.5 s and plasma power of 30 W. The results are displayed per material type for different sphere sizes (indicated by the legend) and as a function of gap size, and compared to the empty reactor at the same residence time of 7.5 s (solid horizontal lines) and a residence time of 28.9 s (corresponding to the same flow rate as the packed-bed reactors) (dashed horizontal lines).

adding a packing material significantly enhances the conversion when compared to an empty reactor at the same residence time (see solid horizontal lines). This will partly be due to the enhanced local reduced electric field between the spheres or fibres (in case of glass wool), but also due to the higher power density, because the same power is deposited over a smaller volume due to the presence of the packing. Comparing the results with the empty reactor of 28.9 s, hence at the same flow rate for a fixed gap, and thus the same SEI, shows however that only some sizes of certain materials can enhance the CO<sub>2</sub> conversion well enough, to compensate for the lower residence time in the packed-bed reactors for the same CO<sub>2</sub> throughput. This occurs only in the two largest gap sizes of the micro reactor, i.e. 705 μm and 1230 μm, as well as in the regular size reactor. The most noticeable results are for the 100-200 μm SiO<sub>2</sub> spheres in a 1230 μm gap, along with glass wool in the two largest gap sizes of the micro reactor, where the conversion rises by a factor 1.46, 1.39, and 1.45, respectively. The packing



materials seem not to be able to enhance the conversion for gap sizes below 705  $\mu\text{m}$ , which might suggest that the conversion values of the empty reactor are already close to reaching an equilibrium value, and that the back reaction starts to become equally important. Indeed, generating a more powerful plasma will also promote the back reaction more. Furthermore, adding extra material in the reaction zone might introduce more electrical surface losses, which can have a detrimental effect on the overall plasma performance, as seen in the (slightly) lower conversion. The worst result is obtained for the 100-200  $\mu\text{m}$   $\text{ZrO}_2$  spheres in the reactors with gap of 455  $\mu\text{m}$  and 705  $\mu\text{m}$ , which drastically lower the conversion with 42%.

It is not possible from these results to distinguish a clear order in the performance of the material type. Either  $\text{SiO}_2$ ,  $\text{Al}_2\text{O}_3$  or glass wool yield the best results, depending on the bead and gap size combination.  $\text{ZrO}_2$  clearly produces the worst results in the smaller size ranges and gaps. It is clear that the size effect is opposite to that observed for the other materials and even (almost) absent for the largest gaps. This suggests that there are a lot of parameters that influence the performance of the materials, besides the dielectric constant, such as the exact material composition, size, shape, surface roughness, electric values, porosity, surface functional groups etc., as also shown by Michielsen *et al.* [58]. Furthermore, the effect of these parameters can change as well, due to interactions with other factors and with set-up parameters, such as the gap size and SEI. Indeed, a clear difference in ‘response’ is visible depending on the type of material with changing gap size.

When comparing the micro gap results with the results obtained in the regular sized gap of 4705  $\mu\text{m}$  in figure 2.8, the drastic increase in conversion can be seen again, as was also the case for the empty reactor. It is interesting to mention that  $\text{SiO}_2$  is typically considered the worst material in the regular gap size [58, 68], while it performs as one of the best materials in the micro gap reactor. This is also the case with glass wool, which gave mixed results in other reactors [58, 68], while it is clearly one of the best materials in our set-up. Glass wool showed to have no significant improvement in the work of Michielsen *et al.* [58], compared to the empty reactor, while it does in ours and the work of Duan *et al.* [68]. This suggests that the performance of glass wool, and perhaps any material, is greatly dependent on the reactor configurations (power, frequency,

gap, flow rate, reactor type); and at the right conditions, some materials can become very competitive compared to others, while at other conditions these beneficial aspects might diminish. Glass wool also has the advantages of being more flexible and having a greater specific surface area. Coating glass wool with a catalytic material might be an interesting approach for plasma catalysis, although coating might be experimentally challenging with respect to a reproducible, stable, and uniform coating. In the next sections, the individual effect of the sphere size and gap size will be discussed in more detail.

***Influence of sphere size (within same gap size)*** For a fixed gap size of 455 μm, 705 μm, or 1230 μm, it can be concluded that for SiO<sub>2</sub> and Al<sub>2</sub>O<sub>3</sub> the conversion increases upon reducing the sphere size. The effect is more pronounced for SiO<sub>2</sub> than for Al<sub>2</sub>O<sub>3</sub>, at least in the 1230 μm gap, where all three sizes were measured. ZrO<sub>2</sub>, on the other hand, shows the complete opposite trend, irrespective of the gap size.

These findings might be explained by a few effects occurring at the same time. First of all, smaller spheres will result in more contact points, yielding local field enhancement, and thus will result in a more reactive plasma. This effect was also predicted in modelling work by Van Laer and Bogaerts [99] for a helium plasma in a DBD reactor with 4500 μm gap. The simulations show that indeed the time-averaged electric field strength increases with decreasing sphere size and becomes more spread out over the whole gap. This should enhance the conversion, as seen with SiO<sub>2</sub> and Al<sub>2</sub>O<sub>3</sub>. There is, however, a second effect at play in the micro gap reactor. Indeed, other modelling work by Van Laer and Bogaerts [99] shows that in a regular sized reactor the electric field rises by using spheres with a higher dielectric constant. However, it gets more localised between the contact points and the electron density slightly lowers. The same simulations in a micro gap reactor also show a higher electric field, as expected, although more localised at the contact points, and the electron density drastically lowers when the dielectric constant rises from  $\epsilon = 3.9$  (i.e. SiO<sub>2</sub>) to  $\epsilon = 25$  (i.e. ZrO<sub>2</sub>). This can explain why the impact of Al<sub>2</sub>O<sub>3</sub> ( $\epsilon = 9$ ) is slightly less pronounced than that of SiO<sub>2</sub>, as well as why ZrO<sub>2</sub> shows the opposite performance, suggesting that the combination of smaller spheres with higher dielectric constant and a micro gap reactor results in a negative outcome

in terms of CO<sub>2</sub> conversion. Nevertheless, other, not yet identified material aspects cannot be excluded.

The glass wool fibres might exhibit an analogous behaviour to the 100-200 μm spheres, given the size of the fibres. The number of contact points will be comparable, but the fibrous nature of the glass wool will induce some extra effects. A spherical packing will have at most 12 contact points with neighbouring spheres, while the fibres can have several tens or hundreds of contact points with other fibres. Charge build-up or charge propagation might be diverted and spread out much faster over the neighbouring fibres, resulting in a more homogeneous plasma. It is also possible that the fibres connect the electrode and the dielectric, leading to a short circuit; although this might only be for a short time before polarisation of the electrode and the fibre surface opposes the discharge.

***Influence of gap size (with same sphere size)*** The influence of the gap size was already discussed for the empty reactor (see section 2.3.1.1), but its effect might be different for the packed reactors, depending on the packing material and sphere size. Figure 2.8(d) shows that the conversion remains about the same upon decreasing gap size when glass wool is put into the micro discharge gaps, compared to the regular sized reactor. This suggests that two phenomena are happening here at the same time. First of all, it looks like glass wool on its own is a very well performing material, being capable of improving the conversion drastically, even for a relatively large gap size of 1230 μm. However, this improvement will induce the back reaction more as well, so that the reactor reaches an observed maximum CO<sub>2</sub> conversion of around 50%, defined by the equilibrium with the back reaction, since extra confinement of the gap size to 268 μm does not improve the conversion much further. This behaviour is similar to figure 2.7 where a maximum conversion of around 50-55% was observed, suggesting that the same power driven equilibrium conversion is reached (see section 2.3.1.3). This is consistent with the high conversion for glass wool, obtained by Duan *et al.* [68] compared to other packing materials.

Figure 2.9 presents a combined graph for all sphere materials and sizes, as a function of the gap size. It shows that for most materials the conversion decreases with increasing gap size, which is expected due to the decreasing electric field.

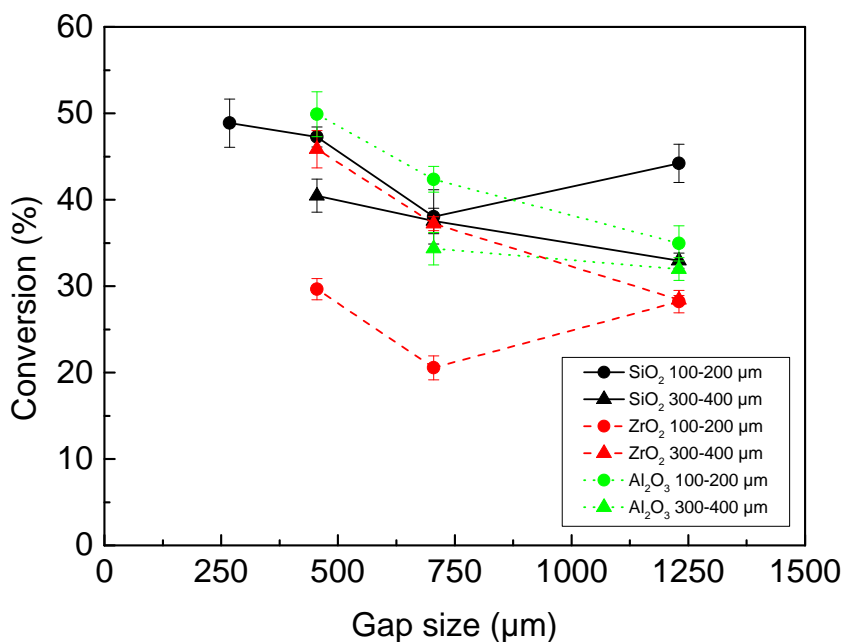


**Figure 2.9:** Conversion for different materials and sphere sizes, as a function of gap size, throughout the micro gap size range, at a constant residence time of 7.5 s and 30 W plasma power.

The 100-200 μm spheres of SiO<sub>2</sub> and ZrO<sub>2</sub>, however, show a somewhat higher conversion in the 1230 μm gap, which cannot yet be explained. In general, the different materials and sphere sizes do not yield very different conversion, with values always between 30 and 50% for all materials, bead sizes and gap sizes, except for the smaller ZrO<sub>2</sub> spheres, which perform somewhat worse. Nevertheless, it is clear from this figure that depending on the gap size, other materials should be chosen to reach the highest conversion.

### 2.3.2.2 Electrical characterisation

In an attempt to reveal the underlying mechanisms of the improvements in conversion observed in 3.2.1, electrical characterisation was performed as well for the packed reactors. Figure 2.10 illustrates as an example the Lissajous plots for the packed-bed reactor with 1230 μm gap, packed with the 300-400 μm spheres of different materials, as well as glass wool. Electrical differences are noticeable between the different materials for the maximum voltage, maximum charge, and burning voltage, but also subtle changes can be observed in the

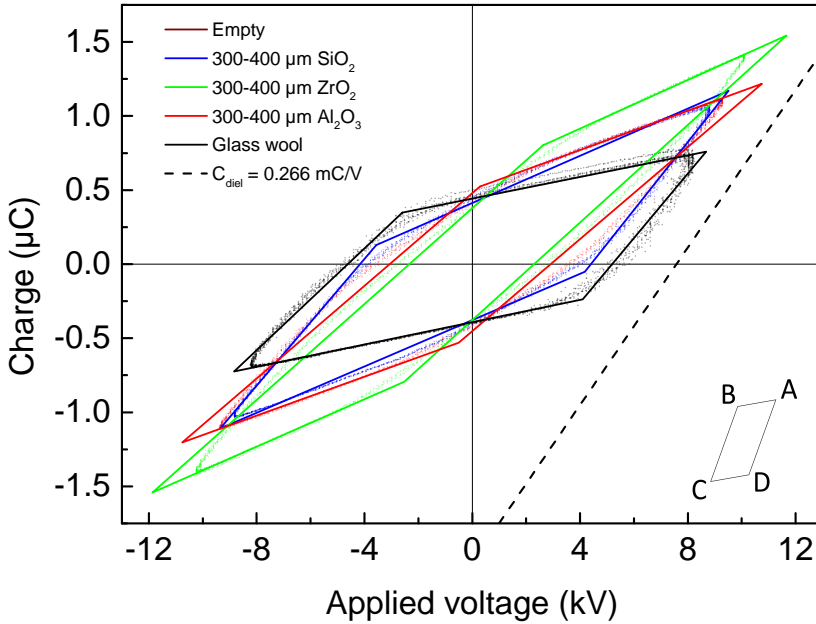


**Figure 2.10:** Raw Lissajous plots (dotted) for a DBD micro reactor with a gap size of  $1230\ \mu\text{m}$  packed with different packing materials (see legend) for a constant residence time of  $7.5\ \text{s}$ , as well as the slopes calculated by the MATLAB script (solid lines). Comparison is also made with the  $C_{\text{diel}}$  value of a completely discharged reactor (dashed line).

effective capacitance  $\zeta_{\text{diel}}$  and the resulting partial discharging  $\alpha$  (see details in appendix A). It is also visible that a packing material can influence the discharge and capacitive phase. For example, zirconia and alumina show a relatively short capacitive phase and a long discharge phase, while silica and glass wool show a relatively long capacitive phase and a shorter discharge phase.

These characteristics change even more with varying sphere and gap size. The investigated parameters in this electrical characterisation are again the peak-to-peak voltage ( $U_{pp}$ ), root-mean-square current ( $I_{RMS}$ ), effective capacitance ( $\zeta_{\text{diel}}$ ), partial discharging fraction ( $\alpha$ ), burning voltage ( $U_{bur}$ ), number of micro discharges per period, and displaced charge per micro discharge, as in section 2.3.1.2. A lot of data is retrieved this way with multiple parameters changed between them, being the material type, material size and gap size. Besides the effect of the packing materials, which can influence the electrical characteristics of the plasma; these electrical parameters can influence the packing material behaviour as well, resulting in coupled interactions until

a steady-state like behaviour is reached. In addition, all the possible inter-electrical and inter-material interactions should be considered. There might be more parameters that have to be taken into account to fully understand the electrical, physical, and chemical behaviour of the plasma in packed-bed reactors; therefore, it is still very complicated to draw fundamental conclusions. This makes it particularly difficult to pinpoint the underlying mechanisms of the conversion results presented in section 2.3.2.1, although a number of observations can be made.

The detailed trends of the electrical characteristics for the various materials, bead sizes and gap sizes are plotted in appendix A (see figures A.2 - A.8). In general, it can be seen that most of the electrical parameters still follow the same trends as seen in the empty reactor (section 2.3.1.2). They do, however, differ between the different packing materials and sizes. Significant trends can be seen for the peak-to-peak voltage, RMS current and the partial discharging behaviour of the plasma for the different sphere sizes. These trends are, however, very dependent on the specific material being used. Some are even completely opposite, suggesting that there are multiple effects at play, influencing the resulting conversion. The burning voltage, on the other hand, is completely unaffected by material composition and sphere size and thus only controlled by the gap size. The number of current pulses is a lot higher, but the pulses are weaker, compared to the empty reactor. Up to 512 micro discharges were observed in the packed reactor, with a maximum transferred charge of 5.9 nC/discharge, while the empty reactor had only a maximum of 49 micro discharges, but with a maximum of 59 nC/discharge.

### 2.3.2.3 Efficiency

In figure 2.8 we showed that adding a packing material to the reactor can indeed drastically enhance the conversion by a factor 3.47, when compared to an empty reactor with the same residence time, and some materials yield even better conversion than the empty reactor with the same flow rate but a residence time almost four times as long. In figure 2.11 the results of the energy efficiency are plotted to check if the packed-bed micro gap reactors can do better overall. Only the energy efficiency is plotted here, since dissociation rate and energy yield show exactly the same trend at a constant power input, with only a difference

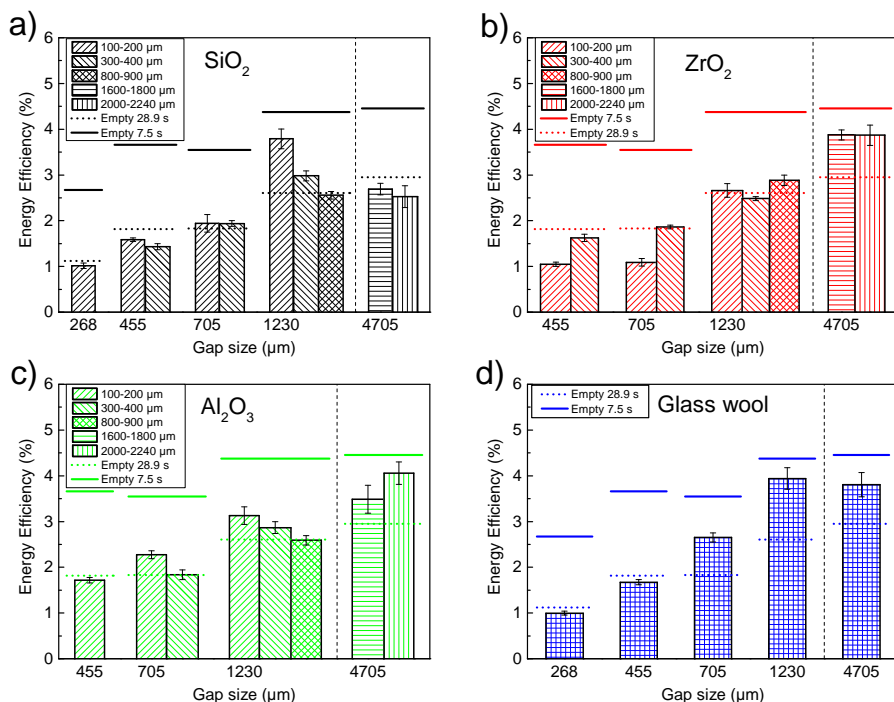


**Figure 2.11:** Energy efficiency in packed-bed DBD (micro) reactors for a constant residence time of 7.5 s and plasma power of 30 W. The results are displayed per material type for different sphere sizes (indicated by the legend) and as a function of gap size, and compared to the empty reactor at the same residence time of 7.5 s (solid horizontal lines) and a residence time of 28.9 s (corresponding to the same flow rate as the packed-bed reactors) (dashed horizontal lines).

of a constant factor, i.e. 0.065 mmol/min% and 0.130 mmol/Wh%, respectively.

The ‘material-size-gap’ combinations that showed a better conversion than the empty micro gap reactor with 28.9 s residence time (hence same flow rate as the packed-bed reactor) also show better energy efficiencies (cfr. the small horizontal dashed lines), which is logical since the energy efficiency is proportional to the conversion and all the other parameters in the formula (i.e. power, flow rate; see equation (2.3)) are the same. Thus, adding a packing material to the reactor, while maintaining the same throughput, increases the efficiency slightly, depending on the material type and size. The best results are obtained in the 1230 μm gap, filled with either 100-200 μm SiO<sub>2</sub> spheres or glass wool; or the original 4705 μm gap with ZrO<sub>2</sub>, Al<sub>2</sub>O<sub>3</sub>, or glass wool packing. In general, glass wool performs best, followed by Al<sub>2</sub>O<sub>3</sub>, as it yields an improvement in the 705 μm gap, as well as in the regular sized reactor.

On the other hand, while the conversions improved significantly when

compared to the empty reactor at the same residence time of 7.5 s (see figure 2.8 above), this improvement is not reflected in the efficiency results, when compared to the empty reactor at the same contact time of 7.5 s. Indeed, the almost four times decrease in flow rate (which negatively affects the energy efficiency, cfr. equation (2.3)) is not compensated by a sufficient increase in conversion (which was typically around a factor of 2). The ‘material-size-gap’ combinations that come closest to the empty reactor at the same residence time are again the 1230 μm gap, filled with either 100-200 μm SiO<sub>2</sub> spheres or glass wool, i.e. the same as above. These materials perform remarkably well, certainly keeping in mind their low dielectric constant, and because the conversion is rather low in the empty reactor at this relatively large gap size, they seem to have more room to improve, before they reach the observed maximum conversion of around 50-55%, dictated by the equilibrium with the back reaction, see section 2.3.1.3.

It can also be deduced from the energy efficiency data that the larger gap size reactors without any packing material show the highest energy efficiency. It should, however, be noted that the performance of the packed-bed reactors was not tested at the flow rates corresponding to those of the empty reactor at 7.5 s residence time. This will result in an even shorter residence time of only 1.9 s, yielding a lower conversion. For some ‘material-size-gap’ combinations, the conversion will probably still be higher than in the empty reactor (as can be deduced from figure 2.8), and therefore in the end perhaps still slightly higher efficiencies could be expected (probably around 5-5.5%, if the same trends can be expected as for the larger residence time).

Finally, it can be concluded from all our results that the best performing ‘material-size-gap’ combination, in terms of both conversion and energy efficiency, at the conditions investigated here (reactor type, reactor shape, power and frequency) corresponds to a gap size between 1230 and 4705 μm, with smaller sized spheres (mainly of SiO<sub>2</sub> or Al<sub>2</sub>O<sub>3</sub>), or glass wool as packing material, at elevated flow rates.



## 2.4 Conclusion

In this chapter, we investigated the effect of gap size, as well as packing material and sphere size, on the CO<sub>2</sub> conversion and corresponding energy efficiency, in both empty and packed-bed DBD reactors. We focused especially on micro gap size reactors (268-1230 μm), but also made the comparison with a regular sized reactor of 4705 μm. Reducing the gap size was shown to significantly enhance the conversion, compared to a regular size DBD reactor, both in an empty reactor and packed-bed reactor. In the empty reactor, the conversion could rise up to 33% and 54% at a residence time of 7.5 s and 28.9 s, respectively, in the smallest gap size. The effect of residence time was further investigated in a gap size of 455 μm and revealed an increasing conversion up to 30 s before levelling off to a maximum conversion of around 50-55%. At the same time, thorough analysis of the Lissajous figures showed that reducing the gap size provides a more uniformly ignited reactor, with a larger amount of micro-discharges and a larger displaced charge in the discharge phase of the reactor, which can explain the higher conversion. This might be related to the higher reduced electric field and power density (resulting from the same applied voltage/power over a smaller gap/volume).

The influence of adding a packing material was greatly dependent on the type of material being used, the corresponding size and the discharge gap. In contrast to results obtained in a regular sized reactor [58, 68], silica and glass wool gave the best improvements in conversion, next to alumina, with maximum conversions reaching around 50%. Furthermore, the effect of size of the packing material is greatly dictated by the material being used. Silica and alumina show better results with decreasing sphere size for a given gap size, while zirconia shows the opposite trend. Electrical analysis of the Lissajous figures showed that several known and unknown parameters might play a role in determining the conversion. The effect of partial discharging, burning voltage, number of micro-discharges, displaced charge, peak-to-peak voltage and current was discussed, and we can conclude that a lot of parameters might play a role in determining the obtained conversion results. Systematic synthesising and testing of packing materials in a controlled environment, such as the apparatus proposed by Butterworth and Allen [100] with one or multiple spheres, might be needed here to pinpoint the exact role of each of these parameters.

While the conversion significantly increased upon decreasing gap size and upon adding a packing in the reactor, the corresponding efficiency shows less impressive results. For the empty reactor, the regular gap size (4705  $\mu\text{m}$ ) appears to be the most energy efficient configuration, despite the immense increase in conversion obtained upon gap size reduction. The maximum energy efficiency obtained was 4.3%. In general, the efficiency was found to be better in the larger gap sizes, when comparing at the same residence time, which is logical as larger gap sizes yield a (significantly) higher flow rate for the same residence time, and the energy efficiency is proportional to both conversion and flow rate. When the reactor was packed with different materials, some 'material-size-gap' combinations yielded higher efficiency compared to the same flow rate in the empty reactor, but when compared at the same residence time, the energy efficiency was always lower than in the empty reactor.

So now we are able to answer the question: Does size matter? The answer is definitely yes. However, the next question is: How does it matter? As illustrated in this chapter, the answer will depend on which specific size, i.e. of the gap or spheres, which type of the material and which desired effect is aimed at, i.e. increased conversion and/or efficiency. We have to be careful when studying the effect of packing materials in DBD reactors. It is almost impossible to predict their exact behaviour, since there are numerous unknown variables of the materials, as well as intertwined parameters of the material-reactor configuration, such as dielectric constant and gap size. This stresses the need for systematic experiments of different material-reactor combinations. The conclusions drawn in this chapter therefore apply to pure CO<sub>2</sub> splitting, and cannot necessarily be generalised to other systems. To draw conclusions for other gases or mixtures, dedicated experiments should be performed. With this work, we contributed to gain some insight in these complex and intertwined effects.

## **Chapter 3**

# **The potential use of core-shell structured spheres in a packed-bed DBD plasma reactor for CO<sub>2</sub> conversion**

Published as:

Y. Uytendhouwen, V. Meynen, P. Cool, and A. Bogaerts, “The Potential Use of Core-Shell Structured Spheres in a Packed-Bed DBD Plasma Reactor for CO<sub>2</sub> Conversion,” *Catalysts*, vol. 10, p. 530, may 2020

## Abstract

This work proposes to use core-shell structured spheres to evaluate whether it allows to individually optimise bulk and surface effects of a packing material, in order to optimise conversion and energy efficiency. Different core-shell materials have been prepared by spray coating, using dense spheres (as core) and powders (as shell) of  $\text{SiO}_2$ ,  $\text{Al}_2\text{O}_3$ , and  $\text{BaTiO}_3$ . The materials are investigated for their performance in  $\text{CO}_2$  dissociation and compared against a benchmark consisting of a packed-bed reactor with the pure dense spheres, as well as an empty reactor. The results in terms of  $\text{CO}_2$  conversion and energy efficiency show various interactions between the core and shell material, depending on their combination.  $\text{Al}_2\text{O}_3$  was found as the best core material under the applied conditions here, followed by  $\text{BaTiO}_3$  and  $\text{SiO}_2$ , in agreement with their behaviour for the pure spheres. Applying a thin shell layer on the cores showed equal performance between the different shell materials. Increasing the layer thickness shifts this behaviour, and strong combination effects were observed depending on the specific material. Therefore, this method of core-shell spheres has the potential to allow tuning of the packing properties more closely to the application by designing an optimal combination of core and shell.

### 3.1 Introduction

As seen in the previous chapter, adding a packing material to the reaction zone will induce both physical and chemical changes, resulting in a wide variety of outcomes [8, 62]. On one hand, the packing material will change physical aspects such as the gas flow behaviour through the reactor – by reducing the discharge volume to small voids between the spheres, altering the flow and mixing patterns, and reducing the residence time – as well as the characteristics of the plasma and the discharging behaviour. The properties of the packing material, i.e. size and shape, dielectric constant, (elemental) composition, surface roughness, thermal and electrical properties, porosity, etc., can influence the type of discharge, electron temperature and density, surface losses, etc. [62, 77, 99]. We can differentiate the effects of material properties into bulk and surface effects, e.g. dielectric constant and electrical conductivity are bulk effects, while surface roughness and adsorption are surface effects. On the other hand, the reactive plasma can influence the packing materials as well, both on a short and long term. Short term effects include the generation of a direct flux of excited species, radicals, or ions towards the surface, lowering the activation barrier, and changing reaction pathways; long term effects are alterations to the material structure, such as changing oxidation states, etching/destruction of the surface/pores, and/or inactivation of doped catalysts [62]. Furthermore, the gas mixture itself will influence the plasma characteristics, and requires specific conditions as well for optimal transfer of electrical energy in chemical energy. It is therefore not at all straightforward to correlate any cause and effect, when introducing and comparing different packing materials.

When searching for the best packing material, using pure, dense bulk materials quickly hits some obstacles, as each material has its fixed and specific properties that cannot be changed individually at the surface and in the bulk. Moreover, changing the material type varies several of the above-mentioned parameters (both physical and chemical; and both surface and bulk), that impact the plasma behaviour and surface chemistry at the same time. Indeed, in our previous work we investigated millimetre-sized spheres from different materials in a packed-bed DBD reactor for both CO<sub>2</sub> dissociation (acting as benchmark in this work as well) and dry reforming of methane (DRM), and

we found it was not a straightforward method to pinpoint the exact origin of the observed effects [58, 84, 92], see also previous chapter. Additionally, using exactly the same reactor with different operating parameters renders different results [58, 84]. Hence, in order to be able to better tune a packing material, combining different properties in bulk (physical) and surface (physical-chemical) behaviour might be needed for optimal performance. The combination of these properties might, however, not be present in one type of material. Therefore, we evaluate in this paper the potential of using millimetre-sized core-shell structured spheres. These spheres consist, as the name implies, of a dense spherical core that is covered with a (thin) shell (of 50-500  $\mu\text{m}$  thickness). The core will mainly determine the bulk effect of the entire sphere such as dielectric constant, thermal and electrical properties; while the shell, will determine mainly the surface effects such as porosity, adsorption, (electrical) surface properties, and surface chemistry, as well as some bulk effects, if the shell is made sufficiently thick, potentially shielding core effects. With this approach, we can test a wide variety of combinations of core and shell material types, and their respective sizes, in order to evaluate the potential of core-shell materials to tune the DBD reactor performance.

Core-shell spheres have been widely used in the past, with examples found in thermal catalysis, electro catalysis, photo catalysis, drug screening, etc. [102–110], and with coated pellets widely used in the pharmaceutical and food industry [111–113]. Usually the core-shell spheres are produced in the micro- to nanometre range via methods such as sol-gel deposition, hydrothermal synthesis, colloidal synthesis, plasma deposition, and micro-fluidic gelation; with only a few examples found in the millimetre-size range made by hydrothermal synthesis or spray coating [103, 111–114]. Although being widely used in different fields of research and application, core-shell spheres are rarely adopted in plasma conversion processes, with only a few cases reported in literature, e.g. Zheng *et al.* used nano-sized core-shell particles for DRM [115, 116]. Coated spheres with dispersed or clustered catalytically active materials, or nano-sized (mono-) layers, have also been used in plasma reactors [117], but to our knowledge, no research has been reported using millimetre-sized core-shell spheres with systematically altered core-shell combinations of different materials as those we propose here. This approach is evaluated for  $\text{CO}_2$  splitting

into CO and O<sub>2</sub> due to its simpler chemistry compared to multi-component mixtures, such as (dry) reforming of methane. Specifically, we will investigate the influence of adding a shell to a spherical core, and how the respective material combinations and shell thickness affect the overall performance of the DBD reactor, in terms of CO<sub>2</sub> conversion and energy efficiency, in order to estimate its potential in design of appropriate packing materials for plasma conversion processes. The purpose is not finding the highest activity but evaluating the potential of core-shell structures to improve packed-bed plasma reactor performance.

## 3.2 Materials and methods

### 3.2.1 Core-shell spheres

The core-shell spheres were synthesised by means of spray coating. With this method, a suspension of the desired shell material is sprayed on the cores in fine droplets, which stick to the surface, and as the solvent evaporates, it leaves a fraction of powder behind. Spraying while turning the core materials in a pan, slowly builds up a full layer over time, that can grow to a desired thickness. A calcination process was applied to fix the layer in place and remove the organic components.

The formulation of the coating suspension is the same for all core-shell combinations and was based on the coating slurry of Lefevre *et al.* for their 3DFD structures [118]. A mixture of distilled water, methyl cellulose as a temporary organic binder (15 cP, Sigma-Aldrich), and colloidal silica as a permanent binder (LUDOX HS-40, Sigma-Aldrich) was used to disperse and suspend the powdery shell material. The final composition was 1 wt% methyl cellulose, 1 wt% LUDOX, and 30 wt% shell powder. Powders made of SiO<sub>2</sub> (0-10 μm, Sigmund Lindner), α-Al<sub>2</sub>O<sub>3</sub> (400 nm A 16 SG, Almatix), and BaTiO<sub>3</sub> (200 nm, Inframat) were used as the shell materials as received. For each new batch, 100 mL of bare spheres, used as the cores, were placed in a rotating bowl with agitation fins to tumble the spheres around and ensure an as even as possible coating of all spheres and sphere surface. Dense SiO<sub>2</sub> (Type-S, Sigmund Lindner), α-Al<sub>2</sub>O<sub>3</sub> (custom made at VITO) [94], and BaTiO<sub>3</sub> (Catal Ltd.) spheres with a size of 1.6-1.8 mm were used as cores. The suspension was coated on the rotating spheres by a

compressed air driven spray gun, and dried at the same time with a hot air gun. The green core-shell spheres were calcined for four hours at 650°C with a heating ramp of 2°C/min. Four shell thicknesses were aimed at being 50 µm, 100 µm, 150 µm, and 200 µm. Maximum layers of approximately 100 µm were applied at a time. The 150 µm and 200 µm coatings were done in two steps with an intermediate calcination step. In practice, deviant shell thicknesses will be obtained however due to the unpredictable suspension losses during the coating process, i.e. premature drying of the sprayed droplets and abrasion losses during tumbling. The shell thickness was analysed after calcination by embedding the spheres in an epoxy resin (ClaroCit, Struers), sanding them down until halfway the spheres, being imaged by 10x microscope (Horiba Scientific, XploRa plus), and being analysed by ImageJ. A schematic representation of the spray coating set-up and an example of four layer thicknesses of BaTiO<sub>3</sub>@SiO<sub>2</sub> core-shell spheres are shown in appendix B.1 and B.2 (figure B.1 and table B.1 respectively).

### 3.2.2 Experimental set-up

Exactly the same reactor and set-up was used as in chapter 2, shown in figure 2.1. In this chapter, the reaction volume was filled with either the reference dense spheres or synthesised core-shell spheres, which were held in place with a layer of glass wool (superfine 8-50 µm, Glaswarenfabrik Karl Hecht) on both sides. The reference spheres are the same cores as in section 3.2.1, in two size ranges, being 1.6-1.8 mm and 2.0-2.24 mm.

A pure CO<sub>2</sub> stream was fed to the reactor via a mass flow controller. A flow rate of 38.98 mL/min was used for both empty and packed reactors, and in addition, a flow rate of 75.35 mL/min was used for the empty reactor to test the performance at equal residence time as the packed reactor at 38.98 mL/min (i.e. 14.07 s for a modelled packing efficiency of 48.27%, see remarks of chapter 2 and appendix C of chapter 4).

The analysis of conversion (equation 2.2), power (equation 2.5), energy efficiency (equation 2.3), and experimental error (equation 2.7) was done analogue to section 2.2.1.



### 3.2.3 Experimental method

The standard operating conditions used in this work were a pure CO<sub>2</sub> stream with a flow rate of 38.98 mL/min, performed at 30 W (3 kHz), and 1 bar in a discharge gap of 4.5 mm. This results in an average residence time of 14.07 s and a specific energy input (SEI) of 46.18 J/mL in the packed reactors. Some of these parameters were varied, as specified in the results section.

## 3.3 Results

Before discussing the effect of using core-shell spheres with different shell thicknesses, the reference will be discussed (empty reactor and pure cores). Note that the results of the pure spheres were obtained in our previous chapter and are more thoroughly discussed there.

### 3.3.1 Benchmark measurements for the empty reactor and the reactor packed with pure spheres

Figure 3.1(a) shows the results for the empty reactor at the standard conditions (denoted as “= Flow”), and a higher flow rate to obtain the same residence time (RT) as the packed reactors (denoted as “= RT”). It shows a base conversion and energy efficiency of 11% and 3.0%, respectively, for a flow rate of 38.98 mL/min (27.20 s RT); while obtaining 6.4% and 3.2%, respectively, for a flow rate of 79.96 mL/min (14.07 s RT). Note that all but one bar in figure 3.1 represent both conversion and energy efficiency since they are just scaled. The measurement of the empty reactor at the same residence time (“= RT”) has two parts of which the lower part depicts the conversion and the upper part the energy efficiency.

Inserting a packing material into the discharge gap shows clear material and size dependent effects, as also shown and discussed in [58, 92] and in previous chapter. All packed reactors show better conversions than the empty reactor at the same residence time, i.e. same gas treatment time. However, when compared with the empty reactor at the same flow rate, i.e. same throughput, only the Al<sub>2</sub>O<sub>3</sub> spheres, and the BaTiO<sub>3</sub> spheres at 1.6-1.8 mm diameter perform better (both in conversion and energy efficiency). SiO<sub>2</sub> with a size range of 1.6-1.8 mm shows a lower conversion of 9.8% and the larger sphere size, 2.0-2.24 mm,

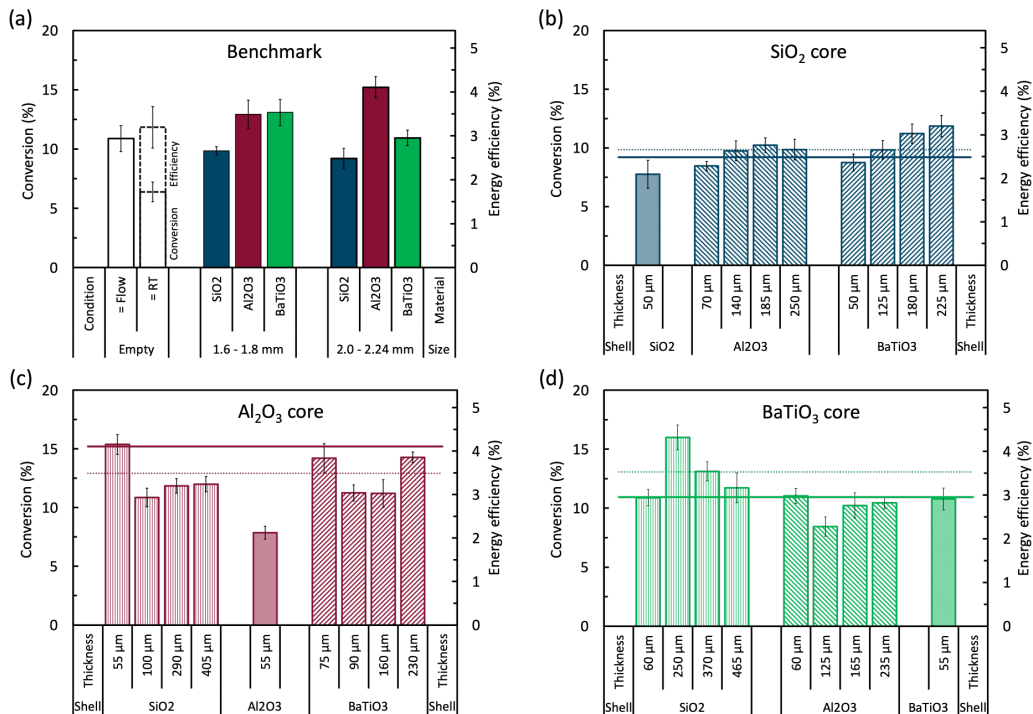


**Figure 3.1:** Overview graph of the conversion and energy efficiency of (a) the benchmark results (i.e. empty reactor and packed reactor with pure spheres [92]), and all core-shell samples with (b) SiO<sub>2</sub> core, (c) Al<sub>2</sub>O<sub>3</sub> core, and (d) BaTiO<sub>3</sub> core. All core-shell samples were coated with SiO<sub>2</sub>, Al<sub>2</sub>O<sub>3</sub>, and BaTiO<sub>3</sub> powder in different shell thicknesses, as indicated in each figure. All measurements were performed at 30W, 38.98 mL/min, and 1 bar; except for the empty reactor, which was also evaluated at the same residence time as the packed reactors (75.35 mL/min). The dotted and solid lines are the performance of the corresponding core spheres in their small and big size, respectively. The exact values can be found in table B.2 in appendix B.3.

even yields a slightly worse conversion of 9.2% (within error bars). This means that SiO<sub>2</sub> is able to enhance the electric properties of the plasma through local electric field enhancements [99], but not enough to compensate for the 48.27% reduction in reaction volume due to the spheres (see section 3.2.2). Adding a packing to the reactor increases the available surface area to promote (catalytic) surface chemistry. If present, this surface chemistry can also inhibit the plasma chemistry, by losses of energetic species upon collision with the surface [56]. Al<sub>2</sub>O<sub>3</sub>, however, can compensate for the reaction volume reduction, with a conversion of 13% at a 1.6-1.8 mm sphere size, and 15.2% at a sphere size of 2.0-2.24 mm. Lastly, BaTiO<sub>3</sub> shows an improved conversion of 13% at 1.6-1.8 mm sphere size, but the 2.0-2.24 mm spheres performed worse, with a conversion of 10.9%. These results illustrate the interaction between sphere

size and material type on the conversion. Both  $\text{SiO}_2$  and  $\text{BaTiO}_3$  exhibit a slight decrease in conversion, while  $\text{Al}_2\text{O}_3$  shows an increase at larger sphere size. This is consistent with the modelling work of Van Laer and Bogaerts [99], which revealed that there is not necessarily a linear correlation between dielectric constant and the plasma parameters (electric field, electron temperature, and electron density), as well as the sphere size (number of spheres in the discharge gap). The trends in energy efficiency are the same as for the conversion, which is logical when the flow rate is kept constant. More considerations about the energy efficiency will be given in section 3.4 below.

Evidently, each material behaves differently based on their size, and this may be attributed to a number of material specific properties – such as dielectric constant, surface roughness, surface chemistry, electrical conductivity, heat capacity, etc. as well as the number of contact points, void space between the spheres, etc., which proved to be difficult to correlate by previous researchers [58, 84]. By comparing these benchmark results with the performance of the core-shell samples in next section, we hope to obtain some clues on the effect of the material properties with respect to their bulk or surface effect.

### **3.3.2 Core-shell spheres**

A matrix of samples has been prepared based on three materials (i.e.  $\text{SiO}_2$ ,  $\text{Al}_2\text{O}_3$ , and  $\text{BaTiO}_3$ ) in different shell thicknesses to investigate the effect of the shell material, the core material, and the shell thickness, as shown in figure 3.1(b – d). However, for an unbiased evaluation, first we will look into the actual influence of adding a shell to the spheres, by coating them with a shell of the same material as the core material.

#### **3.3.2.1 Influence of a shell on the performance of the spheres**

By coating the pure spheres with a thin layer of the same powderous material as the core, we can investigate how a calcined powder layer affects the performance compared to the pure spheres. Figure 3.2 shows the results of the pure spheres coated with a thin layer of approximately  $50\ \mu\text{m}$  to form a shell of the same material. As can be observed, all core-shell spheres show worse results than

their pure non-coated 1.6-1.8 mm variants (shown as a solid line).  $\text{SiO}_2@\text{SiO}_2$  has the smallest drop in conversion (i.e. 8% compared to 9.8% for the pure sphere),  $\text{BaTiO}_3@\text{BaTiO}_3$  shows a somewhat larger drop in conversion (i.e. 10.8% compared to 13%), but the biggest difference is seen with  $\text{Al}_2\text{O}_3@\text{Al}_2\text{O}_3$  where the conversion drops to 7.8% compared to 12.8% for the pure spheres. This negative effect of adding a shell of the same material may be attributed to a different morphology (i.e. macroscopic roughness, powder grain surface, introduced interstitial porosity between the grains etc.), a negative effect of the LUDOX binder, or a masking effect by the shell for a useful property of the core, or a combination of all effects. Indeed, it has been shown that the morphology of the spheres can have a significant impact on the chemistry in plasmas [62]. This is because the morphology can enhance the local electric field by extra contact points, sharp edges, and close surfaces in for example macropores, resulting in different plasma discharges, changing the local chemistry. This may or may not have an effect on the performance, which can be either beneficial or detrimental, depending on the reactions. Additionally, the added LUDOX binder, although necessary for shaping, is an extra material added to the shell which might introduce an unknown effect on the shell performance. Binder effects are known for thermal catalysis [119–121], but have not yet been studied in plasma catalysis, as far as we know. It is also for this reason that we kept the amount of binder limited to 1 wt%, although we cannot exclude its effect even at these small quantities. Furthermore, as plasma can only be formed in pores with diameter larger than the Debye length, which is typically several 100 nm for DBD plasma conditions [122], most of the bulk material of the spheres might be out of reach for the reactive plasma species to promote any reaction. This means that adding a shell, although porous in nature, can shield (most of) the reactive plasma species from the core and thus inhibit any activated core surface chemistry. Apparently, this effect is more present with the  $\text{Al}_2\text{O}_3@\text{Al}_2\text{O}_3$  spheres. Exactly the same source powder of  $\alpha\text{-Al}_2\text{O}_3$  was used to prepare the core spheres and to coat the shells, but they were subject to different synthesis processes (e.g. thermal post-treatments) and different chemicals (e.g. calcium present in the core, a silica binder in the shell). This hints that either (i) the pure  $\text{Al}_2\text{O}_3$  spheres exhibit an effect that is particularly well masked by the shell, e.g. the presence of calcium compounds remaining from the synthesis ( $\text{CaCO}_3$ ,  $\text{CaO}$ ,

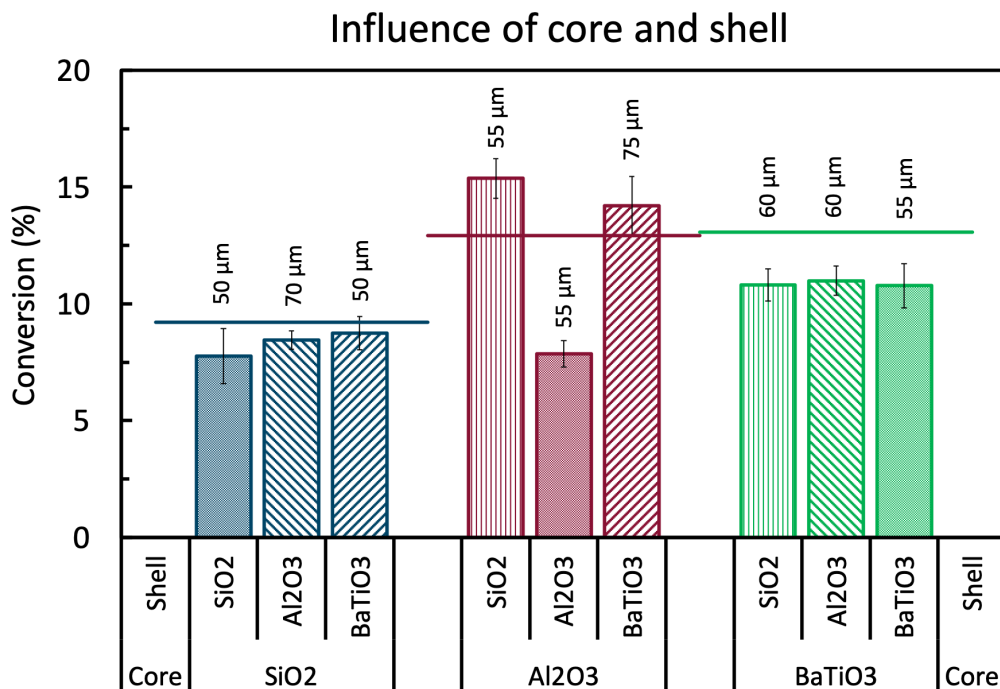


**Figure 3.2:** Influence of the core and shell material tested by approximately 50  $\mu\text{m}$  thick shells applied on different core materials. All samples are compared to the pure spheres (solid line) with 1.6-1.8 mm size. All experiments are performed at the standard conditions. The exact values can be found in table B.2 in appendix B.

and/or  $\text{CaO}\cdot x\text{Al}_2\text{O}_3$  with  $x = 1, 2$  or  $6$ ) [94]; and/or (ii) the  $\text{Al}_2\text{O}_3$  powder has a large inhibiting effect as shell material, by lacking desired surface properties, having unwanted porosity, the presence of the LUDOX binder, or another, yet unidentified, aspect. This clearly indicates that a particular difference in the shell can induce physical aspects that have a relatively large impact on conversion and energy efficiency, necessitating further studies with samples that are well controlled in these properties.

### 3.3.2.2 Influence of core and shell material

By applying a thin shell of approximately 50  $\mu\text{m}$  on a core, we can investigate the individual effect of the shell and core material on the performance of the core-shell sphere, while minimising extra bulk effects that may be caused by the shell. The results of a combination of  $\text{SiO}_2$ ,  $\text{Al}_2\text{O}_3$ , and  $\text{BaTiO}_3$  in figure 3.2 show that no clear order in shell performance can be observed, with the exact (lack

of) impact depending on the core material. The results show that there is little to no difference in performance between the different shell materials when using  $\text{SiO}_2$  cores or  $\text{BaTiO}_3$  cores, while significant differences can be observed when shells are applied on  $\text{Al}_2\text{O}_3$  cores. This suggests that there are no clear surface effects of the different shell materials in the case of  $\text{SiO}_2$  cores or  $\text{BaTiO}_3$  cores and/or that the shells are too thin to have a significant influence on the bulk effects of the whole sphere. However, the  $\text{Al}_2\text{O}_3$  cores show a different story, because  $\text{SiO}_2$  and  $\text{BaTiO}_3$  shells slightly improve the base conversion; but the  $\text{Al}_2\text{O}_3$ - $\text{Al}_2\text{O}_3$  interaction, as already seen in the previous section, clearly has a detrimental effect.

Finally, figure 3.2 illustrates the influence of the core material on the core-shell spheres. The general order of performance puts  $\text{Al}_2\text{O}_3$  cores on top (with the exception of  $\text{Al}_2\text{O}_3@ \text{Al}_2\text{O}_3$ ), followed by  $\text{BaTiO}_3$ , and finally  $\text{SiO}_2$ . The exception of  $\text{Al}_2\text{O}_3@ \text{Al}_2\text{O}_3$  suggests that the  $\text{Al}_2\text{O}_3$  powder (hypothesis (ii) from before) is the culprit of the bad performance and that it is not a core effect. From these results so far, we can conclude that optimal core-shell spheres can be designed by using a strong base material as a core, coupled to a complementary shell material. It is important to realise, that a strong core material is not necessarily also a strong shell material, and vice versa, due to the different (surface and bulk) properties that seem to play a role, as shown by the  $\text{Al}_2\text{O}_3@ \text{Al}_2\text{O}_3$  samples. This illustrates the high potential of core-shell spheres for optimal designed packing materials.

### 3.3.2.3 Influence of shell thickness

Finally, we take a look at the influence of the shell thickness, illustrated in figure 3.1(b – d) with their exact values in table B.2 in appendix B.3. It is clear that the exact effect of extra shell material is very different for all core and shell material combinations.  $\text{SiO}_2$ -based core-shell spheres, which have a low intrinsic performance, show to have opportunity for improvement as thicker  $\text{Al}_2\text{O}_3$  and  $\text{BaTiO}_3$  shells result in higher conversion. The added amount of shell material overcomes any effect of the  $\text{SiO}_2$  cores, resulting in an almost linear increase in added performance.

This is, however, not the case with the  $\text{Al}_2\text{O}_3$  and  $\text{BaTiO}_3$  based core-shell spheres where no continuous increasing or decreasing behaviour is seen in

function of shell thickness for either of the added shell chemistries. This suggests a strong interaction, or even competition, between the more prominently present but shielded surface and bulk effects of the core, and increasing surface and bulk effects of the shell. A combination effect of these properties seems to be present where for example adding more SiO<sub>2</sub> shifts the core-shell performance from pure core material (i.e. Al<sub>2</sub>O<sub>3</sub> or BaTiO<sub>3</sub>) more towards pure SiO<sub>2</sub>, or the conversion of the BaTiO<sub>3</sub>@Al<sub>2</sub>O<sub>3</sub> spheres shifts between pure Al<sub>2</sub>O<sub>3</sub> and BaTiO<sub>3</sub>.

Curiously, SiO<sub>2</sub> shells do show an optimum thickness first, but it is unknown why exactly this ‘poor behaving material’ does this and at this particular thickness. Additionally, Al<sub>2</sub>O<sub>3</sub> shells again show deviant behaviour, i.e. the performance does not rise as much on SiO<sub>2</sub> cores and there is low interaction with BaTiO<sub>3</sub> cores, suggesting that the coated powder has less activity than the shaped spheres (same powder, added binders), see section 3.3.2.2. These results show that optimising core-shell spheres by thickness is possible, but the choice of core and shell material is very important and induces important additional properties. Moreover, it clearly shows that a good core material is not necessarily also a good candidate for a shell. The use of core-shell materials will most likely mainly influence the plasma discharge properties, as they are not necessarily catalytically active, but for specific reactions, they can also promote gas-surface reactions in case of a more porous available surface.

### 3.4 Discussion

A few reflections can be made based on the results from sections 3.3.1 and 3.3.2. First of all, we did not find a core-shell sample with a significant performance improvement within this matrix of materials and shell thicknesses, as was also not intended. The results, however, did shed some light on the bulk and surface effects that different materials have on their performance in a DBD plasma reactor. The present data, however, do not allow us to determine the exact origins of their behaviour but do feature an impact of their relative contribution and thus importance. Better control over the material properties of the core-shell spheres is the next task to identify the underlying features of the results seen here. This requires a separate systematic, more elaborate

study with much more controlled material synthesis based on the knowledge obtained in this work. Additionally, for the further development of tuned (catalytic) (core-shell) packing materials for plasma (catalysis) conversion processes, extra diagnostics would be needed to determine changes in the plasma electrical behaviour and plasma chemistry, such as optical emission spectroscopy or *in-situ* IR spectroscopy. This would allow to determine changes in the chemical species and to provide a more direct way for measuring the material effects on both the plasma gas composition and on the composition of the gas layer near, and adsorbed species on, the material surfaces (by *in-situ* spectroscopic measurements). This might elucidate the reactions that may occur at the surface, indicating any “catalysis”. For instance, IR diagnostics in reflection mode on the surface, i.e. DRIFTS (diffuse reflectance infrared Fourier transform spectroscopy) coupled to mass spectrometry (DRIFTS-MS) was developed by Stere *et al.* [123] for studying plasma-catalytic reactions through observation of changes in the species at the catalyst surface. This work was the first DRIFTS hybrid plasma (DBD) system reported in literature for studying the reaction mechanism during plasma catalysis. The same group also reported another interesting *in-situ* diagnostic [124] for studying the role of plasma in heating on the catalyst structure, using X-ray absorption fine structure (XAFS). Azzolina-Jury and Thibault-Starzyk also applied IR diagnostics, to obtain time-resolved *in-situ* spectroscopic data, directly providing information about adsorbed species under plasma exposure [125, 126]. Note, however, that these techniques are most sensitive to species with large surface density, which are not necessarily the most reactive species. Furthermore, some reactive intermediate species may not be detected, depending on the time resolution. In addition, fast imaging by intensified Charge Coupled Device (iCCD) cameras can be applied to study the plasma behaviour in contact with catalyst materials, and in particular the characteristics of plasma streamers propagating over catalyst surfaces [65, 127, 128]. Finally, plasma dynamic experiments of the spheres in a simplified and standardised packed bed set-up, such as proposed by Butterworth and Allen [100], can provide information on the changes in plasma discharging behaviour for different core-shell materials.

Besides being able to tune and optimise the bulk and surface effects of packing materials through core-shell spheres, the macroporous shell structure forms



interesting opportunities for catalyst doping. It was predicted by modelling that plasma streamers can only penetrate into pores with a size larger than the Debye length [122], which is typically a few 100 nm, depending on the gas and other operating conditions. Hence, full dispersion of a catalytic compound in the entire (microporous) sphere can be a waste of valuable catalyst material. The thin shell layers produced in our work can form the perfect substrate for catalyst doping for more optimal plasma-catalyst interaction. Bulk effects of the core-shell sphere can optimise the plasma and reactive species generation via its physical impact, while the doped shell material can create the optimal accessible surface needed for catalyst reactions, with the possibility to enhance reaction pathways via the plasma-excited species.

Additionally, in chapter 5 we investigated the reaction rate coefficients and equilibrium constants of CO<sub>2</sub> dissociation, CH<sub>4</sub> reforming, and dry reforming of methane under the influence of power, pressure, discharge gap size, and packing materials. By testing packed-bed reactors over an extended residence time range, we discovered that packing materials can individually change the overall reaction rate coefficient, as well as the equilibrium position. By checking only one particular condition, a lot of possible information is lost about the exact effect of a certain type of packing material on the kinetics. Therefore, further endeavours in (catalytic) packing material development will benefit from using this type of analysis to obtain more detailed knowledge.

Finally, figure 3.1 also displays the energy efficiency of the benchmark results and all core-shell samples. It shows the same trends as the conversion, since the energy efficiency is linearly proportional to the conversion when the power and flow rate are constant. The reference energy efficiency of the empty reactor was found to be only 3% for both cases, i.e. same flow rate and same residence time as the packed reactors. Adding the pure un-coated spheres can enhance the energy efficiency, depending on the material and size combination, up to 4.1% for 2.0-2.24 mm Al<sub>2</sub>O<sub>3</sub> spheres. Within the core-shell samples, only the 55 μm SiO<sub>2</sub>@Al<sub>2</sub>O<sub>3</sub> and 250 μm SiO<sub>2</sub>@BaTiO<sub>3</sub> can slightly enhance this energy efficiency further, although all within the same error bars. This matches the maximum values we have found before for CO<sub>2</sub> dissociation in our previous chapter on packed-bed (micro) DBD reactors.

### 3.5 Conclusion

In this chapter we investigated the potential of core-shell structured spheres as packing materials in a DBD reactor, for plasma-based CO<sub>2</sub> conversion. Core-shell spheres have the potential to be tailored to a specific reaction, requiring weak/strong bulk/surface effects, potentially in combination with a catalytically active material for optimal performance. First of all, we found that applying a thin shell layer of approximately 50 μm of the same material as the core significantly reduces the performance of the packing material, indicating that the shell might mask the positive effect of the core and/or induced negative effects due to certain shell properties. Combining different materials showed various interactions between the core and shell material, affecting the conversion. Al<sub>2</sub>O<sub>3</sub> was found to be the best core material, followed by BaTiO<sub>3</sub> and SiO<sub>2</sub>, in agreement with the behaviour of the pure spheres. It was also found that all three shell materials perform equal in low amounts (thin shell), with the exception of Al<sub>2</sub>O<sub>3</sub>@Al<sub>2</sub>O<sub>3</sub>, and that they are not able to provide any significant improvement. A strong mixing behaviour is seen where more active shell materials can improve weak core materials, but will have to compete against strong core materials to show their effect on the performance.

Our results show that surface and bulk effects can have different influences on the performance of the spheres in a plasma reactor. A strong core material is not necessarily also a strong shell material, and vice versa, due to the different (surface and bulk) properties that seem to play a role; as shown by the Al<sub>2</sub>O<sub>3</sub>@Al<sub>2</sub>O<sub>3</sub> sample. This illustrates a great potential, as using core-shell spheres can provide us with the possibility of tuning the packing properties more closely to the application. Furthermore, the thin porous nature of the shell offers possibilities to dope a packing material with just the right amount of catalyst for plasma catalysis, compared to fully porous supports, where catalyst material could be wasted, as the plasma cannot penetrate deeply into pores (with minimum diameter of a few 100 nm).

# Chapter 4

## How process parameters and packing materials tune chemical equilibrium and kinetics

Published as:

Y. Uytendhouwen, K. Bal, I. Michiels, E. Neyts, V. Meynen, P. Cool, and A. Bogaerts, “How process parameters and packing materials tune chemical equilibrium and kinetics in plasma-based CO<sub>2</sub> conversion,” *Chemical Engineering Journal*, vol. 372, pp. 1253–1264, sep 2019

## Abstract

Plasma (catalysis) reactors are increasingly being used for gas-based chemical conversions, providing an alternative method of energy delivery to the molecules. In this work we explore whether classical concepts such as equilibrium constants, (overall) rate coefficients, and catalysis exist under plasma conditions. We specifically investigate the existence of a so-called partial chemical equilibrium (PCE), and how process parameters and packing properties influence this equilibrium, as well as the overall apparent rate coefficient, for CO<sub>2</sub> splitting in a DBD plasma reactor. The results show that a PCE can be reached, and that the position of the equilibrium, in combination with the rate coefficient, greatly depends on the reactor parameters and operating conditions (i.e. power, pressure, and gap size). A higher power, higher pressure, or smaller gap size enhance both the equilibrium constant and the rate coefficient, although they cannot be independently tuned. Inserting a packing material (non-porous SiO<sub>2</sub> and ZrO<sub>2</sub> spheres) in the reactor reveals interesting gap/material effects, where the type of material dictates the position of the equilibrium and the rate (inhibition) independently. As a result, no apparent synergistic effect or plasma-catalytic behaviour is observed for the non-porous packing materials studied in this reaction. Within the investigated parameters, equilibrium conversions are obtained between 23% and 71%, whereas the rate coefficient varied between 0.027 s<sup>-1</sup> and 0.17 s<sup>-1</sup>. This method of analysis can provide a more fundamental insight in the overall reaction kinetics of (catalytic) plasma-based gas conversion, in order to be able to distinguish plasma effects from true catalytic enhancement.

## 4.1 Introduction

While traditional chemical reactors usually require harsh conditions – i.e. up to a few thousand Kelvin and/or hundred bars, to achieve sufficient conversion [8], generally in combination with a catalyst to enhance the kinetics – plasmas can offer similar conversions yet at much milder conditions. A dielectric barrier discharge (DBD) reactor in particular can operate at atmospheric, and slightly elevated pressure (up to several bars), and near room temperature, while the electron temperature can reach a value up to 10 eV (or  $\sim 110000$  K) [45], resulting in a non-thermal equilibrium environment. Indeed, various research groups have reported conversions up to 55% in the case of CO<sub>2</sub> dissociation [8, 38, 39, 58, 68, 74, 92] and up to 40% for DRM [72, 73, 96, 129, 130] in DBD reactors at ambient conditions, whereas traditional thermodynamics require a temperature of around 3100 K at 1 atm to achieve a conversion of 55% for CO<sub>2</sub> dissociation, and a temperature of 800 K to achieve 40% conversion for DRM [8]. Since the overall temperature of the gas remains below 500 K for powers up to 100 W in a DBD reactor at 1 atm [58, 92], the thermal thermodynamic equilibrium is still pointing strongly towards the highly stable reactant molecules (CO<sub>2</sub>), which would give rise to no appreciable conversion in a thermal process. This suggests that plasma chemistry is governed by a partial chemical equilibrium different from the thermal thermodynamic equilibrium at the same pressure and temperature, an apparent equilibrium that depends on the plasma operating conditions and reactor parameters [89–91]. Chapter 2 has indicated this behaviour for a micro DBD reactor, with a gap size of 455  $\mu\text{m}$  and plasma power of 30 W, for the dissociation of CO<sub>2</sub> into CO and O<sub>2</sub>, where the conversion increased with increasing residence time up to 30 s and then reached a plateau value of around 50-55%.

The introduction of (catalytic) packing materials into plasma reactors is an obvious step to further enhance conversions and to selectively steer multi-product reactions. Numerous papers showed promising results with increased conversions, leading to the appearance of terms such as “synergistic effect” and “plasma catalysis” [8, 43, 67, 71, 77, 131]. Unlike thermal catalysis, where the catalyst only modifies the kinetic parameters of the process, the combined application of a catalyst with a non-thermal-equilibrium plasma has the potential to simultaneously affect the reaction rate, as well as the position of the

equilibrium. This is because the (catalytic) packing material can influence the plasma behaviour (e.g. electric field enhancement, altering the electron density and temperature, and changing the discharge type), and vice versa, the plasma can modify the material properties (e.g. reactions with the surface, causing activation, modifications, or alternative pathways), as discussed by Neyts and Bogaerts [62]. In addition, packing materials introduce macro porosity inbetween the spheres, as well as meso porosity inside catalyst pores, in which plasma can be generated, depending on the pore size, material properties, and gas [66, 122, 132]. Nevertheless, since most experiments have only probed a limited range of flow rates and residence times, little is known about the specific effect of packing materials on equilibrium and kinetics, as it is difficult to separate these effects in common experimental observations.

The observation of equilibrium-like behaviour in plasma-based gas conversion raises the question how far exactly this analogy with thermal reactions can be taken. That is, to what extent can concepts such as equilibrium concentrations and constants, (overall) rate coefficients, and catalysis be applied to chemical processes in the inherently non-thermal-equilibrium environment of a plasma? And how do the plasma and process parameters, as well as (catalytic) packing materials, affect these concepts? Being able to assign common equilibrium and kinetic concepts to plasma-based reactions would make it possible to directly compare the intrinsic performance of different plasma reactors (as well as with other technologies, e.g. thermal approaches) on a fundamental level, using the same measuring stick.

In this work, we explicitly investigate the apparent chemical equilibrium-like behaviour (or so-called partial chemical equilibrium), as well as the kinetic parameters, of the CO<sub>2</sub> dissociation reaction in a DBD plasma reactor, by performing conversion experiments for a broad range of residence times. Using this methodology, we investigate how the global chemical equilibrium and conversion rate can be tuned through modification of the plasma, reactor parameters, and operating conditions (*in casu* the plasma power, gas pressure, gap size), and introduction of packing materials.

## 4.2 Methods and theory

### 4.2.1 Experimental set-up

The same reactor and set-up was used as in chapter 2, shown in figure 2.1. Three different discharge gaps of 455  $\mu\text{m}$ , 1230  $\mu\text{m}$ , and 4705  $\mu\text{m}$  were used, of which the 455  $\mu\text{m}$  and 4705  $\mu\text{m}$  reactors were also filled with a non-porous spherical packing material made of  $\text{SiO}_2$  and  $\text{ZrO}_2$  (YSZ, yttria-stabilized zirconia) (both Sigmund Lindner), with a size range of 100-200  $\mu\text{m}$  and 1600-1800  $\mu\text{m}$  in the respective discharge gaps, resulting in similar sphere-to-gap ratios of 0.33 and 0.36.

The gas supply consisted of either a pure  $\text{CO}_2$  stream or a 2/3  $\text{CO}$  and 1/3  $\text{O}_2$  mixture, in order to study both the forward and back reaction of  $\text{CO}_2$  conversion, and to gain more information on the equilibrium-like behaviour. Gas flow rates were set and controlled by mass flow controllers (Bronkhorst EL-FLOW Select series) to provide the required flow rates between 1 mL/min and 400 mL/min, which based on the reactor volume, results in specific residence times desired in the experiments. A correction needs to be applied in the case of a packed reactor, since the added packing material reduces the effective reaction volume. Calculations of spheres filling the coaxial reactor of this work in MATLAB revealed the actual packing efficiency to be  $49.51\% \pm 0.02\%$  in the case of 100-200  $\mu\text{m}$  spheres in the 455  $\mu\text{m}$  gap, and  $48.27\% \pm 0.07\%$  in the case of 1.6-1.8 mm spheres in the 4705  $\mu\text{m}$  gap. These values differ considerably from the maximum spherical packing efficiency of 74.048% in case of a close packing, due to sphere-wall interactions and a more realistic filling behaviour in the calculations in case of finite reactor volumes, such as in our DBD reactor. These adjusted packing efficiencies were used to determine the flow rates for corresponding residence time. A more detailed explanation of the calculation can be found in appendix C. Note that the results can easily be converted to gas hourly space velocity (GHSV) with the values above if desired and will match the reciprocal of the residence time.

Gas analysis was performed by the same gas chromatograph (Compact GC, Interscience) with pressure-less sampling. This GC features a thermal conductivity detector (TCD) channel, able to measure the  $\text{CO}$  and  $\text{O}_2$  composition as one peak and the  $\text{CO}_2$  composition separated by an Rt-Q-Bond column. No

significant amounts of ozone and carbon deposition were detected. The CO<sub>2</sub> or total CO + O<sub>2</sub> conversion derived from the GC data was defined as:

$$X_{GC,y} = \frac{\dot{y}_{in} - \dot{y}_{out}}{\dot{y}_{in}} \quad (4.1)$$

with  $\dot{y}$  the molar flow rate of component  $y$ , being either CO<sub>2</sub> or CO + O<sub>2</sub>. This conversion value must be corrected for a pressure-less sampling set-up, due to gas volume expansion in the case of CO<sub>2</sub> dissociation. It has been previously shown by Pinhão *et al.* [96] and Snoeckx *et al.* [97] that the actual CO<sub>2</sub> conversion ( $X_{CO_2}$ ), in a pure CO<sub>2</sub> system, can be calculated by:

$$X_{GC,CO_2} = 1 - \frac{1 - X_{CO_2}}{1 + \frac{X_{CO_2}}{2}} \Leftrightarrow X_{CO_2} = \frac{2X_{GC,CO_2}}{3 - X_{GC,CO_2}} \quad (4.2)$$

Vice versa, in the case of the back reaction, i.e. CO oxidation, the conversion value calculated in equation 4.1 must be corrected for gas volume reduction. Based on the same method as for equation 4.2, we formulated a new expression to calculate the actual CO conversion by:

$$X_{GC,CO+O_2} = 1 - \frac{1 - X_{CO+O_2}}{1 - \frac{X_{CO+O_2}}{3}} \Leftrightarrow X_{CO+O_2} = \frac{3X_{GC,CO+O_2}}{2 + X_{GC,CO+O_2}} \quad (4.3)$$

A needle valve and pressure sensor (Type TK, Gefran) placed between the reactor and the GC were used to regulate an extra pressure drop to the system at the beginning of the experiment when a higher reactor pressure than atmospheric pressure was desired. Otherwise, it was kept in its fully open position, resulting in no significant pressure drop.

The calculation of power (equation 2.5) and experimental error (equation 2.7) was done analogue to section 2.2.1.

### 4.2.2 Experimental method

The reactor was operated for a minimum amount of time of 40 min, to let it reach a thermal steady-state behaviour. Extended operating times up to 120 min were used for flow rates lower than 10 mL/min, to ensure steady-state behaviour in the reactor and the following tubing, for consistent gas composition analysis. The applied voltage was periodically adjusted on the function generator to obtain and



maintain the desired constant plasma powers between 15 and 45 W. Four GC and oscilloscope measurements were recorded as soon as steady-state behaviour was reached.

### 4.2.3 Partial chemical equilibrium

The plasma in the DBD reactor is not in thermal equilibrium, which means that standard equilibrium thermodynamics is not applicable. However, as pointed out by Vepřek and co-workers [89–91], a kind of chemical equilibrium can still be reached in such a case. This partial chemical equilibrium (PCE) state differs from a general chemical kinetic state because it corresponds to a unique gas composition for a given set of process conditions. A kinetic steady state can be achieved at any point in the reactor, provided that the local concentration  $C_A$  of any species  $A$  remains constant in time, i.e.  $\partial C_A / \partial t = 0$ . However, as long as the total consumption and production rates of  $A$  are not equal, a concentration gradient along the length of the reactor  $z$  will exist, so that  $\partial C_A / \partial z \neq 0$ . In a PCE state, one will also have  $\partial C_A / \partial z \neq 0$ , because the total chemical flux (combined consumption and production rate) is zero. As such, a PCE state fulfils the requirement of chemical equilibrium (consumption and production reaction rates are equal). Furthermore, the PCE can be reached from the reagent and the product side of the equilibrium, unlike any of the other steady states encountered in the reactor. The particular equilibrium composition in the reactor does not reflect any thermal thermodynamic equilibrium, but is dictated by the plasma conditions (energy added as electricity). This plasma-induced equilibrium shift explains why thermal thermodynamically forbidden conversions can still take place inside a plasma.

The PCE state can be used to uniquely characterise a plasma-based conversion process, because it directly depends on the plasma conditions. Introduction of the PCE concept to plasma conversion processes also offers a simple way to extract both the maximum conversion achievable in the plasma (which can be obtained from the PCE gas composition), and the overall conversion rate (i.e. the rate of evolution towards PCE) for an arbitrary reaction. As such, “thermodynamic” and “kinetic” effects can be separated or, more correctly, the characteristic shift in chemical equilibrium due to the non-equilibrium plasma can be distinguished from the increased conversion rate caused by reactive plasma chemistry or

(catalytic) packing materials. This study allows to gain deeper insight, in stark contrast with many previous studies of plasma conversion (including our own), where different process conditions were typically compared at fixed residence time. Indeed, in the latter case, it was not possible to unambiguously relate changes in conversion to either changes in rate (or catalytic effects) on one hand, or shifts in the intrinsic conversions on the other hand.

Assuming that both the production and consumption of any species in the plasma reactor can be described as a single (lumped, effective) first order process, its mole fraction can then be correlated with the residence time,  $t$ , through a general expression:

$$x_y(t) = x_{e,y} - (x_{e,y} - x_{i,y})e^{-k_y t} \quad (4.4)$$

with  $x_y$  the mole fraction of component  $y$ ,  $x_{e,y}$  the mole fraction at PCE,  $x_{i,y}$  the initial mole fraction at  $t = 0$ , and  $k_y$  the overall apparent reaction rate coefficient. Because the PCE should be reachable from either side of the reaction,  $2\text{CO}_2 \rightleftharpoons 2\text{CO} + \text{O}_2$ , it is possible to fit either the  $\text{CO}_2$  conversion (forward reaction, starting from  $x_{i,\text{CO}_2} = 1$ ), or the  $\text{O}_2$  conversion (back reaction, starting from  $x_{i,\text{O}_2} = 1/3$ , but an analogous expression could also use the CO conversion). Although up to a thousand reactions [27, 28, 38, 133] could be considered for the  $\text{CO}_2$  plasma chemistry, drastic assumptions were made to simplify the fitting procedure, and no explicit mechanistic information is used to construct the expression. The only purpose of the analysis is to extract a small number of global parameters for each condition, allowing to more directly compare the different conditions. Therefore, the rate coefficient is assumed to be the overall apparent reaction rate coefficient for the forward or back reaction. The full derivation of the fit equation can be found in appendix C.

The experimental data (consisting of up to 132 data points per parameter and reaction) were first converted into mole fractions as stated above, subsequently imported into MATLAB, where a fit was calculated according to equation 4.4, and finally converted back into conversions. From the resulting fit, the equilibrium conversions and apparent rate coefficients of the forward and back reactions can thus be directly obtained, and hence also the equilibrium constant, from:

$$K = \frac{p_{\text{CO}}^2 p_{\text{O}_2}}{p_{\text{CO}_2}^2} \quad (4.5)$$

with  $p$  the partial pressure calculated based on the final  $\text{CO}_2$  conversion for  $p_{\text{CO}_2}$  and on the total  $\text{CO} + \text{O}_2$  conversion for  $p_{\text{CO}}$  and  $p_{\text{O}_2}$ . The results of the data fits are always plotted below with their respective 95% confidence interval. Finally, the time needed to reach the equilibrium conversion was calculated based on the data fit. This was arbitrarily defined when the mole fraction of  $\text{CO}_2$  (for the forward reaction) and  $\text{O}_2$  (for the back reaction) reaches a value of 1.02 times the equilibrium mole fraction calculated by the fit. Equivalently, 98% of the equilibrium conversion can be used as the threshold value.

## 4.3 Results and discussion

Three series of experiments were performed in order to investigate the research questions postulated in the introduction. First, the existence of an equilibrium-like behaviour was tested by performing both forward and back reaction experiments of  $\text{CO}_2$  dissociation, with a residence time up to 75 s (section 4.3.1). The equilibrium and the associated kinetics were further examined by changing various reactor parameters and operating conditions (section 4.3.2), and finally by investigating the effect of (catalytic) packing materials (section 4.3.3). Various conditions were tested and compared with the reference measurements at 30 W, 455  $\mu\text{m}$  gap size, 1 bara, and without packing material.

### 4.3.1 $\text{CO}_2$ splitting can reach a partial chemical equilibrium

$\text{CO}_2$  dissociation and  $\text{CO}$  oxidation experiments were performed, starting from either pure  $\text{CO}_2$  or a  $2/3 \text{ CO} + 1/3 \text{ O}_2$  mixture, respectively, in a 455  $\mu\text{m}$  gap size DBD reactor. Three different powers were used, i.e. 15 W, 30 W, and 45 W, in an extended residence time range up to 75 s. The results of these experiments are shown in figure 4.1. The total  $\text{CO} + \text{O}_2$  conversion is plotted on a reverse order y-axis (100%  $\rightarrow$  0% conversion) to visualise any partial chemical equilibrium behaviour, i.e. reaching the same chemical equilibrium composition as the forward reaction ( $\text{CO}_2$  conversion). Since only traces of unwanted side products, such as carbon and ozone, were detected in this elementary reaction by lack of carbon deposition and test tubes respectively, we can assume that the

composition, and conversion, at chemical equilibrium is related as:

$$X_{e,CO_2} = 1 - X_{e,CO+O_2} \quad (4.6)$$

The results for the plasma dissociation of  $CO_2$  into  $CO$  and  $O_2$ , displayed in figure 4.1, show that for each applied power a plateau is reached between 50% and 60% conversion after a certain residence time, as was also seen in chapter 2. In this overall reaction, it can be assumed, based on  $CO_2$  plasma chemistry simulations in a DBD by Aerts *et al.* [28, 38], that the  $CO_2$  conversion is mainly attributed to electron impact dissociation of  $CO_2$  into  $CO$  and  $O$ , followed by three-body recombination of 2  $O$  atoms (and a third heavy particle) into  $O_2$ . As the residence time increases and more  $CO$  is created, the back reaction (i.e.  $CO$  oxidation) will become more significant, and  $CO$  and  $O_2$  start to be converted back into  $CO_2$ . This is initiated by electron impact dissociation of  $O_2$  into 2  $O$  atoms, followed by the three-body recombination of  $CO$  and  $O$  (with a third heavy particle) into  $CO_2$ . When the gas mixture spends more time in the plasma reactor, the overall rate of  $CO_2$  dissociation decreases, while the overall rate of  $CO$  oxidation increases, until they match and an equilibrium is reached.

In practice, this process is a bit more intricate, due to the filamentary behaviour of a DBD that exhibits short plasma pulses in the form of micro discharges, which typically last for a few hundred nanoseconds [37]. This gives rise to a sequential intermittent behaviour, where first small fractions of gas, both reagent(s) and product(s), are continuously turned into plasma channels (typically 100  $\mu m$  radius [37]), in which the forward and back reactions can take place. This excited state of the gas fractions is then followed by a “cool-down” in between two micro discharges. In an ideal plug-flow-like DBD reactor with the width of one plasma channel, this would mean a stepwise conversion of reactants as a function of time or distance in the reactor (cfr. figure 7 in [28]) until the rates of the forward and back reaction are equal and an equilibrium conversion is reached. However, in a real DBD reactor, the limited amount of micro discharges per period are spread out over the whole reaction volume. This filamentary behaviour, giving rise to a limited number of small reaction channels during short frames, leads to the possibility of gas fractions taking shortcuts through the reactor, where molecules might never be turned into the plasma phase if gas mixing by radial and axial diffusion of gas molecules is

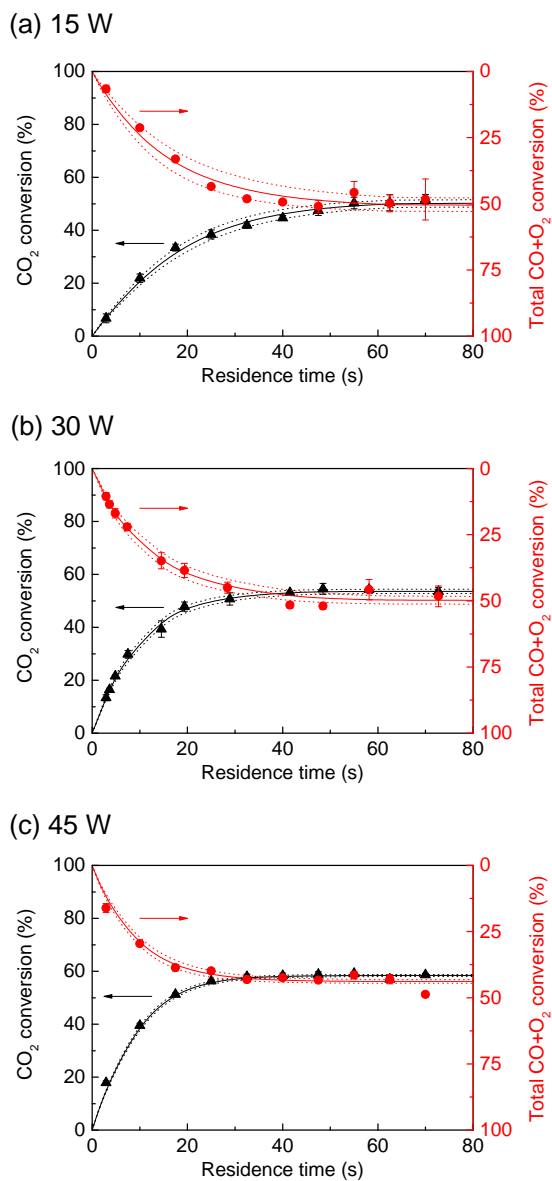


**Figure 4.1:** CO<sub>2</sub> conversion (black triangles) and total CO + O<sub>2</sub> conversion (red circles) in a 455  $\mu\text{m}$  gap size, plotted as a function of residence time for (a) 15 W, (b) 30 W, and (c) 45 W. An apparent first-order reversible reaction fit for both forward and back reaction is applied (solid lines) with its 95% confidence interval (dotted lines).

limited, or the residence time is too short. The reactor does eventually exhibit an equilibrium value when enough time is given, where the forward reaction rate, back reaction rate and the non-ideal (“real”) behaviour converge. In other plasma reactor types, similar intermittent behaviour is apparent, e.g. by subsequent arc discharges (gliding arc reactor [134]) or only once by one homogeneous discharge zone (e.g. glow or microwave discharge reactor [135]).

Similar to the CO<sub>2</sub> splitting process, CO oxidation reaches a plateau after a certain residence time, as evidenced by the total CO + O<sub>2</sub> conversion depicted in figure 4.1. Moreover, the apparent equilibrium conversion  $X_{CO}$  of the CO oxidation reaction is equal to the value of  $1 - X_{CO_2}$  as obtained from the CO<sub>2</sub> splitting reaction. Both processes thus lead to the same gas composition at each tested plasma power. Therefore, we can conclude that plasma-based CO<sub>2</sub> splitting can, in fact, be characterized by its PCE state, which is very different from the thermodynamic equilibrium under thermal conditions, and explains the high CO<sub>2</sub> conversion attainable in a DBD plasma near room temperature.

It should be noted that the specific energy input per mole of CO<sub>2</sub> (defined as the ratio of plasma power over volumetric flow rate) increases drastically with increasing residence time (2.9 s to 70 s) from 36 kJ/L to 900 kJ/L in the case of 30 W. Therefore, when judging these results based on the energy efficiency, longer residence times have a very negative performance, in spite of their higher conversion. This was discussed in more detail in our previous work for CO<sub>2</sub> dissociation at 30 W plasma power (see chapter 2), and will therefore not be further discussed here.

### **4.3.2 Tuning equilibrium and kinetics in plasma-based gas conversion**

In this section, we investigate how three of the most important process parameters, i.e. power, pressure, and gap size, influence the equilibrium and kinetics of the CO<sub>2</sub> dissociation reaction in the DBD (micro) plasma reactor. From this section on, we will only focus on the forward reaction, since section 4.3.1 already proved that the back reaction behaves towards the same equilibrium, and the eventual reaction of interest is the dissociation reaction.

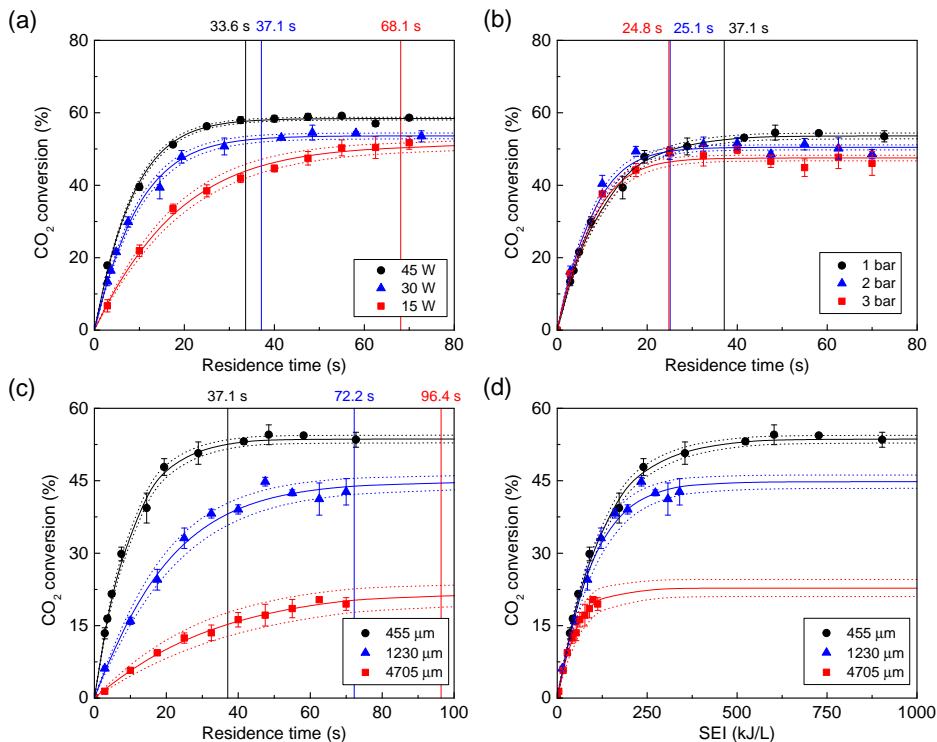


**Figure 4.2:** CO<sub>2</sub> conversion, plotted as a function of residence time, (a) in a 445 μm gap size at 1 bar, for 15 W, 30 W, and 45 W, (b) in a 445 μm gap size at 30 W, for 1 bar, 2 bar, and 3 bar, (c) at 30 W and 1 bar, for a gap size of 455 μm, 705 μm, and 4705 μm. In (d), the same data as in (c) are plotted, rescaled as a function of SEI. An apparent first-order reversible reaction fit is applied for all graphs (solid lines) with its 95% confidence interval (dotted lines). The time point at which the fit in (a), (b), and (c) reaches 98% of the end conversion of CO<sub>2</sub> dissociation is indicated for each case by the vertical line.

#### 4.3.2.1 Influence of power

Section 4.3.1 showed that plasma-based equilibria can be reached in a plasma reactor, and hinted that the time to reach equilibrium, as well as the equilibrium value, depends on the plasma power. The CO<sub>2</sub> conversion data for the three different powers, i.e. 15 W, 30 W, and 45 W, are grouped in figure 4.2(a), to further investigate the differences.

From this figure, we can conclude that the deposited plasma power positively influences the equilibrium conversion, bringing it from around 50% at 15 W to almost 60% at 45 W. Simultaneously, the overall reaction rate also increased, as evidenced by the steeper gradient of the curves with respect to the residence time, which means that partial chemical equilibrium is reached faster. This

**Table 4.1:** Fitted kinetic and equilibrium data for the CO<sub>2</sub> splitting reaction, at a plasma power of 15 W, 30 W, and 45 W, in a 455 μm gap size at 1 bara. The retrieved data are the equilibrium constant  $K$ , calculated from the  $X_e$  values, as well as the apparent reaction rate coefficient  $k$ , equilibrium conversion  $X_e$ , and time to equilibrium conversion  $t_e$ .

Plasma power (W)	15	30 <sup>a</sup>	45
$K$	$0.22 \pm 0.02$	$0.28 \pm 0.02$	$0.45 \pm 0.02$
$k$ (s <sup>-1</sup> )	$0.064 \pm 0.004$	$0.120 \pm 0.005$	$0.139 \pm 0.004$
$X_e$ (%)	$51 \pm 1$	$53.6 \pm 0.8$	$58.4 \pm 0.4$
$t_e$ (s)	68.1	37.1	33.6

<sup>a</sup>: Denoted as standard reference A throughout all measurements (see section 4.3.3 below).

is confirmed by the apparent first-order reversible reaction fit (equation 4.4), plotted as the solid lines with their respective 95% confidence interval, and the retrieved data shown in table 4.1. The derived fit equation is in very good agreement with the experimental data, validating the simplified model. The fit shows that indeed the equilibrium conversion for CO<sub>2</sub> dissociation increases with power, from 51% at 15 W, to 58.4% at 45 W (see table 4.1). The reaction equilibrium constant  $K$ , calculated with equation 4.5, is therefore found to be 0.22 for 15 W, 0.28 for 30 W, and 0.45 for 45 W (see table 4.1). The calculated apparent reaction rate coefficients confirm the observations made above. The overall rate coefficient for CO<sub>2</sub> dissociation doubles from 0.064 to 0.139 s<sup>-1</sup> when increasing the power from 15 W to 45 W, with the largest increase from 15 W to 30 W. As a result, we also see a drop in the time needed to reach the equilibrium conversion, since a higher power results in higher rate coefficients without a massive increase of the equilibrium conversion, ensuring a shorter time towards equilibrium. The time to reach equilibrium is reduced by a factor 2 upon increasing power from 15 W to 45 W, i.e. from 68.1 s at 15 W to 33.6 s at 45 W. In conclusion, the plasma power can tune both the position of the equilibrium and the overall reaction rate, although not independent of each other.

#### 4.3.2.2 Influence of pressure

The reactor pressure in a DBD is typically kept constant at atmospheric pressure. Indeed, increasing the pressure has a negative influence on the gas breakdown and subsequent discharge sustainment through Paschen's law [30]. It is nonetheless a valuable parameter to investigate, due to the widespread use of



**Table 4.2:** Fitted kinetic and equilibrium data for the CO<sub>2</sub> splitting reaction, at a reactor pressure of 1 bara, 2 bara, and 3 bara, in a 455 μm gap size at 30 W. The retrieved data are the equilibrium constant  $K$ , calculated from the  $X_e$  values, as well as the apparent reaction rate coefficient  $k$ , equilibrium conversion  $X_e$ , and time to equilibrium conversion  $t_e$ .

Pressure (bara)	1 <sup>a</sup>	2	3
$K$	$0.28 \pm 0.02$	$0.42 \pm 0.03$	$0.47 \pm 0.04$
$k$ (s <sup>-1</sup> )	$0.120 \pm 0.005$	$0.17 \pm 0.01$	$0.17 \pm 0.01$
$X_e$ (%)	$53.6 \pm 0.8$	$50.5 \pm 0.7$	$47.5 \pm 0.8$
$t_e$ (s)	37.1	25.1	24.8

<sup>a</sup>: Denoted as standard reference A throughout all measurements (see section 4.3.3 below).

high-pressure processes in industrial settings. Thus, we performed experiments at a reactor pressure of 1 bara, 2 bara, and 3 bara, by adjusting a needle valve to add an extra pressure drop in the system.

The results plotted in figure 4.2(b) do not reveal significant differences at first glance, except for a slight change in equilibrium conversion. Applying the simplified model fit to the data, with the retrieved data displayed in table 4.2, reveals the influence of the pressure in more detail. First of all, a higher pressure results in a drop in equilibrium conversion from 53.6% at 1 bara, to 47.5% at 3 bara. This is expected based on Le Chatelier's law, dictating that higher pressures move the equilibrium to the side with the least amount of molecules, thus promoting the back reaction more than the forward reaction. However, due to the stoichiometry of the reaction, we would expect the conversion to drop much more. In traditional thermodynamics, the pressure-based equilibrium constant  $K$ , as used here, should remain constant as the pressure increases, dictating a theoretical drop in equilibrium conversion from 53.6% at 1 bara, over 46.4% at 2 bara, to 42.3% at 3 bara. This suggests that the higher pressure has some positive effect on the plasma characteristics to counteract the behaviour of the standard thermal chemical equilibrium. Of course, standard thermal equilibrium thermodynamics cannot be invoked, which might explain this discrepancy.

In addition to the relatively mild drop in equilibrium conversion (see table 4.2), a higher pressure enhances the reaction rate. The rate coefficient increases from  $0.120 \text{ s}^{-1}$  at 1 bara, to  $0.17 \text{ s}^{-1}$  at 2 bara and keeps that value upon increasing the pressure to 3 bara (see table 4.2). The higher pressure yields more collisions between the plasma species, due to their higher densities, enhancing the rate

coefficient, but it quickly reaches the limits of this reaction pathway. In theory, this higher pressure could enhance three-body reactions, but this is not consistent with the capped rate coefficient in this pressure region, indicating that rate-determining processes are primarily electronic.

The results show that increasing the pressure from 1 bara to 2 bara is more beneficial to enhance the rate coefficient than increasing the plasma power from 30 to 45 W (cfr. table 4.1 and 4.2). As a result, the time to equilibrium is shortened from 37.1 s to around 25 s, when raising the pressure from 1 bara to 2 bara, at the same plasma power of 30 W. Hence, we can conclude that the relatively small pressure increase can also tune both the equilibrium properties and the reaction rate (at least when varying from 1 bara to 2 bara), although in a different way, i.e. a higher pressure yields a lower equilibrium constant, as apposed to a higher rate coefficient, whereas a higher power resulted in both a higher equilibrium constant and reaction rate coefficient (see previous section).

#### 4.3.2.3 Influence of gap size

Finally, we investigated the effect of the discharge gap size. Chapter 2 already touched on this subject by revealing that a longer residence time and smaller gap size resulted in an enhanced CO<sub>2</sub> conversion, due to a higher reduced electric field and specific energy input (SEI) [92]. However, in chapter 2 we only considered two different residence times (i.e. 7.5 s and 28.9 s). Here, we study this effect in more detail, by extending over a larger residence time, for a gap size of 455,  $\mu\text{m}$ , 1230,  $\mu\text{m}$ , and 4705  $\mu\text{m}$ .

Figure 4.2(c), and the retrieved reaction parameters in table 4.3, show the largest changes so far. A larger gap size drastically decreases the equilibrium conversion, from 53.6% at 455  $\mu\text{m}$  to only 23% at 4705  $\mu\text{m}$ . This is due to the lower SEI applied to reach the same residence time, and thus the lower reduced electric field, leading to fewer and less powerful discharges, as explained in chapter 2. We also plot the conversion as a function of SEI in figure 4.2(d), to illustrate the scale of different SEI values used in these experiments. These different SEI values are reached by applying different flow rates, as we apply a constant plasma power of 30 W. We can see that the conversions in the three gaps match each other very closely at low SEI values (i.e. high flow rates), which means that the overall efficiency of each reactor is similar, although the

**Table 4.3:** Fitted kinetic and equilibrium data for the CO<sub>2</sub> splitting reaction, at a gap size of 455,  $\mu\text{m}$ , 1230,  $\mu\text{m}$ , and 4705  $\mu\text{m}$ , at 30 W and 1 bara. The retrieved data are the equilibrium constant  $K$ , calculated from the  $X_e$  values, as well as the apparent reaction rate coefficient  $k$ , equilibrium conversion  $X_e$ , and time to equilibrium conversion  $t_e$ .

Gap size ( $\mu\text{m}$ )	455 <sup>a</sup>	1230	4705 <sup>b</sup>
$K$	$0.28 \pm 0.02$	$0.12 \pm 0.02$	$0.009 \pm 0.002$
$k$ ( $\text{s}^{-1}$ )	$0.120 \pm 0.005$	$0.057 \pm 0.005$	$0.032 \pm 0.005$
$X_e$ (%)	$53.6 \pm 0.8$	$45 \pm 1$	$23 \pm 2$
$t_e$ (s)	37.1	72.2	96.4

<sup>a,b</sup>: Denoted as standard reference A and B throughout all measurements (see section 4.3.3 below).

reaction volume is more efficiently used at smaller gap sizes. At higher SEI values, the limiting effect of the gaps comes into play and determines the maximum conversion that can be reached. The efficient use of the gap size is observed as well from the lower rate coefficients upon increasing the gap size (see table 4.3). The rate coefficient decreases from  $0.120 \text{ s}^{-1}$  at 455  $\mu\text{m}$ , taking 37.1 s to reach equilibrium conversion, to only  $0.032 \text{ s}^{-1}$  at 4705  $\mu\text{m}$ , taking 96.4 s. A smaller gap size is therefore advised, since a larger gap is associated with a lower CO<sub>2</sub> dissociation rate and a lower maximum conversion.

### 4.3.3 Distinguishing catalytic effects from plasma chemistry

In traditional (thermal) catalysis, a catalyst can provide a surface chemical reaction with an alternative reaction pathway with a lower energy barrier, which enhances the overall reaction rate coefficient without altering the underlying thermodynamic equilibrium. Because (catalytic) packing materials can also change the plasma properties [62], we can expect that the introduction of a packing will have a much more complicated impact on a plasma-based conversion process. Indeed, even experiments with identical packing materials have shown very different trends when using different gap sizes, see chapter 2. We therefore performed here two sets of experiments, employing reactors with a gap size of 455  $\mu\text{m}$  and 4705  $\mu\text{m}$ , respectively, both packed with either non-porous SiO<sub>2</sub> or ZrO<sub>2</sub> spheres. By explicitly untangling the effects of kinetics and shifting chemical equilibrium, we hope to elucidate to what extent the influence of a packing material can be purely catalytic (only changing the kinetics), or if the plasma – packing interplay is more complex (and the equilibrium is also shifted).

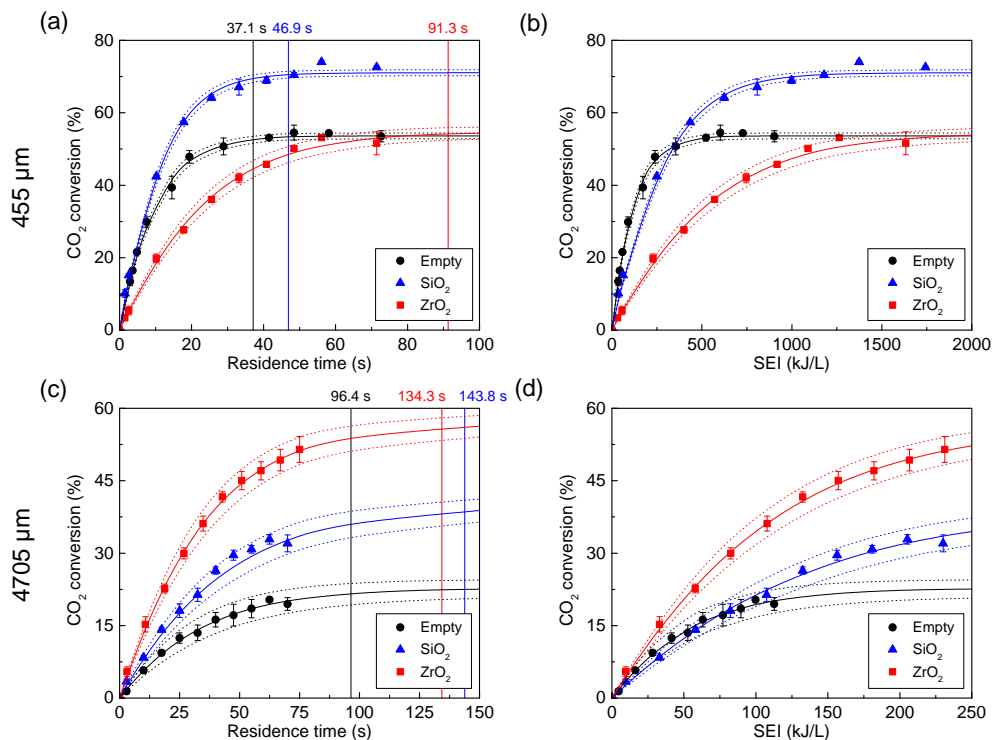


**Figure 4.3:** (a) CO<sub>2</sub> conversion at 30 W, 1 bara, and a gap size of 455 μm, plotted as a function of residence time for an empty reactor, as well as a reactor filled with 100-200 μm spheres of SiO<sub>2</sub> and ZrO<sub>2</sub>. (b) CO<sub>2</sub> conversions of (a) rescaled as a function of SEI. (c) CO<sub>2</sub> conversion at 30 W, 1 bara, and a gap size of 4705 μm, plotted as a function of residence time for an empty reactor, as well as a reactor filled with 1600-1800 μm spheres of SiO<sub>2</sub> and ZrO<sub>2</sub>. (d) CO<sub>2</sub> conversions of (c) rescaled as a function of SEI. An apparent first-order reversible reaction fit is applied for all graphs (solid lines) with its 95% confidence interval (dotted lines). The time point at which the fit in (a) and (c) reaches 98% of the end conversion of CO<sub>2</sub> dissociation is indicated for each case by the vertical line.

#### 4.3.3.1 Influence of packing material in a 455 μm discharge gap

The first set of experiments was performed in a 455 μm gap, with both SiO<sub>2</sub> and ZrO<sub>2</sub> spheres with a size range of 100-200 μm, and the results were compared to the reference empty reactor discussed in previous section 4.3.2. In our previous work we found that, at a constant residence time of 7.5 s, SiO<sub>2</sub> can enhance the CO<sub>2</sub> conversion in comparison with an empty reactor, whereas small (100-200 μm) ZrO<sub>2</sub> spheres have no impact on the conversion (see chapter 2). We now expand these results to the whole residence time range, as shown in figure 4.3(a), with the retrieved reaction parameters in table 4.4.

**Table 4.4:** Fitted kinetic and equilibrium data for the CO<sub>2</sub> splitting reaction, at an empty reactor as well as a reactor filled with either SiO<sub>2</sub> or ZrO<sub>2</sub> spheres, at 30 W, and 1 bara. The 455 μm gap size is filled with 100-200 μm spheres, while the 4705 μm gap size is filled with 1600-1800 μm spheres. The retrieved data are the equilibrium constant  $K$ , calculated from the  $X_e$  values, as well as the apparent reaction rate coefficient  $k$ , equilibrium conversion  $X_e$ , and time to equilibrium conversion  $t_e$ .

<b>455 μm gap</b>	<b>Empty<sup>a</sup></b>	<b>SiO<sub>2</sub></b>	<b>ZrO<sub>2</sub></b>
$K$	$0.28 \pm 0.02$	$1.6 \pm 0.1$	$0.32 \pm 0.05$
$k$ (s <sup>-1</sup> )	$0.120 \pm 0.005$	$0.111 \pm 0.004$	$0.050 \pm 0.003$
$X_e$ (%)	$53.6 \pm 0.8$	$71.1 \pm 0.8$	$55 \pm 2$
$t_e$ (s)	37.1	46.9	91.3
<b>4705 μm gap</b>	<b>Empty<sup>b</sup></b>	<b>SiO<sub>2</sub></b>	<b>ZrO<sub>2</sub></b>
$K$	$0.009 \pm 0.002$	$0.07 \pm 0.02$	$0.39 \pm 0.08$
$k$ (s <sup>-1</sup> )	$0.032 \pm 0.005$	$0.027 \pm 0.003$	$0.034 \pm 0.002$
$X_e$ (%)	$23 \pm 2$	$40 \pm 2$	$57 \pm 2$
$t_e$ (s)	96.4	143.8	134.3

<sup>a,b</sup>: Denoted as standard reference A and B throughout all measurements.

It is clear from figure 4.3(a) and table 4.4 that the two packing materials exhibit an unexpected behaviour. SiO<sub>2</sub> enhances the equilibrium conversion from 53.6% to an impressive 71.1%, which is to our knowledge the highest reported CO<sub>2</sub> conversion in a DBD reactor so far, although it must be realized that this record value in conversion is accompanied by a low energy efficiency. Simultaneously, SiO<sub>2</sub> slightly lowers the overall reaction rate coefficient from 0.120 s<sup>-1</sup> to 0.111 s<sup>-1</sup>. ZrO<sub>2</sub>, on the other hand, does not significantly enhance the equilibrium conversion, when taking the error bars into account, but it drastically lowers the rate coefficient from 0.120 s<sup>-1</sup> to only 0.050 s<sup>-1</sup>. These results show that introduction of these packing materials does not accelerate the kinetics in this reactor. Hence, this implies that it cannot be assumed that the packing merely leads to the creation of small voids that induces a reduced gap effect, since a smaller gap enhances the rate coefficient, as seen in section 4.3.2.3. On the contrary, it suggests that the main reaction pathways, electron impact reactions in a DBD, are at least partially inhibited under the applied conditions here. This can have many causes, such as a lower electron density as a result of more surface losses [99], or perhaps due to a change in discharge type [65], and this seems even more pronounced for ZrO<sub>2</sub> than for SiO<sub>2</sub>. Such an observation is indeed supported by fluid modelling studies of Van Laer and Bogaerts [60] who showed that packing materials with higher dielectric constants (such as ZrO<sub>2</sub>) lead to a drastic decrease of the electron

density in this type of reactor (with the same gap size) (cfr. figure 6 in their work), which in turn lowers the dissociation rate of  $\text{CO}_2$  (cfr. figure 11 in their work). At the same time, however, the packing can increase the maximum conversion, as clearly demonstrated in figure 4.3(a) for  $\text{SiO}_2$ , which can be correlated by a slight elevation of the electron temperature (also predicted by the modelling of Van Laer and Bogaerts [60]), that allows putting more energy into the system and pushing the conversion equilibrium of this endothermic reaction further to the right.

Rescaling the results as a function of the SEI (i.e. the inverse of the flow rate, as we keep the power constant) reveals that at low SEI (high flow rate) the empty reactor is more efficient in converting  $\text{CO}_2$  than the packed reactors, due to its higher rate coefficient, as seen in figure 4.3(b). At higher SEI (lower flow rate) the packed reactors start to catch up, and the  $\text{SiO}_2$  packing performs better than the empty reactor at around 300 kJ/L because of its higher equilibrium conversion. This shows that one should carefully investigate the kinetics and equilibria, to try to work at optimum conditions for a specific application, especially with packed plasma reactors.

It is interesting to note that studying the effect of packing materials at only one, or a limited number of, residence time(s) would not reveal any catalytic activity or whether the packing material enhances either the rate or the equilibrium of the reaction. Our approach allows us to conclude that  $\text{SiO}_2$  improves on the empty reactor only because of its equilibrium enhancement and not by kinetics enhancement (slightly overlapping error bars). The empty reactor, on the other hand, is better than  $\text{ZrO}_2$  only because of rate inhibition by  $\text{ZrO}_2$  and not because of any equilibrium changes.

### 4.3.3.2 Influence of packing material in a 4705 $\mu\text{m}$ discharge gap

The second set of experiments was performed with a 4705  $\mu\text{m}$  gap size, again with either  $\text{SiO}_2$  or  $\text{ZrO}_2$  spheres with a size range of 1600-1800  $\mu\text{m}$ , and the results were again compared to the empty 4705  $\mu\text{m}$  reactor from section 4.3.2.3. This combination of gap size and sphere sizes was also used in chapter 2, as the benchmark, where different trends were found than those observed in section 4.3.3.1, with both  $\text{SiO}_2$  and  $\text{ZrO}_2$  being able to enhance the  $\text{CO}_2$  conversion (i.e. 10% and 14%, respectively) as compared to the empty reactor

(4%) at a constant residence time of 7.5 s [92]. Interestingly, ZrO<sub>2</sub> showed even better results than SiO<sub>2</sub> in those experiments. Here, we performed similar experiments to chapter 2, but in the whole residence time range, and the results are shown in figure 4.3(c) with the retrieved data in table 4.4.

These data confirm the trends observed in chapter 2, with ZrO<sub>2</sub> leading to the highest conversions, followed by SiO<sub>2</sub> and finally the empty reactor. This translates in respective equilibrium conversions of 57%, 40%, and 23% (see table 4.4). In contrast to the smaller gap, the kinetics seem not to be greatly affected by the packing materials in this gap size, showing rate coefficients around  $0.031\text{ s}^{-1}$  with overlapping error bars. This suggests that there is no apparent catalytic effect for these packing materials and this particular reaction, as the packing material only changes the equilibrium and not the kinetics. Again, no rate enhancement is seen due to the reduced discharge gap. Van Laer and Bogaerts [60] indeed showed in their work that the electron density and the CO<sub>2</sub> dissociation rate in a millimetre gap (4.5 mm, hence very similar as used here) are much less affected by the dielectric constant of the packing beads (*ergo* constant rate coefficient), while the electron temperature certainly is (*ergo* change in PCE). It can be noted that the time to reach equilibrium does show some variance despite the similar rate coefficients, due to higher equilibrium and  $K$  values. It is clear from the results from both gap sizes that there is an important material-gap-interaction dictating the behaviour of the plasma, i.e. electric field, electron temperature, and electron density, as was also revealed by numerical modelling [60]. However, the origin of the change in material order is not clear at this moment. Because the modelling results were for a helium DBD, no specific material properties could be incorporated, except for the dielectric constant. Moreover, we could not perform detailed plasma diagnostics in this packed bed DBD, and the electric characterisation showed no different behaviour, as demonstrated in chapter 2. Hence, the underlying reason for the different behaviour will require further investigation.

In contrast to the small gap, rescaling the results as a function of the SEI shows that a ZrO<sub>2</sub>-packed DBD reactor will always show the most efficient conversion for a certain CO<sub>2</sub> flow rate, see figure 4.3(d). The empty reactor performs better than the SiO<sub>2</sub>-packed reactor at low SEI because of its slightly higher rate coefficient, but the order is switched at around 75 kJ/L, as the

equilibrium conversion is higher. Just like we concluded in section 4.3.3.1, it is clear that such information could not be obtained from measurements at fixed residence time, namely that the improved results seen at any particular residence time only originate from changes in the equilibrium and not from kinetics enhancement.

#### 4.3.4 A common underlying connection, or a more complicated story?

Sections 4.3.2 and 4.3.3 have shown that both the process parameters (power, pressure and gap size) as well as the packing materials can influence the kinetics and/or equilibrium of the CO<sub>2</sub> dissociation reaction. The exact origin and connection of these effects is, however, less clear. Plotting the equilibrium constant and rate coefficients as a function of the estimated reduced electric field  $E/N$  for each condition does give us some clues, see figure 4.4. Note that the reduced electric field is indeed often used as a crucial parameter in plasma-based gas conversion experiments, as it determines the electron temperature, which defines the CO<sub>2</sub> equilibrium conversion and energy efficiency [8, 136].  $E/N$  is calculated here according to:

$$\frac{E}{N} = \frac{U_{RMS}}{dN} \quad (4.7)$$

with  $U_{RMS}$  the effective (or root mean square) voltage,  $d$  the gap size, and  $N$  the gas density of an ideal gas at the given pressure, i.e.  $2.5 \times 10^{25} \text{ m}^{-3}$  at 1 atm. Note that  $E/N$  is mostly expressed in Townsend (Td), with  $10^{-21} \text{ Vm}^2$  corresponding to 1 Td.

When changing power, pressure, or gap size, the equilibrium constant and overall rate coefficient appear to move in the same direction, see figure 4.4. For example, an increase of overall rate coefficient coincides with a higher equilibrium constant. This correlation suggests that kinetics and equilibrium cannot be independently tuned (at least for this process and this reactor) purely by changing operating conditions. Introduction of a packing, however, breaks this trend: the overall rate coefficient decreases, compared to the empty reactor, but the equilibrium constant (and equilibrium conversion) goes up. Hence, for this particular setup, we can infer that packing materials bring the plasma to a new regime that allows for a more flexible process optimisation.



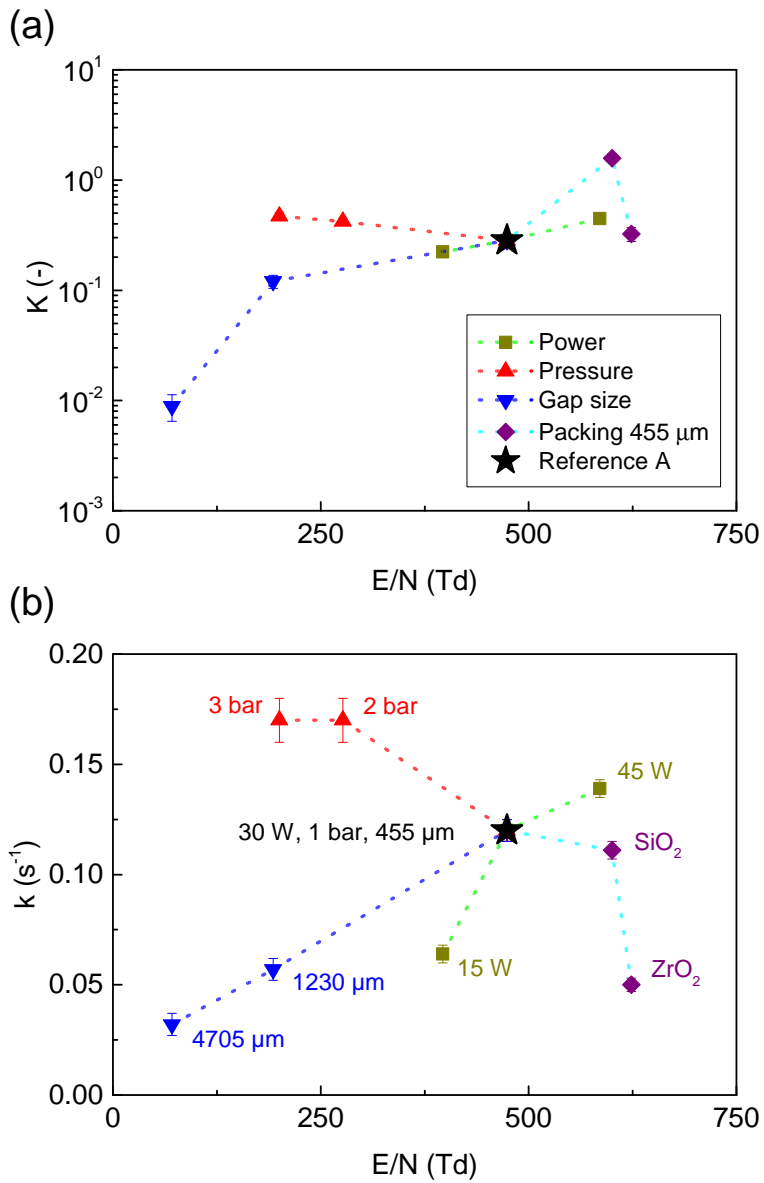


**Figure 4.4:** Combined graph of the (a) equilibrium constants and (b) reaction rate coefficients of sections 4.3.2 and 4.3.3, plotted as a function of the estimated reduced electric field ( $E/N$ ). All the results are compared against the reference empty reactor A (see tables above). The conditions correlated to the  $E/N$  are only annotated in (b) but can be inferred to (a). An additional version with the packed reactor data from 4705  $\mu\text{m}$  can be found in figure C.3 in appendix C.

The question arises how the plasma couples to the gas phase chemistry? As mentioned above, the reduced electric field can be used as a measure for the electron temperature, and as electron impact dissociation is the main dissociation mechanism in a DBD reactor [38], the electron temperature can be seen as the main source of energy for CO<sub>2</sub> splitting in a DBD plasma reactor. More energy should therefore translate into more conversion, since it pushes the equilibrium to the right for this endothermic reaction, and this is what we observe at constant pressure and without packing, in conjunction with an increasing reaction rate (see figure 4.4).

However, this trend is not observed when varying the pressure. Hence, there must be some other parameters that dictate the behaviour of the rate coefficient. A first parameter to consider is the electron density. A higher pressure will lead to a lower  $E/N$ , and thus lower electron temperature, but also to a higher density of all species, including the electron density. This might thus enhance the CO<sub>2</sub> dissociation rate, and compensate for the lower  $E/N$ , and thus lower electron temperature. Moreover, the similarities in the behaviour of the rate coefficient and equilibrium constant for the non-packed reactor suggest that kinetic and equilibrium effects are strongly intertwined, and especially a good understanding of kinetics is required.

Trends for the packed reactors are even harder to discern. First, there is some uncertainty in defining the true exact reduced electric field between the spheres as the total applied voltage is dispersed over all the voids between the spheres. In addition, some possible surface effects might also play a role, such as charging, sorption, local field enhancement, etc. so the effective voltage is still used here. As mentioned in section 4.3.3.1 and as shown by Van Laer and Bogaerts [60], using packing materials can greatly change the electron density, due to their dielectric constant, with the actual magnitude of the effect depending on the gap size, influencing the overall rate coefficient. Furthermore, using packing materials increases the surface area in contact with the plasma, possibly causing some surface losses and the same effects as mentioned above. Secondly, aside from the electron density, there might be (as of yet unknown) other parameters that can influence the overall rate coefficient of CO<sub>2</sub> conversion, which may be especially hard to determine in a packed reactor. Changing from one packing material to another will of course change multiple other packing properties

as well, besides the dielectric constant. These consist of (i) bulk properties of the material, such as size, shape, electric conductivity, thermal capacity, and thermal conductivity, as well as (ii) surface properties, such as crystal phases, roughness, pore size, and functional groups, among others. Their exact effect on the overall rate coefficient, as well as on the equilibrium constant, is very difficult or even impossible to evaluate individually, in addition to the entangled nature of the plasma–material interaction [62,67]. Thirdly, we can consider any catalytic behaviour occurring when using a packing. Our study, as discussed in section 4.3.3, reveals no apparent catalytic behaviour for bare SiO<sub>2</sub> and ZrO<sub>2</sub> in the CO<sub>2</sub> dissociation reaction. However, these materials seem to change the plasma properties more than any catalytic rate coefficient enhancement, unless masked so much by the other changes.

The key importance of kinetics and its correlation to the equilibrium can also be found in our simplified kinetics model, see section 4.2.3. From the detailed derivation of equation 4.4 in appendix C, it follows that both the overall conversion rate coefficient  $k_y$  and the equilibrium concentration  $x_e$  of any product can be expressed as a function of its global consumption rate coefficient  $k_1$  and its global production rate coefficient  $k_2$ . More specifically, the overall rate coefficient  $k_y$  is proportional to the sum of  $k_1$  and  $k_2$  ( $k_y = k_1 + k_2$  according to equation C.33), while  $x_{e,y} = k_2/(k_1 + k_2)$  (according to equation C.34), ignoring any coefficients due to stoichiometry for the sake of clarity.

In thermal catalysis, the activation energy of both consumption and production is lowered equally, and both  $k_1$  and  $k_2$  increase by the same factor. This means that the global conversion rate can increase (still  $k_y = k_1 + k_2$ ), but the thermal equilibrium concentration cannot ( $K_T = k_2/k_1$  must remain constant, and hence  $x_{e,T}$  cannot change), as is also shown by our model equations. However, many of the results in this work demonstrated that in the thermal non-equilibrium environment of the plasma reactor, also the chemical equilibrium concentration can change. This is the result of  $k_1$  and  $k_2$  changing independently. For example, in our packed reactors we have observed that the overall rate did not increase appreciably (it even decreased in some cases): these results can be attributed to an increased CO<sub>2</sub> decomposition rate, compensated by a decreased CO<sub>2</sub> production rate, keeping the sum of the rates constant. Hence, in contrast to traditional catalytic approaches, where forward and reverse reaction rates are

modified in the same fashion, plasma (catalysis) can modify each of these rates independently and thus the overall rate coefficient both positively and negatively; and at the same time changing the position of the equilibrium by an altered correlation as described by equation C.34. Future endeavours in this field could therefore attempt to target specific reactions, allowing to increase both the production rate and equilibrium concentration of a desired product.

In the end, for both thermal (catalytic) processes and plasma (catalytic) processes, net energy is provided to the system. It should therefore be possible to define a clear correlation between plasma power and equilibrium, as well as rate coefficient, as is the case for thermal processes. The reality is, however, more complicated since clearly multiple parameters influence how this power is delivered to a system. Not only input power shifts the equilibrium, but also the gap, pressure, and packing materials. At the same time, the plasma characteristics can also change such as: vibrational versus electronic excitation, magnitude and frequency of discharges, electron temperature and density, etc. Therefore, there is a clear difference between the limited control options of a thermal reactor (only temperature and pressure), versus the wide control options in case of plasma.

### 4.3.5 Future potential of PCE studies

In this work we investigated the existence of a PCE in a DBD plasma reactor, we verified how it is affected by reactor and packing parameters, and we reviewed the associated kinetics by using an apparent first-order reversible reaction fit equation. In this first proof-of-concept of our method, very valuable information was obtained, even for the simple but paradigmatic CO<sub>2</sub> splitting reaction with non-porous packing materials, i.e. SiO<sub>2</sub> and ZrO<sub>2</sub>. Our novel analysis methodology can be a valuable tool in future research, regardless of the specific plasma research area. It is able to yield process parameters that allow for a comparison of different plasma reactor types, set-ups, reactions, and packing materials, which is very useful, especially considering the huge diversity in published plasma-based conversion experiments in which the role of certain reaction configurations and introduced materials is often only visible as a mere positive or negative effect.

Furthermore, specific reactions ask for specific needs and conditions, which, to some extent, can be selected and optimised through our proposed procedure. Also here, the rate coefficient and position of the equilibrium are essential in understanding the overall chemistry allowing some insights to optimise the reaction. Depending on the reaction, it allows to determine the conditions to achieve a certain conversion level, predict the time evolution of the composition, and possibly steer the product distribution in more complicated mixtures. Additionally, the presence, or lack, of a catalytic effect can be investigated: candidate catalysts can be systematically screened (e.g. on composition, available surface area, and doped elements), for their impact on rate or PCE, and their application in plasma-based conversion processes can be readily compared with pure plasma processes, as well as thermal catalysis.

Untangling the highly complex physical chemistry of plasma-catalytic conversion processes, and comparing it with the well-known processes in thermal catalysis, requires a strategic (stepwise) analysis, based on well-defined and preferably easy to obtain fundamental insights, such as those provided by the method suggested in this work. Combination of this approach with more detailed experimental diagnostics and computational modelling, if available, can therefore bring our understanding to the next level, in the quest for new advanced gas conversion technologies.

## 4.4 Conclusion

In this chapter we have shown that a partial chemical equilibrium does exist in a DBD (micro) plasma reactor, as both the forward (pure CO<sub>2</sub>) and back reaction ( $2/3 \text{ CO} + 1/3 \text{ O}_2$ ) converge to a common equilibrium state upon increasing residence time. Furthermore, by performing experiments within an extended range of residence times, and developing an apparent first-order reversible reaction fit equation, we can describe the operational behaviour of the reactor and retrieve essential kinetics and thermodynamics data from the experimental results. This way we could determine equilibrium concentrations and constants, (overall) rate coefficients, and the presence or absence of catalysis of chemical processes in the inherently non-thermal-equilibrium environment of a plasma, that could otherwise not be described.

Analysis of the effect of different process parameters (i.e. power, pressure, and gap size) on the equilibrium and rate coefficient, showed that a higher power shifts the equilibrium in the forward direction and enhances the rate. The pressure showed a different effect, with a drop for the equilibrium conversion and a rise for the rate coefficient, upon increasing pressure. Finally, decreasing the gap size has a general positive effect, drastically enhancing the equilibrium conversion and the rate coefficient.

When inserting a packing ( $\text{SiO}_2$  and  $\text{ZrO}_2$  spheres), a clear gap/material effect becomes apparent. In the case of the  $455\ \mu\text{m}$  gap, the  $\text{SiO}_2$ -packed reactor showed better conversions than the empty reactor due to a shift of the equilibrium, and not by enhancement of the kinetics.  $\text{ZrO}_2$ , on the other hand, showed worse results, because of a drop in the rate while maintaining the same equilibrium conversion. In the case of the  $4705\ \mu\text{m}$  gap, we observed no significant effect on the rate coefficients for both materials, while the equilibrium conversion was enhanced for both the  $\text{SiO}_2$  and  $\text{ZrO}_2$  packings. Interestingly,  $\text{ZrO}_2$  performed better than  $\text{SiO}_2$  in the larger gap indicating important material-gap-interactions on the kinetics. Hence, in general, both packing materials did not positively affect the rate coefficients compared to the empty reactors in both gap sizes, while either increasing or decreasing the equilibrium conversion, and thus enhancing or inhibiting some plasma properties. It is therefore not possible to declare any apparent synergistic effect or plasma-catalytic behaviour from these results for  $\text{SiO}_2$  and  $\text{ZrO}_2$  in  $\text{CO}_2$  dissociation.

Our method therefore reveals an intriguing opportunity to independently tune the equilibrium conversion and rate coefficient, depending on the plasma and process parameters. Within the investigated parameter ranges, equilibrium conversions were obtained between 23% and 71%; to our knowledge, 71% is the highest value reported up to now for a DBD reactor (although accompanied by a low energy efficiency). The reduced electric field  $E/N$  was shown to have a prominent underlying effect in determining the equilibrium conversion, as a higher  $E/N$  yields a higher electron temperature, which is the main energy source for  $\text{CO}_2$  splitting in a DBD plasma, therefore shifting the equilibrium of this endothermic reaction to the right. The rate coefficient, on the other hand, varied between  $0.027\ \text{s}^{-1}$  and  $0.17\ \text{s}^{-1}$ , being determined by more underlying effects apart from the reduced electric field.

In conclusion, the proposed definition of an effective global rate coefficient (here for the CO<sub>2</sub> splitting reaction), in combination with the partial chemical equilibrium constant, can be used to characterise the intrinsic properties of a conversion process in a plasma reactor, and directly compare the performance of different conditions and set-ups on a fundamental level. Depending on the desired properties (e.g. high equilibrium conversion vs. high rates), such performance indicators can be used to select or optimise the operating conditions. We therefore advise to implement similar analyses in other plasma-based gas conversion studies, and especially when studying the mechanisms behind plasma catalysis, to obtain a more fundamental insight in the overall reaction kinetics and being able to distinguish plasma effects from true catalytic enhancement.





# Chapter 5

## On the kinetics and equilibria of plasma-based dry reforming of methane

Published as:

Y. Uytendhouwen, K. Bal, E. Neyts, V. Meynen, P. Cool, and A. Bogaerts, “On the kinetics and equilibria of plasma-based dry reforming of methane,” *Chemical Engineering Journal*, vol. 405, p. 126630, feb 2021

## Abstract

Plasma reactors are interesting for gas-based chemical conversion but the fundamental relation between the plasma chemistry and selected conditions remains poorly understood. Apparent kinetic parameters for the loss and formation processes of individual components of gas conversion processes, can however be extracted by performing experiments in an extended residence time range (2-75 s) and fitting the gas composition to a first-order kinetic model of the evolution towards partial chemical equilibrium (PCE). We specifically investigated the differences in kinetic characteristics and PCE state of the CO<sub>2</sub> dissociation and CH<sub>4</sub> reforming reactions in a dielectric barrier discharge reactor (DBD), how these are mutually affected when combining both gases in the dry reforming of methane (DRM) reaction, and how they change when a packing material (non-porous SiO<sub>2</sub>) is added to the reactor. We find that CO<sub>2</sub> dissociation is characterised by a comparatively high reaction rate coefficient of 0.120 s<sup>-1</sup> compared to CH<sub>4</sub> reforming at 0.041 s<sup>-1</sup>; whereas CH<sub>4</sub> reforming reaches higher equilibrium conversions, 82% compared to 53.6% for CO<sub>2</sub> dissociation. Combining both feed gases makes the DRM reaction to proceed at a relatively high rate coefficient (0.088 s<sup>-1</sup>), and high conversion (75.4%) compared to CO<sub>2</sub> dissociation, through accessing new chemical pathways between the products of CO<sub>2</sub> and CH<sub>4</sub>. The addition of the packing material can also distinctly influence the conversion rate and position of the equilibrium, but its precise effect depends strongly on the gas composition. Comparing different CO<sub>2</sub>:CH<sub>4</sub> ratios reveals the delicate balance of the combined chemistry. CO<sub>2</sub> drives the loss reactions in DRM, whereas CH<sub>4</sub> in the mixture suppresses back reactions. As a result, our methodology provides some of the insight necessary to systematically tune the conversion process.

## 5.1 Introduction

In the previous chapter, we have investigated the kinetics of CO<sub>2</sub> dissociation in a DBD reactor. Here, we found that the concentration of CO<sub>2</sub>, CO, and O<sub>2</sub> in the driven, out-of-equilibrium plasma evolves to a final composition in a similar manner as a thermal system would evolve to its equilibrium state, i.e. the same final composition is reached when starting from a pure CO<sub>2</sub> flow or a stoichiometric mixture of CO and O<sub>2</sub>. The position of the partial chemical equilibrium (PCE) is specific to the discharge conditions at hand. Note that in all cases the measured PCE state corresponded to a very large CO<sub>2</sub> conversion (up to 70% in a SiO<sub>2</sub>-packed 455 μm reactor, see chapter 4), which would thermally only be attainable at very high temperatures (> 3000 K) [8]. A simple PCE-based approach can show that the kinetics of plasma (catalysis) are different from traditional thermal kinetics, but can still be described by the same key criteria (i.e. rate coefficient and equilibrium). In contrast to thermal processes, these are however affected by more and different parameters, allowing for additional flexibility to tune the maximal conversion and rate.

The interesting observations of chapter 4 form the basis for more elaborate research into more complex chemistry sets, such as dry reforming of methane (DRM), where CO<sub>2</sub> and CH<sub>4</sub> are converted together into syngas and higher (oxygenated) hydrocarbons. Indeed, CH<sub>4</sub> reforming on its own already shows a more complex chemistry, compared to pure CO<sub>2</sub> conversion, since its products vary from C to H<sub>2</sub> to C<sub>x</sub>H<sub>y</sub> molecules, with thousands of reactions among them [138]. High conversions of methane up to 80% have been reported, with hydrocarbons up to C<sub>6</sub> being detected [139–142]. Combining the chemistries of CO<sub>2</sub> dissociation and CH<sub>4</sub> reforming leads to even more possibilities towards oxygenated hydrocarbons C<sub>x</sub>H<sub>y</sub>O<sub>z</sub>. This ability of DRM to produce economically valuable products from greenhouse gases, has made it one of the most widely investigated reactions in plasma chemistry, with varying results [46, 72, 84, 88, 130, 143, 144]. However, the highly complex chemistry of plasma-based DRM, combined with its technological potential, require a deeper insight into the fundamental characteristics of the process. A lot of knowledge is available from detailed reaction schemes obtained through modelling, e.g. those in [86, 138, 145], but they only partially capture the complexity of experimental reactors and how set-up parameters change the overall kinetics.

In this work we will therefore investigate how the kinetics of CO<sub>2</sub> dissociation change upon addition of CH<sub>4</sub> in a DBD reactor. For this purpose, we generalise our PCE model (that was specifically developed and only applicable for CO<sub>2</sub> splitting) to arbitrary gas mixtures with a priori unknown stoichiometry. Hence, this novel method does not require knowledge on the precise process stoichiometry, and can be applied to multicomponent mixtures, also for other gas conversion applications. This approach will allow other researchers as well to compare the conversion characteristics of certain individual components across different reactors and gas mixtures.

In order to understand the occurring changes, pure CH<sub>4</sub> reforming will be tested and compared at the same conditions as used in chapter 4 on CO<sub>2</sub> splitting, being the benchmark. In this way we can elucidate how the apparent kinetics of these pure reactions are different from their combination in the DRM reaction. Also, we will evaluate the impact of a non-porous SiO<sub>2</sub> spheres as packing on the kinetics of CH<sub>4</sub> reforming and DRM, compared with CO<sub>2</sub> dissociation, and how the CO<sub>2</sub>:CH<sub>4</sub> ratio in DRM shifts the kinetics. Despite the simplicity of the experimental set-up, salient mechanistic insights are obtained. Eventually, information on the maximal conversion in a DBD plasma and its overall kinetics will be useful in the determination of optimal process conditions, and to compare different set-ups and packing materials on a systematic basis.

## 5.2 Methods and theory

### 5.2.1 Experimental set-up

The experiments were performed in the same reactor and set-up as in chapter 4, shown in figure 2.1. A 455 μm gap size was used as the reference gap size, also showing the highest rate coefficients of the various gap sizes tested. Besides studying the empty reactor, the reactor was also packed with non-porous SiO<sub>2</sub> spheres (Sigmund Lindner) with a size range of 100-200 μm. We used a SiO<sub>2</sub> packing to be able to compare with our previous results for pure CO<sub>2</sub> splitting, and because the other packing material used in our previous work (ZrO<sub>2</sub>) did not reach the desired 30 W (triggering the current safety switch of the power supply) in CH<sub>4</sub> or CO<sub>2</sub>/CH<sub>4</sub> mixtures for DRM. Although many different materials have been studied in literature in packed bed DBD, we focus on SiO<sub>2</sub>. Indeed, the

inert nature of non-porous SiO<sub>2</sub> is beneficial to minimise any additional effects that a packing material could have on the reactor performance (e.g. catalysis), and to focus on the basic kinetics for this study. The packing was added to the reactor and vibrated for one minute via an external device to ensure the closest packing possible in a repeatable fashion. No significant material degradation was observed during the experiments.

The reactor was fed with pure CO<sub>2</sub>, CH<sub>4</sub>, or a mixture of both, at different flow rates to obtain the desired residence times between 2 s and 75 s in the reactor. The flow rates were set and monitored by two mass flow controllers (Bronkhorst EL-FLOW Select series). The pressure in the tubing between the reactor and the GC was kept at 1.2 bara  $\pm$  0.2 bara. In the case of the SiO<sub>2</sub> packed reactor, adjusted, lower flow rates were used to account for the loss in reaction volume by the packing. A packing efficiency of 49.5% was estimated, based on the computational results of chapter 4 (see also the remarks of chapter 2) for the identical case of 100-200  $\mu$ m spheres in the 455  $\mu$ m gap. Note that we have no data point at 70 s for the SiO<sub>2</sub> packed DRM experiment. This point could not be measured due to the lower limit of the mass flow controller, being 0.65 mL/min. Note that alteration of the flow rate was done to achieve different residence times, rather than changing the reactor length, in order to maintain the same power density, i.e. power-to-volume ratio, and thus constant plasma characteristics. While changing the flow rate might affect the mass and heat transfer rates, the gas temperature was estimated only slightly above room temperature (based on the measured temperature immediately after shutdown, being always below 50°C), so heat transfer should not be an issue here, like it could be in thermal reactors.

The gaseous products were again analysed by the same gas chromatograph (Compact GC, Interscience) with pressure-less sampling. The first TCD channel (TCD B) contains a Rt-Q-Bond column able to separate CO<sub>2</sub> and large hydrocarbons from permanent gases, the second TCD channel (TCD M) contains a Rt-Q-bond pre-column to delay CO<sub>2</sub> and the larger components and only inject the permanent gases on a Molsieve 5A column and separate them. The FID has a Rtx-1, 5u column to separate and detect (oxygenated) hydrocarbons. CO<sub>2</sub>, CO, O<sub>2</sub>, CH<sub>4</sub>, H<sub>2</sub>, C<sub>2</sub>H<sub>6</sub>, C<sub>2</sub>H<sub>4</sub>, C<sub>3</sub>H<sub>8</sub>, and C<sub>2</sub>H<sub>5</sub>OH were calibrated by using calibration standards (Air Liquide). More peaks could be identified but were not

calibrated, since either no calibration standard was available (vapour injection identification) or they coincide with other peaks; they will not be discussed in the main text but the results are available in section D.4 and D.5 of appendix D. A list of all detected components can be found there as well in table D.2.

The CO<sub>2</sub> or CH<sub>4</sub> conversion derived from the GC data was defined as:

$$X_y = \frac{\dot{y}_{in} - \dot{y}_{out}}{\dot{y}_{in}} \quad (5.1)$$

with  $\dot{y}$  the molar flow rate of component  $y$ , being either CO<sub>2</sub> or CH<sub>4</sub>. The total conversion was calculated according to the CO<sub>2</sub>:CH<sub>4</sub> molar ratio of the mixture, A:B, as:

$$X_{Total} = \frac{A X_{CO_2} + B X_{CH_4}}{A + B} \quad (5.2)$$

The power (equation 2.5) and experimental error (equation 2.7) are calculated analogue to section 2.2.1.

### 5.2.2 Experimental method

The standard experimental conditions in this work are set at 30 W and 3 kHz, a 455 μm discharge gap size, and 1.2 bara, at various residence times up to 75 s. The reactor was operated for at least 40 min to let it reach a thermal steady-state behaviour, i.e. a stable reactor temperature and voltage is reached due to heat losses towards the reactor and environment. Extended operating times up to 120 min were used for flow rates below 10 mL/min, to ensure steady-state behaviour in the reactor and following tubing, for consistent gas composition analysis. The applied voltage was periodically adjusted on the function generator to obtain and maintain the desired constant plasma power of 30 W.

### 5.2.3 Partial chemical equilibrium (PCE)

The overall reaction rate coefficient and location of the PCE are determined by applying an apparent first order reversible reaction fit to the residence time measurements. In chapter 4, we explicitly derived an expression for the time evolution of molecular concentrations towards the PCE state of the CO<sub>2</sub>/CO/O<sub>2</sub> system, wherein we assumed first order kinetics and stoichiometric conversion between the aforementioned molecules only [56]. Such an approach is no longer

valid for more complex gas mixtures, such as those obtained for CH<sub>4</sub> conversion or DRM. However, a slight generalisation of the equilibrium model permits its application to the conversion of any molecule in an arbitrary gas mixture, without requiring any detailed information on reaction products or mechanisms. Only first order kinetics—reaction rate proportional to the concentration of reacting molecules—is assumed. Each process could progress through many different possible individual mechanisms, between which we cannot distinguish experimentally. The measured rate coefficient is therefore a weighted average for all these individual reactions which, by construction, is assumed to be constant over time.

The loss and formation rate of a gas molecule  $A$  through unspecified pathways with rate coefficients  $k_{loss}$  and  $k_{form}$  are:

$$r_{A,loss}(x_A) = k_{loss}x_A \quad (5.3)$$

$$r_{A,form}(x_A) = k_{form}(1 - x_A)f \quad (5.4)$$

Not all of the (non- $A$ ) molecules in the system can directly be converted into  $A$ , because only a fraction  $f$  has the “right” reactivity. We assume that  $f$  is a constant that depends on the elemental composition of the system. By construction, it is therefore a time-averaged stoichiometric parameter throughout all stages of the conversion process, just like the rate coefficient to which it is tied. Derivation of the formula, that is shown in detail in appendix D leads to the fit equation describing the concentration (in mole fraction) of  $A$  in time:

$$x_A(t) = x_{A,e} - (x_{A,e} - x_{A,i})e^{-kt} \quad (5.5)$$

where  $x_{A,e}$  and  $x_{A,i}$  are the equilibrium and initial mole fraction of  $A$  and

$$k = fk_{form} + k_{loss} \quad (5.6)$$

$$x_{A,e} = \frac{fk_{form}}{fk_{form} + k_{loss}} \quad (5.7)$$

This equilibrium mole fraction  $x_{A,e}$  can be rewritten in terms of the total

equilibrium conversion  $X_{Total,e}$  as:

$$X_{Total,e} = \frac{k_{loss}}{fk_{form} + k_{loss}} \quad (5.8)$$

The fit was applied by importing the experimental data (consisting of up to 132 data points per parameter and reaction) into MATLAB as gas fractions, calculating a fit according to equation 5.5 resulting in  $k$  and  $x_e$  (converted to  $X_e$ ), and finally converted back into conversions for plotting on the graphs.  $x_{A,i}$  is equal to 1 for pure CO<sub>2</sub> and CH<sub>4</sub>, as well as for fitting the overall DRM trend (where  $x_A = x_{CO_2} + x_{CH_4}$ ), while the respective CO<sub>2</sub> and CH<sub>4</sub> fractions were taken for their individual fits in mixed DRM cases.  $k_{loss}$  and  $fk_{form}$  are calculated from equations 5.6 and 5.7.

## 5.3 Results and discussion

### 5.3.1 The benchmark: Separate CO<sub>2</sub> and CH<sub>4</sub> conversion

CO<sub>2</sub> dissociation was performed in chapter 4 at the standard conditions mentioned in the experimental method. Note that the thermodynamic equilibrium at the considered (ambient) temperature and pressure is virtually 0% for all gas compositions (pure CO<sub>2</sub> and CH<sub>4</sub>, as well as all DRM mixtures) [8]. The results, plotted as the black curve in figure 5.1(a), however show that the CO<sub>2</sub> splitting reaction under the considered plasma conditions was characterised by an equilibrium conversion of 53.6% with an apparent overall reaction rate coefficient of 0.120 s<sup>-1</sup> (table 5.1), found by the apparent first order reversible reaction fit. Viewing these results through the lens of our simplified equilibrium model, and more specifically the expressions for the apparent reaction rate coefficient and equilibrium conversion in equations 5.6 and 5.7, we get a  $k_{loss}$  term of 0.066 s<sup>-1</sup> and a  $fk_{form}$  term of 0.056 s<sup>-1</sup>. The dominant reactions in the DBD reactor are electron-impact dissociation of CO<sub>2</sub> as main CO<sub>2</sub> loss process, while three-body recombination of CO and O is the most important formation reaction, as reported by Aerts *et al.* [38].

CH<sub>4</sub> reforming was carried out at the same conditions, and the results are shown in figure 5.1(a) and table 5.1 as well. They exhibit completely different behaviour from CO<sub>2</sub> dissociation with a higher equilibrium conversion of 82%.



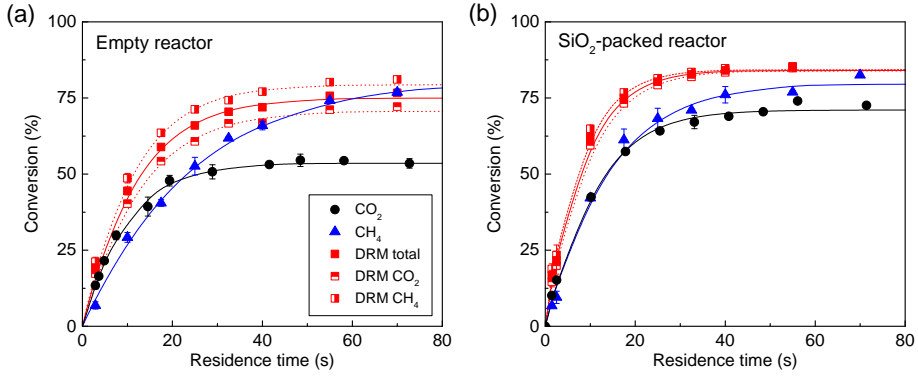


**Figure 5.1:** Conversion of CO<sub>2</sub> (black circles), CH<sub>4</sub> (blue triangles), and DRM (red squares), plotted as a function of residence time for both the empty and SiO<sub>2</sub>-packed reactor. The individual conversion of CO<sub>2</sub> (horizontal half red squares) and CH<sub>4</sub> (vertical half red squares) during DRM are plotted as well. An apparent first-order reversible reaction fit for all reactions is applied (solid/dotted lines). The exact values can be found in table D.1 in appendix D.

**Table 5.1:** Fitted kinetic and partial chemical equilibrium data for CO<sub>2</sub> dissociation, CH<sub>4</sub> reforming, and DRM, as well as its sub-reactions, for both the empty and SiO<sub>2</sub>-packed reactor at the standard conditions.

	Reaction	CO <sub>2</sub> splitting [56]	CH <sub>4</sub> reforming	DRM total	DRM CO <sub>2</sub>	DRM CH <sub>4</sub>
Empty	$k$ (s <sup>-1</sup> )	0.120 ± 0.005	0.041 ± 0.002	0.088 ± 0.003	0.083 ± 0.002	0.093 ± 0.003
	$k_{loss}$ (s <sup>-1</sup> )	0.066 ± 0.003	0.034 ± 0.003	0.066 ± 0.003	0.059 ± 0.003	0.074 ± 0.003
	$f k_{form}$ (s <sup>-1</sup> )	0.056 ± 0.003	0.0073 ± 0.0006	0.0217 ± 0.0009	0.024 ± 0.001	0.0190 ± 0.0008
	$X_e$ (%)	53.6 ± 0.8	82 ± 2	75.4 ± 0.6	71.2 ± 0.7	79.7 ± 0.7
SiO <sub>2</sub>	$k$ (s <sup>-1</sup> )	0.111 ± 0.004	0.074 ± 0.005	0.130 ± 0.005	0.118 ± 0.004	0.143 ± 0.006
	$k_{loss}$ (s <sup>-1</sup> )	0.079 ± 0.004	0.059 ± 0.005	0.109 ± 0.005	0.099 ± 0.004	0.121 ± 0.006
	$f k_{form}$ (s <sup>-1</sup> )	0.032 ± 0.002	0.014 ± 0.001	0.020 ± 0.001	0.018 ± 0.001	0.022 ± 0.001
	$X_e$ (%)	71.1 ± 0.8	81 ± 2	84.3 ± 0.8	84.3 ± 0.8	84.4 ± 0.8

However, the overall apparent reaction rate coefficient of CH<sub>4</sub> reforming is only a third of the value for CO<sub>2</sub> dissociation, i.e. 0.041 s<sup>-1</sup>. Our equilibrium model shows that  $k_{loss}$  and  $f k_{form}$  both have much lower values than those seen with CO<sub>2</sub> dissociation, being 0.034 s<sup>-1</sup> and 0.0073 s<sup>-1</sup> respectively (cfr. equations 5.6 and 5.7). From our modelling work it was established that the CH<sub>4</sub> loss reactions in a DBD reactor are dominated by electron impact ionisation and dissociation of CH<sub>4</sub>, yielding CH<sub>4</sub><sup>+</sup> and CH<sub>3</sub><sup>+</sup> ions, as well as CH<sub>3</sub>, CH<sub>2</sub>, and CH radicals, cfr. equations R1-5 in [138] and table 2 in [86]. In view of the small value of  $k_{loss}$ , these processes are therefore not as efficient as in the pure CO<sub>2</sub> plasma, which seems counterintuitive based on the reaction enthalpies. However, as shown by Snoeckx *et al.* [86], electron impact dissociation of CH<sub>4</sub> is very fast, but the recombination of the produced CH<sub>x</sub> radicals back towards CH<sub>4</sub>, is also very quick, resulting in a net low conversion and thus low effective rate coefficient. On the

other hand, the products of CO<sub>2</sub> electron impact dissociation are more stable: CO is a saturated molecule, and the O atoms can recombine into O<sub>2</sub>, ultimately leading to the higher effective loss rate from electron impact-driven processes.

The net CH<sub>4</sub> formation is mainly due to electron impact dissociation of C<sub>3</sub>H<sub>6</sub> and C<sub>3</sub>H<sub>8</sub> (cfr. equations R12 and R14 in [138]). These C3 hydrocarbons are however not very abundant in our CH<sub>4</sub> plasma, with a maximum product fraction of 2.46% measured in all our CH<sub>4</sub> experiments at steady state (see table D.3 in appendix D). In addition, experiments in the packed reactor (section 5.3.3) indeed confirm that both loss and formation processes are primarily electron impact-driven. Essentially, this means that CH<sub>4</sub> formation is hampered by a small  $f$  factor, which leads to a smaller effective formation rate coefficient  $f k_{form}$ , thus shifting the conversion equilibrium away from CH<sub>4</sub>. Because the electron impact-driven processes in this system are not as efficient as in the CO<sub>2</sub> system, the overall evolution rate towards this high equilibrium conversion is however lower.

Note that, although the plasma chemistry processes on the micro-scale are inherently fast in nature (milliseconds), the conversion on the macro-scale is still a rather slow process in this DBD reactor. This is due to the balance act of short and select random micro-discharges per second (with a diameter of typically 100 μm and duration of about 200 ns), in combination with reactions in the afterglow, diffusion, convection, and back reactions, resulting an overall slower conversion process, requiring about 40 s to 80 s to reach PCE, depending on the composition.

### 5.3.2 DRM: The best of both worlds

Subsequently, both gases were combined in an equimolar ratio to perform the DRM reaction at the same standard conditions (figure 5.1(a) and table 5.1). The combination of CO<sub>2</sub> and CH<sub>4</sub> leads to a high overall equilibrium conversion of 75.4%, associated with a high rate coefficient of 0.088 s<sup>-1</sup>, which is higher than the numerical average of the individual reactions would have been. This is a manifestation of  $k_{loss}$  being high at 0.066 s<sup>-1</sup>, which is the same as for CO<sub>2</sub> dissociation, and  $f k_{form}$  staying fairly low at 0.0217 s<sup>-1</sup>. When performing a similar analysis purely on the respective concentrations of CO<sub>2</sub> and CH<sub>4</sub> in DRM, we can see that, compared to the pure gases,  $k_{loss,CH_4}$  and  $f_{CH_4} k_{form,CH_4}$  are

more than two times larger, whereas  $f_{CO_2}k_{form,CO_2}$  is more than halved. This means that additional reaction pathways have become available for the processes producing and consuming  $CH_4$ , while  $CO_2$  formation pathways are suppressed due to the mixing of the two gases. These observations were also predicted by kinetic modelling [86, 146]. The density of O atoms is very low in the  $CO_2:CH_4$  mixture (there is less than 0.023%  $O_2$ , see section 5.3.5.3) and this limits  $CO_2$  formation by lowering its  $f$  factor, an effect that cannot be fully compensated by new “combustion-type” reactions of  $CH_4$ . These latter reactions, however, do affect the consumption of  $CH_4$ , because it can react with species such as  $O^-$ ,  $OH^\bullet$ , and  $CO_2^+$ .  $CH_4$  formation benefits from the availability of more radicals for three-body recombinations in DRM [86], hence explaining the increase of  $f_{CH_4}k_{form,CH_4}$  when  $CO_2$  is present.

These changes result in mixing of the characteristics of the individual reactions, towards the overall DRM kinetics trend seen above. In total, we effectively see  $CO_2$  boosting the conversion rate coefficient of  $CH_4$  while it reduces its own rate coefficient although to a smaller extent. Moreover,  $CH_4$  addition increases the (equilibrium) conversion of  $CO_2$  while slightly reducing its own equilibrium conversion. The overall result is that we obtain the best of both worlds in DRM, i.e. high apparent rate coefficients, like in  $CO_2$  dissociation, and high equilibrium conversions, like in  $CH_4$  reforming. In the most practical sense, the changes in kinetics and PCE state, resulting from mixing  $CO_2$  and  $CH_4$ , ensure that for any “practical” (short) residence time, the DRM process significantly outperforms its pure gas counterparts in terms of obtained conversion for both compounds, as can be seen in figure 5.1(a). It should also be noted that the individual  $CO_2$  and  $CH_4$  conversion in our DRM reaction, under the applied conditions here, are very close to each other, in comparison to other studies [72,84,96,131]. These papers report typical  $X_{CH_4}:X_{CO_2}$  ratios between 1.5 and 2, while ours are between 1.22 and 1.12 at the shortest and longest residence time, respectively.

### 5.3.3 Tuning the kinetics by packing material

Chapter 4 showed that adding a packing material to the reactor can tune both the rate coefficient and equilibrium conversion of plasma-induced  $CO_2$  dissociation individually, while at most enhancing only the rate in traditional thermal reactors (in case of a catalytic packing) [56]. These changes are usually

attributed to alteration of the plasma properties by physical effects of the packing materials on the discharge [62]: when a plasma changes, also the associated PCE can change. Generally speaking, adding a packing material will increase the local electric field near the contact points, and thus increase the electron temperature, while slightly lowering densities of some species due to more surface losses, depending on the material-gap combination [60]. Indeed, the applied peak-to-peak voltage (a measure for the reduced electric field  $E/N$  as the discharge gap remains constant and thus also for the electron temperature) increases significantly for all compositions upon adding the SiO<sub>2</sub> packing, see table D.10 in appendix D. This should result in a boost of the electron impact reactions, i.e. the major loss reactions for CO<sub>2</sub> and CH<sub>4</sub>, therefore increasing  $k_{loss}$ ,  $k$ , and  $X_e$ .

A SiO<sub>2</sub> packing was previously found to significantly increase the CO<sub>2</sub> equilibrium conversion from 53.6% to 71.1%, while only slightly decreasing the rate coefficient from 0.120 s<sup>-1</sup> to 0.111 s<sup>-1</sup> (see chapter 4), as shown when comparing figure 5.1(a and b) and table 5.1. Indeed,  $k_{loss}$  increases because electron impact-based loss reactions are stimulated by the increased electron temperature, whereas  $f k_{form}$  does not, because three-body neutral recombinations are unaffected by the electron temperature [38]. In fact,  $f k_{form}$  even decreases, which may be explained by the larger surface/volume ratio in the packed reactor: the presence of a large surface area will facilitate surface-mediated O atom recombination, thus reducing the density of O atoms in the gas phase, and hence suppressing the formation of CO<sub>2</sub> along the three-body recombination pathway by lowering the  $f$  factor [147]. The opposite effect of the packing on the respective CO<sub>2</sub> dissociation and formation rates therefore explains how the CO<sub>2</sub> equilibrium conversion can increase, while its overall conversion rate coefficient slightly decreases.

The same experiments for CH<sub>4</sub> reforming show a (almost) doubling of both  $k_{loss}$  and  $f k_{form}$  upon packing the reactor. While the SiO<sub>2</sub> packing does not enhance the equilibrium conversion, the apparent rate coefficient almost doubles from 0.041 s<sup>-1</sup> to 0.074 s<sup>-1</sup> (see table 5.1). As discussed in section 5.3.1, the most prominent reactions for both loss and formation of CH<sub>4</sub> in a DBD are again electron impact reactions – i.e. dissociation and ionisation for CH<sub>4</sub> loss and dissociation of C<sub>3</sub>H<sub>6</sub> and C<sub>3</sub>H<sub>8</sub> for CH<sub>4</sub> formation, respectively. This

means that both loss and formation are equally affected by a change in electron temperature, so that the ratio of  $k_{loss}$  and  $k_{form}$  is constant (as well as the equilibrium conversion), but their sum (and the overall reaction rate) increases.

Finally, the addition of a SiO<sub>2</sub> packing in DRM increases both the total equilibrium conversion, from 75.4% to 84.3%, and the apparent total rate coefficient, from 0.088 s<sup>-1</sup> to 0.130 s<sup>-1</sup> (cfr. table 5.1). Although the individual CO<sub>2</sub> and CH<sub>4</sub> rate coefficients (0.118 s<sup>-1</sup> and 0.143 s<sup>-1</sup> respectively) differ more compared to the empty reactor (section 5.3.2), the individual equilibrium conversions become roughly equal (84.3%), which is different from the empty reactor where the CH<sub>4</sub> conversion remained higher than the CO<sub>2</sub> conversion. This results in X<sub>CH<sub>4</sub></sub>:X<sub>CO<sub>2</sub></sub> ratios being even closer to 1, i.e. 1.29 to 0.99 at the shortest and longest residence times, respectively. The data shows that for both CO<sub>2</sub> and CH<sub>4</sub>, and thus in total for DRM as well,  $k_{loss}$  strongly increases while  $k_{form}$  stays about the same when the packing material is added. The changes in kinetics are again expected since both CO<sub>2</sub> and CH<sub>4</sub> losses are based on electron impact reactions, resulting in a rise of  $k_{loss}$  due to the higher electron temperature in case of the SiO<sub>2</sub> packing. The formation reactions have been predicted to be mostly based on ion and neutral chemistry for CO<sub>2</sub>, and three-body recombination, electron impact on C3 (which are barely present), and C2 three-body reactions for CH<sub>4</sub>, meaning that  $k_{form}$  is almost unaffected [86,146].

#### 5.3.4 Tuning the kinetics by mixing ratio

In section 5.3.1 we discussed how CO<sub>2</sub> dissociation is characterised by a high apparent rate coefficient but low equilibrium conversion, while CH<sub>4</sub> reforming displays a low apparent rate coefficient but high equilibrium conversion. Combining both in DRM results in total rates and conversions in between these values. In this section we look further into the mechanistic aspects of this mixing, by also testing 3:1 and 1:3 CO<sub>2</sub>:CH<sub>4</sub> ratios.

The time evolution of the conversions shown in figure 5.2 – with their associated kinetic and equilibrium parameters compared to the pure gases in table 5.2 – further clarifies the extent of the mixing effect seen in section 5.3.2. The rate constants and equilibrium conversion for the different gas mixing ratios interpolates continuously, but not linearly, between those for pure CO<sub>2</sub> and pure CH<sub>4</sub>. The more CO<sub>2</sub> is added to the mixture, the higher the overall

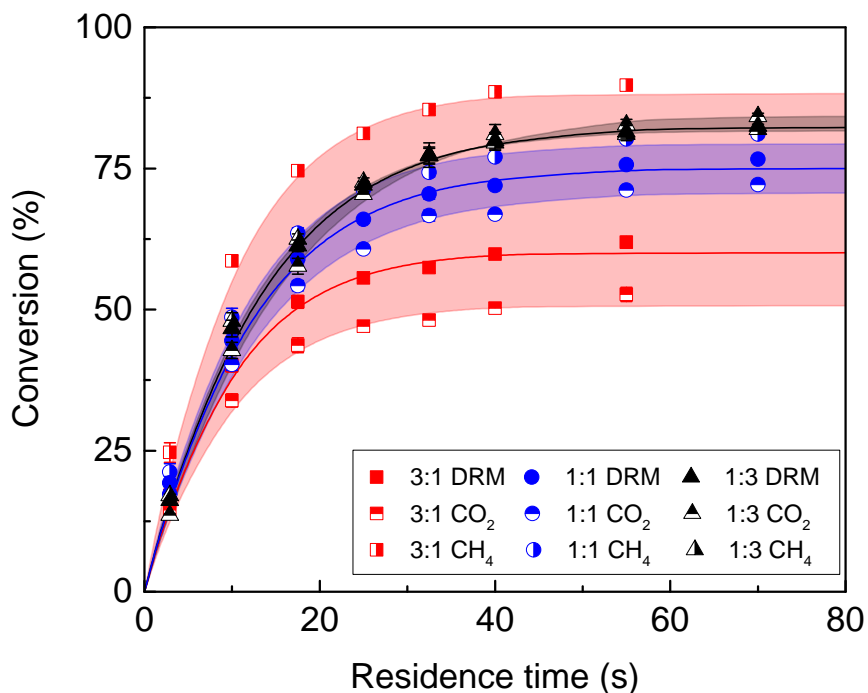


**Figure 5.2:** Total conversion of DRM with a  $\text{CO}_2:\text{CH}_4$  ratio of 3:1 (red squares), 1:1 (blue circles), and 1:3 (black triangles); plotted as a function of residence time in an empty reactor. The individual conversions of  $\text{CO}_2$  (horizontal half shapes) and  $\text{CH}_4$  (vertical half shapes) are plotted as well. Apparent first-order reversible reaction fits for all conversions are shown for the total conversion (solid lines) and the individual conversions (by the edges of the corresponding coloured regions). The exact values can be found in table D.1 in appendix D.

**Table 5.2:** Fitted kinetic and equilibrium data for DRM at different  $\text{CO}_2:\text{CH}_4$  ratios, and for the pure  $\text{CO}_2$  and  $\text{CH}_4$  reactions, in an empty reactor. The fit was applied for the total conversion as well as the sub-reactions.

$\text{CO}_2:\text{CH}_4$ ratio		1:0 [56]	3:1	1:1	1:3	0:1
Total	$k$ ( $\text{s}^{-1}$ )	$0.120 \pm 0.005$	$0.108 \pm 0.004$	$0.088 \pm 0.003$	$0.080 \pm 0.002$	$0.041 \pm 0.002$
	$k_{\text{loss}}$ ( $\text{s}^{-1}$ )	$0.066 \pm 0.003$	$0.065 \pm 0.003$	$0.066 \pm 0.003$	$0.066 \pm 0.002$	$0.034 \pm 0.003$
	$f k_{\text{form}}$ ( $\text{s}^{-1}$ )	$0.056 \pm 0.003$	$0.042 \pm 0.002$	$0.0217 \pm 0.0009$	$0.0136 \pm 0.0005$	$0.0073 \pm 0.0006$
	$X_e$ (%)	$53.6 \pm 0.8$	$60.5 \pm 0.6$	$75.4 \pm 0.6$	$83.0 \pm 0.7$	$82 \pm 2$
$\text{CO}_2$	$k$ ( $\text{s}^{-1}$ )	$0.120 \pm 0.005$	$0.109 \pm 0.006$	$0.083 \pm 0.002$	$0.067 \pm 0.003$	-
	$k_{\text{loss}}$ ( $\text{s}^{-1}$ )	$0.066 \pm 0.003$	$0.055 \pm 0.004$	$0.059 \pm 0.003$	$0.058 \pm 0.003$	-
	$f k_{\text{form}}$ ( $\text{s}^{-1}$ )	$0.056 \pm 0.003$	$0.053 \pm 0.004$	$0.024 \pm 0.001$	$0.0096 \pm 0.0005$	-
	$X_e$ (%)	$53.6 \pm 0.8$	$51.1 \pm 0.7$	$71.2 \pm 0.7$	$86 \pm 1$	-
$\text{CH}_4$	$k$ ( $\text{s}^{-1}$ )	-	$0.106 \pm 0.003$	$0.093 \pm 0.003$	$0.085 \pm 0.002$	$0.041 \pm 0.002$
	$k_{\text{loss}}$ ( $\text{s}^{-1}$ )	-	$0.094 \pm 0.003$	$0.074 \pm 0.003$	$0.070 \pm 0.002$	$0.034 \pm 0.003$
	$f k_{\text{form}}$ ( $\text{s}^{-1}$ )	-	$0.0117 \pm 0.0004$	$0.0190 \pm 0.0008$	$0.0151 \pm 0.0005$	$0.0073 \pm 0.0006$
	$X_e$ (%)	-	$89.0 \pm 0.6$	$79.7 \pm 0.7$	$82.2 \pm 0.6$	$82 \pm 2$

rate coefficient is, skewed towards that of the pure CO<sub>2</sub> system. The equilibrium conversion, however, is mainly affected by the CH<sub>4</sub> concentration (i.e. skewed towards the pure CH<sub>4</sub> case), with higher equilibrium conversions obtained with more CH<sub>4</sub> in the mixture. The changes in  $k_{loss}$  and  $f k_{form}$  curiously show that as long as there is CO<sub>2</sub> in the mixture, the loss rate coefficient  $k_{loss}$  of DRM is constant and equal to  $k_{loss}$  of pure CO<sub>2</sub>. At first sight, the shifts in  $k$  and  $X_e$  as a function of the CO<sub>2</sub>:CH<sub>4</sub> ratio may therefore seem to be fully attributable to a change of  $f k_{form}$ , which decreases with increasing CH<sub>4</sub> concentration. Analysis of the effective kinetics of CO<sub>2</sub> and CH<sub>4</sub> shown in table 5.2 (based on their individual conversion within DRM), however, shows how these shifts of  $k$  and  $X_e$  arise.  $k_{loss,CO_2}$  is independent of the mixing ratio although slightly lower than in a pure CO<sub>2</sub> plasma (i.e. around  $0.057\text{ s}^{-1}$  within error bars), while a slightly higher  $k_{loss,CH_4}$  does shift with the mixing ratio but only to some extent so that the overall  $k_{loss}$  of DRM stays constant at  $0.066\text{ s}^{-1}$ . The formation rate coefficients for both gases generally decrease with increasing CH<sub>4</sub> concentration, although at the 3:1 ratio,  $f_{CH_4} k_{form,CH_4}$  is lower than at the 1:1 ratio, whereas  $f_{CO_2} k_{form,CO_2}$  at the 3:1 ratio is close to the value for pure CO<sub>2</sub>. As a result, the 3:1 mixture exhibits a much higher conversion of CH<sub>4</sub> than of CO<sub>2</sub> (89.0% and 51.1%, respectively).

In the most general sense, changing the CO<sub>2</sub>:CH<sub>4</sub> ratio therefore mainly changes the formation aspect of the overall reaction, allowing us to tune both the kinetics as well as the PCE of DRM. From the trends in the loss and formation rates, we conclude that CO<sub>2</sub> drives the loss reactions in DRM, whereas the presence of CH<sub>4</sub> in the mixture suppresses formation reactions. The combination of these effects results in both high equilibrium conversions and high conversion rates in DRM. Combining this knowledge with insight gleaned from the experiments with the SiO<sub>2</sub>-packed reactor, it can be inferred that electron impact-driven processes are very efficient with CO<sub>2</sub>, and they dominate the non-equilibrium loss processes even at fairly low CO<sub>2</sub> fractions (25% in our experiments). CH<sub>4</sub> loss is enhanced by species produced in CO<sub>2</sub> loss reactions which, in turn, chemically suppress CO<sub>2</sub> formation. To have an appreciable effect on the CO<sub>2</sub> conversion, the CH<sub>4</sub> fraction must however be sufficiently high (50% in our experiments).

Table D.10 in appendix D shows the applied peak-to-peak voltage for the

different gas mixing ratios investigated. Because we keep the discharge gap constant, the peak-to-peak voltage can be considered as a measure for the reduced electric field, and thus for the electron temperature. In contrast to the addition of the SiO<sub>2</sub> packing, we see no clear correlation between this peak-to-peak voltage and the kinetic data derived in our study, for the different gas mixtures. This indicates that besides the electron temperature, additional unknown factors will have an impact as well.

### **5.3.5 How residence time and gas mixture tune product composition**

Besides the CO<sub>2</sub>, CH<sub>4</sub>, and total conversions reported above, it is interesting to understand how these differences influence the formed products. As mentioned in section 5.2.1, only a number of components could be quantified, and those will be discussed here. The results of the remaining components can be found with their peak areas in appendix D. During the experiments with CH<sub>4</sub>, mostly at longer residence times, we could collect small amounts of carbon deposition and highly viscous fluids. GC-MS analysis showed ppm levels of C1 to C4 acids and unidentified carbon polymers. This and the uncalibrated components will of course result in an incomplete atom balance after the reactor, which is further discussed in section 5.3.6.1.

#### **5.3.5.1 CO<sub>2</sub> dissociation**

The products formed in CO<sub>2</sub> dissociation are limited to CO, O<sub>2</sub>, O<sub>3</sub>, and C deposits. Only trace amounts of O<sub>3</sub> were detected and no C deposition was observed in or after the reactor, so these will be neglected further on. The production of CO and O<sub>2</sub> in the empty reactor is shown in figure 5.3(a). We can see that the production of CO and O<sub>2</sub> respects the stoichiometric 2:1 ratio of the CO<sub>2</sub> splitting reaction, with CO reaching a maximum concentration of around 36% and O<sub>2</sub> reaching around 18%.

Adding a SiO<sub>2</sub> packing to the reactor enhances the conversion, as discussed in section 5.3.3, which also results in higher CO and O<sub>2</sub> concentrations, as shown in figure 5.3(b). The maximum CO concentration obtained, increases to about 49% while the O<sub>2</sub> concentration increases to 24%, again respecting the stoichiometric 2:1 ratio of the CO<sub>2</sub> splitting reaction.



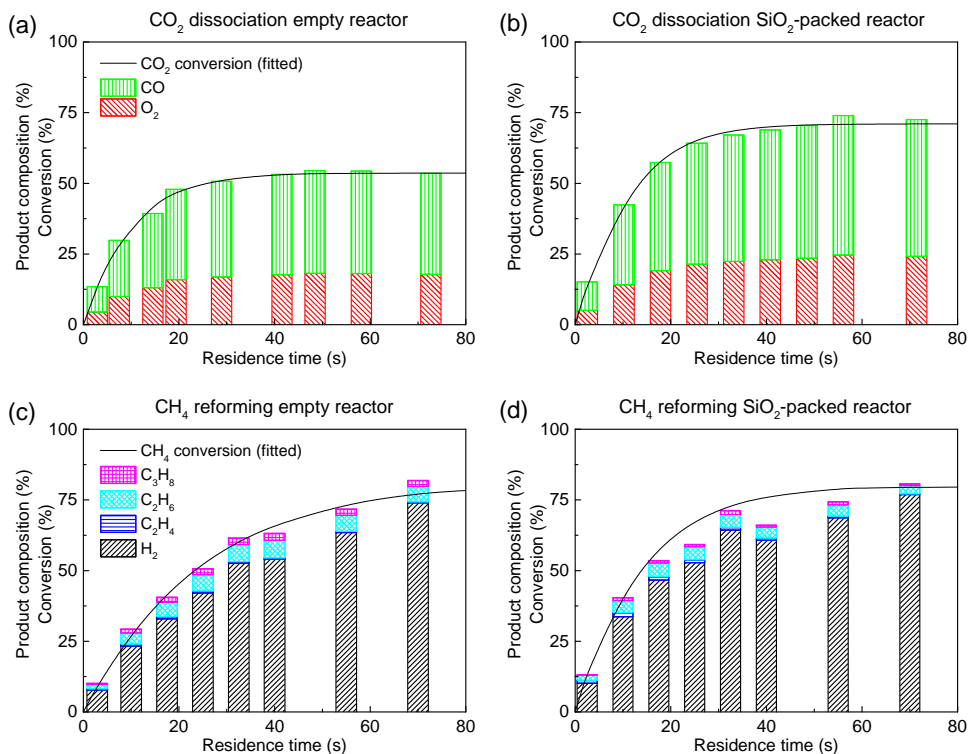


**Figure 5.3:** Measured concentration of different calibrated components after CO<sub>2</sub> dissociation for (a) the empty reactor and (b) the SiO<sub>2</sub>-packed reactor, as well as after CH<sub>4</sub> reforming for (c) the empty reactor and (d) the SiO<sub>2</sub>-packed reactor, plotted as stacked bars as a function of residence time. The fitted CO<sub>2</sub> and CH<sub>4</sub> conversions are displayed as well, as a reference for all cases. All components are measured on the TCD. The exact values of the concentrations can be found in table D.3 in appendix D.

### 5.3.5.2 CH<sub>4</sub> reforming

Figure 5.3(c) shows the calibrated product composition after CH<sub>4</sub> reforming for the empty reactor (the exact concentration of every component can again be found in table D.3 in appendix D). The main component formed during CH<sub>4</sub> reforming is H<sub>2</sub>, followed by ethane, propane, and ethene. A steady increase in H<sub>2</sub> concentration is seen from 8% to 74% upon increasing the residence time, following the increasing conversion. This trend is, however, not followed by the other components, of which the concentration first increases to a maximum value, and then decreases again. Ethane reaches a maximum concentration of 6.21% at 40s, and slightly decreases to 5.5% at 70s. Propane shows the same behaviour with a maximum concentration of 2.46% at 40s, dropping to 2.1% at 70s. Ethene reaches its maximum concentration of 0.79% already at

17.5 s, and decreases significantly to only 0.35% at 70 s. This means that these small hydrocarbons are actually intermediates that are consumed, either in the production of higher hydrocarbons or back into formation of CH<sub>4</sub>, as well as H<sub>2</sub> and C, at longer residence times. Also, it can be inferred that alkenes are more prone to react further or be decomposed again, since they are more reactive.

Adding the SiO<sub>2</sub> packing to the reaction zone has two major effects on the product composition after CH<sub>4</sub> reforming. A higher share of H<sub>2</sub> is observed over the entire residence time range, but the changes in C<sub>2</sub> and C<sub>3</sub> concentration depend on the exact residence time and there are also lower amounts of all higher hydrocarbons.

### 5.3.5.3 Dry reforming of methane

Figure 5.4 shows the calibrated product composition for DRM. All concentrations can again be found in appendix D (table D.6). The addition of CO<sub>2</sub> to the mixture results in high fractions of CO in the reactor effluent, as it is the main product from electron impact dissociation of CO<sub>2</sub>. The concentration starts at 10.2% at the shortest residence time and rises to 37.4% at the longest residence time. The other main product from CO<sub>2</sub> dissociation, O<sub>2</sub>, is however barely detected; its concentration only reaches up to 0.023%. Indeed, the O atoms formed by CO<sub>2</sub> splitting will react further into oxygenated hydrocarbons and water, or back into CO<sub>x</sub>, and only a small fraction recombines into O<sub>2</sub>, whereas CO appears as one of the more stable end products of DRM. Again, we observe high concentrations of H<sub>2</sub>, up to 39%, and producing H<sub>2</sub>:CO ratios close to 1 (0.91-1.04), see table D.6. This syngas ratio is too low for optimal Fischer-Tropsch synthesis, where a ratio of 2 is desired [148]. Ethane, ethene, and propane show similar behaviour as seen with CH<sub>4</sub> reforming, i.e. a low-high-low concentration profile, but at lower values; only the ethane concentration surpasses the 1% mark, reaching 1.96% at 10 s and decreasing to 1.04%. Ethanol, the sole oxygenated hydrocarbon that could be quantified, is only formed in small amounts from 300 ppm to 90 ppm.

Although some changes can be observed in ratios of different products, adding a SiO<sub>2</sub> packing to the reactor does not have a large impact on the product formation. In figure 5.4(b) we see that the H<sub>2</sub> concentration reaches the same end value, although it does so faster due to the higher overall rate coefficient, but a slightly larger amount of CO is formed at equilibrium (42.7% compared

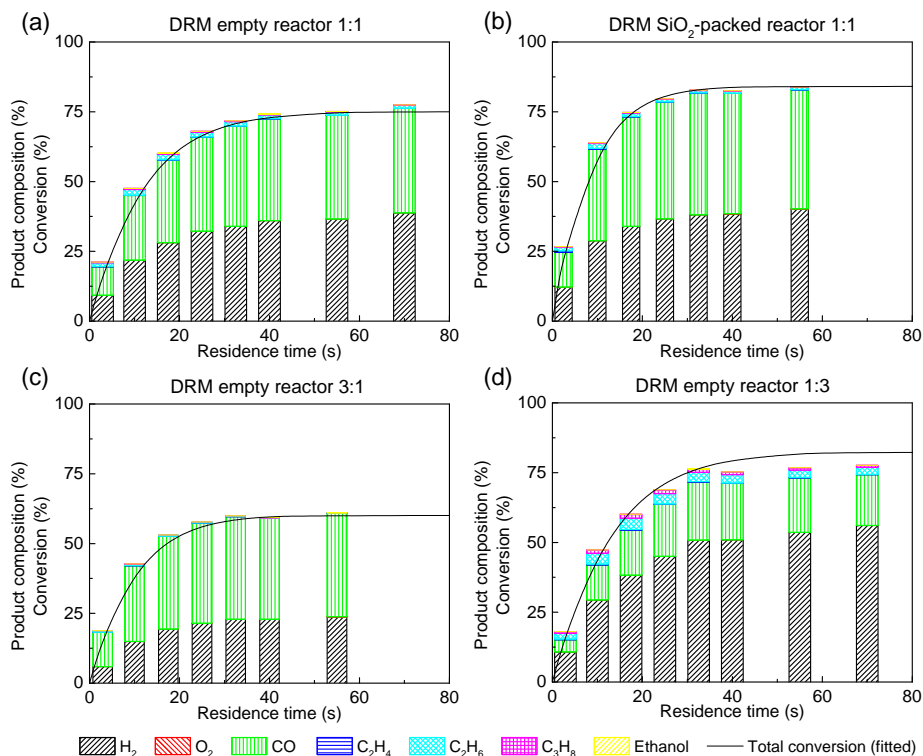


**Figure 5.4:** Measured concentration of different calibrated components for DRM, plotted as stacked bars as a function of residence time, for (a) the empty reactor with a  $\text{CO}_2:\text{CH}_4$  ratio of 1:1, (b) the  $\text{SiO}_2$ -packed reactor at 1:1 ratio, (c) the empty reactor at 3:1 ratio, and (d) the empty reactor at 1:3 ratio. The fitted DRM conversion is displayed as well, as a reference for each case. All components are measured on the TCD. The exact values of the concentrations can be found in table D.6 in appendix D.

to 37.4%). As a result, the  $\text{H}_2:\text{CO}$  ratio slightly changes to 0.98 at the shortest residence time, and to 0.94 at the longest. The other components remain almost constant.

Changing the  $\text{CO}_2:\text{CH}_4$  ratio has a large impact on the product formation, as can be seen in figure 5.4(c and d). A larger fraction of  $\text{CO}_2$  in the mixture (3:1 ratio) increases the CO fraction after a short residence time, but eventually reaches the same maximum concentration as for the 1:1 ratio, i.e. 37.1% vs. 37.4%, respectively. The  $\text{H}_2$  concentration, on the other hand, is significantly reduced over the entire residence time by almost a third, reaching a maximum of 23.8%, compared to 39% for the 1:1 ratio. The  $\text{H}_2:\text{CO}$  ratio therefore decreases as well, to values between 0.49 and 0.64. The higher  $\text{CO}_2$  fraction leads to a slight increase in the  $\text{O}_2$  concentration, which is 0.008% at the shortest residence time

and 0.0114% at the longest, but is still very low compared to pure CO<sub>2</sub> splitting, as explained above. The concentration of the remaining components strongly decreases to values well below 1%, as can be seen in table D.6.

Vice versa, a large fraction of CH<sub>4</sub> in the mixture (1:3 ratio) seems to be more beneficial overall. The CO concentrations are half the values reached for the 1:1 ratio across the entire range of residence times, but the H<sub>2</sub> concentration increases by a factor 1.2 to 1.5, showing a maximum of 56.1%, and thus resulting in large H<sub>2</sub>:CO ratios between 2.34 and 3.08, which is more optimal for the production of (oxygenated) alkanes and alkenes via the Fischer-Tropsch process [148]. The ethane, ethene and propane production rises as well, with concentrations up to 4.02%, 0.32% and 1.43%, respectively, at 17.5 s. Higher CH<sub>4</sub> fractions are however more susceptible to carbon depositions, requiring periodic physical cleaning, or chemical cleaning by e.g. pure O<sub>2</sub> or H<sub>2</sub>. For this reason it could be interesting to add more CO<sub>2</sub> in the mix, to prevent carbon deposition.

An interesting observation can be made for the CO and CO<sub>2</sub> concentrations. For all DRM experiments—except at a 1:3 ratio and at long residence times, when most condensable products are being made—the sum of CO<sub>out</sub> and CO<sub>2,out</sub> after the experiment is equal to CO<sub>2,in</sub> before the experiment, as can be seen in table D.6. This means that in DRM, on a global scale, all net CO<sub>2</sub> conversion is dominated by the transformation of CO<sub>2</sub> into CO, without further reaction towards hydrocarbons. It might be possible that on the molecular scale some CO reacts towards elemental C and O, or towards C1 oxygenates, and some hydrocarbons (or elemental C) partially oxidise to CO. However, on a reactor scale, CO<sub>2</sub>, besides mainly being a source of ‘non-reactive’ CO, seems to act only as an oxygen source for the oxygenated hydrocarbons and water, which means that CH<sub>4</sub> is expected to be the actual carbon source for the production of the (oxygenated) hydrocarbons. A comparative study to partial oxidation of CH<sub>4</sub> ( $\text{CH}_4 + \text{O}_2 \longrightarrow \text{C}_x\text{H}_y\text{O}_z$ ) might be of interest to check the conversion efficiency (both on a rate coefficient and energy basis) towards (oxygenated) hydrocarbons.

Also, we observe that the produced fraction of CO in the empty reactor during CO<sub>2</sub> dissociation matches the maximum produced fractions of CO in DRM with CO<sub>2</sub>:CH<sub>4</sub> fractions of 3:1 and 1:1. As the CO<sub>2</sub> fraction in the mixture is reduced, the effective CO<sub>2</sub> conversion increases, to maintain the same overall

CO<sub>2</sub> consumption, and thus CO production. It seems that the equilibrium concentration of CO<sub>2</sub> in the empty reactor, in both CO<sub>2</sub> dissociation and DRM, is limited to the same power-dependent maximum value of 36%, independent of the DRM ratio. Only when lowering the initial CO<sub>2</sub> fraction to 25%, as in the 1:3 DRM ratio, we obtain lower fractions of CO, which is logical due to the low initial concentration of CO<sub>2</sub>. Hence, it confirms our conclusion of no noticeable production of CO from CH<sub>4</sub>. Also, when adding the SiO<sub>2</sub> packing material, we observe a higher CO production, due to the optimised kinetics, as discussed in section 5.3.3, although the maximum CO fraction here does not match the maximum CO fraction from SiO<sub>2</sub>-packed CO<sub>2</sub> dissociation.

### 5.3.6 Further considerations

#### 5.3.6.1 Strengths and limitations of this PCE study

The focus of this study is to accurately quantify the amount of (reacted) CO<sub>2</sub> and CH<sub>4</sub>, as it is the input of the PCE model equation. Characterising the other components in the reactor exhaust gas is a more difficult matter. First of all, it is impossible to know all the possible products that can be formed in the reactor beforehand, let alone quantify them all. This is because we cannot calibrate for them or collect them (in the case of solid or liquid depositions) in a reliable way; up to C7 and C4-OH were detected but only few calibrated, see table D.2 in appendix D.

Although we cannot determine all components, we can still correctly quantify all components for which the GC was calibrated because we measured no significant gas expansion nor contraction in the DRM and CH<sub>4</sub> reforming experiments; in the case of pure CO<sub>2</sub> dissociation we did measure gas expansion consistent with the reaction stoichiometry and this was corrected accordingly (see also chapter 4). Therefore, the conversion of CH<sub>4</sub> and CO<sub>2</sub> could always be measured in a reliable way. As a result of the limited set of calibrated components, the atom balances in our experiments are not complete. Depending on the exact conditions, we missed up to 75% of a specific atom balance (most pronounced at low flow rates, SiO<sub>2</sub> packing, and high methane content). This is for example visible in the pure CH<sub>4</sub> experiments where the H<sub>2</sub> concentration is on average 88% of that of the converted CH<sub>4</sub> and thus most of the remaining CH<sub>2</sub> from CH<sub>4</sub> is missing and most likely will be deposited as liquid C<sub>x</sub>H<sub>y</sub> and

solid C. A similar example can be seen for DRM: in section 5.3.5.3 we saw that, on a global reactor scale, CH<sub>4</sub> acted like the sole carbon source for higher hydrocarbons as equimolar amounts of CO were formed compared to the reacted CO<sub>2</sub>. Still only a few extra (oxygenated) hydrocarbons and a minor amount of O<sub>2</sub> could be quantified, resulting in incomplete C, H, and O balances. Table D.9 in appendix D shows all atom balances for all gas mixtures and for both empty and SiO<sub>2</sub>-packed reactors (if applicable).

Also, one can think about the validity of applying the partial chemical equilibrium (PCE) concept in these more complex chemical reactions (CH<sub>4</sub> reforming and DRM), in comparison to CO<sub>2</sub> dissociation. In the latter, CO<sub>2</sub> is split into CO and O<sub>2</sub>, which are usually the only end products, unless significant O<sub>3</sub> or carbon deposition would be present due to some conditions. Once the CO<sub>2</sub> loss rate is equal to the formation rate by CO oxidation, PCE is reached and further extension of the residence time has no influence on the overall CO<sub>2</sub> conversion, or CO and O<sub>2</sub> formation. However, the chemistry in CH<sub>4</sub> reforming and DRM is much more complex, which means that the manifestation of the PCE might be different for each component. In sections 5.3.1 to 5.3.4, we showed that the PCE appears to be reached in CH<sub>4</sub> reforming and DRM, based on the CO<sub>2</sub> or CH<sub>4</sub> conversions alone. An explicit proof for the existence of a global PCE state, however, would entail running the same conversion process starting from the pure products and verifying if this results in the same final gas composition, as we did in chapter 4. Such an approach is precluded here by the difficulty of identifying all species in these more complex gas mixtures. As noted earlier, smaller hydrocarbons might for example still polymerise to higher hydrocarbons, while the latter can dissociate back into lower hydrocarbons, and it is not clear from our results if true equilibrium was already reached in our experiments. For this reason, the PCE analysis in this work was mostly restricted to the easy-to-characterise initial reactants. At least for these gases, time-dependent concentrations appear to be consistent with PCE behaviour, in line with our previous more rigorous investigation of the chemically more simple CO<sub>2</sub> dissociation process in chapter 4. As a result, we can confidently report PCE conversions of the feed gases, but not PCE yields for all the products. Additionally, despite the extensive nature of the (plasma) chemistry in CH<sub>4</sub> reforming and DRM, our results confidently prove that the overall gas conversion

processes resulting from even these complex reactions can be described by our apparent first order kinetics PCE model, demonstrating opportunities towards other reaction and reactor types.

### 5.3.6.2 Interpreting the energy cost

Finally, we shortly reflect on the efficiency of the reactor configurations used in this work. For this, we invoke the concept of the energy cost (EC), i.e. the amount of energy necessary to convert one mole of reactant mixture, according to:

$$EC = \frac{SEI \cdot V_m}{X_{Total}} \quad (5.9)$$

with  $SEI$  the specific energy input based on the ratio of the plasma power and  $\dot{V}$  the volumetric flow rate ( $SEI = \frac{P}{\dot{V}}$ ), and  $V_m$  the molar volume (22.4 L/mol). The calculated EC for all experiments can be found in table D.1 in appendix D.

The fact that the plasma conversion processes under consideration can be characterised by PCE behaviour has important consequences for their energy cost. The conversion asymptotically reaches the equilibrium conversion as an upper limit, which cannot be further improved by increasing the specific energy input (for a given set of plasma conditions). As a result, accurate determination of the location of the PCE, and the rate of evolution towards it, requires running conversion experiments at long residence time, resulting in very low energy efficiencies. However, such experiments would only have to be carried out once for a given process/reactor combination. Afterwards, the obtained information can be used to design or select an optimal process or conditions, determined by economical or practical considerations. More specifically, the rate coefficient and equilibrium conversion allow to predict the conversion as a function of residence time, which can be contrasted with energy cost at the same residence time; an optimal balance between the two can be selected, and compared with another process.

From the calculated EC data we can see that the minimum EC for almost all cases is reached at the shortest residence time (or highest flow rate), except for pure  $\text{CH}_4$  reforming. This is due to the fact that, generally, the conversion rises too slowly with increasing residence time, or in other words, the rate at which the flow rate decreases cannot be matched by the increase in total conversion.

For CO<sub>2</sub> dissociation we find a minimum EC of 1.7 kWh/mol at 2.9 s, while the minimum EC of CH<sub>4</sub> reforming is even higher, i.e. 2.6 kWh/mol at 10 s. In both cases, adding a packing material to the reactor does not yield a lower EC. Interestingly, DRM in a 1:1 ratio shows better results, with a minimum EC of 1.16 kWh/mol at 2.9 s. Both the 3:1 and 1:3 ratios perform slightly worse, with values of 1.32 and 1.38 kWh/mol, respectively. From these data we conclude that the most effective use of the DBD plasma reactor is at shorter residence times. This conclusion might change however if we take other aspects into account, such as separation processes and the (liquid) higher hydrocarbons. Indeed, the separation of a low converted gas mixture might suffer from high running costs, rendering less energy efficient conditions but with higher overall conversion. An optimum can probably be found here, depending on the physical process volume and process parameters. Moreover, we found in sections 5.3.5.2 and 5.3.5.3 that the longer residence times produced higher amounts of products, and also more diverse products. Depending on the desired end products, i.e. either syngas, lower hydrocarbons, or liquids, different operating conditions might be preferred. Therefore, a careful analysis of this type of experiments is very useful for the design of optimised processes for specific purposes.

### 5.4 Conclusion

In this chapter we investigated the kinetics of the CO<sub>2</sub> dissociation and CH<sub>4</sub> reforming reactions and how they influence each other when both gases are combined in DRM. Fitting the time evolution of the gas composition to a new generalised first order kinetic model for the partial chemical equilibrium made it possible to determine multiple trends, elucidate macroscopic changes in the plasma chemistry, and link them to changes in the loss or formation reactions of the reagents. CO<sub>2</sub> dissociation exhibits a higher apparent rate coefficient ( $0.120\text{ s}^{-1}$ ) than CH<sub>4</sub> reforming ( $0.041\text{ s}^{-1}$ ), but CH<sub>4</sub> reforming has a higher equilibrium conversion (82%) than CO<sub>2</sub> dissociation (53.6%). The lower rate coefficient of CH<sub>4</sub> reforming is attributed to fast dissociation and recombination reactions, rendering a slow net overall rate. Mixing both gases in a 1:1 ratio combines the best of both worlds, i.e. the higher equilibrium conversion of CH<sub>4</sub> reforming, yielding 75.4%, and the higher rate coefficient of CO<sub>2</sub> dissociation,



ending up at  $0.088\text{ s}^{-1}$ . These results point to additional interactions of the two gases, which open new pathways by the individual gas products.

Adding a spherical non-porous  $\text{SiO}_2$  packing material to the reactor increases the electron temperature and thus further stimulates electron impact-based processes, causing gas-specific effects. In a pure  $\text{CO}_2$  plasma, the equilibrium shifts further away to 71.1%, at the cost of slightly reducing the overall conversion rate coefficient to  $0.111\text{ s}^{-1}$ , whereas for  $\text{CH}_4$  reforming the equilibrium conversion stays about the same at 81% and the apparent rate coefficient increases to  $0.074\text{ s}^{-1}$ . Mixing the gases results in an increase of both equilibrium and rate coefficient in 1:1 DRM to 84.3% and  $0.130\text{ s}^{-1}$ , respectively.

Comparing different  $\text{CO}_2:\text{CH}_4$  ratios reveals the delicate balance of the combined chemistry.  $\text{CO}_2$  drives the loss reactions in DRM, resulting in higher reaction rate coefficients when present in higher fractions; the presence of  $\text{CH}_4$  in the mixture suppresses back reactions, resulting in higher equilibrium conversions when it is more abundant.

Finally, analysis of the effluent of all experiments revealed not only how the product composition changes and is influenced by mixing the  $\text{CO}_2$  and  $\text{CH}_4$ , but also how it changes in time. We see trade-offs between producing larger amounts of hydrocarbons (when more  $\text{CH}_4$  is present in the mixture), and optimal  $\text{H}_2:\text{CO}$  syngas ratios (when more  $\text{CH}_4$  is present).

The method for kinetic analysis used in this work is shown to be a practical way to describe the plasma-based conversion of molecules of interest in arbitrary gas mixtures with a priori unknown stoichiometry. In addition, we have shown how analysis of the derived kinetic parameters can elucidate key mechanistic aspects of the conversion process and help bridge the gap with detailed kinetic models. We therefore highly advise this method for any further research in plasma (catalysis) based gas conversion.



# Chapter 6

## How gas flow design can influence the performance of a DBD plasma reactor for dry reforming of methane

Published as:

Y. Uytendhouwen, J. Hereijgers, T. Breugelmans, P. Cool, and A. Bogaerts, “How gas flow design can influence the performance of a DBD plasma reactor for dry reforming of methane,” *Chemical Engineering Journal*, vol. 405, p. 126618, feb 2021

## **Abstract**

DBD plasma reactors are commonly used in a static ‘one inlet – one outlet’ design that goes against reactor design principles for multi-component reactions, such as dry reforming of methane (DRM). Therefore, in this chapter we have developed a novel reactor design, and investigated how the shape and size of the reaction zone, as well as gradual gas addition, and the method of mixing CO<sub>2</sub> and CH<sub>4</sub> can influence the conversion and product composition of DRM. Even in the standard ‘one inlet – one outlet’ design, the direction of the gas flow (i.e. short or long path through the reactor, which defines the gas velocity at fixed residence time), as well as the dimensions of the reaction zone and the power delivery to the reactor, largely affect the performance. Using gradual gas addition and separate plasma activation zones for the individual gases give increased conversions within the same operational parameters, by optimising mixing ratios and kinetics. The choice of the main (pre-activated) gas and the direction of gas flow largely affect the conversion and energy cost, while the gas inlet position during separate addition only influences the product distribution.

## 6.1 Introduction

During most investigations in DBD reactors, little creative engineering is done besides such optimisations, i.e. the DBD reactor (in either parallel plate or coaxial design, with or without packing) is virtually always used in a static ‘one inlet – one outlet’ design. While this is not really an issue with a single-gas inlet stream, it is known from reaction engineering that such a design is rarely the best configuration for multi-gas inlet streams [79]. It can lead to reactor operation at non-ideal kinetic conditions, resulting in improper conversions of one or more of the reagents, e.g. more  $\text{CH}_4$  conversion than the more desired  $\text{CO}_2$  conversion in DRM (see table 1 from Michielsen *et al.* [84]) or “optimal conversions” at stoichiometric unfavourable ratios, e.g. optimal  $\text{NH}_3$  conversions at  $\text{H}_2:\text{N}_2$  ratios (far) below 1 instead of 3 [47, 150–153]. This non-ideal behaviour of multi-gas reactions could be resolved by correct reactor design, such as the size or type of reactor (batch, perfect mixer, plug-flow, or combined “real” reactor), reactors in series and/or parallel, recycling, and/or separate addition of reactants [79].

Few researchers have tried innovative solutions and alterations to the traditional DBD reactor design in an attempt to optimise its performance. Examples are a fluidised (catalytic) bed [46], forcing the gas flow through a thin-walled porous (catalytic) tube [47, 48], a sintered metal fibre (catalytic) electrode for product draining [49], a combined AC/DC DBD reactor for honeycomb structures [50], and a DBD reactor combined with a solid oxide electrolyser cell (SOEC) [51]. Although (significant) improvements were reported in these investigations, they still applied a ‘one inlet – one outlet’ design. To our knowledge, only Huang and co-workers took a new approach by designing a Y-shaped reactor, allowing separate addition of  $\text{CO}_2$  and  $\text{CH}_4$  for DRM [52, 53]. This design allowed them to pre-activate one or both of the individual gases before mixing them together as excited species, showing enhanced conversion and energy efficiency. Moreover, even this separate plasma activation was able to produce hydrocarbons, and plasma activation of only one the gases could react with unactivated gas. Based on these findings and the knowledge from traditional reactor engineering, we believe that a lot of improvements can still be expected, in terms of the design of DBD reactors for multi-gas reactions.

Therefore, in this work, we investigate how the performance of a DBD reactor can be improved by changing the way in which CO<sub>2</sub> and CH<sub>4</sub> are added to, and mixed in, the reactor. We designed a new multi inlet/outlet parallel plate DBD reactor that allows us to quickly change the geometry of the reaction volume, in order to accommodate a multitude of different flow and mixing patterns. We will elucidate how electrode length, different gas ratios, gradual gas addition, and separate plasma activation zones for the individual gases will influence the reactor performance compared to the standard ‘one inlet – one outlet’ design.

## 6.2 Methods and theory

### 6.2.1 Novel multi-purpose DBD reactor

We designed and built (CNC mill, Isel Euromod MP45) a new DBD reactor with maximum adaptability in mind, as shown in figure 6.1. The parallel plate design was chosen over the more popular co-axial design because the ceramic dielectric tubes of the latter (typically glass, quartz, or alumina) require a lot of intricate and expensive work to change the geometry, and to add for example side inlets/outlets. Our design allows us to modify only one plastic ‘spacer’ layer, which is easy and cheap to manufacture (along with the corresponding gas connections), in order to change the entire gas flow and mixing pattern in the reactor.

The main body of the reactor consists of a PMMA ‘bottom holder’ (1) that holds all components of the DBD reactor together. It features a rectangular access hole to allow grounding of the grounded electrode (2), sixteen small holes to pass-through any number of desired gas connections to the grounded electrode (2), and 16 threaded holes to receive M5 bolts. The grounded aluminium electrode (2) (200x100x3.5 mm) is added to the bottom holder, which features sixteen 1/4”-28 UNF threaded 3 mm deep holes on the bottom side to receive the desired number of gas connections (XP-330X flangeless nuts, IDEX), sixteen 1 mm holes on the top side to pass-through the gas, and a 2 mm deep cut groove around the edges to accommodate a 3 mm thick O-ring (3). A POM ‘spacer’ layer (4) (200x100x3.5 mm) is added on top of the grounded electrode. By changing the inner shape of the spacer, we can shape and define the geometry of the reaction volume. This layer also has a groove and O-ring (3). A sheet of borosilicate glass

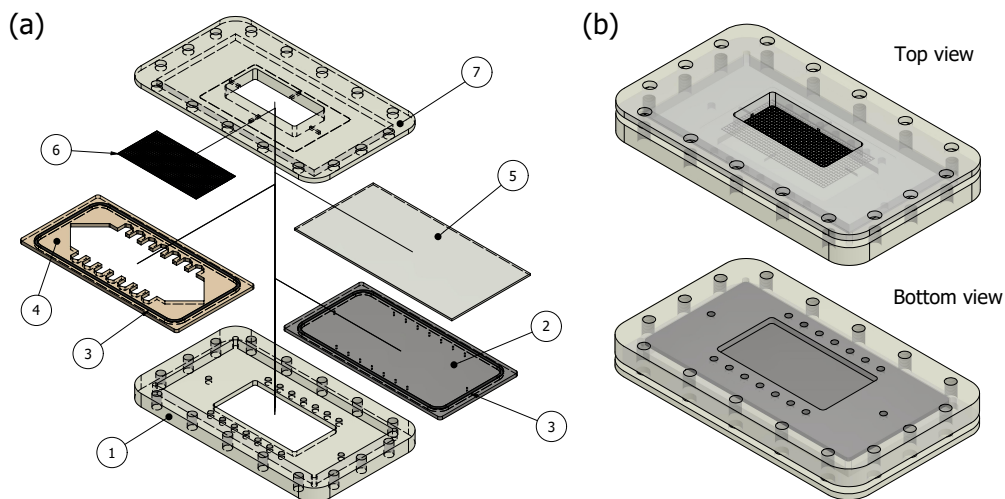


**Figure 6.1:** (a) Expanded view and (b) assembled views of the novel parallel plate DBD reactor design used in this work, comprised of PMMA holders (1 and 7), a grounded aluminium electrode (2), O-rings (3), POM spacer (4), borosilicate glass dielectric (5), and high voltage stainless steel mesh electrode (6).

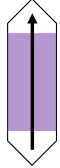
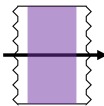
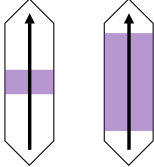
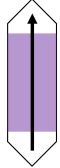
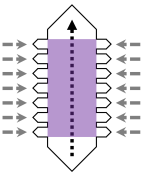
(5) (200x100x2.25 mm) (Borofloat, Glasatelier Saillaert) and a stainless steel mesh (6) (100x50 mm) were added on top of the spacer to complete the DBD configuration. Finally, a PMMA ‘top holder’ was added on top of the entire layer stack, featuring a rectangular access hole to connect the stainless steel mesh to the high voltage, and sixteen 5 mm holes around the edge of the holder to bolt everything airtight with sixteen M5 bolts.

### 6.2.2 Reactor configurations

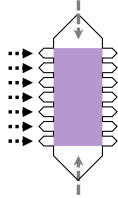
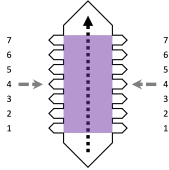
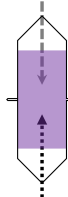
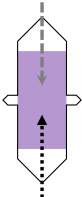
Different configurations have been tested in this work. Table 6.1 summarises all configurations with the abbreviation, a short description, a schematic picture, and the conditions being used.

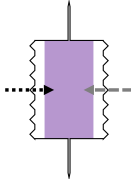
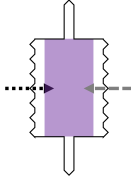
The standard operating conditions used in this work are a total flow rate of 50 mL/min consisting of a 1:1 CO<sub>2</sub>:CH<sub>4</sub> ratio, performed at 30 W (3 kHz) and 1 bar, a spacer thickness of 3.5 mm, and a 100x50 mm high-voltage electrode. This results in a residence time of 21 s, a specific energy input (SEI) of 36 J/mL (or 8.36 eV/molecule), and a power surface density (PSD) of 0.6 W/cm<sup>2</sup>. Variations to these parameters for the individual configurations will be listed in the results section.

**Table 6.1:** Different configurations used in this work with the associated abbreviation, short description, and schematic picture.

Configuration	Abbreviation	Description	Schematic picture	Conditions
Long (Benchmark)	L	Traditional long 'one inlet – one outlet' design, 1:1 DRM mixture fed through the bottom hole and exit via the top hole. This configuration acts as the benchmark for our results. Performed at standard conditions.		$P = 30 \text{ W}$ $\dot{V}_t = 50 \text{ mL/min}$ $\dot{V}_{CO_2} = 25 \text{ mL/min}$ $\dot{V}_{CO_2} = 25 \text{ mL/min}$
Short	S	Traditional 'one inlet – one outlet' design, but gas flow $90^\circ$ shifted, 1:1 DRM mixture fed through the 7 left side holes and exit via the 7 right side holes. This configuration evaluates the influence of a narrow vs wide geometry, while keeping the same residence time as in the long reactor. Performed at standard conditions.		$P = 30 \text{ W}$ $\dot{V}_t = 50 \text{ mL/min}$ $\dot{V}_{CO_2} = 25 \text{ mL/min}$ $\dot{V}_{CO_2} = 25 \text{ mL/min}$
Electrode length	25 50 75 100 (L)	Traditional long 'one inlet – one outlet' design, 1:1 DRM mixture fed through the bottom hole and exit via the top hole. The electrode length is varied by replacing the standard high-voltage electrode of the long reactor (100 mm) with electrode lengths between 25 and 75 mm.		$P = \text{variable}$ $\dot{V}_t = \text{variable}$ $\dot{V}_{CO_2} = \dot{V}_t/2 \text{ mL/min}$ $\dot{V}_{CO_2} = \dot{V}_t/2 \text{ mL/min}$
CO <sub>2</sub> :CH <sub>4</sub> ratio	1:0 6:1 3:1 1:1 (L) 1:3 1:6 0:1	Traditional long 'one inlet – one outlet' design, in which different gas mixing ratios are fed through the bottom hole and exit via the top hole. This configuration evaluates how different ratios show different conversions, because non-equimolar mixing will occur in the next configurations. Note that the 1:1 ratio is the same result as in the L configuration.		$P = 30 \text{ W}$ $\dot{V}_t = 50 \text{ mL/min}$ $\dot{V}_{CO_2} = \text{variable}$ $\dot{V}_{CO_2} = \text{variable}$
Long with gradual addition	LGA	Long reactor where the main gas (either CO <sub>2</sub> or CH <sub>4</sub> ; black arrow) enters from the bottom hole, with gradual addition of the secondary gas (grey arrows) through the 14 side inlets, and one combined exit at the top hole. This configuration allows for a constant addition of unreacted secondary gas. Performed at standard conditions; each side inlet thus receives a 14th of the individual flow rate.		$P = 30 \text{ W}$ $\dot{V}_t = 50 \text{ mL/min}$ $\dot{V}_{CO_2} = 25 \text{ mL/min}$ $\dot{V}_{CO_2} = 25 \text{ mL/min}$



Short with gradual addition	SGA	Short reactor where the main gas (either CO <sub>2</sub> or CH <sub>4</sub> ; black arrows) enters from the left 7 side holes, with gradual addition of the secondary gas through the top and bottom inlets (grey arrows), and one combined outlet stream via the 7 right side holes. Performed at standard conditions; each side inlet thus receives a 7th of the individual flow rate and the top and bottom inlet receive half the individual flow rate. (similar to LGA but 90° shifted)		$P = 30 \text{ W}$ $\dot{V}_t = 50 \text{ mL/min}$ $\dot{V}_{CO_2} = 25 \text{ mL/min}$ $\dot{V}_{CO_2} = 25 \text{ mL/min}$
Long with one side addition	1 2 3 4 5 6 7	Long reactor where the main gas (either CO <sub>2</sub> or CH <sub>4</sub> ) enters from the bottom hole, with side addition of the secondary gas through one of the 7 side inlet pairs (hence, always two at the same time), and one combined exit at the top hole. Early addition will show similar behaviour as the benchmark, while a delay of the secondary gas allows pre-activation of the main gas by the plasma. All positions for the side addition are tested individually, with the bottom side pair being "inlet 1" and the top side pair being "inlet 7". Performed at standard conditions; each side inlet being used thus receives half the individual flow rate.		$P = 30 \text{ W}$ $\dot{V}_t = 50 \text{ mL/min}$ $\dot{V}_{CO_2} = 25 \text{ mL/min}$ $\dot{V}_{CO_2} = 25 \text{ mL/min}$
Long with separate addition and narrow side outlets	LSN	Long reactor where one gas (either CO <sub>2</sub> or CH <sub>4</sub> ) enters via the top inlet and the other gas via the bottom inlet. The gases are allowed to react individually before mixing in the middle and exiting via two narrow side outlets (one at each side). Performed at standard conditions.		$P = 30 \text{ W}$ $\dot{V}_t = 50 \text{ mL/min}$ $\dot{V}_{CO_2} = 25 \text{ mL/min}$ $\dot{V}_{CO_2} = 25 \text{ mL/min}$
Long with separate addition and wide side outlets	LSW	Long reactor where one gas (either CO <sub>2</sub> or CH <sub>4</sub> ) enters via the top inlet and the other gas via the bottom inlet. The gases are allowed to react individually before mixing in the middle and exiting via two wider side outlets (one at each side). Performed at standard conditions.		$P = 30 \text{ W}$ $\dot{V}_t = 50 \text{ mL/min}$ $\dot{V}_{CO_2} = 25 \text{ mL/min}$ $\dot{V}_{CO_2} = 25 \text{ mL/min}$

Short with separate addition and narrow side outlets	SSN	Short reactor where one gas (either CO <sub>2</sub> or CH <sub>4</sub> ) enters via the 7 left inlets and the other gas via the 7 right inlets. The gases are allowed to react individually before mixing in the middle and exiting via narrow top and bottom outlets. Performed at standard conditions.		$P = 30 \text{ W}$ $\dot{V}_t = 50 \text{ mL/min}$ $\dot{V}_{CO_2} = 25 \text{ mL/min}$ $\dot{V}_{CO_2} = 25 \text{ mL/min}$
Short with separate addition and wide side outlets	SSW	Short reactor where one gas (either CO <sub>2</sub> or CH <sub>4</sub> ) enters via the 7 left inlets and the other gas via the 7 right inlets. The gases are allowed to react individually before mixing in the middle and exiting via wider top and bottom outlets. Performed at standard conditions.		$P = 30 \text{ W}$ $\dot{V}_t = 50 \text{ mL/min}$ $\dot{V}_{CO_2} = 25 \text{ mL/min}$ $\dot{V}_{CO_2} = 25 \text{ mL/min}$

### 6.2.3 Experimental set-up

The reactor used in this chapter was placed and tested in the same set-up as previous chapters, see description in chapter 2 and figure 6.2 for schematic representation.

The calculation of power (equation 2.5), energy cost (equation 5.9), and experimental error (equation 2.7) are analogue to section 2.2.1. Gas analysis was done analogue to chapter 5.

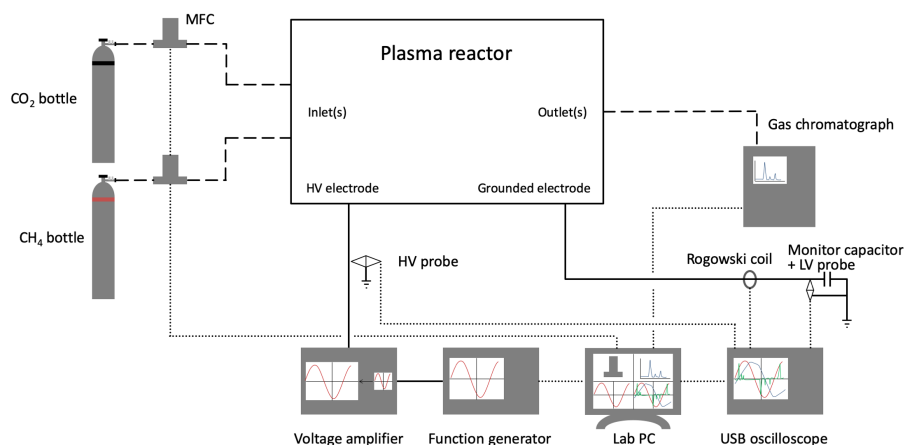


Figure 6.2: DBD plasma reactor set-up used in this work with analytical equipment.

## 6.3 Results

The results are split up into two sections to explore the possibilities of adding and mixing CO<sub>2</sub> and CH<sub>4</sub> in the reactor. First we will use the traditional ‘one inlet – one outlet’ design to set the benchmark for the rest of the paper, and investigate how the dimensions of the reaction zone and the power delivery to the reactor influence the performance. Next we will introduce gradual addition of one of the gas components to the reactor and survey the effect, including studying the impact of pre-activating the individual gases by the plasma and mixing them later in the reactor. All configurations will be tested at standard conditions (see section 6.2.2) unless stated otherwise.

### 6.3.1 One inlet – one outlet

#### 6.3.1.1 L and S configuration

The benchmark for this work is the most simple and traditional configuration, being the ‘one inlet – one outlet’ reactor in its lengthwise orientation (length > width), denoted as L, as shown in section 6.2.2. The benchmark conditions are 30 W, 50 mL/min of a 1:1 CO<sub>2</sub>:CH<sub>4</sub> mixture, and 1 bar for reactor dimensions of 100x50x3.5 mm. The results of this benchmark are shown in figure 6.3(a). Furthermore, its total conversion will also be plotted as a dotted line where applicable in any further figures, for reference. The CO<sub>2</sub> and CH<sub>4</sub> conversions are 12.9% and 14.6%, respectively, resulting in a total conversion of 13.7%. The main products formed are 6.0% H<sub>2</sub> and 6.4% CO, giving a H<sub>2</sub>:CO ratio of 0.94. This is a bit low to use this gas mixture (syngas) for Fischer-Tropsch synthesis, where a ratio close to 2 is more desirable [148]. Also, 0.094% ethene, 0.97% ethane, 0.16% propane, and 66 ppm ethanol were formed, as can be seen in figure 6.3(b), with the exact values listed in table E.4 in appendix E. In figure 6.3(c) we plot the uncalibrated products that were formed and detected on the TCD (propene) and FID. Because the response factor of an FID for non-oxygenated hydrocarbons is proportional to the number of C atoms in the molecule, we can cautiously compare all FID detectable components on a ‘mole equivalent basis’ by dividing the individual peak areas by their respective carbon number. We can see that the total CH<sub>4</sub>-equivalent peak area (i.e. a measuring stick of the total hydrocarbon fractions) is  $24.32 \times 10^4$ , with the

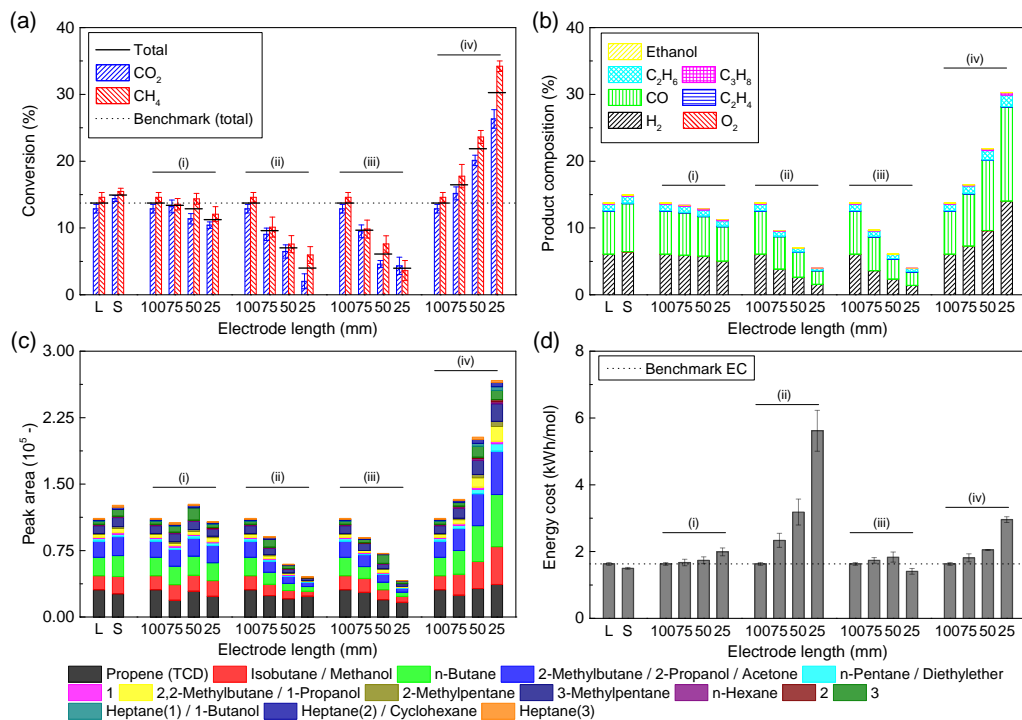


**Figure 6.3:** (a) CO<sub>2</sub>, CH<sub>4</sub>, and total conversion, (b) product composition, (c) peak areas of the uncalibrated gas components, and (d) energy cost of 1:1 DRM, plotted for different reactor geometries, i.e. the benchmark in the long (L) and short (S) configurations, the influence of the electrode length, (i) at constant power (30 W) and flow rate (50 mL/min), (ii) at constant residence time (21 s) and SEI (36 kJ/L), (iii) at constant flow rate (50 mL/min) and power surface density (0.6 W/cm<sup>2</sup>), and (iv) at constant power (30 W) and residence time (21 s). The total conversion of the 'L configuration' is also indicated with a dotted line, as the benchmark throughout all measurements. All exact values can be found in table E.4, table E.5, table E.6 and table E.3 in appendix E.

major products being C<sub>2</sub> hydrocarbons (83%), followed by C<sub>3</sub> hydrocarbons (10%), isobutane (2%), n-butane (2%), and 2-methylbutane (2%); see table E.6. All other detectable components have a share lower than 1%. Finally, we calculated the energy cost (EC), i.e. the amount of energy necessary to convert one mole of reactant mixture, and obtained a benchmark value of 1.63 kWh/mol.

A few modifications can easily be applied to the L configuration within the same operating window. This L configuration is characterised by a relatively long but narrow geometry, giving rise to a small cross-section and thus high gas velocity. A first modification is to shift the general flow of gases by 90 degrees, yielding a relatively short but wide geometry, including a wider gas inlet, so that the gas velocity will be much lower. As a result, the residence time is kept the same. This configuration with the same overall dimensions

(50x100x3.5 mm) is denoted as the S configuration and the results are also plotted in figure 6.3. Despite having the same operating conditions and thus the same power deposition and residence time, the S configuration shows a slightly improved performance on almost all aspects. The CO<sub>2</sub> and CH<sub>4</sub> conversion increases to 14.4% and 15.5%, respectively, resulting in a total conversion of 14.9%. The H<sub>2</sub> and CO concentrations increase to 6.4% and 7.2%, respectively, but their ratio slightly decreases to 0.90. The hydrocarbon production increases and shifts a bit more towards C<sub>3</sub> components. These observations are most likely an effect of the reduced gas velocity, giving more opportunity for diffusion and thus mixing of the products and remaining reactants, as all seven side-inlets are used here to ensure an even flow pattern through this bigger cross-section.

### 6.3.1.2 Effect of electrode length

Further modifications within the L configuration are realised by changing the electrode dimensions. Reducing the length of the electrode results not only in a smaller reaction volume, but also the residence time, SEI, and power surface density (PSD; i.e. power per HV electrode area) change. Therefore, we can investigate a few different scenarios by separately changing the plasma power and flow rate or keeping either or both constant. All conditions and associated parameters are listed in table 6.2.

The first scenario (i) investigates the balance of residence time and PSD. Decreasing the electrode length, while keeping the power and flow rate (and the resulting SEI) constant, results in a shorter residence time but also in a higher PSD. This might provide more powerful plasma micro-discharges, because the same amount of energy is applied on a smaller area (or in a smaller volume), and this might compensate for the shorter residence time. The results plotted in figure 6.3 show, however, that this is not the case as the total conversion (and thus also total product composition) decreases from 13.7% to 11.2% when the residence time decreases from 21 s to 5.25 s. Still, this is an interesting result, as the drop in conversion is much more limited than the drop in residence time. In our previous work, we investigated the influence of residence time on the conversion of CO<sub>2</sub> and CH<sub>4</sub> in the pure gases, as well as in the mixture (DRM) [56, 137] in a coaxial micro DBD reactor, by changing the flow rate while keeping the reaction volume constant. These results showed a more

**Table 6.2:** Conditions used when varying the electrode length. As the electrode becomes shorter, scenario (i) maintains a constant flow rate and power, thus yielding a shorter residence time but constant SEI and larger power surface density (PSD), scenario (ii) proportionally adapts the flow rate and power, to keep the residence time, SEI and PSD constant, scenario (iii) maintains a constant flow rate and uses a proportional power, so keeping the PSD constant, and scenario (iv) uses a proportional flow rate (to keep the residence time constant) and maintains a constant power (yielding a larger SEI and PSD). Note that the electrode length of 100 mm corresponds to the benchmark L configuration.

Scenario	Electrode length (mm)	Reaction volume (cm <sup>3</sup> )	Flow rate (mL/min)	Residence time (s)	Power (W)	SEI (J/mL)	PSD (W/cm <sup>2</sup> )
(i)	100 (L)	17.5	50	21	30	36	0.6
	75	13.125	50	15.75	30	36	0.8
	50	8.75	50	10.5	30	36	1.2
	25	4.375	50	5.25	30	36	2.4
(ii)	100 (L)	17.5	50	21	30	36	0.6
	75	13.125	37.5	21	22.5	36	0.6
	50	8.75	25	21	15	36	0.6
	25	4.375	12.5	21	7.5	36	0.6
(iii)	100 (L)	17.5	50	21	30	36	0.6
	75	13.125	50	15.75	22.5	27	0.6
	50	8.75	50	10.51	15	18	0.6
	25	4.375	50	5.25	7.5	9	0.6
(iv)	100 (L)	17.5	50	21	30	36	0.6
	75	13.125	37.5	21	30	48	0.8
	50	8.75	25	21	30	72	1.2
	25	4.375	12.5	21	30	144	2.4

pronounced drop in conversion upon shortening the residence time, compared to the trend seen here. To investigate this in more detail, we performed similar experiments as in [56, 137] in the present reactor configuration, with a fixed electrode length of 100 mm and a wide range of flow rates, to vary only the residence time while keeping the PSD constant. The results confirm the trend obtained in our previous work, as can be seen in figure 6.4. We see a steady decrease of the conversion for shorter residence times, reaching about 14% at 21 s and only 4% conversion at 5.25 s, which is indeed much more pronounced than in the experiments of scenario (i). Therefore, the higher PSD of scenario (i) in fact results in an enhanced plasma discharge, because the drop was less pronounced than when only varying the residence time, but it cannot entirely compensate for the shorter residence time to provide a better conversion. Since the SEI remains constant in this scenario and the conversion slightly decreases, the EC increases accordingly, up to 2.0 kWh/mol (see figure 6.3(d)).

The second scenario (ii) keeps the residence time constant as the electrode gets shorter (i.e. by lowering the flow rate), while also maintaining a constant SEI (i.e. by lowering the power and thus also maintaining a constant PSD). Theoretically,

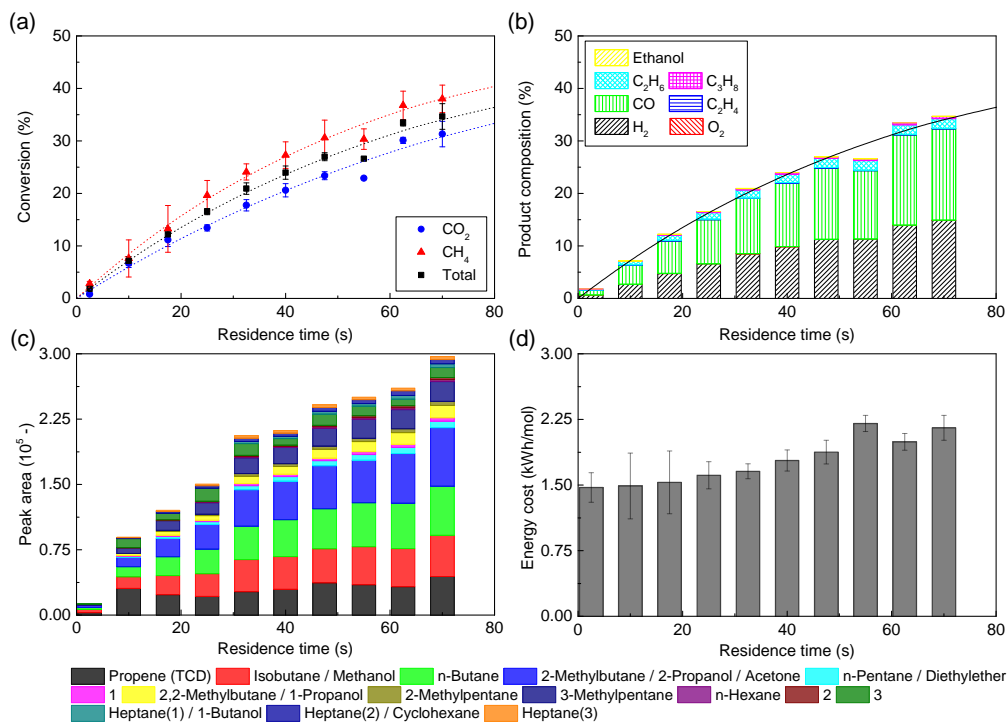


**Figure 6.4:** (a)  $\text{CO}_2$ ,  $\text{CH}_4$ , and total conversion, (b) product composition, (c) peak areas of the uncalibrated gas components, and (d) energy cost for 1:1 DRM, plotted as a function of residence time in the benchmark ‘L’ reactor at 30 W, by changing the flow rate. All exact values can be found in table E.4, table E.5, table E.6, and table E.3 in appendix E.

this results in identical cases as the benchmark, with only the gas velocity being different because only the electrode length is reduced but the width is kept constant. The results in figure 6.3 show that the drop in power is much more dominant in determining the conversion than the drop in flow rate, at constant SEI and PSD. It has indeed been shown before that the SEI is not always the best “determining parameter” for the energy input [38], although it is commonly used in plasma-based gas conversion [8]. Therefore, the total conversion drops almost linearly from 13.7% to 4%, when the power drops from 30 to 7.5 W, in spite of the constant residence time, SEI, and PSD. Consequently, the product composition decreases for all components (see figure 6.3(b,c)), and the EC rises by the same factor, to 5.6 kWh/mol (see figure 6.3(d)).

Scenario (iii) maintains a constant flow rate as the electrode becomes shorter, resulting in a shorter residence time, while lowering the power to keep a constant PSD. As a result, the SEI decreases by a factor of four. Both the shorter residence

time, as well as the lower power, result in a large decrease in total conversion, from 13.7% to 4%. Surprisingly, these results are comparable to those from scenario (ii) despite using higher flow rates. The EC is slightly lower, because the SEI drops a bit faster than the conversion.

Finally, scenario (iv) evaluates the last combination of maintaining a constant power and adjusting the flow rate to keep the residence time constant. As a result, both the SEI and PSD increase by a factor four. The results in figure 6.3 show an increase in total conversion from 13.7% to 30%. Note, however, that this is an increase by only a factor 2.2, while the SEI and PSD increase by a factor 4. This means that almost half of the energy is wasted, resulting in a higher EC of 2.96 kWh/mol. Due to the higher conversion, more products are formed, mainly H<sub>2</sub> and CO (a bit more H<sub>2</sub>, thus enhancing the H<sub>2</sub>:CO ratio to 0.99), and shifting the hydrocarbons towards C<sub>3</sub>.

In summary, concentrating the same amount of power on a smaller electrode, while maintaining the same gas flow rate (scenario i), is not able to improve the conversion, because the higher PSD cannot compensate for the shorter residence time. Also, the power has a more important effect than the flow rate in determining the SEI, but no reduced EC values were found despite enhanced conversions.

### 6.3.1.3 Effect of gas mixing ratio

Finally, we investigated the effect of different gas mixing ratios in the ‘one inlet – one outlet’ reactor. We performed these experiments to compare with the results of the multiple inlets and outlets, where we gradually add the second gas (either CO<sub>2</sub> or CH<sub>4</sub>) or have separate injection of CO<sub>2</sub> and CH<sub>4</sub>, so that different parts of the reaction zone will exhibit different gas mixing ratios, varying actually between pure CO<sub>2</sub> and pure CH<sub>4</sub>. Of course, reactions and diffusion of the produced components will occur at every point in the reactor, so the present measurements render somewhat idealised conditions, but are still interesting to study.

Figure 6.5 shows the results for different CO<sub>2</sub>:CH<sub>4</sub> ratios performed at the standard conditions. Pure CO<sub>2</sub> has a base conversion of 6% and results exclusively in stoichiometric O<sub>2</sub> and CO fractions of 2.10% and 4.20%, respectively. Adding CH<sub>4</sub> to the mixture (6:1 ratio) results in a large increase of



the CO<sub>2</sub> conversion to 13%, combined with a large CH<sub>4</sub> conversion of 24.5%, giving an overall conversion of 14%. As a consequence, we see an enhanced CO fraction of 9.06% but only 0.04% O<sub>2</sub> due to further reactions with CH<sub>4</sub>-derived products. In addition, we also produce 5.1% H<sub>2</sub>, 0.26% ethane, 0.012% propane, and 0.208% ethene. The product share based on the total mole equivalent of the FID peak areas shows the C2 hydrocarbons indeed as the dominant hydrocarbon product (92%), followed by C3 hydrocarbons (2%), isobutane (2%), n-butane (1%), and 2-methylbutane (1%).

Gradually adding more CH<sub>4</sub> first enhances the CO<sub>2</sub> conversion up to a maximum of 15% (3:1 ratio), but then it decreases back to 6.3% (1:6 ratio). The CH<sub>4</sub> conversion, on the other hand, steadily decreases towards 7.3% in the pure CH<sub>4</sub> plasma. As a result, the total conversion shows a slight improvement and a maximum at the 3:1 ratio, followed by a steady decrease. The product distribution therefore shifts as more CH<sub>4</sub> is added. The CO fraction gradually decreases from 8.8% (3:1 ratio) to 0% (0:1 ratio), while the O<sub>2</sub> fraction remains near 0% and the H<sub>2</sub> fraction slightly increases to a maximum of 6.1% (1:3 ratio), followed by a decrease to 5.0% (0:1 ratio). The fraction of calibrated hydrocarbons slowly increases towards pure CH<sub>4</sub> where they reach their maximum values of 1.57% ethane, 0.42% propane, and 0.208% ethene. The product distribution of all FID detectable products therefore shifts towards higher carbon numbers with 72% C2, 17% C3, 2% isobutane, 5% n-butane, and 2% 2-methylbutane.

These results are consistent with our previous work on the kinetics and equilibria in CO<sub>2</sub>:CH<sub>4</sub> plasmas (see chapters 4 and 5), where we found that CO<sub>2</sub> dissociation has a relatively high reaction rate coefficient but a low equilibrium conversion, while CH<sub>4</sub> has a relatively low reaction rate coefficient but a higher equilibrium conversion. This results in similar conversions at the moderate residence time of 21 s, but boosts the total conversion when both of them are combined. More CO<sub>2</sub> effectively promotes the overall reaction rates and thus the conversion, while more CH<sub>4</sub> effectively promotes the equilibrium conversion. This results in a balance of two effects, with apparently CO<sub>2</sub> being slightly dominant in this set-up and conditions, shown by the optimal conversion at a 3:1 (or even 6:1) ratio.

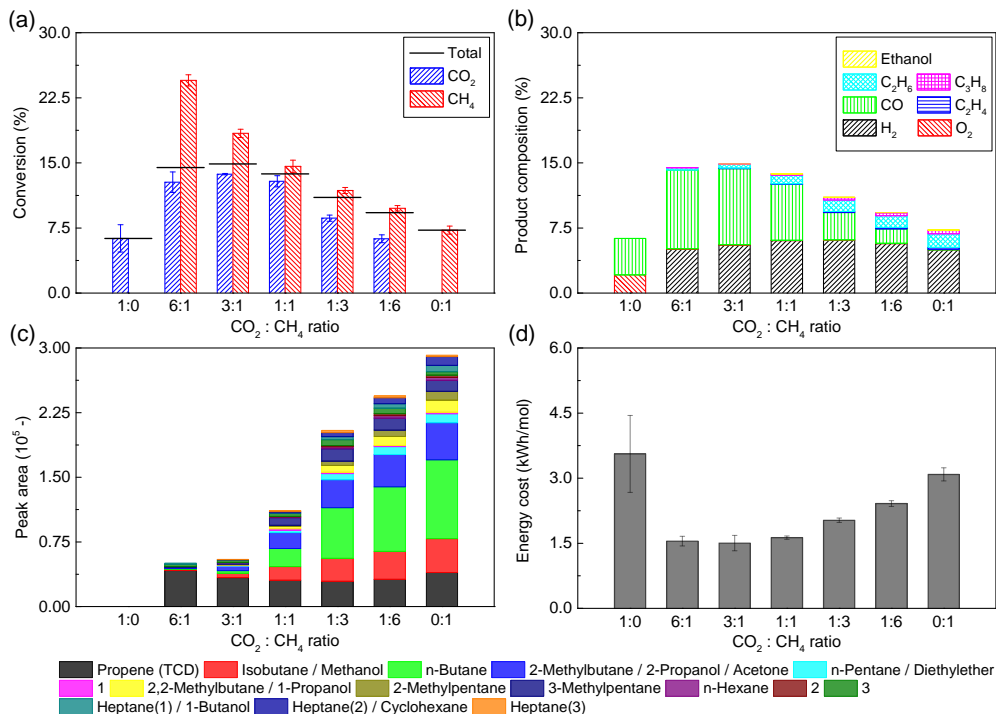


**Figure 6.5:** (a)  $\text{CO}_2$ ,  $\text{CH}_4$ , and total conversion, (b) product composition, (c) peak areas of the uncalibrated gas components, and (d) energy cost, plotted for different  $\text{CO}_2:\text{CH}_4$  ratios varying between pure  $\text{CO}_2$  and pure  $\text{CH}_4$ , in the benchmark ‘L’ reactor at 30 W and 50 mL/min total gas flow rate. All exact values can be found in table E.4, table E.5, table E.6, and table E.3 in appendix E.

As  $\text{CH}_4$  was found to be almost exclusively the hydrocarbon source, optimal hydrocarbon production is therefore only present at higher  $\text{CH}_4$  ratios, while conversion-wise, figure 6.5 shows that it is indeed more beneficial to operate at  $\text{CO}_2:\text{CH}_4$  gas ratios around 6:1 to 3:1. This is also reflected in slightly lower EC-values of 1.5 kWh/mol, as seen in figure 6.5(d).

### 6.3.2 Multiple inlets and outlets

When multiple elementary reactions occur in a reactor, i.e. reactions in parallel or in series, immediate mixing of the reactants and feeding them in the reactor might not be the most desirable way [79]. Therefore, it can be beneficial to gradually add one of the reactants in order to keep its local concentration low in the reactor, or to introduce both gases at separate locations, so that they can be pre-activated by the plasma before mixing. These effects will be explored below.

### 6.3.2.1 Gradual addition of one of the gases

Gradual addition of one of the reactants can be done in our reactor in two ways. The first, denoted by LGA, is gradual addition in the long pathway orientation (similar to configuration L) by using the bottom hole as the main gas inlet, the fourteen side holes as the inlets of the gradually added gas, and the top hole as the outlet (see section 6.2.2). The other way, denoted by SGA, is the equivalent short S configuration by using the left seven holes as the main gas inlet, the top and bottom holes as the inlet of the second gas, and the right seven holes as the outlets. Figure 6.6(a, c, e, and g) shows the result of these configurations where  $\text{CO}_2$  is introduced as the main gas and  $\text{CH}_4$  as the added gas.

We see that the LGA configuration only slightly improves the total conversion to 14.2% (compared to 13.7% for the benchmark L configuration), which is mainly attributed by the enhanced  $\text{CH}_4$  conversion. As a result, primarily the amount of hydrocarbons increases among all products formed. The SGA configuration with its inherent lower gas velocity, however, did improve the performance significantly to 19.2%, resulting in a rise for all products and the lowest EC in this work (1.17 kWh/mol; see figure 6.6(g)).

Introducing  $\text{CH}_4$  as the main gas and  $\text{CO}_2$  as the gradually added gas, shows totally different results, see figure 6.6(b, d, f, and h). We now also see improved conversion for the LGA configuration (18.3%), and consequently also increased product formation. Compared to the benchmark conversion of 13.7% for the L configuration, and the marginally improved LGA conversion of the reverse gas configuration (14.2%), this is a big leap forward by just mixing the gases differently. Apparently it is preferred to use  $\text{CH}_4$  as the main gas and keep  $\text{CO}_2$  at lower local concentrations. Indeed,  $\text{CH}_4$  will start to become dissociated at the beginning of the reactor at low local  $\text{CO}_2:\text{CH}_4$  ratios, by electron impact reactions, and possibly also upon reaction with the  $\text{CO}_2$  that is gradually being introduced. When  $\text{CH}_4$  travels further in the reactor, and becomes further converted, while gradually more  $\text{CO}_2$  will be mixed in, the gas ratio will shift above one and boost the  $\text{CO}_2$  conversion, in agreement with the results presented in figure 6.5. This results in a higher overall conversion. The reverse configuration, i.e. with  $\text{CO}_2$  as the main gas, starts out at the more optimal gas mixing ratios, but when  $\text{CO}_2$  is being converted, the ratio drops below one, resulting in a lower total conversion, as depicted in figure 6.5. Although both

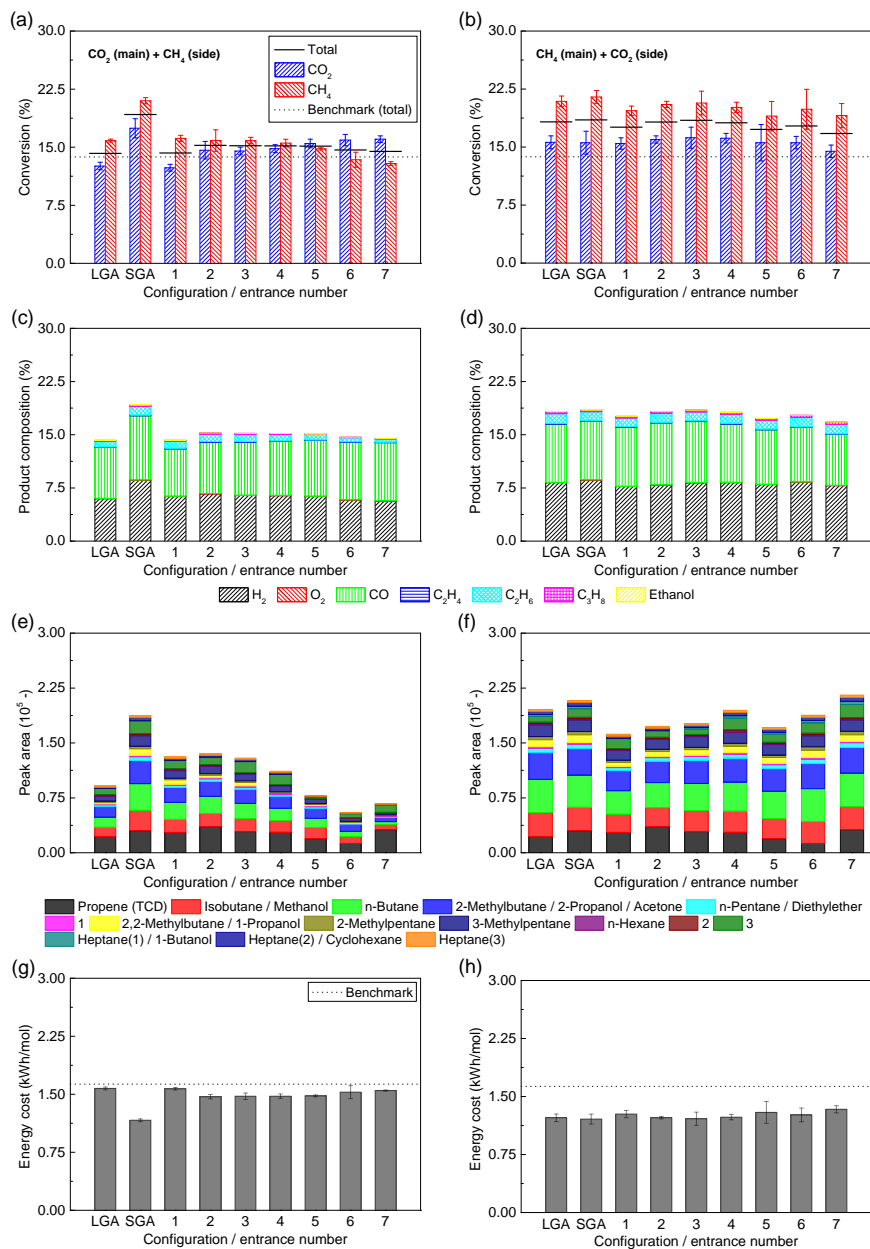


**Figure 6.6:** (a and b) CO<sub>2</sub>, CH<sub>4</sub>, and total conversion, (c and d) product composition, (e and f) peak areas of the uncalibrated gas components, and (g and h) energy cost of 1:1 DRM, plotted for different reactor configurations (see text and table 6.1). In (a, c, e, and g) CO<sub>2</sub> is the main gas and CH<sub>4</sub> is the side-added gas, while in (b, d, f, and h) CH<sub>4</sub> is the main gas and CO<sub>2</sub> is the side-added gas. All experiments are performed at 30 W and 50 mL/min total gas flow rate. All exact values can be found in table E.4, table E.5, table E.6, and table E.3 in appendix E.

configurations appear similar, our results demonstrate that one is preferred over the other. Comparing both LGA configurations with the SGA configurations suggests that there is a time or velocity dependent factor that is dependant on the gas configuration being used.

Evidently, the gradual addition of one of the components seems useful to improve the total conversion of a DBD plasma reactor. Detailed knowledge on the chemical kinetics, e.g. by numerical modelling [86,146], could help in designing to most optimal configuration.

### 6.3.2.2 Introducing both gases at separate locations to allow pre-activation in the plasma

**Side addition** In DRM, a direct collision between  $\text{CO}_2$  and  $\text{CH}_4$  will not result in a reaction between both molecules [86,146].  $\text{CO}_2$  will mainly dissociate in CO and O (although reactions with  $\text{CH}_2$  to  $\text{CH}_2\text{O}$  are also possible), while  $\text{CH}_4$  will mainly dissociate in  $\text{CH}_3$  and H (and other  $\text{CH}_x$  radicals), and these products will react with each other into (oxygenated) hydrocarbons [145]. Therefore, it might be beneficial to pre-activate the reactants, to generate reactive or excited species, or intermediate products, before mixing them together. We will first explore this concept by introducing the main gas through the bottom hole, and the second gas through one pair of the seven side inlet pairs. This allows us to vary the amount of pre-activation of both gases.

In figure 6.6(a, c, e, and g) we can see the results for  $\text{CO}_2$  as the main gas and  $\text{CH}_4$  as the added gas at the different inlets. The later  $\text{CH}_4$  is added to the reactor, the more  $\text{CO}_2$  is converted (12.4% for side inlets 1, vs. 16.0% for side inlets 7) while less  $\text{CH}_4$  is converted (16.1% vs. 12.9%). This can be explained by the individual residence times in the reactor, confirmed by computational fluid dynamics (CFD) simulations and similar experimental E-curve measurements for the residence time distribution (RTD) [79], see appendix E for the principle and detailed results. Note that we will have (much) higher residence times in the experimental measurements because of delays due to tubing and the trace analyser (an MS in these RTD tests). Consequently, we cannot directly compare the experimental RTD to those simulated, but we can compare at best the relative trends (i.e. time differences between side inlets 1 and 7). The simulated average residence time when using the first side inlets is about 21 s for both gases, while it

is about 39 s for CO<sub>2</sub> and 4 s for CH<sub>4</sub> when using the last side inlets (see table E.2 in appendix E.1.4). This also yields an average overall residence time of 21 s. Experimentally we also see a decrease in residence time from 99.1 s (for side inlets 1) to 66.7 s (for side inlets 7) for CH<sub>4</sub>. In both cases, i.e. simulations and experiments, the CH<sub>4</sub> residence time is of course much shorter for side inlets 7 compared to side inlets 1, because of the shorter path from inlet to outlet (25 mL/min over short reaction volume), while the CO<sub>2</sub> residence time is longer, because of the lower gas velocity (25 mL/min over almost all reaction volume). It is quite surprising that, even at these very short residence times for CH<sub>4</sub>, this gas still reaches a relatively high conversion.

Although both individual conversions shift (up for CO<sub>2</sub> and down for CH<sub>4</sub>) when the side inlets are further away from the bottom inlet, the total conversion stays constant within the error bars and is about the same as the LGA configuration. Thus, based on the conversion, the product distribution, and the EC, as seen in figure 6.6(a, c and g), we can conclude that it does not really matter which side inlet is used. Only slightly more CO (8.2% vs. 6.7%) and slightly less H<sub>2</sub> (5.7% vs. 6.3%) is produced when CH<sub>4</sub> is introduced later in the reactor (inlets 7 vs. inlets 1). The main effect of changing the inlet position is found in the amount and distribution of hydrocarbons produced, as seen in figure 6.6(e). Indeed, the amount of hydrocarbons produced is reduced by a factor two, and the distribution shifts towards lower carbon numbers when CH<sub>4</sub> is introduced later in the reactor.

Changing the gas flow to CH<sub>4</sub> as the main gas and CO<sub>2</sub> as the added gas from the side inlets, gives totally different results, as can be seen in figure 6.6(b, d, f, and h). Again, the average residence times vary a lot, being 21 s vs. 38 s for CH<sub>4</sub> (main gas) and 22 s vs. 4 s for CO<sub>2</sub> (added gas), for inlets 1 to 7, respectively, based on our CFD simulations. Experimentally, we see a decrease from 100.2 s to 80.8 s for CO<sub>2</sub>. Despite this difference in residence times, the conversions, CO and H<sub>2</sub> formation, and the EC seem to be relatively constant, irrespective of the inlet pair being used, and very similar to those in the LGA and SGA configuration. Again, with the very short residence time of the added gas (i.e. CO<sub>2</sub> here), it is still possible to obtain 15.5% CO<sub>2</sub> conversion. In addition, no significant amounts of O<sub>2</sub> are present in the outlet, indicating that almost all O atoms react within a short time with the CH<sub>4</sub>-derived products. Only slight differences are seen in

the hydrocarbon production, which increases slightly and the distribution shifts a bit more to C3, upon introducing CO<sub>2</sub> later in the reactor.

These results are rather peculiar. First, the high conversion (of both CO<sub>2</sub> and CH<sub>4</sub>) when introducing this gas at side inlets 7, corresponding to a short residence time (3-4 s predicted by the CFD simulations), suggests that either the conversion starts early and saturates after some time (but this contradicts the data from figure 6.4 and from model calculations [146]), or more mixing is present due to higher diffusion coefficients. Secondly, the total conversion appears constant, irrespective of which side inlet is used, and furthermore, also the individual conversions are constant when CH<sub>4</sub> is the main gas, which is a bit unexpected. It is hard to know exactly how gas fractions shift along the reactor due to individual conversion, mixing, and reacting further on. Perhaps the local CO<sub>2</sub>:CH<sub>4</sub> ratios are accidentally in the perfect range for high reaction rates, resulting in unusually high conversion at short residence time. Further investigations with spectroscopic techniques are needed to uncover this phenomenon.

***Separate pre-activation zones*** We further investigate the concept of gas pre-activation with the extreme case of opposite inlets, yielding purely individual plasma activation zones for CO<sub>2</sub> and CH<sub>4</sub>, that only mix right at the end. In practice, we use the bottom hole of the reactor as the inlet for the first gas, the top hole as the inlet of the second gas, and the centre side holes (see table 6.1) as the outlets. By changing the width of the outlets, we influence the size of the mixing zone. This yields a long reactor either with narrow or wide outlets, denoted as LSN and LSW, respectively (see table 6.1). In addition, we shift the inlets and outlets by 90 degrees, resulting in a short reactor with narrow and wide outlets, denoted as SSN and SSW, respectively.

Figure 6.7 shows that the LSN configuration performs a bit better than the benchmark L configuration, i.e. the total conversion reaches 14.7% compared to 13.7% in the benchmark. This is due to a higher CH<sub>4</sub> conversion, while the CO<sub>2</sub> conversion stays the same. Enlarging the mixing zone in the LSW configuration slightly enhances the CO<sub>2</sub> conversion but reduces the CH<sub>4</sub> conversion, resulting in a small drop of the total conversion to 14%.

Using the 'short' orientation of the reactor again results in slightly better results. The SSN configuration reaches a total conversion of 16%, while the SSW

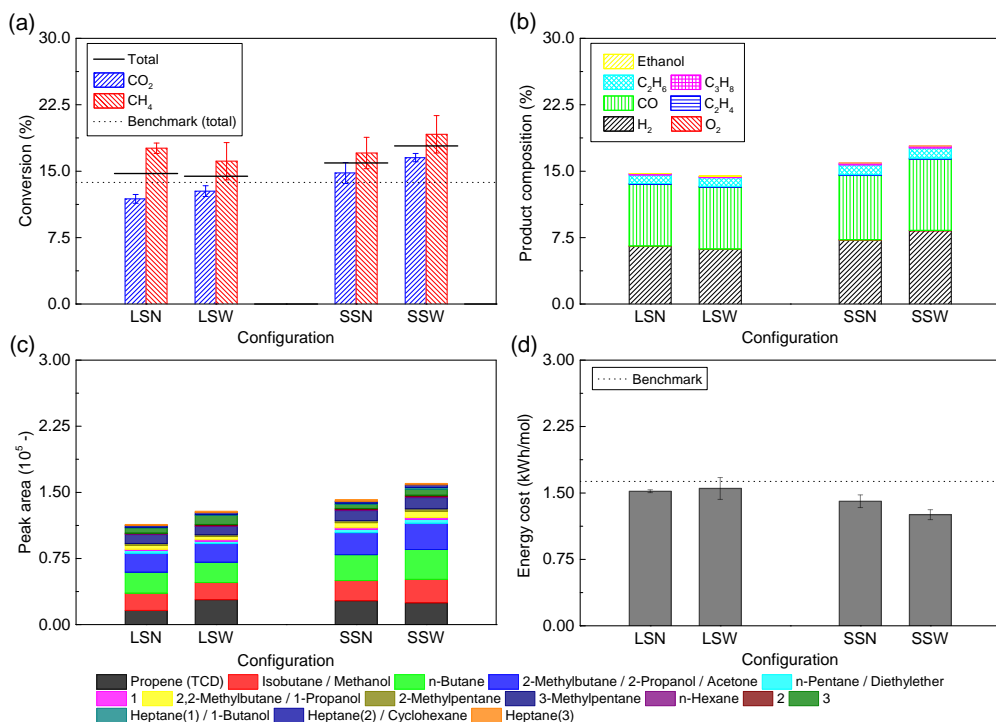


**Figure 6.7:** (a)  $\text{CO}_2$ ,  $\text{CH}_4$ , and total conversion, (b) product composition, (c) peak areas of the uncalibrated gas components, and (d) energy cost of 1:1 DRM, plotted for different reactor configurations, where  $\text{CO}_2$  and  $\text{CH}_4$  are inserted through opposite inlets and are separately activated in the plasma before mixing. For the exact configuration, see table 6.1. All experiments are performed at 30 W and 50 mL/min total flow rate. All exact values can be found in table E.4, table E.5, table E.6, and table E.3 in appendix E.

configuration performs even better, with 18% total conversion. This is probably again due to the lower gas velocity, but in addition, the S orientation allows for a larger mixing zone, resulting in more conversion upon mixing, at the more optimal ‘around 1:1’ ratios. It is interesting to note that even these short mixing zones allow sufficient reaction between the  $\text{CO}_2$  and  $\text{CH}_4$  decomposition products, as is evident by the lack of  $\text{O}_2$  in the outlet.

Finally, we see somewhat higher product formation, and the product ratios slightly shift towards higher carbon numbers, while the energy cost drops to 1.26 kWh/mol.



## 6.4 Discussion

The results in section 6.3 have shown that definite improvements on both conversion and product composition are possible by changing the reactor geometry. The most likely optimal configuration would be an SGA reactor with optimised (more) side-inlets, preferably with CH<sub>4</sub> as the main gas and CO<sub>2</sub> as the co-reactant. Extra tests with slightly altered CO<sub>2</sub>:CH<sub>4</sub> mixing ratio towards 3:1 could improve the conversion even more.

A lot of research has been performed on improving the performance of DBD reactors through different strategies, but to our knowledge with no major steps forward of bringing DBD plasma technology closer to industrial use (e.g. [38,39,58,68,70,72,74,84,92,151,154,155]). The hypothesis of our work was that more drastic improvements to the reactor design could offer a leap forward to further advance from. We have shown how reactor geometry and gradual addition of the reactant gases can significantly alter the performance of a DBD plasma reactor and the product composition, while still using the same feed, but the actual conversion and energy cost improvements are still limited compared to the reference reactor. Therefore, we have to conclude that despite the interesting findings of our work, even bigger improvements are required to make DBD plasma-based DRM a competing technology.

The question arises whether knowledge from this work can be transferred to other gas mixtures. Our findings from section 6.3.1 can indeed be transferred, because in these configurations fundamental “plasma properties”, i.e. reaction time and plasma density, are varied. Our findings from section 6.3.2, on the other hand, apply to individual reactions and mixing behaviours of the individual gasses, and therefore, these results cannot simply be transferred to other chemical conversions. For instance, we evaluated the same configuration of section 6.3.2 to an N<sub>2</sub>/H<sub>2</sub> plasma for NH<sub>3</sub> synthesis, and found no positive effects of varying the configurations, see chapter 7. This can be explained because pure N<sub>2</sub> and H<sub>2</sub>, occurring in their separate reaction zones before mixing, do not generate long-living products, but only short-living atoms, ions and excited species. Therefore, any moment they are not mixed, power and residence time are wasted, resulting in decreased conversions. Thus, non-reactive molecules will not benefit from any time not being mixed. However, in the case of reactive molecules, the general idea that alternative gas mixing can optimise performance is still valid, but the

actual changes will depend on the specific chemistry.

The exact origin of the changes in reactor performance observed in this work is still not entirely understood. How do these different configurations influence the reaction kinetics and equilibrium position? In chapters 4 and 5 we developed a method of retrieving more fundamental kinetics data on plasma reactor performance, by recording the conversion over an extended residence time range. Fitting these data by a generalised fit equation reveals the overall rate coefficient, its individual loss and formation components, and the position of the so-called 'partial chemical equilibrium'. We applied this method in figure 6.4, for the L-configuration, to test whether changing the residence time by means of the flow rate is equal to changing it by means of the reactor length. Following the procedure of our previous DRM kinetics work [137], this L-configuration yields an overall reaction rate coefficient of  $0.015\text{ s}^{-1} \pm 0.004\text{ s}^{-1}$ , with equilibrium conversion around 53%. These values are lower than for the coaxial micro-DBD reactor studied in [137] ( $0.088\text{ s}^{-1} \pm 0.003\text{ s}^{-1}$  and  $75.4\% \pm 0.6\%$  for 1:1  $\text{CO}_2:\text{CH}_4$  ratio), due to the bigger gap size. This method is very time-consuming, because it requires studying at multiple and long residence times, so it is beyond the scope of this paper, but in the future we might be able to apply such a study to the various reactor configurations in this paper, with the aim to reveal the more precise nature of the altered reactor performance, i.e. changes in rate coefficients and/or position of the equilibrium.

When looking for the industrial application of alternative reactor configurations, and perhaps also other types of plasma reactors, we have to consider several different aspects. Chemically speaking, the configuration yielding the highest conversion at the lowest energy cost is the most optimal configuration for scaling-up to higher throughputs. However, from an engineering point of view, we need to focus our attention to the performance vs. complexity balance, when looking at scale-up possibilities. Indeed, the added complexity of the novel design must be small enough, so that it does not counteract the performance enhancement. At this moment, the most suitable method for allowing more throughput in DBD reactors is scaling the length and width (or tube circumference for co-axial design) of the reactor, and/or putting multiple units in parallel. It is important to realise that the gap dimension has to stay within the micrometre to millimetre range, to limit the required discharge

voltage. Taking this aspect into account, it seems that the extra complexity of adding multiple side inlets to an already semi-complex parallel multi-DBD device, such as the industrial ozone generators [37], may not outweigh the performance benefits. An economical and engineering analysis should be made to evaluate whether the standard ‘one inlet – one outlet’ configuration would still remain the best option or whether multiple side inlets would be feasible for up-scaling.

In general, it may well be that other plasma reactor types, besides DBD, are more promising for DRM, more specifically gliding arc plasmas [144,156,157], as well as microwave plasmas [158–164], nanosecond pulsed plasmas [165], and atmospheric pressure glow discharges [34] (based on the good results obtained for CO<sub>2</sub> splitting). Indeed, these so-called warm plasmas exhibit much higher energy efficiency (see detailed assessment in [8]). The reason is that they are characterised by higher populations of the vibrationally excited levels, which provide the most efficient dissociation pathway, and they operate at higher temperatures, so that the thermal dissociation reactions are also faster. On the other hand, the higher temperature also reduces the overpopulation of the vibrational levels. Moreover, it is less straightforward to integrate catalysts in these warm plasmas, due to their higher temperatures; hence, for plasma catalysis, DBD plasmas are much better suited.

We believe that overall the optimal plasma reactor should combine a high conversion with high energy efficiency, and be compatible with catalysts, to provide high product selectivity. The conversion should be enhanced by increasing the fraction of gas treated by the plasma, i.e. by smart plasma reactor design (including gas inlet/outlet), based on fluid dynamics simulations, as demonstrated partly in this paper, as well as in e.g. [34,166].

As far as the energy efficiency is concerned, in theory, the highest values can be reached when the reduced electric field (i.e. electric field divided by gas number density, typically expressed in Townsend, with  $1 \text{ Td} = 10^{-21} \text{ Vm}^2$ ) in the plasma is around 50 Td or below, combined with a high plasma power (to maximise vibrational excitation) and with a low gas temperature (to minimise vibrational losses upon collision with other gas molecules), or in other words, a strong vibrational-translational (VT) non-equilibrium [135]. However, both experiments and modelling have revealed that in warm plasmas at

(sub)atmospheric pressure the conversion proceeds mainly by thermal reactions, and the vibrational distribution is in equilibrium with the gas temperature (VT equilibrium) [135, 158–163, 167, 168]. DBD plasmas operate at much lower temperature, so they could in theory give rise to more pronounced VT non-equilibrium, if they can operate at a reduced electric field that promotes vibrational excitation. However, DBD reactors typically operate at reduced electric fields above 200 Td, where the electron energy is rather used for other processes than vibrational excitation of the molecules. Hence, major research efforts should be devoted, e.g. by designing new power supplies, to tune DBD conditions into producing the right reduced electric field (and thus electron energy) for maximising vibrational excitation. This is, however, beyond the scope of our present paper.

Finally, in terms of product selectivity, when targeting higher hydrocarbons or oxygenates, the plasma will need to be combined with catalysts, because otherwise the DRM reaction will mainly produce syngas. For this purpose, plasma reactors must be designed to enable optimised transport of plasma species to the catalyst surface, and DBD plasmas are in general most suited for this. However, in addition, catalysts must be developed which are suited for surface reactions of reactive plasma species (i.e. radicals, electronically and vibrationally excited molecules, electrons, ions). These catalysts are most likely different from thermal catalysts. Therefore, more insight in the plasma-catalyst interactions is crucial for designing catalysts tailored to the plasma environment [67, 169].

In conclusion, plasma-based DRM is quite promising, but the complex mechanisms require more fundamental investigations towards the optimum plasma reactor configuration. We believe that modelling-based plasma reactor design is key to realise these goals.

## 6.5 Conclusion

In this paper we present a novel multi-inlet/outlet parallel plate DBD plasma reactor that we have designed to achieve different gas flow and mixing patterns, and to quickly change the geometry of the reaction volume. This allows us to investigate how the shape and length of the reaction zone, gradual gas addition, and the method of mixing CO<sub>2</sub> and CH<sub>4</sub> can influence the conversion, energy

cost, and product composition of dry reforming of methane (DRM).

First we presented the results of a benchmark reactor (long pathway L configuration, with one inlet and outlet for both gases combined), yielding a total conversion of 13.7%. Using the same reactor dimensions but in the short orientation (S configuration) can slightly improve the conversion up to 14.9%, which is attributed to the lower gas velocities (allowing more reaction of the plasma components) as a result of the wider cross-section, because all other parameters, including the residence time, are kept constant.

Subsequently we modified the length of the reaction zone by changing the electrode length, and we varied the operating parameters (total gas flow rate and power), resulting in various parameters being kept constant or varied, i.e. residence time, specific energy input (SEI), and power surface density (PSD). Concentrating the same amount of power on a smaller electrode (hence higher PSD), while maintaining the same flow rate (constant SEI, but shorter residence time), cannot improve the conversion, because the higher PSD cannot compensate for the shorter residence time. Further permutations of flow rate and power, by either proportionally varying them or keeping them constant, thereby affecting the residence time, SEI, and PSD, showed that the power has a more important effect than the flow rate in determining the SEI. The same power and residence time, but shorter electrode length and thus higher PSD, significantly enhanced the conversion (up to 30% for an electrode length four times smaller than the standard length, i.e. 25 vs. 100 mm), but at the expense of a higher energy cost (i.e. 2.96 kWh/mol at 25 mm electrode length, and 1.63 kWh/mol at 100 mm electrode length).

Varying the  $\text{CO}_2:\text{CH}_4$  ratio in the standard (benchmark) geometry revealed that the optimum ratio is between 6:1 and 3:1, and up to 1:1, due to more optimal kinetics at these ratios. This information was very valuable to investigate the effect of both separate and gradual addition of one of the gases. Indeed, the latter shifts the local gas mixing ratios while still maintaining an overall 1:1 ratio as input in the reactor.

Our results show that gradual addition of one of the gases, i.e. via 14 side inlets along the length of the reactor, improves the conversion, but the extent of the improvement highly depends on which gas is used as main gas and added gas (generally higher with  $\text{CH}_4$  as main gas), as well as on the long (LGA) or

short (SGA) orientation of the reactor (effect by  $\text{CO}_2$  as main gas). Pre-activation of the main gas, by delaying a separate side addition of the other gas via one pair of side inlets, showed improvements when  $\text{CH}_4$  was used as the main gas, although we did not see a significant influence of the position of the inlet. Total conversions up to 19.2% were obtained in this way at the same standard conditions as the benchmark (yielding only 13.7%), while the EC was improved in the same way, from 1.63 kWh/mol for the benchmark, down to 1.17 kWh/mol for these modifications of gradual or separate gas addition through only one set of inlets.

Finally, pre-activation of the separate gases by using inlets from opposite sides in the reactor, with last-minute mixing of the products, was evaluated as an extreme case of separate addition. Improved conversions up to 18% were found, depending on the orientation and size of the mixing zone. No negative effects were noticed, despite the short time of reactant mixing.

These results show that improvements in the DBD reactor performance for DRM can be made by simple variations in the reactor geometry, especially by varying the way of combining the reactants. Nevertheless, the improvements shown for this DBD reactor configuration remain limited, and larger improvements are required to make DBD plasma-based DRM a competing technology.

## **Chapter 7**

**How gas flow design can influence the performance of a DBD plasma reactor for ammonia synthesis**

## 7.1 Introduction

In the previous chapter, we introduced a novel multi inlet-outlet parallel plate DBD reactor to investigate how the performance of a DBD reactor can be improved by changing the way CO<sub>2</sub> and CH<sub>4</sub> are added to, and mixed in, the reactor for DRM. This investigation will now be extended to ammonia synthesis from pure N<sub>2</sub> and H<sub>2</sub> to examine if there are reaction specific trends. Where CO<sub>2</sub> and CH<sub>4</sub> can dissociate into stable products and react further on, N<sub>2</sub> and H<sub>2</sub> will have to react together to form any products. Therefore, the results will differ, especially regarding pre-reaction capabilities.

## 7.2 Methods and theory

The same parallel plate DBD reactor from chapter 6 is used. Ammonia yield is determined by a mass spectrometer (HPR20, Hiden). The standard operating conditions used in this work are a flow rate of 50 mL/min consisting of a 1:3 N<sub>2</sub>:H<sub>2</sub> ratio, performed at 30 W (3 kHz) and 1 bar. This results in an average residence time of 21 s, a specific energy input (SEI) of 36 kJ/L, and a power surface density (PSD) of 0.6 W/cm<sup>2</sup> in the case of a 100x50 mm electrode. Adaptations to these parameters will specifically be mentioned in the results section.

Different configurations will be tested in this chapter. Table 6.2 in chapter 6 gives an overview of all configurations with the abbreviation, a short description, and a schematic depiction.

## 7.3 Results

The results in this work are, similarly to chapter 6, split up into two main sections and directly compared against the results of DRM from chapter 6. This way we will explore the different behaviour of adding and mixing N<sub>2</sub> and H<sub>2</sub> in the reactor. First the traditional 'one inlet – one outlet' design is used to set the benchmark for the rest of this chapter, and the influence of the dimensions of the reaction zone and the power delivery to the reactor on the performance will be investigated. Secondly, we will introduce gradual addition of one of the gas



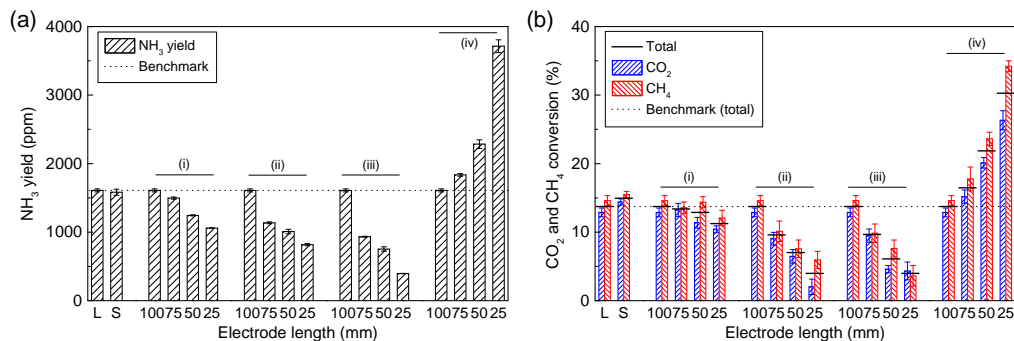


**Figure 7.1:** (a) Ammonia yield of stoichiometric ammonia synthesis and (b) conversion of 1:1 DRM plotted for different reactor geometry cases with the benchmark in the long (L) and short (S) configurations, the influence of the electrode length (i) at constant power (30 W) and flow rate (50 mL/min), (ii) at constant residence time (21 s) and SEI (36 kJ/L), (iii) at constant flow rate (50 mL/min) and power surface density (0.6 W/cm<sup>2</sup>), and (iv) at constant power (30 W) and residence time (21 s). The total conversion of the L configuration is highlighted as the dotted line as the benchmark throughout all measurements. All exact values can be found in table F.1 in appendix F.

components to the reactor, and investigate the impact of “pre-reacting” one of the gases and mixing them later, on the reactor. All configurations will be tested at standard conditions (see section 7.2) unless stated otherwise.

### 7.3.1 One inlet – one outlet

#### 7.3.1.1 L and S configuration

The traditional ‘one inlet – one outlet’ long reactor (length > width) that will be denoted as L, see also section 6.2.2, is the benchmark for this work. A base ammonia yield of 1610 ppm was found for this configuration at the standard conditions, as shown in figure 7.1(a), with an energy cost (EC) of 139 kWh/mol, see table F.1 in appendix F.

In chapter 6 we saw that the gas velocity had an influence on the conversion, even when all other parameters were kept constant, and that this is easy to be adapted in this reactor. A 90° shift of the entrance and exit makes that the gas mixture enters and exits through the long sides of the rectangular reaction zone. This shorter pathway, denoted as the S configuration, effectively enlarges the cross section and lowers the average gas velocity while maintaining a constant residence time. Figure 7.1(a) shows that there is no apparent effect for ammonia synthesis, with a yield of 1580 ppm, and stays within error bars. The lower gas velocity offers more opportunity for lateral diffusion and thus mixing of

the reactants in the reactor. Since DBD reactors operate in a micro discharge regime, i.e. equivalent to random mini and short batch reactors ( $\sim 100\ \mu\text{m}$  for  $\sim 100\ \text{ns}$  [37]), it is kinetically beneficial to have the reactants optimally mixed for enhanced reaction rates. DRM, whose reactants have relatively low diffusion coefficients ( $\sim 0.15\ \text{cm}^2/\text{s}$  [170]), can benefit from this, while it is less important for ammonia synthesis whose reactants have relatively high diffusion coefficients ( $\sim 1.2\ \text{cm}^2/\text{s}$  [170]). However, the fact that the conversion for both L and S configuration is so low, i.e. less than 1%, might also be the main reason that no effect of the gas velocity is observed since no significant concentration gradients are present.

### 7.3.1.2 Effect of electrode length

The size of the reaction zone, here varied by the electrode length between 25 mm and 100 mm, is a parameter that has a big influence on a number of reactor parameters and subsequently the performance. Depending on input parameters, i.e. the flow rate and power, the residence time, specific energy input (power to volume ratio; SEI), and power surface density (power to electrode area ratio; PSD) will either change or remain constant. Therefore, four scenarios are investigated to check the influence of these parameters, i.e. (i) constant flow rate and power, (ii) proportional flow rate and power, (iii) constant flow rate and proportional power, and (iv) proportional flow rate and constant power. All conditions and associated parameters are listed in table 7.1.

The first scenario (i) holds a constant flow rate and power as the electrode shortens, effectively decreasing the residence time but increasing the power surface density at the same time. The results in figure 7.1(a) show that the more concentrated discharge zone cannot compensate for the shorter residence time. The yield drops from 1610 ppm to 1058 ppm when the electrode shortens from 100 mm to 25 mm, and subsequently the residence time from 21 s to 5.25 s. A small positive effect of the higher power surface density is visible though when comparing these results to residence time measurements in the L configured reactor by changing the flow rate. As shown in figure 7.2, the yield in the corresponding residence time window shows lower values than scenario (i), i.e.  $\sim 1600\ \text{ppm}$  at 21 s and  $\sim 525\ \text{ppm}$  at 2.25 s. The rest of the residence time results show a slow increase as the residence time increases, with a projected maximum

**Table 7.1:** Conditions used when varying the electrode length. As the electrode becomes shorter, scenario (i) maintains a constant flow rate and power, thus yielding a shorter residence time but constant SEI and larger power surface density (PSD), scenario (ii) proportionally adapts the flow rate and power, to keep the residence time, SEI and PSD constant, scenario (iii) maintains a constant flow rate and uses a proportional power, so keeping the PSD constant, and scenario (iv) uses a proportional flow rate (to keep the residence time constant) and maintains a constant power (yielding a larger SEI and PSD). Note that the electrode length of 100 mm corresponds to the benchmark L configuration.

Scenario	Electrode length (mm)	Reaction volume (cm <sup>3</sup> )	Flow rate (mL/min)	Residence time (s)	Power (W)	SEI (J/mL)	PSD (W/cm <sup>2</sup> )
(i)	100 (L)	17.5	50	21	30	36	0.6
	75	13.125	50	15.75	30	36	0.8
	50	8.75	50	10.5	30	36	1.2
	25	4.375	50	5.25	30	36	2.4
(ii)	100 (L)	17.5	50	21	30	36	0.6
	75	13.125	37.5	21	22.5	36	0.6
	50	8.75	25	21	15	36	0.6
	25	4.375	12.5	21	7.5	36	0.6
(iii)	100 (L)	17.5	50	21	30	36	0.6
	75	13.125	50	15.75	22.5	27	0.6
	50	8.75	50	10.51	15	18	0.6
	25	4.375	50	5.25	7.5	9	0.6
(iv)	100 (L)	17.5	50	21	30	36	0.6
	75	13.125	37.5	21	30	48	0.8
	50	8.75	25	21	30	72	1.2
	25	4.375	12.5	21	30	144	2.4

yield of only around 3550 ppm for 30 W, 1 bar, and a 3.5 mm gap. Scenario (i) shows the same trend as for DRM seen in chapter 6 where the conversion decreased from 13.7% to 11.2%, whereas the residence time measurements showed a decrease from about 14% to only 4%.

In scenario (ii), both the flow rate and power are proportionally lowered as the electrode gets shorter. This results in a constant residence time, SEI, and PSD. Despite these four electrode lengths having the same conditions on paper, the results for DRM in chapter 6 have shown that using a shorter electrode length is not beneficial as the reduced power has a dominant effect on the conversion, despite the constant SEI and PSD. Ammonia synthesis confirms this behaviour with the yield dropping from 1610 ppm to 820 ppm.

The third scenario (iii) holds a constant flow rate but proportionally scales the power with the electrode length. This lowers the residence time and SEI while keeping the PSD constant. As with DRM, the yield decreases proportionally with the electrode length from 1610 ppm to 396 ppm. As a result, the energy cost (EC) remains about the same, see table F.1 in appendix F.

Lastly, scenario (iv) uses a proportional flow rate but a constant power to

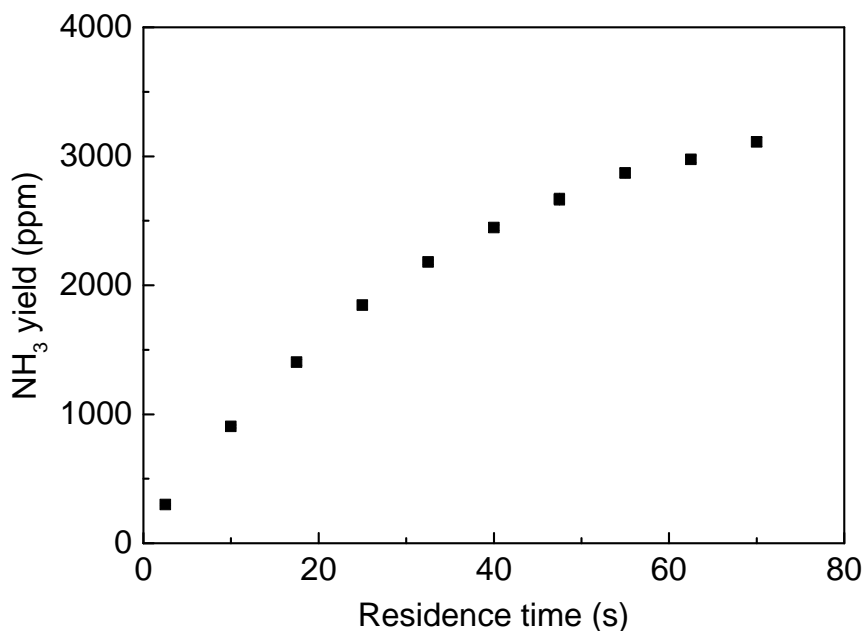


**Figure 7.2:** Ammonia yield for stoichiometric ammonia synthesis plotted as a function of residence time in the benchmark straight 'L' reactor at 30 W by changing the flow rate. All exact values can be found in table F.1 in appendix F.

obtain a constant residence time but yielding increased SEI and PSD values. As a result, the ammonia yield drastically increases to 3710 ppm but of course at a great energy cost due to the high SEI. The yield only increases by a factor 2.3 whereas the SEI increases by a factor 4, wasting almost half the energy, which reflects in the energy cost.

### 7.3.1.3 Effect of gas mixing ratio

In this section, we will investigate the effect of different gas mixture ratios. In chapter 6, we saw for DRM that the most optimal ratio for maximal conversion was a CO<sub>2</sub>:CH<sub>4</sub> ratio between 6:1 and 3:1. If the desired outcome of the process is more hydrocarbon production, then high CH<sub>4</sub> ratios were preferential. Knowing which effect is desired is important when the presented gas feed ratio is different from the more optimal ratio. The design of the reactor can therefore be altered to mix the gases in an alternative way, e.g. gradual addition, and then operate

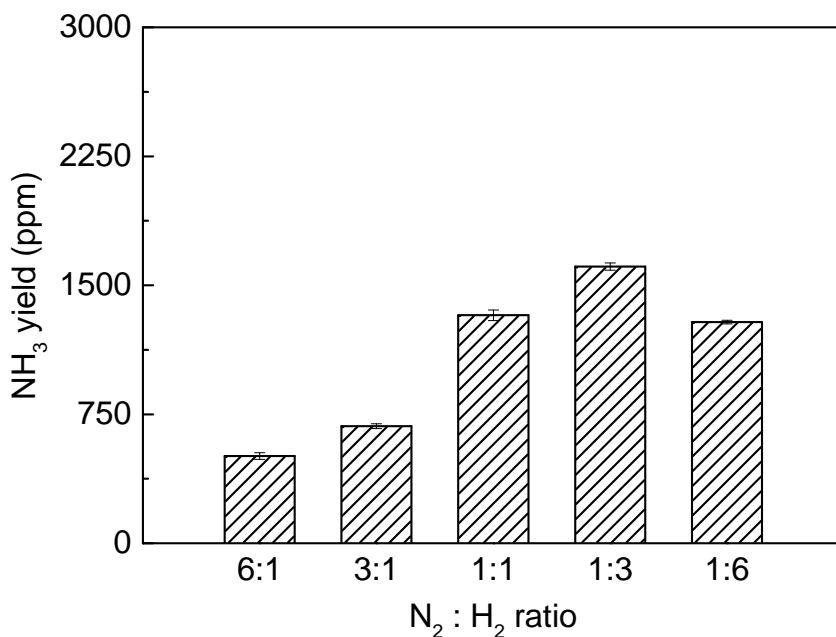


**Figure 7.3:** Ammonia yield plotted for different N<sub>2</sub>:H<sub>2</sub> ratios varying between pure N<sub>2</sub> and pure H<sub>2</sub> in the benchmark straight ‘L’ reactor at 30 W and 50 mL/min. All exact values can be found in table F.1 in appendix F.

at more optimal conditions. So far, a stoichiometric N<sub>2</sub>:H<sub>2</sub> ratio of 1:3 has been used to produce ammonia. The results in figure 7.3 show that this is in fact the most optimal ratio for maximal yield. Small deviations towards 1:1 and 1:6 are tolerable with slightly lower yields of 1330 and 1286 ppm, respectively. The 1:3 N<sub>2</sub>:H<sub>2</sub> ratio being the most optimal is not always found in research though, 1:1 to 3:1 N<sub>2</sub>:H<sub>2</sub> in [47, 150–153].

### 7.3.2 Multiple inlets and outlets

Straight mixing of reactants and feeding them in the reactor might not be the most desirable way when multiple reactions occur in a reactor. Gradual addition or sequential addition with pre-reaction of one of the reactants could shift the local gas ratio and enhance the conversion. This concept has shown to have a significant impact on the DRM reaction, as seen in chapter 6. Both conversion and product distribution could be significantly adapted depending

on the configuration used in this reaction. Ammonia synthesis, on the other hand, is a completely different reaction, i.e. no pre-reaction of the reactants into long-living intermediates is possible and there is only one major product next to trace amounts of hydrazine.

### 7.3.2.1 Gradual addition of one of the gases

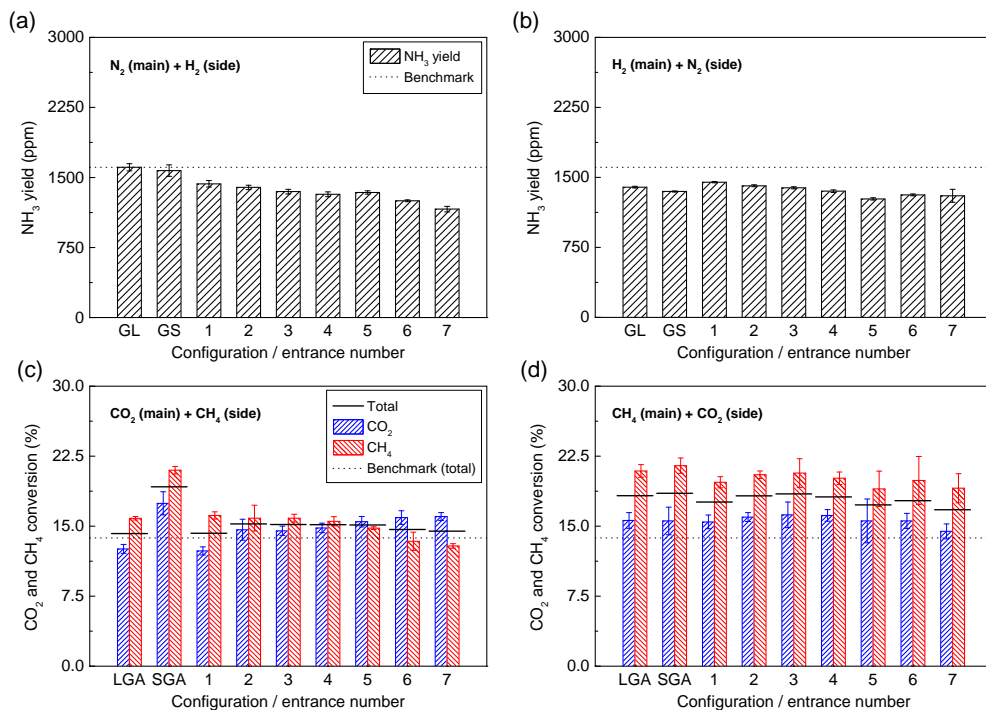
Gradual addition of one of the reactants can be done in our reactor in both the L and S configuration as shown in section 6.2.2. Fourteen side holes in the L configuration will allow the added gas to be mixed in along the long axis of the reactor, denoted as LGA; whereas two side holes in the S configuration will provide the same effect along the short axis, denoted as SGA.

Figure 7.4(a) shows these results for  $N_2$  as the main gas and  $H_2$  as the added gas. Both LGA and SGA configuration show no significant change in ammonia yield compared to the benchmark 1610 ppm. Changing the gases to  $H_2$  as the main gas and  $N_2$  as the added gas, see figure 7.4(b), makes both LGA and SGA configuration perform worse than the benchmark at a yield of 1396 ppm and 1349 ppm, respectively. Using  $N_2$  as the main gas is the best choice, suggesting that the reaction towards  $NH_3$  is determined by the dissociation of  $N_2$  as the rate determining step and then followed by the stepwise addition of  $H_2$ .

### 7.3.2.2 Introducing both gases at separate locations to allow pre-activation in the plasma

From chapter 6 we know that in the case of DRM, pre-reaction of one of the reactants can be a valuable tool.  $CO_2$  and  $CH_4$  rarely react directly with each other, but rather their direct reactants after individual dissociation, therefore separate pre-reaction or gradual addition can increase the conversion with optimized concentration gradients. However,  $N_2$  and  $H_2$  cannot pre-react, meaning producing stable and long lived species that can react later on in the reactor. As a result, minimal effects would be expected.

**Side addition** First the LGA configuration is used with the main gas fed from the entrance at the bottom, while the added gas will be added by only one set of entrances, resulting in seven options with 1 the earliest and 7 the latest side addition.



**Figure 7.4:** (a and b) Ammonia yield of stoichiometric ammonia synthesis and (c and d) conversion of 1:1 DRM plotted for different reactor geometry cases where in (a) N<sub>2</sub> is the main gas and H<sub>2</sub> is the side-added gas, in (b) H<sub>2</sub> is the main gas and N<sub>2</sub> is the side-added gas, in (c) CO<sub>2</sub> is the main gas and CH<sub>4</sub> is the side-added gas, in (d) CH<sub>4</sub> is the main gas and CO<sub>2</sub> is the side-added gas. All experiments are performed at 30 W and 50 mL/min. All exact values can be found in table F.1 in appendix F.

Figure 7.4(a and b) show that no higher yield than the benchmark could be obtained, and that the later the additional gas is added, the lower the ammonia yield will be. Also, there is not much difference in yield values between using N<sub>2</sub> or H<sub>2</sub> as the main gas. Remarkably, even late mixing, i.e. entrances 7, can reach a substantial yield of 1160 ppm for N<sub>2</sub> as the main gas and 1300 ppm for H<sub>2</sub> as the main gas. Even at these late addition points, enough gas mixing occurs to achieve these yields where the chances of gas short-cuts are higher, probably due to high diffusion coefficients compared to the flow rate (or thus gas velocities), see section 7.3.1.1.

**Separate pre-activation zones** Finally the extreme of pre-reaction will be tested with long individual zones that only mix right at the exit. An adapted version of the L and S configuration is used for this, where the original entrance and exit are now the individual entrances, and new exits are provided halfway the reactor,

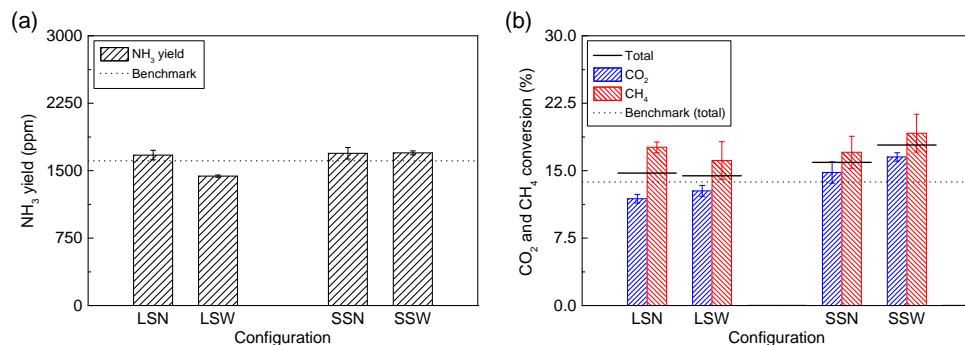


**Figure 7.5:** (a) Ammonia yield of stoichiometric ammonia synthesis and (b) conversion of 1:1 DRM plotted for different reactor geometry cases where the gases are added and reacted separately before mixing. All experiments are performed at 30 W and 50 mL/min. All exact values can be found in table F.1 in appendix F.

see section 6.2.2. Both L and S configurations are made with narrow and wide exit canals to change the size of the mixing zone, resulting in four configurations: LSN, LSW, SSN, and SSW.

Figure 7.5 shows the results for these configurations and surprisingly they obtain similar results as the benchmark despite the assumed reaction-less pre-reacting zones. This behaviour confirms that the magnitude of gas diffusion is indeed a lot higher than the gas velocity so that the reactor is pretty much perfectly mixed despite the separate addition. It is otherwise pretty unlikely that either (i) the excited nitrogen and hydrogen species can live long enough in the reactor and react quickly when finally mixing together, or (ii) the reaction rate coefficient is so high that a short mixing time at the end of the reactor is enough to produce a benchmark-amount of ammonia, which does not fit our residence time measurements in figure 7.2. This sheds a different light on the previous cases from figure 7.4, and perhaps as well on the equivalent results of chapter 6.

### 7.3.3 Discussion

A few thoughts can be made on these results. The yields obtained in this chapter are far from comparable with the values reached by other researchers. Yields up to 9% have been seen, which is clearly a lot higher than ours [171, 172]. This is however not that big of a problem since most other researchers have focussed on obtaining high conversions through clever (catalysed) designs, while our focus was on investigating the effect of gas flow patterns. However, reviewing the



results from this chapter, it does not look advantageous for ammonia synthesis to optimise the reactor flow pattern. It seems to be not susceptible due to the unreactive nature of its pure reactants, the high diffusion coefficient versus low gas velocity, and the optimal reaction mixture ratio actually being stoichiometric. The 1:3  $\text{N}_2:\text{H}_2$  ratio being the most optimal is not always found in research though, 1:1 to 3:1  $\text{N}_2:\text{H}_2$  in [47, 150–153].

Also, the gas flow rate (and thus gas velocity) was clearly poorly chosen compared to the high diffusion coefficient. In chapter 6 we already ran into unforeseen mixing in the reactor with DRM, using reactants with a diffusion coefficient a tenfold higher in this chapter, only made the problem bigger. This could have been fixed by using higher flow rates to minimise the effect, however, it would impact all possible observable effects by lowering the conversion — especially for ammonia synthesis — too much. Therefore, future work should try to mitigate this effect as much as possible if it hinders the research objective.

## 7.4 Conclusion

In this chapter we further investigated how the shape of the reaction zone, gas addition, and the method of mixing both reaction gases can influence the conversion by testing it for ammonia synthesis. It was shown that all observed trends regarding the ‘one inlet – one outlet’ design also hold for ammonia synthesis. The change in reaction did show deviant trends when the input of both gases got separated. As the optimal  $\text{N}_2:\text{H}_2$  ratio was found to be the stoichiometric ratio (that was already used as the standard condition), both gases are not able to produce stable products on their own, and the diffusion coefficient was too high compared with the gas velocity; no additional benefits could be found from gradual addition nor gas pre-reaction. Gradual addition showed equal performance with  $\text{N}_2$  as the main gas, but decreased yields with  $\text{H}_2$  as the main gas, suggesting  $\text{N}_2$  dissociation as the rate determining step. Separate addition also showed either equal yield compared to the benchmark due to enough diffusion, or lower yield due to not enough residence time of one of the reactants.



# Chapter 8

## Future outlook

Within the realms of DBD plasma reactors, we can definitely see how our work on the PCE study can help in quantifying performance gains in different topics. Touching this thesis, PCE studies on the effect of reactor geometry was not within the time frame of this PhD but is certainly of interest to further pinpoint how the different geometries influence the kinetics in the reactor. Also in the further development of packing materials, in this work the core-shell spheres, but also in general for others, PCE studies hold an essential spot in the experimental design and analysis of reactor performance changes. Further expansion of this type of study to other reactions and reactor types is certainly of interest to test and proof the validity of the PCE study concept.

Further development of precisely engineered packing materials fitted to specific plasma and chemistry processes holds a lot of value. Optimising production selectivity, selective adsorption of species to shift the reaction equilibrium, using adsorbing packing materials in swing-feed type systems, structured (3D printed) packing materials, etc. are only a few of the possibilities.

However, despite all the advancements made in this thesis and by the work of many others, the eventual efficiency gains (expressed in energy efficiency, energy cost, energy yield, etc.) of the 'DBD reactor' are very limited and still render very low values. Adding packing materials, reducing the gap size, altering the reactor geometry, etc. does significantly alter the plasma discharges and product distributions, but the gains are always accompanied by other losses such as lower throughput and shorter residence times, fouling of packing materials and reactor, etc. Also plasma catalysis in DBD reactors does not seem to be the perfect synergetic hybrid we expected. Although the DBD reactor has a lot of advantages,

the low base performance appears to be too low with no solution found so far to drastically improve it. Perhaps more focus should be put on other plasma types such as APGD or GA, or even (hybrids with) non-plasma technologies.

One of the bigger problems with plasma technology is the absurdly complex matrix of interactions between parameters, processes, and species. Everything is connected in some way, one influences the other, making each plasma conversion process unique. A millimetre difference, a percent of composition change, differently applied power signal, sphere stacking errors, imperfections, etc., every small difference has its own effect so that no set-up is alike. This makes comparative work impossible and each research work unique and non-repeatable. The utopian solution would require us to completely understand every small detail of every process that will not be feasible any time soon. More standardised testing might already go a far way.

This is especially important with packing material testing. Standardised set-ups representative for certain reactor types (e.g. one for DBD, one for close post-plasma treatment for MW, APGD, and GA, etc.) could provide uniform data for packing performance comparison. If possible, investigation could be performed in a three-step process where (1) the packing materials are tested on their influence on the plasma parameters and bulk plasma species (electrons and direct ions from reagent(s)), (2) the materials are tested on their influence on gas conversion via surface interactions by chemically ‘simulating the plasma’, and (3) combine the knowledge from (1) and (2) in actual plasma conversion testing. Combination of this process with a PCE study can help pinpoint performance gains.

Finally, more precise goals and target values for CO<sub>2</sub> conversion processes should be set. What should be the target throughput to make it an industrially viable process? What should be the minimum conversion/efficiency? What purifying techniques are viable? What reactor conversion levels are necessary to make purifying efficient? What about the technologies’ resilience to gas impurities? Do we really need an on-off process for CO<sub>2</sub> conversion or will it actually require continuous processes? ... If these goals and targets are set, which plasma reactor type(s) can promise this with “minimal” further research? Are other technologies perhaps a better solution?

---

Answering to these questions could genuinely help all research into a coordinated strategy towards the liberation of peoplekind of our self inflicted tyranny of CO<sub>2</sub>.



# List of publications

1. I. Michielsens, Y. Uytendhouwen, J. Pype, B. Michielsens, J. Mertens, F. Reniers, V. Meynen, and A. Bogaerts, "CO<sub>2</sub> dissociation in a packed bed DBD reactor: First steps towards a better understanding of plasma catalysis," *Chemical Engineering Journal*, vol. 326, pp. 477–488, 2017
2. Y. Uytendhouwen, S. Van Alphen, I. Michielsens, V. Meynen, P. Cool, and A. Bogaerts, "A packed-bed DBD micro plasma reactor for CO<sub>2</sub> dissociation: Does size matter?," *Chemical Engineering Journal*, vol. 348, pp. 557–568, 2018
3. I. Michielsens, Y. Uytendhouwen, A. Bogaerts, and V. Meynen, "Altering Conversion and Product Selectivity of Dry Reforming of Methane in a Dielectric Barrier Discharge by Changing the Dielectric Packing Material," *Catalysts*, vol. 9, p. 51, jan 2019
4. Y. Uytendhouwen, K. Bal, I. Michielsens, E. Neyts, V. Meynen, P. Cool, and A. Bogaerts, "How process parameters and packing materials tune chemical equilibrium and kinetics in plasma-based CO<sub>2</sub> conversion," *Chemical Engineering Journal*, vol. 372, pp. 1253–1264, sep 2019
5. Y. Uytendhouwen, K. Bal, E. Neyts, V. Meynen, P. Cool, and A. Bogaerts, "On the kinetics and equilibria of plasma-based dry reforming of methane," *Chemical Engineering Journal*, vol. 405, p. 126630, feb 2021
6. Y. Uytendhouwen, V. Meynen, P. Cool, and A. Bogaerts, "The Potential Use of Core-Shell Structured Spheres in a Packed-Bed DBD Plasma Reactor for CO<sub>2</sub> Conversion," *Catalysts*, vol. 10, p. 530, may 2020

7. Y. Uytendhouwen, J. Hereijgers, T. Breugelmans, P. Cool, and A. Bogaerts, "How gas flow design can influence the performance of a DBD plasma reactor for dry reforming of methane," *Chemical Engineering Journal*, vol. 405, p. 126618, feb 2021
8. P. Kaliyappan, A. Paulus, J. D'Haen, P. Samyn, K. Leyssens, Y. Uytendhouwen, S. Defossé, N. Hafezkhiabani, A. Bogaerts, V. Meynen, K. Elen, A. Hardy, and M. K. Van Bael, "Probing the impact of material properties of core-shell SiO<sub>2</sub>@TiO<sub>2</sub> spheres on the plasma catalytic CO<sub>2</sub> dissociation using packed bed DBD plasma reactor," *Journal of CO<sub>2</sub> Utilization (Submitted)*, 2020
9. S. Rana, Y. Uytendhouwen, A. Bogaerts, and V. Meynen, "A detailed study on the effect of calcination temperatures of gamma alumina on chemical equilibrium and kinetics in plasma-based DRM reaction," *In preparation*, 2020



# List of presentations

1. I. Michielsen, Y. Uytendhouwen, V. Meynen, and A. Bogaerts, “Influence of reactor and packing parameters on the CO<sub>2</sub> conversion in a packed-bed DBD reactor.,” Informal Plasma-Catalysis Workshop, Antwerpen, 2016. **(Oral presentation)**
2. Y. Uytendhouwen, I. Michielsen, K. V. Laer, V. Meynen, P. Cool, and A. Bogaerts, “Effect of discharge gap size and packing materials on CO<sub>2</sub> splitting in a packed bed micro plasma reactor: Does size matter?,” IWPEEA 2016, Liverpool, 2016. **(Oral presentation)**
3. Y. Uytendhouwen, I. Michielsen, V. Meynen, P. Cool, and A. Bogaerts, “Untangling the influence of bulk and surface effects of spherical packings in a packed-bed DBD plasma reactor for CO<sub>2</sub> splitting.,” ICCDU 2016, Sheffield, 2016. **(Poster and oral flash presentation)**
4. Y. Uytendhouwen, I. Michielsen, V. Meynen, P. Cool, and A. Bogaerts, “Plasma catalysis for CO<sub>2</sub> utilisation: steering reactor and packing parameters towards viable industrial applications.,” CRF 1, Blankenberge, 2016. **(Oral presentation)**
5. N. HafezKhiabani, I. Michielsen, Y. Uytendhouwen, A. Bogaerts, and V. Meynen, “CO<sub>2</sub> conversion in a packed-bed DBD with plasma catalysis.,” Informal Plasma-Catalysis Workshop, Eindhoven, 2016. **(Oral presentation)**
6. Y. Uytendhouwen, V. Meynen, P. Cool, and A. Bogaerts, “Untangling bulk and surface effects of spherical packing materials in a DBD plasma reactor by core-shell structured spheres.,” Informal Plasma-Catalysis Workshop, Twente, 2018. **(Oral presentation)**



# Appendix A

## Appendix of Chapter 2: Micro gap

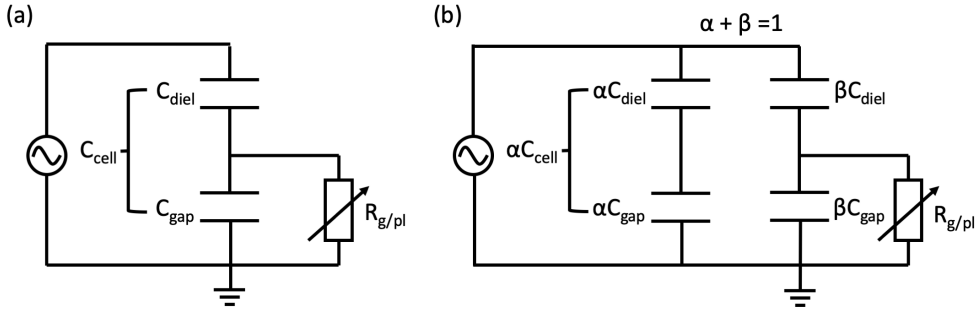
### A.1 Electrical characterisation: Theory

Figure 2.2 of chapter 2 shows a typical oscillogram and a simplified Lissajous figure. The oscillogram obtained from each experiment can be directly analysed to calculate the peak-to-peak voltage ( $U_{pp}$ ) and root-mean-square current ( $I_{RMS}$ ) of the plasma reactor.

Further analysis of the Lissajous figures gives information about the electrical behaviour of the plasma. The Lissajous figure can be divided into four regions, representing the four phases occurring during one voltage period. They consist of two capacitive phases, AB and CD, where the reactor behaves like a capacitor with no activity in the reaction volume; as well as two discharge phases, BC and DA, where the gas present in the reaction volume is (partially) transformed into a plasma and a net flow of electrons through the reactor is present, resulting in a combined resistive-capacitive behaviour of the reactor. The Q-U Lissajous figure has the benefit that the slopes directly relate to a physical value, i.e. the capacitance of the reactor during that specific phase, since  $dQ/dU = C$ . In the capacitive phases, the slopes show the total capacitance of the reactor  $C_{cell}$  which can be represented in a simplified electrical model, shown in figure A.1(a), by two capacitors in series, representing the capacitance of the dielectric barrier  $C_{diel}$  and the discharge gap  $C_{gap}$  according to the following equation:

$$\frac{1}{C_{cell}} = \frac{1}{C_{diel}} + \frac{1}{C_{gap}} \tag{A.1}$$

In the discharge phase, the charge built up by the applied voltage reaches a threshold, which ignites the plasma. The capacitance of the discharge gap is then electrically bypassed due to the conductivity of the plasma and only the capacitance of the dielectric barrier remains, shown by the respective slopes. This phase is depicted in the simplified model by the dielectric barrier capacitance bypassed by a low value resistor. In the capacitance phase the model uses an infinitely high value resistor.



**Figure A.1:** (a) Simplified electrical model for a DBD reactor. (b) Extended model for a DBD reactor incorporating partial discharging.

The flaw with this model is its assumption of a fully discharged reaction volume, leaving only the capacitance of the dielectric tube  $C_{diel}$  as the source of the slope of the discharge phase. However, if the reaction volume is not entirely discharged and not all accumulated charge is used, we get an intermediate phase, i.e. a partial discharge, with an effective capacitance and slope  $\zeta_{diel}$  that has a value between  $C_{diel}$  and  $C_{cell}$ , depending on the degree of partial discharging. A new model was proposed by Peeters and van de Sanden [41] to accommodate this partial discharging of the DBD reactor, as shown in figure A.1(b). The

electrical model is now divided into two parts: a non-discharging  $\alpha$  part and a discharging  $\beta$  part. When the reactor is in the discharge phase, the volume  $\alpha$  of the reactor that is not ignited is now represented by a partial capacitance for the dielectric barrier and the discharge gap; while the ignited volume  $\beta$  is represented by the complementary capacitances configured like the original model. However, during the capacitive phase of the reactor, the resistor in the  $\beta$  part again has an infinitely high value, resulting in the cumulated capacitive behaviour of the dielectric barrier and reaction volume like before. Using this model, the fraction of partial discharging can now be quantified and used as a measure of efficient behaviour of a particular reactor setup. This fraction of partial discharging  $\alpha$  is calculated by the formula of Peeters and van de Sanden [41]:

$$\alpha = \frac{C_{diel} - \zeta_{diel}}{C_{diel} - C_{cell}} \quad (\text{A.2})$$

$C_{cell}$  and  $\zeta_{diel}$  can directly be determined by calculating the respective slopes of the Lissajous figure; the capacitance of the ideal, fully discharged reactor  $C_{diel}$  however, cannot. Butterworth *et al.* [70] showed that this value can be obtained by using an argon plasma, making this the closest approximation compared with roughly calculated values, since this method uses the actual reactor set-up. A dielectric capacitance  $C_{diel}$  of  $26.6 \text{ mC/V} \pm 0.2 \text{ mC/V}$  is measured, independent of the discharge gap size.

Next, the burning voltage can be determined. The burning voltage is the minimum voltage required to maintain the plasma discharge during the experiment and is normally determined in the Lissajous figure as half of the voltage difference between the intersects with the x-axis. This value needs to be corrected for the partial discharging of the reactor according to the formula of Peeters and van de Sanden [41]:

$$U_{bur} = \frac{1 - \frac{C_{cell}}{C_{diel}}}{1 - \frac{C_{cell}}{\zeta_{diel}}} \Delta U \quad (\text{A.3})$$

Finally, the displaced charge during the discharge phase  $Q_{disp}$  and the number of micro discharges are calculated. This is done to analyse the average strength of the discharges. The displaced charge  $Q_{disp}$  is calculated by taking the difference in charge between points A and D in the Lissajous figure, see

also figure 2.2 in chapter 2. Individual micro discharges are determined after normalisation of the current profile and applying height and width threshold values to exclude signal noise, resonance, and systematic measuring errors. The Picoscope 6402D oscilloscope from Picotech used a sample rate of 625 MS/s in our set-up, corresponding to a sample interval of 1.6 ns, which is well below the typical duration of a micro discharge of around (a few) hundred nano seconds. Different threshold values were used for empty and packed reactors due to the large difference in discharge intensity (width and height). This does mean that not every single discharge in the reactor can be measured, e.g. if they are too short, too small, or coincide with a bigger peak or resonance. Therefore, the returned value will not be the exact number of discharges in the plasma but will still be a systematically calculated and representable number.

## **A.2 Electrical characterisation: Results of the packed reactor**

To explain the results of conversion in the packed reactor for different gap-sphere-material combinations, we can again look at the electrical characteristics, like in the empty reactor, although the underlying mechanisms are more complicated than in the empty reactor, due to many intertwined effects.

For the peak-to-peak voltage, three general trends are visible in figure A.2. First, smaller gaps require somewhat lower voltages to maintain a constant plasma power of 30 W for a constant sphere size, which was not the case in the empty reactor, as shown in section 2.3.1.2 of chapter 2. Second, smaller spheres in a certain gap size require a larger voltage to maintain the plasma power. Although the local inter-sphere discharge gap is smaller and should ignite quicker, the larger number of spheres require a greater applied potential to be distributed over each sphere-gap-sphere micro reactor. Third, the general order of materials requiring an increasing voltage is glass wool < silica < alumina < zirconia.

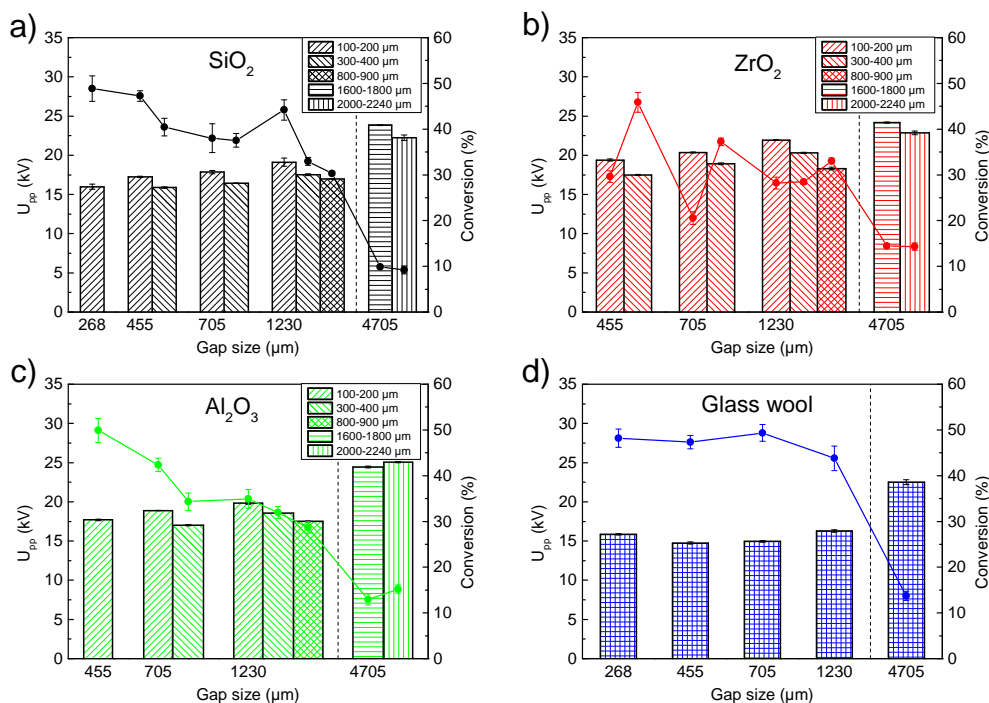


**Figure A.2:** Peak-to-peak voltage of packed bed DBD (micro) reactors at a constant residence time of 7.5 s. Results are displayed per material type for different sphere sizes (as indicated by the legend) and as a function of gap size, and compared to the conversion of the corresponding packed reactor (solid line).

The RMS current shows partially the same trends in figure A.3. The current flowing through the reactor is slightly higher with smaller spheres and the same overall order of materials as with the peak-to-peak voltage is found. It does raise the question why zirconia needs the highest voltage and current, while the conversion is lower than the other materials. A suggestion might be that zirconia has a more electrically conductive behaviour than the other materials and that more of the applied power is lost due to surface losses.



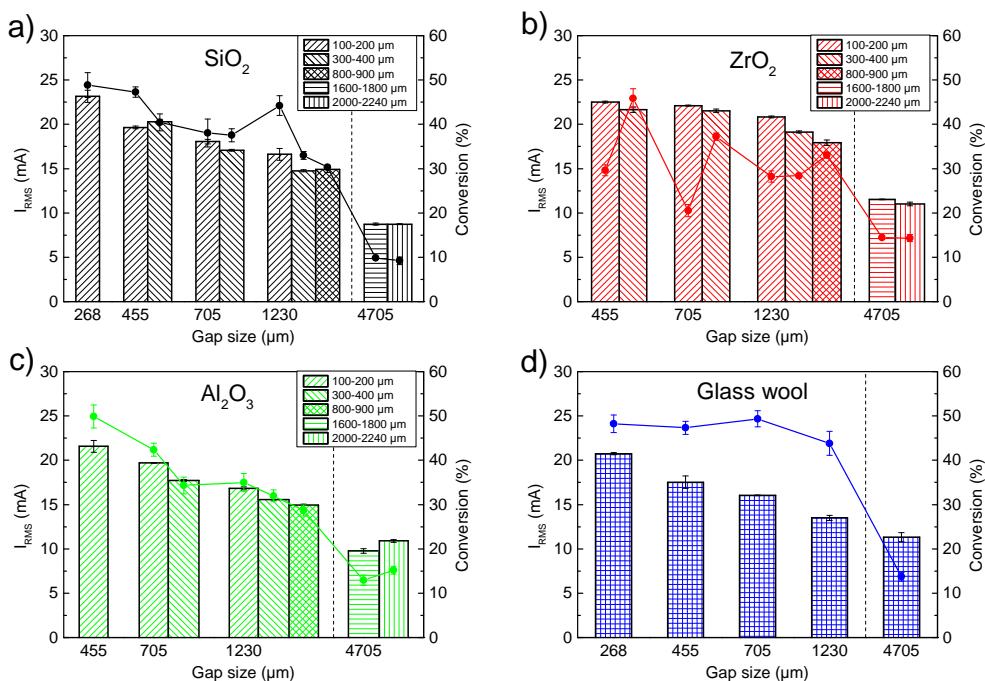


**Figure A.3:** Average current flow (root mean square) of packed bed DBD (micro) reactors at a constant residence time of 7.5 s. Results are displayed per material type for different sphere sizes (as indicated by the legend) and as a function of gap size, and compared to the conversion of the corresponding packed reactor (solid line).

The effective capacitance and the derived partial discharging fraction of the reactor, displayed in figure A.4 and figure A.5, show some counterintuitive trends. The trend of the empty reactor, where a smaller discharge gap results in less partial discharging and thus a higher conversion, is still visible. However, this is clearly material dependent, as the decrease of  $\alpha$  follows the order glass wool » silica > alumina / zirconia. Moreover, in packed bed reactors, less partial discharging does not always mean higher conversion. Zirconia spheres within a fixed discharge gap cohere to this trend, but silica and alumina show the opposite results. It shows that decreasing the sphere size leads to more partial discharging, since the plasma cannot be so easily ignited, but that the conversion still increases. Glass wool shows very low partial discharging behaviour with some of the highest conversions as a result.

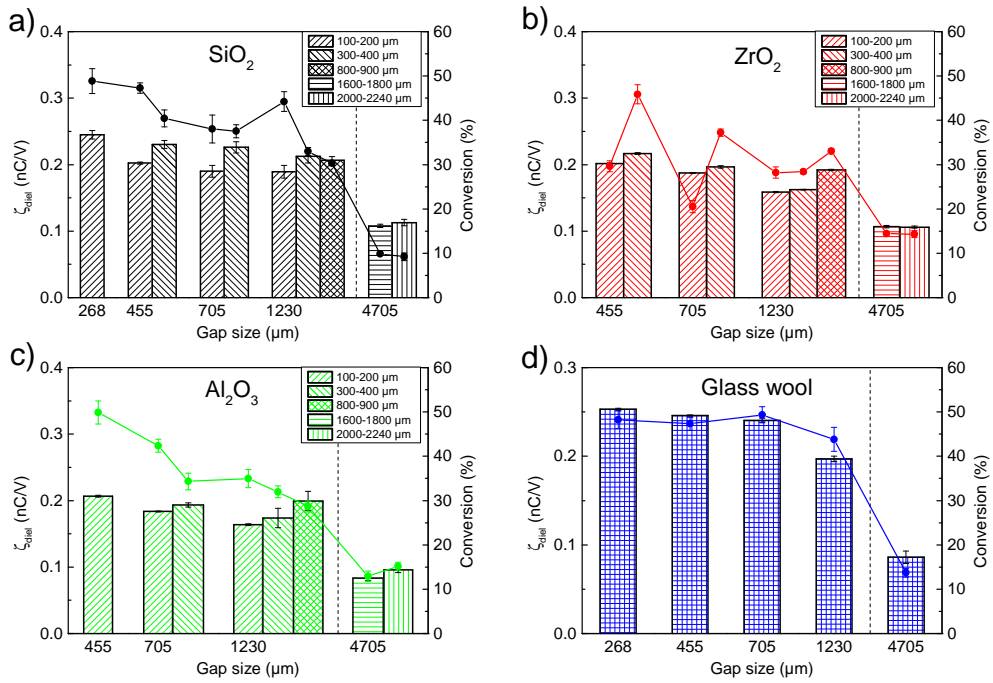


**Figure A.4:** Effective capacitance of packed bed DBD (micro) reactors at a constant residence time of 7.5 s. Results are displayed per material type for different sphere sizes (as indicated by the legend) and as a function of gap size, and compared to the conversion of the corresponding packed reactor (solid line).

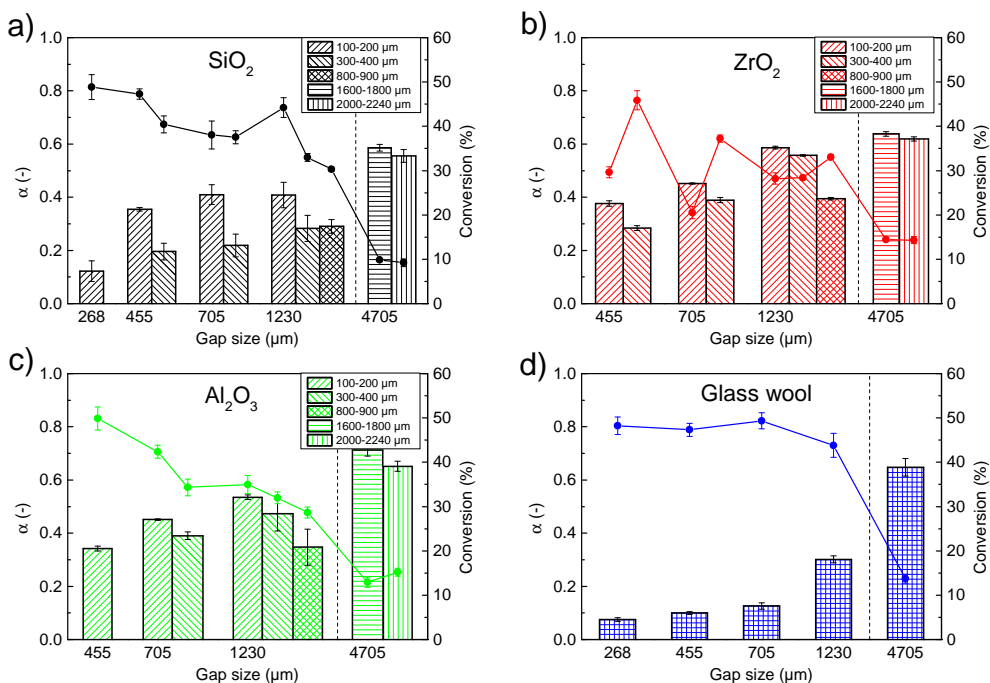


**Figure A.5:** Partial discharging of packed bed DBD (micro) reactors at a constant residence time of 7.5 s. Results are displayed per material type for different sphere sizes (as indicated by the legend) and as a function of gap size, and compared to the conversion of the corresponding packed reactor (solid line).

The burning voltage does not reveal any clear trends, as seen in figure A.6, aside from being mostly discharge gap dependent. Silica, alumina, and glass wool give comparable results, while zirconia is the only exception. It requires the lowest burning voltage, but in contrast the highest peak-to-peak voltage.

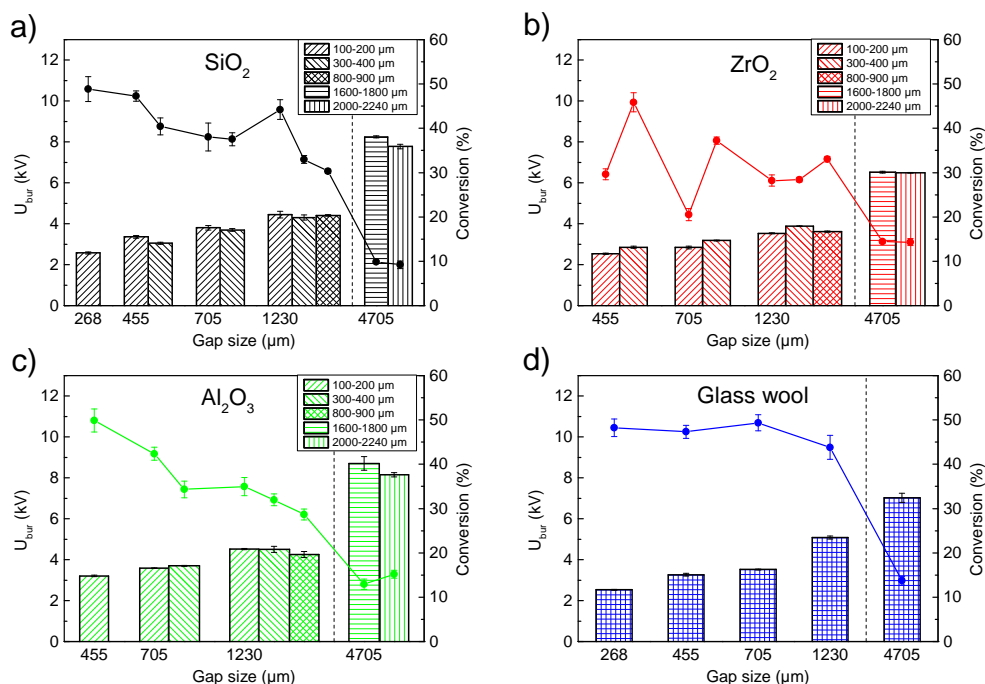


**Figure A.6:** Burning voltage of packed bed DBD (micro) reactors at a constant residence time of 7.5 s. Results are displayed per material type for different sphere sizes (as indicated by the legend) and as a function of gap size, and compared to the conversion of the corresponding packed reactor (solid line).

Finally, the effect of the number of micro discharges can be deduced from figure A.7 and figure A.8. Zirconia gives rise to the highest number of current pulses throughout the whole gap size range. Additionally, silica and zirconia tend to give more micro discharges with smaller spheres within a fixed gap size, while alumina does not show this trend. Glass wool shows a steady increase in number of micro discharges with decreasing gap size. Interestingly, the micro discharges all have about the same average delivered charge, independent of the ‘material-size-gap’ combination.

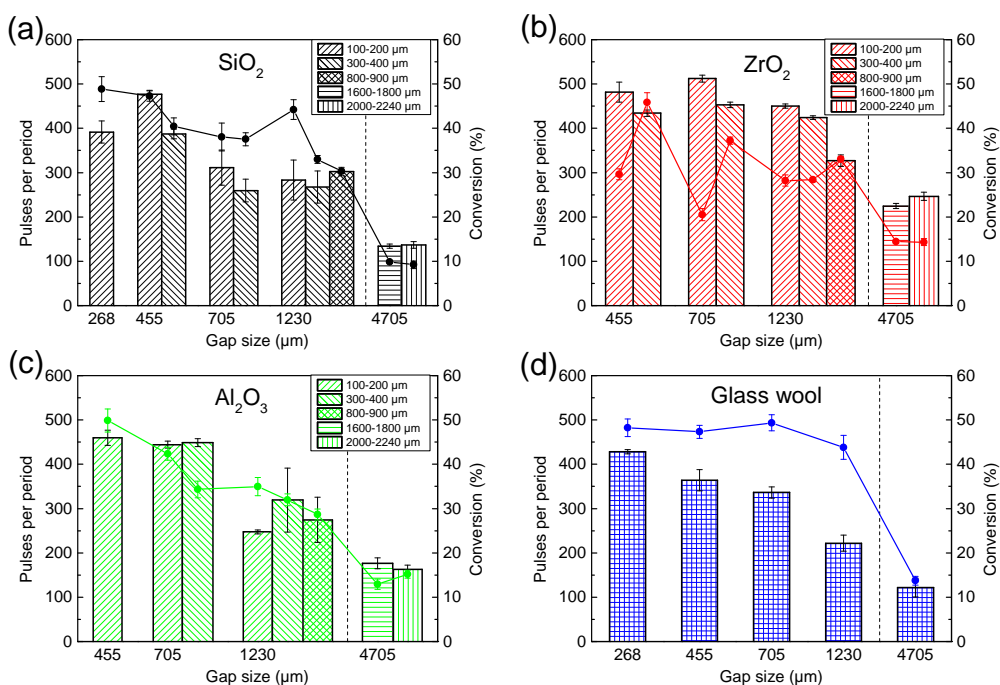


**Figure A.7:** Number of micro discharges in packed bed DBD (micro) reactors at a constant residence time of 7.5 s. Results are displayed per material type for different sphere sizes (as indicated by the legend) and as a function of gap size, and compared to the conversion of the corresponding packed reactor (solid line).

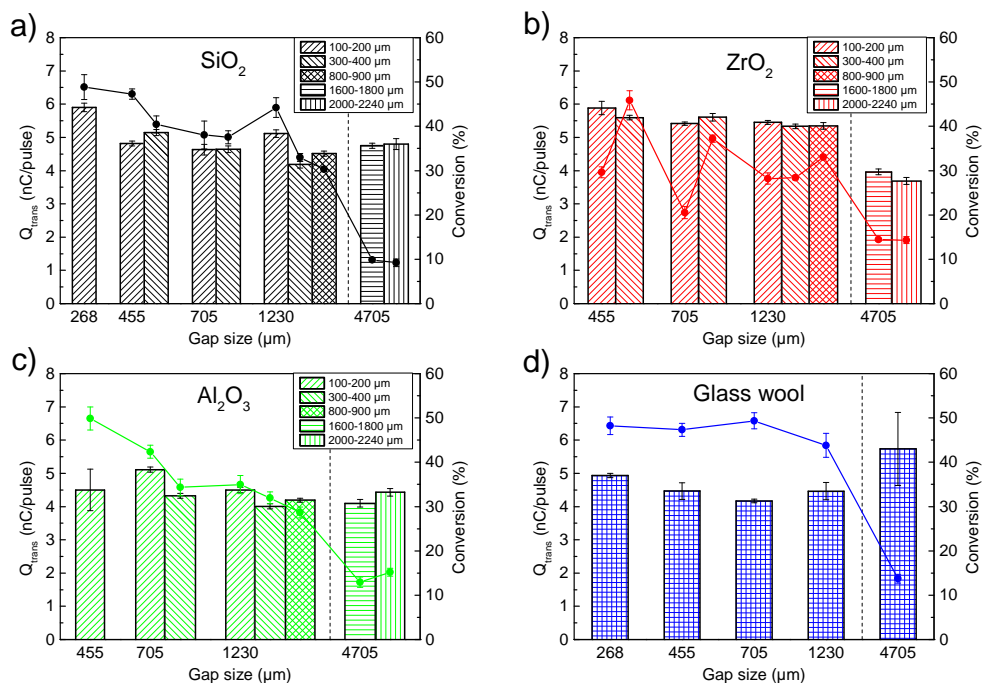


**Figure A.8:** Average displaced charge per micro discharge in packed bed DBD (micro) reactors at a constant residence time of 7.5 s. Results are displayed per material type for different sphere sizes (as indicated by the legend) and as a function of gap size, and compared to the conversion of the corresponding packed reactor (solid line).



```
data=data.data;
```

```
f=3000;
```

```
t=1;
```

```
Q=2;
```

```
U=3;
```

```
Ip=4;
```

```
Ib=5;
```

### Calculation of $U_{min}$ .

```
smoothvoltage=sgolayfilt(data(:,U),3,5001);
smoothcurrent1=sgolayfilt(data(:,Ip),3,1001);
smoothcharge=sgolayfilt(data(:,Q),3,5001);
zero_Q=find(diff(sign(smoothcharge(:,1)))~=0);
zero_dataUmin=data(zero_Q,U);
posUminrows=find(zero_dataUmin(:,1)>0);
negUminrows=find(zero_dataUmin(:,1)<0);
posUmindata=zeros_dataUmin(posUminrows,1);
negUmindata=zeros_dataUmin(negUminrows,1);
posUmin=mean(posUmindata);
negUmin=mean(negUmindata);
```

The slopes of the different sections are calculated next. This section has underwent some versions throughout the years. Visually, determining the 'turning points' or section endpoints  $B$  and  $D$ , are easy to identify. In code however, this is not straightforward, especially in the packed reactors where the Lissajous figures start to look more like ovals instead of parallelograms. Early versions (i) calculated a fit of the first  $x$  points after the min/max points  $A$  and  $C$ , or (ii) determined them via the second derivative of the charge curve as a function of time. These was not always successful due to the ovalness and noise on the signal. Finally the surprisingly easy method used below was made. It first defines the min/max points  $A$  and  $C$ , defines a point  $B$  between  $AC$ , and then fits two linear functions between  $AB$  and  $BC$ . Both fits are scored on their  $R^2$ , the point is moved over a step and the process repeats. When all steps are taken, the point with the highest combined  $R^2$  is taken and dubbed the actual section endpoint  $B$ . The same is done for endpoint  $D$  between  $CA$ . The slopes of four consecutive periods are calculated and averaged.



```

%   B-----A
%   /           /
%   /           /
%   C-----D

Period=1/f*1000;
t0=find(diff(sign(data(:,t)))>0);
t0=t0(1,1);

[c t1]=min(abs(data(:,t)-Period*1));
[c t2]=min(abs(data(:,t)-Period*2));
[c t3]=min(abs(data(:,t)-Period*3));
[c t4]=min(abs(data(:,t)-Period*4));

Periodrows=floor(mean([t1;t2;t3;t4]-[t0;t1;t2;t3]));

U_A=max(smoothvoltage(t0:t1,1));
U_C=min(smoothvoltage(t0:t1,1));
AU=t0+floor(mean(find(smoothvoltage(t0:t1,1)==U_A)));
CU=t0+floor(mean(find(smoothvoltage(t0:t1,1)==U_C)));
U_A1=max(smoothvoltage(t1:t2,1));
AU1=t1+floor(mean(find(smoothvoltage(t1:t2,1)==U_A1)));

Q_A=max(smoothcharge(t0:t1,1));
Q_C=min(smoothcharge(t0:t1,1));
AQ=t0+floor(mean(find(smoothcharge(t0:t1,1)==Q_A)));
CQ=t0+floor(mean(find(smoothcharge(t0:t1,1)==Q_C)));

linfit_AB=[];
linfit_BC=[];
dx=floor(1/16*Periodrows);
dy=floor(1/32*Periodrows);
step=100;
for jj = AQ+dx:step:CU-dx
    [fitobject,gof]=fit(smoothvoltage(AQ:jj,1),smoothcharge(AQ:jj,1),'
        poly1');
    R2_AB=gof.rsquare;
    [fitobject,gof]=fit(smoothvoltage(jj:CU,1),smoothcharge(jj:CU,1),'
        poly1');

```

```

R2_BC=gof.rsquare;
linfit_AB=[linfit_AB;R2_AB];
linfit_BC=[linfit_BC;R2_BC];
end
linfit=[];
for kk=1:length(linfit_AB)
    linfit=[linfit;(1-linfit_AB(kk,1))+(1-linfit_BC(kk,1))];
end
[val, ind]=min(linfit);
B=ind*step+AQ+dx;

B1=B+1*Periodrows;
B2=B+2*Periodrows;
B3=B+3*Periodrows;

linfit_CD=[];
linfit_DA=[];
for jj = CQ+dx:step:AU1-dx
    [fitobject,gof]=fit(smoothvoltage(CQ:jj,1),smoothcharge(CQ:jj,1),'
        poly1');
    R2_CD=gof.rsquare;
    [fitobject,gof]=fit(smoothvoltage(jj:AU1,1),smoothcharge(jj:AU1,1),'
        poly1');
    R2_DA=gof.rsquare;
    linfit_CD=[linfit_CD;R2_CD];
    linfit_DA=[linfit_DA;R2_DA];
end
linfit=[];
for kk=1:length(linfit_CD)
    linfit=[linfit;(1-linfit_CD(kk,1))+(1-linfit_DA(kk,1))];
end
[val, ind]=min(linfit);
D=ind*step+CQ+dx;

D1=D+1*Periodrows;
D2=D+2*Periodrows;
D3=D+3*Periodrows;

```

```

AQ1=AQ+1*Periodrows;
AQ2=AQ+2*Periodrows;
AQ3=AQ+3*Periodrows;
AQ4=AQ+4*Periodrows;
AU4=AU+4*Periodrows;
AU1=AU+1*Periodrows;
AU2=AU+2*Periodrows;
AU3=AU+3*Periodrows;
AU4=AU+4*Periodrows;

CQ1=CQ+1*Periodrows;
CQ2=CQ+2*Periodrows;
CQ3=CQ+3*Periodrows;
CU1=CU+1*Periodrows;
CU2=CU+2*Periodrows;
CU3=CU+3*Periodrows;

AB=coeffvalues(fit(smoothvoltage(AQ:B,1),smoothcharge(AQ:B,1),'poly1'));
BC=coeffvalues(fit(smoothvoltage(B:CU,1),smoothcharge(B:CU,1),'poly1'));
CD=coeffvalues(fit(smoothvoltage(CQ:D,1),smoothcharge(CQ:D,1),'poly1'));
DA1=coeffvalues(fit(smoothvoltage(D:AU1,1),smoothcharge(D:AU1,1),'poly1')
);
A1B1=coeffvalues(fit(smoothvoltage(AQ1:B1,1),smoothcharge(AQ1:B1,1),'
poly1'));
B1C1=coeffvalues(fit(smoothvoltage(B1:CU1,1),smoothcharge(B1:CU1,1),'
poly1'));
C1D1=coeffvalues(fit(smoothvoltage(CQ1:D1,1),smoothcharge(CQ1:D1,1),'
poly1'));
D1A2=coeffvalues(fit(smoothvoltage(D1:AU2,1),smoothcharge(D1:AU2,1),'
poly1'));
A2B2=coeffvalues(fit(smoothvoltage(AQ2:B2,1),smoothcharge(AQ2:B2,1),'
poly1'));
B2C2=coeffvalues(fit(smoothvoltage(B2:CU2,1),smoothcharge(B2:CU2,1),'
poly1'));
C2D2=coeffvalues(fit(smoothvoltage(CQ2:D2,1),smoothcharge(CQ2:D2,1),'
poly1'));
D2A3=coeffvalues(fit(smoothvoltage(D2:AU3,1),smoothcharge(D2:AU3,1),'
poly1'));
A3B3=coeffvalues(fit(smoothvoltage(AQ3:B3,1),smoothcharge(AQ3:B3,1),'

```

```

    poly1'));
B3C3=coeffvalues(fit(smoothvoltage(B3:CU3,1),smoothcharge(B3:CU3,1),'
    poly1'));
C3D3=coeffvalues(fit(smoothvoltage(CQ3:D3,1),smoothcharge(CQ3:D3,1),'
    poly1'));
D3A4=coeffvalues(fit(smoothvoltage(D3:AU4,1),smoothcharge(D3:AU4,1),'
    poly1'));

meanAB=mean([AB;A1B1;A2B2;A3B3]);
meanBC=mean([BC;B1C1;B2C2;B3C3]);
meanCD=mean([CD;C1D1;C2D2;C3D3]);
meanDA=mean([DA1;D1A2;D2A3;D3A4]);

xline=[-10:0.1:10];
lineAB=xline*meanAB(1,1)+meanAB(1,2);
lineBC=xline*meanBC(1,1)+meanBC(1,2);
lineCD=xline*meanCD(1,1)+meanCD(1,2);
lineDA=xline*meanDA(1,1)+meanDA(1,2);

plot(data(t0:t4,U),data(t0:t4,Q),xline,lineAB,xline,lineBC,xline,lineCD,
    xline,lineDA)
axis([-20 20 -2 2]);

```

The number of microdischarges are determined in the DA section by smoothing and flattening the current curve, taking the first derivative via the Riemann sum, and counting the discharges as sharp slope changes. A threshold is used to differentiate the actual pulses from the resonant pulses.

```

%% Count number of micro discharges
% Detect discharges
smoothcurrent1=sgolayfilt(data(:,Ip),3,10001);
correctedIp=data(:,Ip)-smoothcurrent1(:,1);
smoothcurrent2=sgolayfilt(correctedIp(:,1),3,251);
smoothcurrent2(smoothcurrent2<0)=0;
% Calculating first derivative of current to detect pulses in DA region
eafgI1=zeros(250,1);
parfor jj = D:AQ1
    eafgI1=[eafgI1;(mean(smoothcurrent2(jj:(jj+250),1))-mean(
        smoothcurrent2((jj-250):jj,1)))/(250*(data(2,t)-data(1,t)))]];
end

```

---

```

eafgI2=zeros(250,1);
parfor jj = D1:AQ2
    eafgI2=[eafgI2;(mean(smoothcurrent2(jj:(jj+250),1))-mean(
        smoothcurrent2((jj-250):jj,1)))/(250*(data(2,t)-data(1,t)))];
end
eafgI3=zeros(250,1);
parfor jj = D2:AQ3
    eafgI3=[eafgI3;(mean(smoothcurrent2(jj:(jj+250),1))-mean(
        smoothcurrent2((jj-250):jj,1)))/(250*(data(2,t)-data(1,t)))];
end
eafgI4=zeros(250,1);
parfor jj = D3:AQ4
    eafgI4=[eafgI4;(mean(smoothcurrent2(jj:(jj+250),1))-mean(
        smoothcurrent2((jj-250):jj,1)))/(250*(data(2,t)-data(1,t)))];
end

eafgI1=eafgI1-0.5;
eafgI2=eafgI2-0.5;
eafgI3=eafgI3-0.5;
eafgI4=eafgI4-0.5;
Num_zeros1=diff(sign(eafgI1));
indx_down1=find(Num_zeros1<0);
Num_zeros2=diff(sign(eafgI2));
indx_down2=find(Num_zeros2<0);
Num_zeros3=diff(sign(eafgI3));
indx_down3=find(Num_zeros3<0);
Num_zeros4=diff(sign(eafgI4));
indx_down4=find(Num_zeros4<0);

Num_peaksI=length(indx_down1)+length(indx_down2)+length(indx_down3)+
    length(indx_down4);
Av_num_peaksI=Num_peaksI/4;

The remaining parameters are calculated, i.e. displaced current per cycle,
average displaced charge per discharge, plasma power, power source power,
plasma RMS current, power source RMS current, and peak-to-peak voltage. All
are exported to the .dat file. A plot of the fit is made and saved as a .gif file.

Q_disp=mean(lineAB-lineCD);
ak)

```

---

```
Av_Q_peak=Q_disp/Av_num_peaksI*1000;

plasmapower=mean(data(t0:t4,U).*data(t0:t4,Ip))*1000;

sourcepower=mean(data(t0:t4,U).*data(t0:t4,Ib));

RMSIp=rms(data(t0:t4,Ip))*1000;

RMSIb=rms(data(t0:t4,Ib));

Upp=abs(U_A)+abs(U_C);

fprintf(fileID,'%s \t%6.4f \t%6.4f \t%6.4f \t%6.4f \t%6.4f \t%6.4f \t%6.4f \t%6.4f \t%6.4f \t%6.4f \t%6.4f \t%6.4f \t%6.4f \t%6.4f \t%6.4f \t%6.4f \n',file,posUmin, negUmin,Upp,meanAB(1,1),meanBC(1,1),meanCD(1,1),meanDA(1,1), plasmapower,sourcepower,RMSIp,RMSIb,Av_num_peaksI,Av_Q_peak);

file=strcat(file,'.png');
print(gcf,file,'-dpng');
end
disp('Done')
```

### A.3.2 Packed reactor

In the packed reactor, adjusted smoothing and threshold values are used for the micro discharge determination due to their smaller magnitude. The rest of the code is the same.

```
smoothcurrent1=sgolayfilt(data(:,Ip),3,10001);
correctedIp=data(:,Ip)-smoothcurrent1(:,1);
smoothcurrent2=sgolayfilt(correctedIp(:,1),3,31);
smoothcurrent2(smoothcurrent2<0.0005)=0;

eafgI1=zeros(30,1);
parfor jj = D:AQ1
    eafgI1=[eafgI1;(mean(smoothcurrent2(jj:(jj+30),1))-mean(smoothcurrent2((jj-30):jj,1)))/(30*(data(2,t)-data(1,t)))]';
end
eafgI2=zeros(30,1);
```

```

parfor jj = D1:AQ2
    eafgI2=[eafgI2;(mean(smoothcurrent2(jj:(jj+30),1))-mean(smoothcurrent2
        ((jj-30):jj,1)))/(30*(data(2,t)-data(1,t)))]];
end
eafgI3=zeros(30,1);
parfor jj = D2:AQ3
    eafgI3=[eafgI3;(mean(smoothcurrent2(jj:(jj+30),1))-mean(smoothcurrent2
        ((jj-30):jj,1)))/(30*(data(2,t)-data(1,t)))]];
end
eafgI4=zeros(30,1);
parfor jj = D3:AQ4
    eafgI4=[eafgI4;(mean(smoothcurrent2(jj:(jj+30),1))-mean(smoothcurrent2
        ((jj-30):jj,1)))/(30*(data(2,t)-data(1,t)))]];
end

Num_zerosI1=diff(sign(eafgI1));
indx_downI1=find(Num_zerosI1<0);
Num_zerosI2=diff(sign(eafgI2));
indx_downI2=find(Num_zerosI2<0);
Num_zerosI3=diff(sign(eafgI3));
indx_downI3=find(Num_zerosI3<0);
Num_zerosI4=diff(sign(eafgI4));
indx_downI4=find(Num_zerosI4<0);

Num_peaksI=length(indx_downI1)+length(indx_downI2)+length(indx_downI3)+
    length(indx_downI4);
Av_num_peaksI=(Num_peaksI/4);

```





# Appendix B

## Appendix of Chapter 3: Core-shell

### B.1 Schematic representation of the spray coating set-up used

Figure B.1 shows a schematic representation of the spray coating set-up used in this work. It is an in-house built pan coating set-up comprised of a rotating pan with agitation fins added to the inside to disturb the rolling spheres into tumbling over each other. The coating suspension is added by a gravity fed spray gun operated with compressed dry air at 1-1.5 barg. The suspension is gradually added and sprayed on the spheres in the pan, while the remaining fraction is left in a beaker on a stirring plate. The pan and contents are continuously heated by a hot air gun operated at maximum heat but medium air flow rate, to maximise the heating capacity but to minimise deflection of the sprayed droplets away from the tumbling spheres.

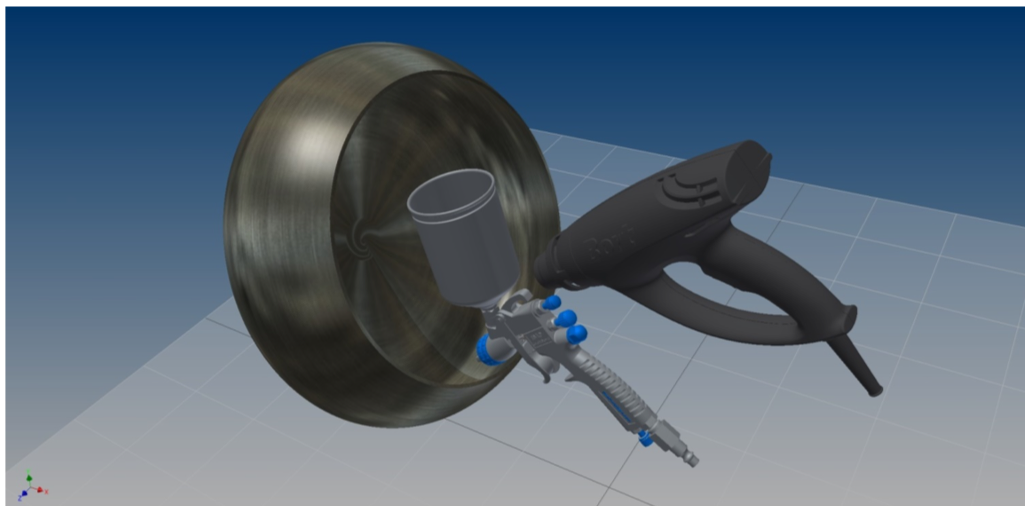


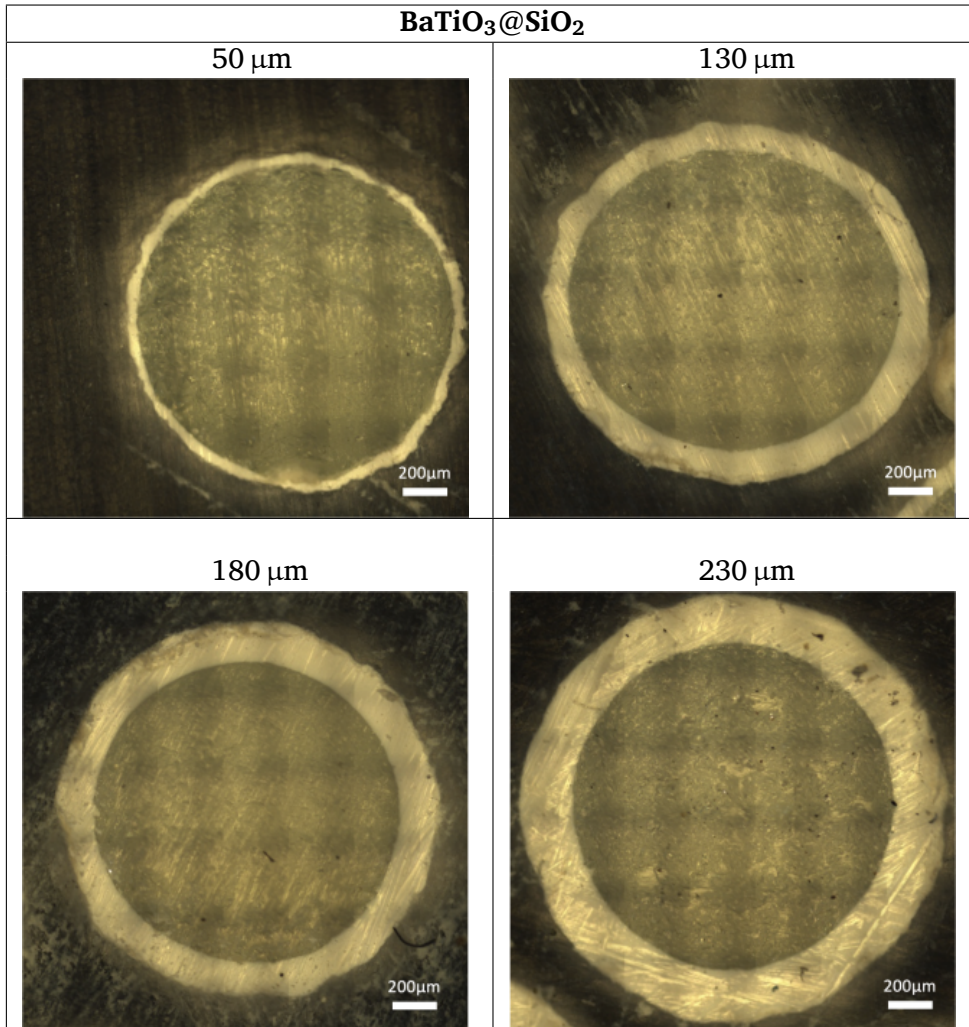
**Figure B.1:** Schematic representation of the spray coating set-up used in this work.

## **B.2 Example of four layer thicknesses of BaTiO<sub>3</sub>@SiO<sub>2</sub> core-shell spheres**

Table B.1 shows an example of the four layer thicknesses of BaTiO<sub>3</sub> applied on the 1.6-1.8 mm SiO<sub>2</sub> cores. These images are obtained by embedding samples of about 25 spheres of the different core-shell spheres in an epoxy resin and sanding it down to about half-way the spheres. The spheres were then imaged by light microscopy by overlapping multiple exposures (hence the visible rectangular pattern). The average layer thicknesses were measured by ImageJ analysis.

Uniform coverage of the entire spheres was obtained for every layer thickness but some shell roughness is present due to the tumbling spray coating method.

Table B.1: Example of four layer thicknesses of BaTiO<sub>3</sub>@SiO<sub>2</sub> core-shell spheres.



## B.3 Raw data of figure 3.1 and figure 3.2

**Table B.2:** Conversion and energy efficiency of (i) the empty DBD reactor, both at the same flow rate and residence time (RT) as the packed bed reactor, and (ii) of all samples used in this work (including pure uncoated spheres and the various combinations of core-shell spheres) as shown in figure 3.1 and figure 3.2.

Sample	Size (mm) / Shell thickness ( $\mu\text{m}$ )	Conversion (%)	Energy efficiency (%)
Empty (= Flow)	/	$11 \pm 1$	$3.0 \pm 0.3$
Empty (= RT)	/	$6.4 \pm 0.8$	$3.2 \pm 0.5$
SiO <sub>2</sub>	1.6-1.8	$9.8 \pm 0.3$	$2.7 \pm 0.1$
Al <sub>2</sub> O <sub>3</sub>	1.6-1.8	$13 \pm 1$	$3.5 \pm 0.3$
BaTiO <sub>3</sub>	1.6-1.8	$13 \pm 1$	$3.5 \pm 0.3$
SiO <sub>2</sub>	2.0-2.24	$9.2 \pm 0.8$	$2.5 \pm 0.2$
Al <sub>2</sub> O <sub>3</sub>	2.0-2.24	$15.2 \pm 0.9$	$4.1 \pm 0.2$
BaTiO <sub>3</sub>	2.0-2.24	$10.9 \pm 0.7$	$3.0 \pm 0.2$
SiO <sub>2</sub> @SiO <sub>2</sub>	50	$8 \pm 1$	$2.1 \pm 0.3$
Al <sub>2</sub> O <sub>3</sub> @SiO <sub>2</sub>	70	$8.5 \pm 0.4$	$2.2 \pm 0.1$
Al <sub>2</sub> O <sub>3</sub> @SiO <sub>2</sub>	140	$9.7 \pm 0.9$	$2.7 \pm 0.2$
Al <sub>2</sub> O <sub>3</sub> @SiO <sub>2</sub>	185	$10.2 \pm 0.6$	$2.7 \pm 0.2$
Al <sub>2</sub> O <sub>3</sub> @SiO <sub>2</sub>	250	$9.9 \pm 0.9$	$2.7 \pm 0.2$
BaTiO <sub>3</sub> @SiO <sub>2</sub>	50	$8.7 \pm 0.7$	$2.4 \pm 0.2$
BaTiO <sub>3</sub> @SiO <sub>2</sub>	125	$9.8 \pm 0.8$	$2.7 \pm 0.2$
BaTiO <sub>3</sub> @SiO <sub>2</sub>	180	$11.2 \pm 0.8$	$3.0 \pm 0.2$
BaTiO <sub>3</sub> @SiO <sub>2</sub>	225	$11.9 \pm 0.9$	$3.2 \pm 0.2$
SiO <sub>2</sub> @Al <sub>2</sub> O <sub>3</sub>	55	$15.4 \pm 0.9$	$4.2 \pm 0.2$
SiO <sub>2</sub> @Al <sub>2</sub> O <sub>3</sub>	100	$10.8 \pm 0.8$	$2.9 \pm 0.2$
SiO <sub>2</sub> @Al <sub>2</sub> O <sub>3</sub>	290	$11.8 \pm 0.6$	$3.2 \pm 0.2$
SiO <sub>2</sub> @Al <sub>2</sub> O <sub>3</sub>	405	$12.0 \pm 0.7$	$3.3 \pm 0.2$
Al <sub>2</sub> O <sub>3</sub> @Al <sub>2</sub> O <sub>3</sub>	55	$7.9 \pm 0.6$	$2.2 \pm 0.2$
BaTiO <sub>3</sub> @Al <sub>2</sub> O <sub>3</sub>	75	$14 \pm 1$	$3.8 \pm 0.3$
BaTiO <sub>3</sub> @Al <sub>2</sub> O <sub>3</sub>	90	$11.3 \pm 0.7$	$3.0 \pm 0.2$
BaTiO <sub>3</sub> @Al <sub>2</sub> O <sub>3</sub>	160	$11 \pm 1$	$3.2 \pm 0.3$
BaTiO <sub>3</sub> @Al <sub>2</sub> O <sub>3</sub>	230	$14.3 \pm 0.4$	$3.8 \pm 0.1$
SiO <sub>2</sub> @BaTiO <sub>3</sub>	60	$10.8 \pm 0.7$	$2.9 \pm 0.2$
SiO <sub>2</sub> @BaTiO <sub>3</sub>	250	$16 \pm 1$	$4.3 \pm 0.3$
SiO <sub>2</sub> @BaTiO <sub>3</sub>	370	$13.0 \pm 0.8$	$3.5 \pm 0.2$
SiO <sub>2</sub> @BaTiO <sub>3</sub>	465	$12 \pm 1$	$3.2 \pm 0.3$
Al <sub>2</sub> O <sub>3</sub> @BaTiO <sub>3</sub>	60	$11.0 \pm 0.6$	$3.0 \pm 0.2$
Al <sub>2</sub> O <sub>3</sub> @BaTiO <sub>3</sub>	125	$8.3 \pm 0.8$	$2.3 \pm 0.2$
Al <sub>2</sub> O <sub>3</sub> @BaTiO <sub>3</sub>	165	$10 \pm 1$	$2.8 \pm 0.3$
Al <sub>2</sub> O <sub>3</sub> @BaTiO <sub>3</sub>	235	$10.2 \pm 0.4$	$2.8 \pm 0.1$
BaTiO <sub>3</sub> @BaTiO <sub>3</sub>	55	$10.8 \pm 0.9$	$2.9 \pm 0.2$



# Appendix C

## Appendix of Chapter 4: CO<sub>2</sub> kinetics

### C.1 Calculation of the packing efficiency in a coaxial DBD (micro) plasma reactor

#### C.1.1 Description

In order to compare the effect of residence time when adding a spherical packing material to the reactor, adjusted flow rates are needed to compensate for the loss of available reaction volume. One might assume a close packing efficiency of 0.74048 in an infinitely big volume, but this value is far from reality due to inefficient stacking of spheres, while loading the coaxial small reactor volume and due to the existence of walls.

Therefore, we developed a code that simulates the stacking of spheres in a coaxial reactor in a simple but realistic way. The main principle of the code is the sequential “dropping” of spheres in the reactor. This is done by repeatedly generating random spheres within the reactor boundaries, stepwise lowering them until they collide with either the bottom of the reactor or another sphere, and picking the one with the lowest potential, until the reactor is filled to its height  $h$ , as schematically displayed in figure C.1. A vertical tube is assumed with the dimensions given in chapter 4, and subdivided in a number of radial segments depending on the reactor circumference to sphere radius ratio (6% segments for the 100-200  $\mu\text{m}$  spheres in the 455  $\mu\text{m}$  gap to full circle for the 1600-1800  $\mu\text{m}$  spheres in the 4705  $\mu\text{m}$  gap). A random sphere radius (between the

maximum radius  $S_{\max}$  and minimum radius  $S_{\min}$ ) and 1000 x- and y-coordinates are generated within a segment, with a z-value of 10 times  $S_{\max}$  above the bottom of the reactor or the last placed sphere, representing 1000 random spheres that will fall in the reactor. These spheres are consecutively lowered with decreasing steps until they hit either the bottom of the reactor or another sphere, and their end location is stored. If a sphere hits the bottom of the reactor, the generation is stopped and the coordinates and radius are recorded, otherwise the sphere with the lowest potential (z-value) will be picked and recorded, as the placed sphere. The code repeats itself, moving over one segment per sphere, to gradually fill the reactor with a large enough generated density, until the whole reactor is filled and the height  $h$  of the reaction volume is reached. Since the z-value is the center of the sphere, spheres just overlapping the bottom and the top of the reaction volume are deleted, and the packing efficiency is calculated based on the reaction volume and the individual sphere volumes (based on individual radii).

This calculation was performed in MATLAB and repeated 10 times for statistical review. 1000 random spheres, in combination with the restricted consecutive segments, showed to be optimal in obtaining an as dense as possible packed reactor. Higher sphere numbers only resulted in longer calculation times. Examples of spheres packed in the reactor via this code, are displayed in figure C.2. These are just fractions of the whole simulated packing for demonstration purposes, actual calculation of packing efficiency is done for the entire 100 mm reaction zone.



## C.1 Calculation of the packing efficiency in a coaxial DBD (micro) plasma reactor

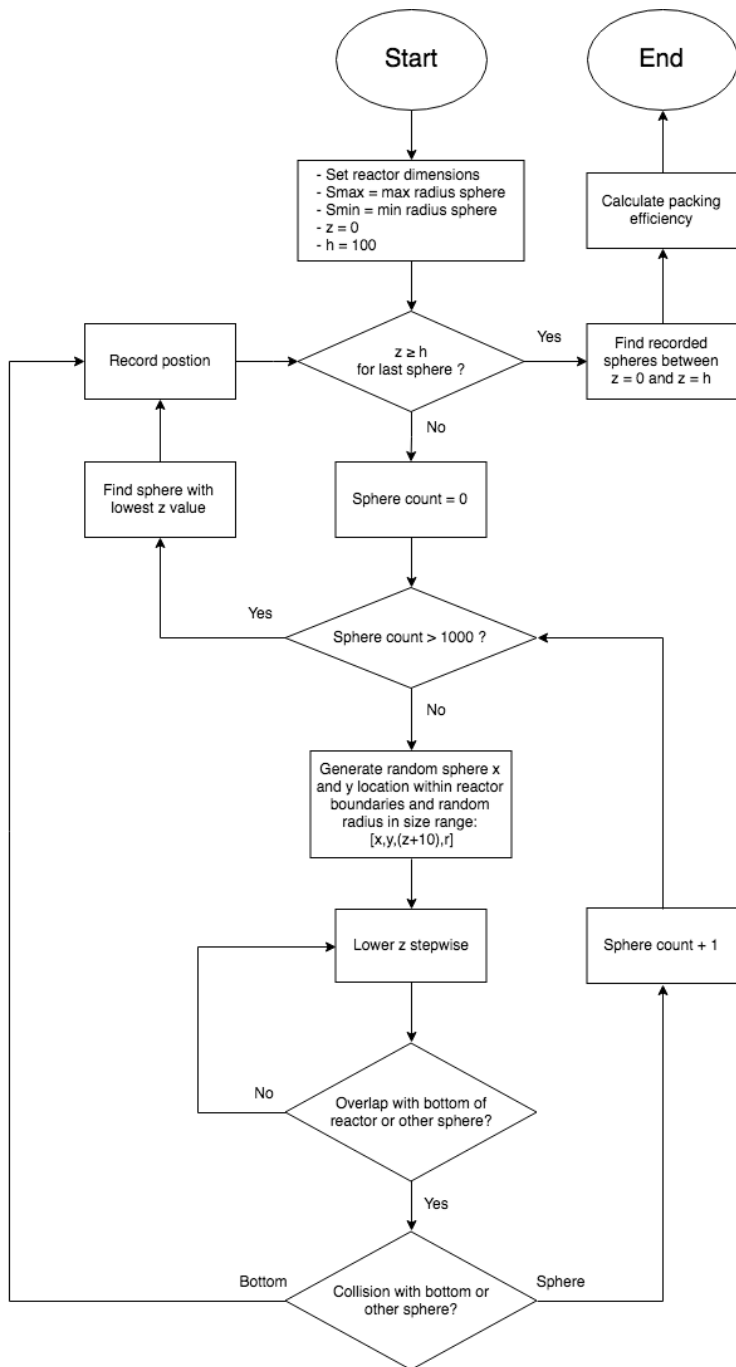


**Figure C.1:** Schematic representation of the MATLAB code used to calculate the packing efficiency of the spherical packing materials in a coaxial DBD (micro) reactor.

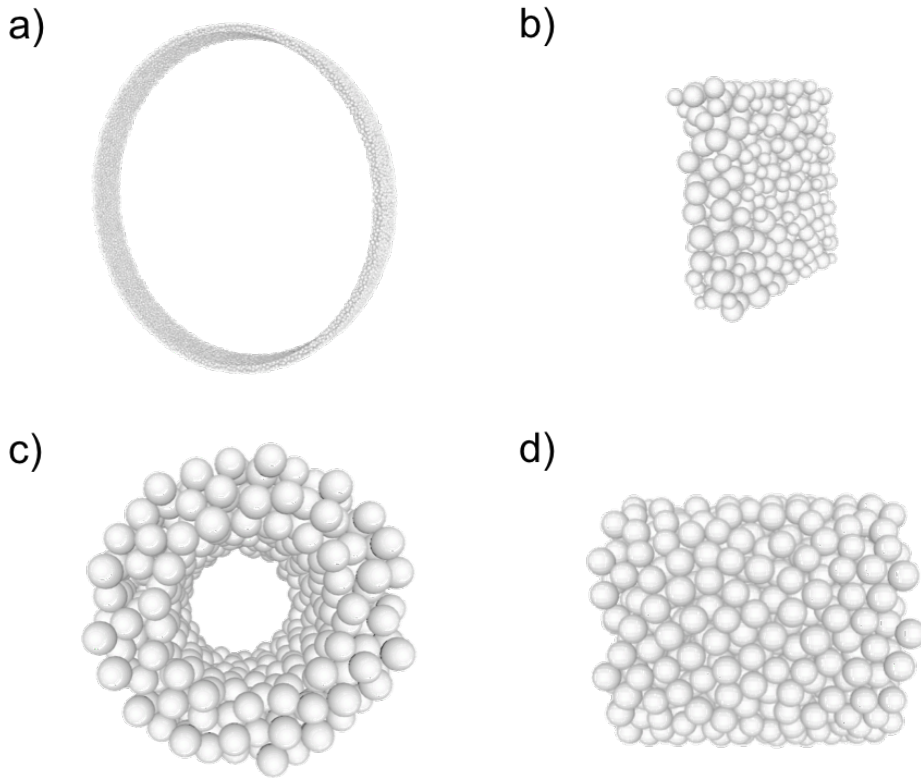


**Figure C.2:** Examples of different generated packings by the MATLAB code, for (a) 100-200  $\mu\text{m}$  spheres in a 455  $\mu\text{m}$  gap for a height of 2mm and (b) a zoomed-in section of (a); as well (c) 1600-1800  $\mu\text{m}$  spheres in a 4705  $\mu\text{m}$  gap for a height of 20 mm in top-view and (d) side-view.

### C.1.2 MATLAB code

This code shows an example code for the 455  $\mu\text{m}$  gap filled with 100-200  $\mu\text{m}$  spheres. All size units are in mm.

Initialize settings such as tube radii, height, reactor volume, size range of spheres, some empty matrices for later, and sphere coordinates for later plotting of the spheres in a 3D graph.

```
clear all

fileID = fopen('Sphere_number.dat','w');

Ro=17.41/2;
Ri=16.5/2;
```

## C.1 Calculation of the packing efficiency in a coaxial DBD (micro) plasma reactor

---

```
h=100;
volume_r=(Ro^2-Ri^2)*pi*h;

size=[0.1,0.2];

sphere_number=[];

Smax=size(1,2)/2;
Smin=size(1,1)/2;

sphere_numbers=[];

centers=[];
rads=[];
test=0;

[X,Y,Z]=sphere;
```

Next the main routine of the code starts, i.e. generation and dropping of spheres. A random sphere radius  $r$  is generated, followed by a for-loop that sequentially generates a sphere location based on an tube angle  $A$  and radius  $R$  at a height  $z$   $h$  mm above the reactor bottom or two times  $r$  above the highest dropped sphere so far. Within the for-loop, the sphere is dropped in five ( $k$ ) sequentially smaller steps until it either touches the bottom (immediate stop of the for-loop) or it touches another sphere; this is tested by the 'overlap\_frac'-subroutine, see lower. All 1000 (or less in case of a floor hit) sphere end locations are recorded in the *spheres* matrix for the next step.

Note that the sphere angle  $A$  is randomly generated in a 6% section of the tube. Originally, 1/16th (6.25%) sections were used but this creates hard edges of the sections. 6% (slightly lower than 1/16) ensures that sections overlap after a whole turn around the reactor, requiring 50 sections to finally get the same section again. This effect is enhanced by the  $j/4$  term in the code line, shifting the dropping section over by a quarter of the section providing an overlap between sequential sections.

The *frac* term seen in the code is a speed optimisation in the code. The original 'overlap'-subroutine checked the current sphere compared to all withheld spheres in previous for-loops. This gets time intensive if every 1000 possible spheres

have to be compared to up to 10000's of spheres. Therefore, the 'frac counter' counts how many spheres fit in two layers of stacked spheres. The 'overlap\_frac'-subroutine then compares the current dropped spheres only to the last *frac* number of spheres in the *spheres* matrix.

```

j=1;
frac=-1;

while test<(h+4*Smax)
    hit=0;
    r=Smin+(Smax-Smin).*rand(1); % radius varies between
    spheres=[];
    floor_hit=0;
    falling=[];
    if j==1
        frac=frac+1;
    else
        if centers(end,3)<(((Smax+Smin)/2)*4)
            frac=frac+1;
        end
    end
end
for n=1:1000
    R=(Ri+r)+((Ro-r)-(Ri+r)).*rand(1);
    A=(j/4-1/4)*2*pi*0.06+2*pi*0.06*rand(1);
    x=cos(A)*R;
    y=sin(A)*R;
    decrease=r;
    if j==1
        z=h;
    else
        z=max(centers(end-frac+1:end,3))+decrease/10+2*r;
    end
    falling=[x,y,z];
    not_ovlp=1;
    not_ovlp_f=1;
    not_ovlp_w=1;
    for k=1:5
        stop=0;
        while stop~=1

```

```

        if not_ovlp==1 & not_ovlp_f==1
            z=z-decrease/(10^k);
        elseif not_ovlp_f==0
            stop=1;
            z=z+decrease/(10^k);
            floor_hit=1;
        else
            stop=1;
            z=z+decrease/(10^k);
        end
        falling=[falling(end,1),falling(end,2),z];
        if j==1
            not_ovlp=1;
            not_ovlp_f=(z-r)>0;
        else
            [not_ovlp, not_ovlp_f]=overlap_frac( centers, rads, r
                , falling, frac);
        end
    end
end
spheres=[spheres;falling];
end

```

The 'overlap\_frac'-subroutine:

```

function [no, nof] = overlap( centers, rads, r, falling, frac)
    center_dist = sqrt(sum(bsxfun(@minus,centers(end-frac+1:end,:),falling
        (end,:)).^2,2));
    radsum = rads(end-frac+1:end,:) + r;
    no = all(center_dist >= radsum);
    nof=(falling(end,3)-r)>0;
end

```

Subsequently, the sphere with the lowest potential (read lowest z-value) is calculated and its center coordinates and radius is recoded in *centers* and *rads*. A status (sphere number, last z-value, target height, and progress in %) is displayed in the MATLAB command window to check the calculation progress.

```

[c low_pot]=min(spheres(:,3));
centers=[centers;spheres(low_pot,:)];
rads=[rads;r];

```

```
surf(X.*rads(end,1)+centers(end,1),Y.*rads(end,1)+centers(end,2),Z.*
     rads(end,1)+centers(end,3))
hold on

display=[j,centers(end,3),(h+4*Smax),centers(end,3)/(h+4*Smax)*100];
disp(display)
```

Finally, the code checks if the target height is reached ( $h$  plus 4 times  $S_{max}$ ). If not, the code repeats; if so, the code selects all dropped spheres that are positioned between the tube bottom and top. A packing efficiency is calculated and reported in the .dat file. Notice that the tube in the code shifted upwards by  $S_{max}$  giving the shifted test margins of  $2 * S_{max}$  and  $h$  as the centers of the spheres are tested.

```
j=j+1;
test=centers(end,3)+rads(end,1);
if test>(h+4*Smax)
    list=find(centers(:,3)>(2*Smax) & centers(:,3)<h);
    centers=centers(list,:);
    rads=rads(list,:);
    volume_s=rads.^3*4/3*pi;
    sphere_number=[size(s,1),length(list),(sum(volume_s)/volume_r)];
end
end

fprintf(fileID,'%6.4f \t%6.4f \t%6.4f \n',sphere_numbers(1,1),
        sphere_numbers(1,2),sphere_numbers(1,3));
disp('Done')
```

### C.1.3 Results for different gap and sphere sizes

Table C.1: Calculated packing efficiencies for the gap and sphere size combinations used in this work.

Gap size ( $\mu\text{m}$ )	Sphere size ( $\mu\text{m}$ )	Packing efficiency (%)
268	100-200	$44.08 \pm 0.04$
455	100-200	$49.51 \pm 0.02$
	300-400	$42.51 \pm 0.02$
705	100-200	$50.55 \pm 0.02$
	300-400	$47.57 \pm 0.04$
1230	100-200	$52.10 \pm 0.03$
	300-400	$49.14 \pm 0.03$
	800-900	$40.16 \pm 0.04$
4705	1600-1800	$48.27 \pm 0.07$
	2000-2240	$46.51 \pm 0.06$

## C.2 Fit equation

### C.2.1 Derivation of general operational fit equation

A general operational fit equation was derived to fit the data obtained from the experiments, to further characterize them with an operational rate coefficient and operational equilibrium for the CO<sub>2</sub> dissociation reaction:



The forward and back reactions are assumed to obey simple first order rate laws, lumping together the more complex mechanisms at play. This functional form allows to directly fit experimental mole fractions; for the dissociation reaction, only the CO<sub>2</sub> concentration can be used, whereas the back reaction can be equivalently written as a first order in either the measured O<sub>2</sub> or CO concentration. As such, the used reaction rate expressions do not directly correspond to any known elementary reaction. Rather, a first order approximation of the global reaction rate is used to derive a simple analytic expression that can describe the dependence of the conversion on the residence time. As can be observed in figure 4.1 in chapter 4, this relation can indeed capture the key characteristics of the overall process, justifying the somewhat crude simplifications used here. Constant pressure is assumed (maintained during measurements) for components  $y$  and we have:

$$P_y \sim x_y \quad (C.2)$$

$$P \sim cte \Rightarrow V_y \sim x_y \quad (C.3)$$

### C.2.2 Dissociation reaction

CO<sub>2</sub> loss and formation rates are defined based on reaction rate coefficients  $k$  and mole fractions  $x$ :

$$-r_{CO_2} = k_1 x_{CO_2} \quad (C.4)$$

$$r_{CO_2} = 2k_2 x_{O_2} \quad (C.5)$$



Combining equations C.4 and C.5 in an overall rate:

$$\frac{dx_{CO_2}}{dt} = 2k_2x_{O_2} - k_1x_{CO_2} \quad (C.6)$$

Knowing that  $2x_{O_2} \cong x_{CO}$  and that:

$$x_{CO_2} + x_{CO} + x_{O_2} = 1 \Leftrightarrow x_{O_2} = \frac{1 - x_{CO_2}}{3} \quad (C.7)$$

We can replace  $x_{O_2}$  in equation C.6:

$$\frac{dx_{CO_2}}{dt} = \frac{2k_2}{3} - \left(k_1 + \frac{2}{3}k_2\right)x_{CO_2} \quad (C.8)$$

Let:

$$\begin{aligned} A &= \frac{2k_2}{3} \\ B &= k_1 + \frac{2}{3}k_2 \end{aligned} \quad (C.9)$$

Replacing equations C.9 in equation C.8 results in:

$$\frac{dx_{CO_2}}{dt} = A - Bx_{CO_2} \quad (C.10)$$

Integrating equation C.10 from  $t = 0 \rightarrow t$  and rewriting it for  $x_{CO_2}$ :

$$\int_1^{x_{CO_2}} \frac{dx_{CO_2}}{A - Bx_{CO_2}} = \int_0^t dt \quad (C.11)$$

$$-\frac{1}{B} [\ln(A - Bx_{CO_2})]_1^{x_{CO_2}} = [t]_0^t \quad (C.12)$$

$$\ln(A - Bx_{CO_2}) - \ln(A - B) = -Bt \quad (C.13)$$

$$\ln\left(\frac{A - Bx_{CO_2}}{A - B}\right) = -Bt \quad (C.14)$$

$$\frac{A}{A - B} - \frac{B}{A - B}x_{CO_2} = e^{-Bt} \quad (C.15)$$

$$x_{CO_2} = \frac{A}{B} - \frac{A - B}{B}e^{-Bt} \quad (C.16)$$

Rewriting equation C.16 gives an exponentially decreasing expression, dictated by a rate constant  $B$ , as expressed in equation C.9 above, corresponding to an overall rate coefficient for the dissociation reaction  $k_d$ , and a limiting value  $A/B$  (at infinite residence time) corresponding to an equilibrium mole fraction  $x_{e,CO_2}$  for CO<sub>2</sub>:

$$x_{CO_2} = \frac{A}{B} - \left( \frac{A-B}{B} - 1 \right) e^{-Bt} \Leftrightarrow x_{CO_2} = x_{e,CO_2} - (x_{e,CO_2} - 1) e^{-k_d t} \quad (C.17)$$

### C.2.3 Oxidation reaction

O<sub>2</sub> loss and formation rates are defined:

$$-r_{O_2} = k_2 x_{O_2} \quad (C.18)$$

$$r_{O_2} = \frac{1}{2} k_1 x_{CO_2} \quad (C.19)$$

Combining equations C.18 and C.19 in an overall rate:

$$\frac{dx_{O_2}}{dt} = \frac{1}{2} k_1 x_{CO_2} - k_2 x_{O_2} \quad (C.20)$$

Replacing  $x_{CO_2}$  in equation C.20, in a similar way as above:

$$x_{CO_2} + x_{CO} + x_{O_2} = 1 \Leftrightarrow x_{CO_2} = 1 - 3x_{O_2} \quad (C.21)$$

Yields:

$$\frac{dx_{O_2}}{dt} = \frac{k_1}{2} - \left( \frac{3}{2} k_1 + k_2 \right) x_{O_2} \quad (C.22)$$

Let:

$$C = \frac{k_1}{2} \quad (C.23)$$

$$B = \frac{3}{2} k_1 + k_2$$

Replacing equations C.23 in equation C.22 results in:

$$\frac{dx_{O_2}}{dt} = C - Bx_{O_2} \quad (C.24)$$

Integrating equation C.24 from  $t = 0 \rightarrow t$  and rewriting it for  $x_{O_2}$ :

$$\int_{1/3}^{x_{CO_2}} \frac{dx_{O_2}}{C - Dx_{O_2}} = \int_0^t dt \quad (C.25)$$

$$-\frac{1}{D} [\ln(C - Dx_{O_2})]_{1/3}^{x_{O_2}} = [t]_0^t \quad (C.26)$$

$$\ln(C - Dx_{O_2}) - \ln\left(C - \frac{D}{3}\right) = -Dt \quad (C.27)$$

$$\ln\left(\frac{C - Dx_{O_2}}{C - \frac{D}{3}}\right) = -Dt \quad (C.28)$$

$$\frac{C}{C - \frac{D}{3}} - \frac{D}{C - \frac{D}{3}}x_{O_2} = e^{-Dt} \quad (C.29)$$

$$x_{O_2} = \frac{C}{D} - \frac{C - \frac{D}{3}}{D}e^{-Dt} \quad (C.30)$$

Rewriting equation C.30 gives an exponentially decreasing expression dictated by a rate defining constant  $D$  corresponding to an overall rate coefficient for the oxidation reaction  $k_o$  and a limiting value  $C/D$  corresponding an equilibrium mole fraction  $x_{e,O_2}$  for  $O_2$ :

$$x_{O_2} = \frac{C}{D} - \left(\frac{C}{D} - \frac{1}{3}\right)e^{-Dt} \Leftrightarrow x_{O_2} = x_{e,O_2} - \left(x_{e,O_2} - \frac{1}{3}\right)e^{-k_o t} \quad (C.31)$$

#### C.2.4 General reaction

Comparison of the two derived rate equations gives a general rate equation with the initial mole fraction  $x_{i,y}$  (like in equation 4.4 of chapter 4):

$$x_y = x_{e,y} - (x_{e,y} - x_{i,y})e^{-k_y t} \quad (C.32)$$

Furthermore, for any given molecule  $y$ , that is consumed by a reaction with rate coefficient  $k_1$  and produced by a reaction with rate coefficient  $k_2$ , the overall conversion rate coefficient  $k_y$  and equilibrium concentration  $x_{e,y}$  will be of the following form, bearing any coefficient (a, b, c, d, and e) originating from stoichiometry:

$$k_y = ak_1 + bk_2 \quad (C.33)$$

$$x_{e,y} = \frac{ck_2}{dk_1 + ek_2} \quad (\text{C.34})$$

Since  $k$  is correlated to  $C$  and  $D$ , and  $x_e$  is correlated to  $A/B$  and  $C/D$ , in the derivation in sections C.2.2 and C.2.3. This means that the PCE concentration of any molecule can be written as a manifestation of the overall kinetics.

### C.2.5 MATLAB code for kinetic data fitting

```
%to clear workspace: typ "clear all" in 'Command window'
%open excel file via "Import data" on "Home" tab
%Go to correct Excel tab
%Select residence times and fractions that you want to fit
%Change output type to "Numeric matrix" in the top ribbon
%"Import selection"
%Go back to MATLAB main screen, check the workspace name that appeared.
%It should start with the name of your excel file
%Copy that name and paste below in the script d='matrixname';.
%Click "Run" in "editor" tab
%If asked, click "add to path"
%Check graph if fit is good!!!

d=matrixname; %Change name to workspace file name
data=[[d(:,1);d(:,1);d(:,1);d(:,1)],[d(:,2);d(:,3);d(:,4);d(:,5)]];
data(any(isnan(data), 2), :) = [];
g=fittype('C-(C-1)*exp(-k*t)', 'independent', 't', 'dependent', 'Y', '
    coefficients',{'C','k'});
myfit=fit(data(:,1),data(:,2),g)
plot(myfit,data(:,1),data(:,2))
```

### C.3 Extra version of figure 4.4

Extra version of figure 4.4 from chapter 4 with the data of the 4705 μm gap added.

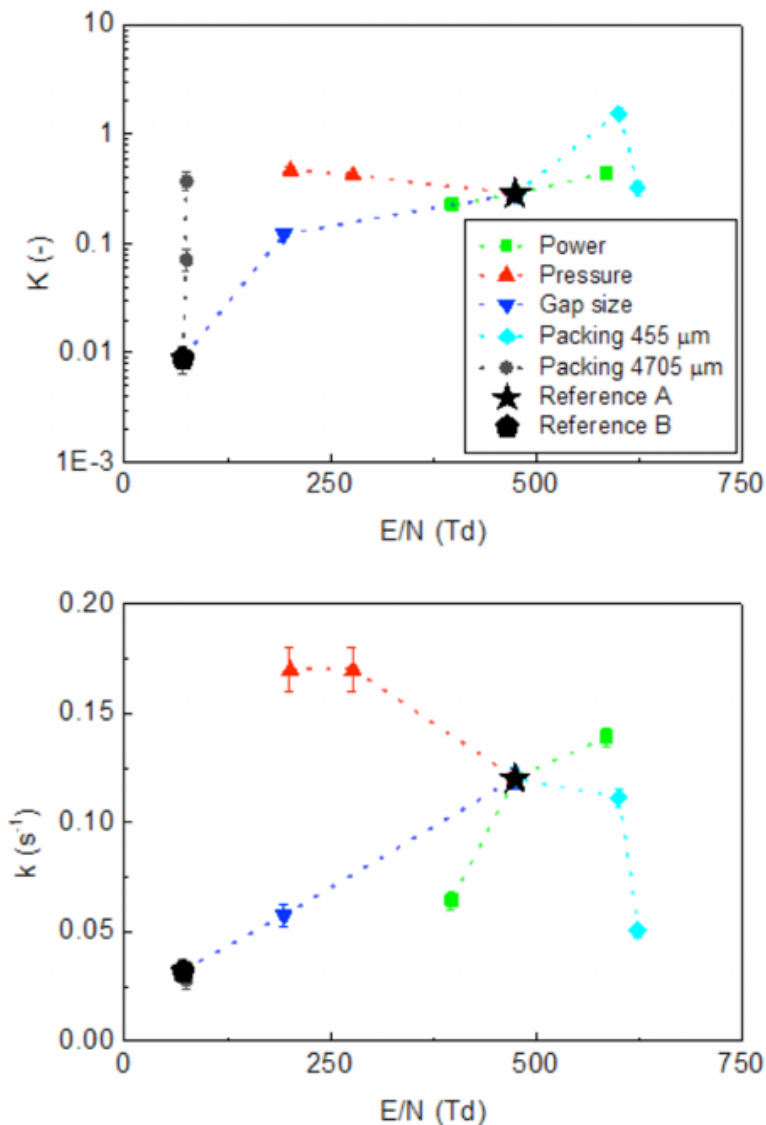


**Figure C.3:** Combined graph of the (a) equilibrium constants and (b) reaction rate coefficients of sections 4.3.2 and 4.3.3, plotted as a function of the estimated reduced electric field ( $E/N$ ). All the results are compared against the reference empty reactor A and B (see tables chapter 4).

# Appendix D

## Appendix of Chapter 5: DRM kinetics

### D.1 Derivation of the generalised reaction fit equation for reaction rate coefficient and PCE determination.

The overall reaction rate coefficient and location of the PCE are determined by applying an apparent first order reversible reaction fit to the residence time measurements. In our previous work, we explicitly derived an expression for the time evolution of molecular concentrations towards the PCE state of the CO<sub>2</sub>/CO/O<sub>2</sub> system, wherein we assumed first order kinetics and stoichiometric conversion between the aforementioned molecules only [56]. Such an approach is no longer valid for more complex gas mixtures, such as those obtained for CH<sub>4</sub> conversion or DRM. However, a slight generalisation of the equilibrium model permits its application to arbitrary gas conversion processes, without requiring any detailed information on reaction products or mechanisms. Only first order kinetics—reaction rate proportional to the concentration of reacting molecules—is assumed. Each process could progress through many different possible individual mechanisms, between which we cannot distinguish experimentally. The measured rate coefficient is therefore a weighted average for all these individual reactions which, by construction, is assumed to be constant over time.

A gas molecule of type *A* can be converted into a number of different species through several unspecified pathways. The overall loss rate can then be

characterised by a rate coefficient  $k_{loss}$ :

$$r_{A,loss}(x_a) = k_{loss}x_A \quad (D.1)$$

$A$  could also be formed again through a variety of pathways. Not all of the (non- $A$ ) molecules in the system can directly be converted into  $A$ , but only a (constant) fraction  $f$  has the “right” reactivity. We assume that  $f$  depends on the elemental composition of the system, and remains a constant time-averaged stoichiometric parameter by construction throughout all stages of the conversion process, like the rate coefficient to which it is tied. The formation rate of  $A$  can thus be written as:

$$r_{A,form}(x_a) = k_{form}(1 - x_A)f \quad (D.2)$$

The overall change in the concentration of  $A$  then becomes:

$$\frac{dx_A}{dt} = k_{form}(1 - x_A)f - k_{loss}x_A, \quad (D.3)$$

leading to

$$\int_{x_{A,i}}^{x_A} \frac{dx_A}{fk_{form} - (fk_{form} + k_{loss})x_A} = \int_0^t dt \quad (D.4)$$

Here,  $x_{A,i}$  is the initial concentration of  $A$ . Evaluation of the integral yields:

$$- \frac{1}{fk_{form} + k_{loss}} \ln \frac{fk_{form} - (fk_{form} + k_{loss})x_A}{fk_{form} - (fk_{form} + k_{loss})x_{A,i}} = t \quad (D.5)$$

and

$$x_A = \frac{fk_{form}}{fk_{form} + k_{loss}} - \left( \frac{fk_{form}}{fk_{form} + k_{loss}} - x_{A,i} \right) e^{-(fk_{form} + k_{loss})t} \quad (D.6)$$

The above expression can be compared to

$$x_A(t) = x_{A,e} - (x_{A,e} - x_{A,i}) e^{-kt}, \quad (D.7)$$

so that the apparent overall rate coefficient  $k$  of the conversion processes is

$$k = fk_{form} + k_{loss}, \quad (D.8)$$



whereas the equilibrium concentration of  $A$ ,  $x_{A,e}$ , reads

$$x_{A,e} = \frac{fk_{form}}{fk_{form} + k_{loss}} \quad (\text{D.9})$$

This equilibrium concentration  $x_{A,e}$  can be rewritten in terms of the total equilibrium conversion  $X_{Total,e}$  as:

$$X_{Total,e} = \frac{k_{loss}}{fk_{form} + k_{loss}} \quad (\text{D.10})$$

## D.2 Raw conversion and energy cost data of figures 5.1 and 5.2

**Table D.1:** (a) Conversion (X) and (b) Energy cost (EC), i.e. energy needed to convert one mole of reactant mixture, as a function of residence time, for all gas mixtures and for both empty and SiO<sub>2</sub>-packed reactors (if applicable).

(a)										
	CO <sub>2</sub>		DRM 3:1		DRM 1:1		DRM 1:3		CH <sub>4</sub>	
	t (s)	X (%)	t (s)	X (%)	t (s)	X (%)	t (s)	X (%)	t (s)	X (%)
Empty	2.9	13 ± 1	2.9	17 ± 1	2.9	19 ± 1	2.9	16.2 ± 0.2	2.9	7 ± 1
	7.5	30 ± 1	10	40 ± 1	10	44 ± 1	10	47 ± 2	10	29 ± 2
	14.5	39 ± 3	17.5	51 ± 1	17.5	58.9 ± 0.9	17.5	61 ± 1	17.5	41 ± 1
	19.4	48 ± 2	25	55.6 ± 0.4	25	66.0 ± 0.4	25	72.1 ± 0.6	25	53 ± 3
	28.9	51 ± 2	32.5	57.4 ± 0.8	32.5	70.5 ± 0.9	32.5	77 ± 2	32.5	61.8 ± 0.5
	41.5	53.1 ± 0.6	40	59.8 ± 0.7	40	72 ± 0.3	40	80 ± 1	40	66 ± 1
	48.5	55 ± 2	55	62 ± 1	55	75.7 ± 0.6	55	82 ± 1	55	74.1 ± 0.4
	58.2	54.4 ± 0.4			70	76.6 ± 0.3	70	82.5 ± 0.3	70	77 ± 1
	72.7	54 ± 2								
SiO <sub>2</sub>	2.6	15.2 ± 0.5			2.5	22 ± 3			2.5	10 ± 2
	10.2	42.4 ± 0.4			10	62 ± 1			10	42.1 ± 0.9
	17.9	57.4 ± 0.3			17.5	75.0 ± 0.7			17.5	61 ± 4
	25.5	64.2 ± 0.8			25	80.3 ± 0.6			25	68 ± 3
	33.2	67 ± 2			32.5	82.7 ± 0.2			32.5	71.0 ± 0.4
	40.8	69.0 ± 0.9			40	84.1 ± 0.4			40	76 ± 3
	48.5	70.5 ± 0.6			55	85.1 ± 0.2			55	76.9 ± 0.5
	56.1	74.0 ± 0.5							70	82.5 ± 0.6
	71.4	72.6 ± 0.3								

(b)										
	CO <sub>2</sub>		DRM 3:1		DRM 1:1		DRM 1:3		CH <sub>4</sub>	
	t (s)	EC (kWh/mol)	t (s)	EC (kWh/mol)	t (s)	EC (kWh/mol)	t (s)	EC (kWh/mol)	t (s)	EC (kWh/mol)
Empty	2.9	1.7 ± 0.1	2.9	1.32 ± 0.09	2.9	1.16 ± 0.07	2.9	1.38 ± 0.02	2.9	3.3 ± 0.6
	7.5	1.94 ± 0.09	10	1.92 ± 0.05	10	1.73 ± 0.05	10	1.65 ± 0.05	10	2.6 ± 0.1
	14.5	2.8 ± 0.2	17.5	2.62 ± 0.06	17.5	2.29 ± 0.04	17.5	2.20 ± 0.04	17.5	3.33 ± 0.09
	19.4	3.1 ± 0.1	25	3.46 ± 0.03	25	2.92 ± 0.02	25	2.67 ± 0.02	25	3.7 ± 0.2
	28.9	4.4 ± 0.2	32.5	4.36 ± 0.06	32.5	3.55 ± 0.04	32.5	3.24 ± 0.06	32.5	4.05 ± 0.03
	41.5	6.02 ± 0.07	40	5.15 ± 0.06	40	4.28 ± 0.02	40	3.86 ± 0.07	40	4.68 ± 0.09
	48.5	6.8 ± 0.3	55	6.8 ± 0.1	55	5.60 ± 0.04	55	5.20 ± 0.07	55	5.71 ± 0.03
	58.2	8.24 ± 0.06			70	7.04 ± 0.03	70	6.54 ± 0.02	70	7.02 ± 0.09
	72.7	10.5 ± 0.3								
SiO <sub>2</sub>	2.6	2.57 ± 0.08			2.5	1.8 ± 0.2			2.5	4.0 ± 0.8
	10.2	3.67 ± 0.04			10	2.45 ± 0.05			10	3.62 ± 0.08
	17.9	4.74 ± 0.03			17.5	3.56 ± 0.03			17.5	4.4 ± 0.3
	25.5	6.06 ± 0.08			25	4.75 ± 0.03			25	5.6 ± 0.3
	33.2	7.5 ± 0.2			32.5	5.99 ± 0.01			32.5	6.98 ± 0.04
	40.8	9.0 ± 0.1			40	7.26 ± 0.03			40	8.0 ± 0.3
	48.5	10.49 ± 0.09			55	9.86 ± 0.03			55	10.91 ± 0.07
	56.1	11.56 ± 0.08							70	12.94 ± 0.09
	71.4	15.01 ± 0.07								

## D.3 Overview of measured components

All measured components are listed in table D.2. Nine peaks could be calibrated by using calibration standards (Air Liquide). 22 more peaks could be identified but not calibrated, since either no calibration standard was available (vapour injection identification) or they coincide with other peaks. Heptane(1) to heptane(3) are three identified heptanes but no further information about the configuration is known. Finally, three more peaks remained unknown; thus they will be reported with their peak area, to still compare them throughout the measurements.

**Table D.2:** Overview of the components measured by the GC used in this work. The components are split into those that are (i) measured, identified, and calibrated, (ii) measured and identified (indicated as “known”), and (iii) only measured (indicated as “unknown”).

Status	Detector	Components
Calibrated	TCD	CO <sub>2</sub> , CO, O <sub>2</sub> , CH <sub>4</sub> , H <sub>2</sub> , Ethane, Ethene, Propane, Ethanol
Known	TCD	Water, Propene
	FID	C2's, C3's, Isobutane, Methanol, n-Butane, 2-Methylbutane, 2-Propanol, Acetone, n-Pentane, Diethylether, 2,2-Methylbutane, 1-Propanol, 2-Methylpentane, 3-Methylpentane, n-Hexane, Heptane(1), 1-Butanol, Heptane(2), Cyclohexane, Heptane(3)
Unknown	FID	1, 2, 3

The response factor of an FID for non-oxygenated hydrocarbons is proportional to the number of C atoms in the molecule. Therefore an FID product distribution of the non-oxygenated hydrocarbons can be calculated as:

$$x_{FID,i} = \frac{\frac{A_{FID,i}}{\text{carbonnumber}}}{\sum_{i=1}^n \frac{A_{FID,i}}{\text{carbonnumber}}}, \quad (\text{D.11})$$

with  $x_{FID,i}$  the share of component  $i$ ,  $A_{FID,i}$  the FID area, and  $i$  being any non-oxygenated component on the FID from table D.2.

## **D.4 How residence time and gas mixture tune product composition: uncalibrated products**

This section reads parallel to section 5.3.5 of chapter 5. Section D.4.x in the supplementary information follows section 5.3.5.x in chapter 5.

### **D.4.1 CO<sub>2</sub> dissociation**

No extra information.

### **D.4.2 CH<sub>4</sub> reforming**

Looking at the other hydrocarbons formed by CH<sub>4</sub> reforming, shown in figure D.1(a) with their detailed values in table D.4, we see the same trend. All formed components reach their maximum between 25 and 40 s, after which their concentration, and the global amount of measurable products, decreases. This means that either (i) the long residence time breaks down all formed components back into CH<sub>4</sub>, H<sub>2</sub>, and C, or (ii) even higher hydrocarbons are produced that are not measurable. Both pathways are probably occurring, since (i) increasing amounts of H<sub>2</sub> are detected, and (ii) viscous (yellowish) liquid deposition is found afterwards in the reactor. Since the response factor of an FID for non-oxygenated hydrocarbons is proportional to the number of C atoms in the molecule, we can qualitatively compare all FID detectable components on a 'mole equivalent basis' by dividing the individual peak areas by their respective carbon number, although this comparison must of course be considered with caution. The total CH<sub>4</sub> peak area (as a measure for the total hydrocarbon fractions) starts at  $51.61 \times 10^4$ , rises to  $230.74 \times 10^4$  at 40 s, and drops again to  $193.35 \times 10^4$ . The most produced components are C2 (70-59% of the total mole equivalent peak area, from lowest to highest residence time), C3 (18-22%), n-butane (5-7%), isobutane (3-4%), and 2-methylbutane (3-4%). All others have a contribution below 1% of all FID detectable components. All the exact values can be found in table D.4.

A lower amount of FID detectable components is seen by adding SiO<sub>2</sub>, as seen in figure D.1(b). Second, the point of maximum peak areas lies already at 17.5 s—as compared to 40 s in the empty reactor—which is due to the higher

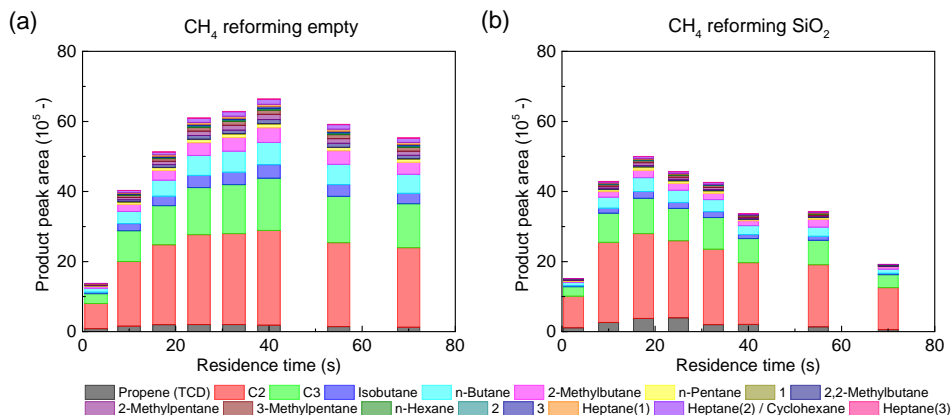


**Figure D.1:** GC peak areas of different uncalibrated components after  $\text{CH}_4$  reforming, plotted as stacked bars as a function of residence time, for (a) the empty reactor and (b) the  $\text{SiO}_2$ -packed reactor. All components are measured on the FID, except for propene (TCD: see legend). The exact values of the peak areas can be found in table D.4.

apparent rate coefficient discussed in section 5.3.1. The mole equivalent peak areas of the FID confirm this, with the overall area starting at  $33.66 \times 10^4$ , rising to  $179.49 \times 10^4$  at 25 s, and back down to  $129.39 \times 10^4$  at 70 s. The most produced fractions of the total mole equivalent peak areas change slightly, with C2 taking a higher share (77-76%, from lowest to highest residence time), followed by C3 (15%), n-butane (4%), 2-methylbutane (1-2%), and isobutane (1%). Both changes, due to the addition of  $\text{SiO}_2$  packing, again show the combination of product breakdown into  $\text{CH}_4$ ,  $\text{H}_2$ , and C, and/or polymerisation (cfr. above for the empty reactor), although much earlier in time, i.e. at 17.5-25 s. The deposition found inside the reactor (in between the spheres) after the experiments was found to be a combination of black carbon-like powder, combined with a similar viscous (yellowish) liquid, as described earlier.

### D.4.3 Dry reforming of methane

figure D.2(a) again shows that the concentration profiles of the uncalibrated (oxygenated) hydrocarbons reach their maximum at a residence time of 10 s. Rescaling to mole equivalent peak areas (neglecting overlapping oxygenated hydrocarbons, since their response factor is usually much lower than non-oxygenated hydrocarbons) shows first of all a lower amount of total area and thus total amount of measurable hydrocarbons, i.e.  $36.38 \times 10^4$  over  $53.26 \times 10^4$

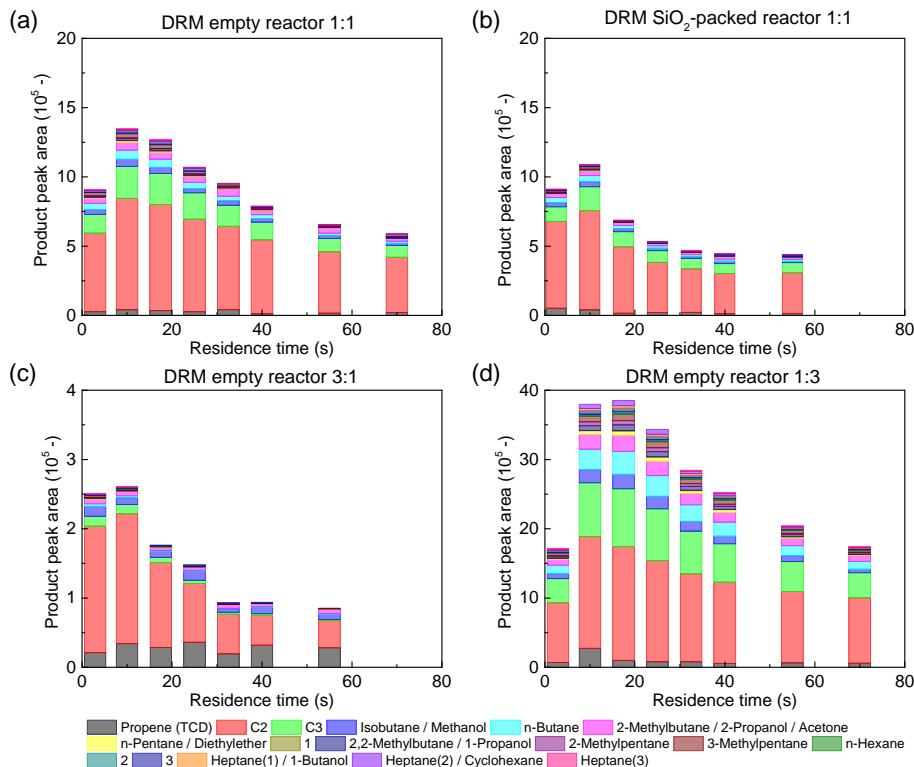


**Figure D.2:** GC peak areas of different uncalibrated components for DRM, plotted as stacked bars as a function of residence time, for (a) the empty reactor with a CO<sub>2</sub>:CH<sub>4</sub> ratio of 1:1, (b) the SiO<sub>2</sub>-packed reactor at 1:1 ratio, (c) the empty reactor at 3:1 ratio, and (d) the empty reactor at 1:3 ratio. All components are measured on the FID, except for propene (TCD: see legend). The exact values of the peak areas can be found in table D.7.

at 10 s, to  $24.27 \times 10^4$ . C2 and C3 are again the most formed products (around 80% and 13% of the total mole equivalent FID area respectively) followed by small amounts of n-butane, 2-methylbutane, and isobutane (all about 2%). The unfortunate overlap of all oxygenated hydrocarbons in the C1-C4 range limits the information that can be deduced.

Although some changes can be observed in ratios of different products, adding a SiO<sub>2</sub> packing to the reactor does not have a large impact on the product formation. The biggest impact is seen in figure D.2(b), where the product peak areas strongly decrease from 10 ns onwards ( $44.85 \times 10^4$  to  $18.17 \times 10^4$ ), although maintaining the same product fraction as in the empty reactor from above.

Changing the CO<sub>2</sub>:CH<sub>4</sub> ratio has a large impact on the product formation, as

can be seen in figure D.2(c and d). The concentration of the uncalibrated FID components strongly decreases as well, as seen in figure D.2(c): after rescaling, only a maximum total mole equivalent FID peak area of  $10.32 \times 10^4$  is found at a residence time of 10 s. Around 90% of this peak area is allocated to C2, with the remaining area divided over, in decreasing order, C3, isobutane, 2-methylbutane, and n-butane.

Vice versa, a large fraction of  $\text{CH}_4$  in the mixture (1:3 ratio) seems to be more beneficial overall. The product amounts detected on the FID increase by a factor 1.7 to 2.8, depending on the residence time, with a maximum total mole equivalent peak area of  $134.98 \times 10^4$ . The product composition on the FID slightly shifts to higher carbon numbers, although still with C2 as the main component at around 65%, but followed by C3 (20%), n-butane (5%), isobutane, and 2-methylbutane (both 3%).

## D.5 Raw product composition data of all experiments

**Table D.3:** Measured concentration of different calibrated components for CO<sub>2</sub> dissociation and CH<sub>4</sub> reforming, as a function of residence time, for the empty reactor and SiO<sub>2</sub>-packed reactor. All components are measured on the TCD. These data are plotted in figure 5.3 of chapter 5.

		CO <sub>2</sub> dissociation				CH <sub>4</sub> reforming			
t (s)	CO <sub>2</sub> (%)	O <sub>2</sub> (%)	CO (%)	t (s)	CH <sub>4</sub> (%)	H <sub>2</sub> (%)	Ethene (%)	Ethane (%)	Propane (%)
Empty									
2.9	81 ± 1	6.3 ± 0.5	13 ± 1	2.9	86.3 ± 0.9	8 ± 1	0.42 ± 0.08	1.5 ± 0.2	0.46 ± 0.04
7.5	61 ± 1	13.0 ± 0.6	26 ± 1	10	66 ± 1	23 ± 2	0.70 ± 0.07	3.90 ± 0.09	1.37 ± 0.04
14.5	51 ± 3	16 ± 1	33 ± 3	17.5	55 ± 1	33 ± 2	0.79 ± 0.09	5.02 ± 0.08	1.82 ± 0.07
19.4	42 ± 1	19.3 ± 0.7	39 ± 1	25	44 ± 2	42 ± 3	0.69 ± 0.06	5.74 ± 0.08	2.19 ± 0.05
28.9	39 ± 2	20.2 ± 0.9	40 ± 2	32.5	35.4 ± 0.5	52.6 ± 0.6	0.64 ± 0.06	6.0 ± 0.3	2.3 ± 0.1
41.5	37.0 ± 0.5	21.0 ± 0.2	42.0 ± 0.5	40	31 ± 1	54 ± 3	0.57 ± 0.04	6.21 ± 0.06	2.46 ± 0.04
48.5	36 ± 2	21.4 ± 0.8	43 ± 2	55	24.0 ± 0.4	63 ± 5	0.388 ± 0.008	5.7 ± 0.1	2.23 ± 0.05
58.2	35.9 ± 0.3	21.4 ± 0.2	42.7 ± 0.3	70	21.3 ± 0.9	74 ± 3	0.35 ± 0.05	5.5 ± 0.2	2.1 ± 0.1
72.7	37 ± 1	21.1 ± 0.6	42 ± 1						
SiO <sub>2</sub>									
2.6	78.9 ± 0.5	7.0 ± 0.2	14.1 ± 0.5	2.5	83 ± 2	10 ± 2	1.0 ± 0.1	1.7 ± 0.3	0.30 ± 0.09
10.2	47.5 ± 0.3	17.5 ± 0.2	35.0 ± 0.3	10	53.7 ± 0.9	34 ± 2	1.45 ± 0.06	4.2 ± 0.2	1.13 ± 0.07
17.9	33.1 ± 0.3	22.3 ± 0.1	44.6 ± 0.3	17.5	36 ± 4	47 ± 2	1.2 ± 0.1	4.9 ± 0.2	0.8 ± 0.5
25.5	27.1 ± 0.6	24.3 ± 0.3	48.6 ± 0.6	25	29 ± 3	53 ± 3	1.0 ± 0.2	4.6 ± 0.1	0.8 ± 0.5
33.2	25 ± 2	25.1 ± 0.8	50 ± 2	32.5	27.1 ± 0.4	64 ± 1	0.92 ± 0.03	4.5 ± 0.1	1.42 ± 0.04
40.8	23.1 ± 0.6	25.6 ± 0.3	51.3 ± 0.6	40	22 ± 2	61 ± 4	0.7 ± 0.2	3.9 ± 0.3	0.7 ± 0.5
48.5	21.8 ± 0.5	26.1 ± 0.2	52.1 ± 0.5	55	21.3 ± 0.5	69 ± 7	0.6 ± 0.1	4.0 ± 0.2	1.14 ± 0.04
56.1	19.0 ± 0.4	27.0 ± 0.2	54.0 ± 0.4	70	16.3 ± 0.5	76.9 ± 0.5	0.286 ± 0.007	2.93 ± 0.09	0.62 ± 0.02
71.4	20.1 ± 0.2	26.6 ± 0.1	53.3 ± 0.2						



## D.5 Raw product composition data of all experiments

**Table D.4:** GC peak areas for different uncalibrated components for CH<sub>4</sub> reforming, as a function of residence time, for the empty reactor and SiO<sub>2</sub>-packed reactor. All components are measured on the FID, except for propene (TCD), and rescaled per column, as mentioned in the second row. These data are plotted in figure D.1.

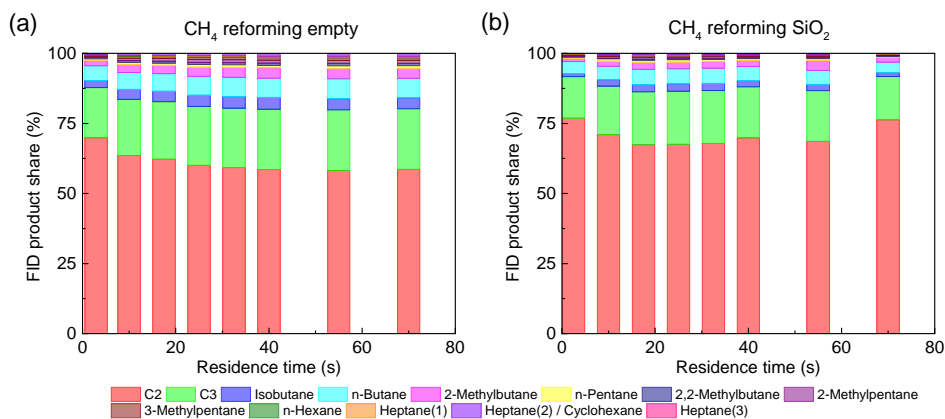
Component	Propene (TCD)	C2	C3	Isobutane	n-Butane	2-methyl butane	n-Pentane	1	2,2-Dimethyl butane	
										x 1000
CH <sub>4</sub> Empty	t (s)	80 ± 10	140 ± 20	830 ± 80	52 ± 1	110 ± 10	51 ± 4	120 ± 20	39 ± 6	141 ± 5
	2.9	160 ± 20	369 ± 2	2610 ± 50	206 ± 8	351 ± 9	209 ± 7	530 ± 20	120 ± 10	580 ± 60
	10	200 ± 30	455 ± 1	3360 ± 80	280 ± 10	456 ± 8	280 ± 10	720 ± 20	150 ± 20	780 ± 80
	17.5	200 ± 30	513 ± 6	4040 ± 10	349 ± 2	567 ± 5	360 ± 10	930 ± 30	160 ± 20	1020 ± 40
	25	200 ± 30	520 ± 20	4200 ± 200	360 ± 30	600 ± 30	390 ± 20	990 ± 60	131 ± 5	1000 ± 100
	32.5	190 ± 30	540 ± 4	4478 ± 9	385 ± 5	638 ± 2	410 ± 10	1090 ± 30	140 ± 20	1150 ± 50
	40	140 ± 20	479 ± 8	3990 ± 70	335 ± 7	580 ± 7	378 ± 6	990 ± 20	100 ± 10	1110 ± 30
55	130 ± 10	450 ± 20	3800 ± 200	310 ± 20	540 ± 30	340 ± 20	890 ± 40	80 ± 10	1013 ± 3	
70	110 ± 40	180 ± 40	800 ± 200	27 ± 8	100 ± 20	32 ± 8	160 ± 40	80 ± 20	80 ± 20	
CH <sub>4</sub> SiO <sub>2</sub>	t (s)	260 ± 20	457 ± 8	2500 ± 100	140 ± 10	310 ± 10	150 ± 10	570 ± 30	207 ± 6	320 ± 20
	10	400 ± 200	484 ± 1	3000 ± 200	190 ± 20	390 ± 20	220 ± 30	710 ± 50	190 ± 10	430 ± 60
	17.5	400 ± 200	440 ± 20	2770 ± 10	170 ± 2	352 ± 5	200 ± 10	630 ± 10	150 ± 20	360 ± 20
	25	197 ± 5	432 ± 7	2700 ± 60	162 ± 4	350 ± 10	188 ± 6	590 ± 20	126 ± 1	310 ± 10
	32.5	200 ± 100	350 ± 50	2100 ± 400	110 ± 30	250 ± 50	140 ± 30	400 ± 100	80 ± 30	210 ± 50
	40	130 ± 20	355 ± 5	2110 ± 40	116 ± 7	259 ± 5	230 ± 70	420 ± 10	80 ± 10	225 ± 6
	55	50 ± 10	240 ± 7	1100 ± 30	45 ± 2	119 ± 4	63 ± 3	167 ± 6	24 ± 1	73 ± 3
70	110 ± 40	180 ± 40	800 ± 200	27 ± 8	100 ± 20	32 ± 8	160 ± 40	80 ± 20	80 ± 20	

Component	2-Methyl pentane	3-Methyl pentane	n-Hexane	2	3	Heptane(1)	Heptane(2)	Heptane(3)
CH <sub>4</sub> Empty	t (s)	150 ± 20	140 ± 20	40 ± 10	21 ± 3	30 ± 3	63 ± 3	13 ± 1
	2.9	700 ± 40	560 ± 30	160 ± 30	150 ± 30	190 ± 30	280 ± 30	590 ± 40
	10	960 ± 40	730 ± 40	220 ± 30	200 ± 30	270 ± 40	380 ± 30	800 ± 40
	17.5	1290 ± 30	990 ± 50	280 ± 30	270 ± 30	390 ± 30	510 ± 30	1140 ± 30
	25	1400 ± 100	1110 ± 70	269 ± 2	250 ± 30	420 ± 60	520 ± 60	1200 ± 100
	32.5	1500 ± 30	1170 ± 50	310 ± 40	300 ± 40	470 ± 50	600 ± 30	1380 ± 30
	40	1300 ± 30	1140 ± 20	280 ± 20	260 ± 30	490 ± 20	580 ± 20	1250 ± 30
55	1210 ± 90	1046 ± 9	240 ± 10	222 ± 4	430 ± 30	545 ± 4	1180 ± 60	
70	120 ± 30	90 ± 20	80 ± 20	22 ± 5	20 ± 5	40 ± 10	50 ± 30	
CH <sub>4</sub> SiO <sub>2</sub>	t (s)	550 ± 30	380 ± 20	190 ± 10	78 ± 7	100 ± 10	170 ± 10	370 ± 30
	10	730 ± 60	560 ± 60	220 ± 20	90 ± 10	150 ± 30	210 ± 20	550 ± 70
	17.5	610 ± 10	510 ± 40	190 ± 10	70 ± 10	120 ± 20	160 ± 10	480 ± 30
	25	580 ± 20	500 ± 20	166 ± 4	57 ± 2	103 ± 6	145 ± 7	450 ± 20
	32.5	400 ± 100	370 ± 70	120 ± 30	40 ± 10	80 ± 30	90 ± 30	300 ± 80
	40	370 ± 30	392 ± 9	121 ± 9	35 ± 8	110 ± 20	97 ± 5	300 ± 20
	55	110 ± 4	159 ± 5	47 ± 2	10 ± 4	20 ± 10	19 ± 5	92 ± 8
70	110 ± 4	159 ± 5	47 ± 2	10 ± 4	20 ± 10	19 ± 5	92 ± 8	

**Table D.5:** Total mole equivalent of the FID peak areas, based on the number of C atoms per molecule (second column), and the individual shares of each component (third to last column), for CH<sub>4</sub> reforming, for the empty reactor and SiO<sub>2</sub>-packed reactor.

	t (s)	Mole equivalent area (x 1E4)	C2	C3	Isobutane	n-Butane	2-methyl butane	n-Pentane	2,2-Dimethyl butane
CH <sub>4</sub> Empty	2.9	51.61	0.70	0.18	0.03	0.05	0.02	0.005	0.005
	10	144.98	0.64	0.20	0.04	0.06	0.03	0.007	0.007
	17.5	182.75	0.62	0.20	0.04	0.06	0.03	0.008	0.007
	25	213.50	0.60	0.21	0.04	0.07	0.03	0.009	0.008
	32.5	219.03	0.59	0.21	0.04	0.07	0.04	0.009	0.008
	40	230.74	0.59	0.22	0.04	0.07	0.04	0.009	0.008
	55	205.56	0.58	0.22	0.04	0.07	0.04	0.010	0.009
70	193.35	0.59	0.22	0.04	0.07	0.04	0.009	0.009	
CH <sub>4</sub> SiO <sub>2</sub>	2.5	33.66	0.77	0.15	0.01	0.04	0.01	0.006	0.002
	10	59.24	0.71	0.17	0.02	0.05	0.02	0.007	0.003
	17.5	160.83	0.67	0.19	0.03	0.05	0.02	0.008	0.004
	25	179.49	0.68	0.19	0.03	0.05	0.02	0.008	0.004
	32.5	162.82	0.68	0.19	0.03	0.05	0.02	0.007	0.003
	40	159.18	0.70	0.18	0.02	0.05	0.02	0.007	0.003
	55	126.13	0.69	0.18	0.02	0.05	0.04	0.006	0.003
70	129.39	0.76	0.15	0.01	0.04	0.02	0.004	0.002	
	t (s)	Mole equivalent area (x 1E4)	2-Methyl pentane	3-Methyl pentane	n-Hexane	Heptane(1)	Heptane(2)	Heptane(3)	
CH <sub>4</sub> Empty	2.9	51.61	0.005	0.004	0.001	0.0017	0.003	0.0004	
	10	144.98	0.008	0.006	0.002	0.0028	0.006	0.0007	
	17.5	182.75	0.009	0.007	0.002	0.0029	0.006	0.0007	
	25	213.50	0.010	0.008	0.002	0.0034	0.008	0.0009	
	32.5	219.03	0.010	0.008	0.002	0.0034	0.008	0.0010	
	40	230.74	0.011	0.008	0.002	0.0037	0.009	0.0010	
	55	205.56	0.011	0.009	0.002	0.0041	0.009	0.0009	
70	193.35	0.010	0.009	0.002	0.0040	0.009	0.0011		
CH <sub>4</sub> SiO <sub>2</sub>	2.5	33.66	0.003	0.002	0.002	0.0010	0.001	0.0003	
	10	59.24	0.006	0.004	0.002	0.0015	0.003	0.0005	
	17.5	160.83	0.007	0.005	0.002	0.0016	0.004	0.0005	
	25	179.49	0.006	0.005	0.002	0.0014	0.004	0.0004	
	32.5	162.82	0.006	0.005	0.002	0.0013	0.004	0.0004	
	40	159.18	0.005	0.005	0.002	0.0011	0.003	0.0004	
	55	126.13	0.005	0.005	0.002	0.0011	0.003	0.0003	
70	129.39	0.002	0.003	0.001	0.0003	0.002	0.0001		



**Figure D.3:** Product shares based on the total mole equivalent FID peak area are shown for (a) the empty reactor and (b) the SiO<sub>2</sub>-packed reactor. The exact values of the peak areas can be found in table D.3.



## D.5 Raw product composition data of all experiments

**Table D.6:** Measured concentration of different calibrated components for DRM, as a function of residence time, for the empty reactor with a CO<sub>2</sub>:CH<sub>4</sub> ratio of 1:1, the SiO<sub>2</sub>-packed reactor with 1:1 ratio, the empty reactor with 3:1 ratio, and the empty reactor with 1:3 ratio. All components are measured on the TCD. These data are plotted in figure 5.4 in chapter 5. The H<sub>2</sub>:CO ratio is shown in the last column.

t (s)	CO <sub>2</sub> (%)	CH <sub>4</sub> (%)	H <sub>2</sub> (%)	O <sub>2</sub> (%)	CO (%)	Ethene (%)	Ethane (%)	Propane (%)	Ethanol (ppm)	H <sub>2</sub> :CO
DRM Empty 1:1										
2.9	41.9 ± 0.4	39.9 ± 0.8	9.3 ± 0.2	0.0066 ± 0.0003	10.2 ± 0.4	0.146 ± 0.007	1.3 ± 0.1	0.23 ± 0.01	270 ± 30	0.91
10	30.2 ± 0.5	26.0 ± 0.8	21.9 ± 0.6	0.007 ± 0.003	23.2 ± 0.6	0.126 ± 0.006	1.96 ± 0.04	0.41 ± 0.04	340 ± 20	0.94
17.5	23.2 ± 0.5	18.4 ± 0.5	28.1 ± 0.7	0.007 ± 0.004	29.6 ± 0.7	0.097 ± 0.007	1.90 ± 0.04	0.34 ± 0.04	300 ± 40	0.95
25	19.2 ± 0.4	14.4 ± 0.2	32.2 ± 0.6	0.009 ± 0.003	34 ± 1	0.076 ± 0.007	1.68 ± 0.04	0.34 ± 0.02	180 ± 90	0.96
32.5	16.9 ± 0.5	13.0 ± 0.4	34.0 ± 0.6	0.014 ± 0.004	35.9 ± 0.8	0.069 ± 0.006	1.53 ± 0.06	0.30 ± 0.02	257 ± 6	0.95
40	16.2 ± 0.4	11.5 ± 0.1	36.0 ± 0.4	0.0119 ± 0.0004	36.5 ± 0.8	0.058 ± 0.006	1.34 ± 0.03	0.23 ± 0.02	220 ± 10	0.99
55	14.6 ± 0.3	10 ± 0.3	36.6 ± 0.8	0.016 ± 0.001	37 ± 1	0.054 ± 0.007	1.12 ± 0.06	0.18 ± 0.02	190 ± 70	0.98
70	14.1 ± 0.1	9.6 ± 0.2	39 ± 3	0.023 ± 0.007	37.4 ± 0.9	0.049 ± 0.007	1.04 ± 0.04	0.17 ± 0.02	90 ± 50	1.04
DRM SiO <sub>2</sub> 1:1										
2.5	39 ± 1	37 ± 1	12 ± 1	0.008 ± 0.001	12 ± 1	0.55 ± 0.04	1.3 ± 0.1	0.15 ± 0.03	340 ± 40	0.98
10	20.1 ± 0.6	17.3 ± 0.6	28.8 ± 0.8	0.013 ± 0.002	32.8 ± 0.9	0.21 ± 0.02	1.76 ± 0.07	0.31 ± 0.02	290 ± 40	0.88
17.5	13.3 ± 0.4	11.4 ± 0.3	33.9 ± 0.9	0.017 ± 0.004	39 ± 1	0.11 ± 0.01	1.22 ± 0.03	0.19 ± 0.01	182 ± 5	0.86
25	10.3 ± 0.3	9.1 ± 0.3	36.7 ± 0.4	0.029 ± 0.005	41.8 ± 0.5	0.084 ± 0.008	0.95 ± 0.06	0.16 ± 0.01	122 ± 2	0.88
32.5	8.89 ± 0.09	8.01 ± 0.08	38.1 ± 0.5	0.026 ± 0.004	43.6 ± 0.3	0.082 ± 0.007	0.83 ± 0.05	0.15 ± 0.02	76 ± 8	0.87
40	8.1 ± 0.3	7.4 ± 0.2	38.5 ± 0.5	0.05 ± 0.01	43.1 ± 0.6	0.069 ± 0.007	0.75 ± 0.04	0.132 ± 0.008	160 ± 60	0.89
55	7.3 ± 0.2	7.49 ± 0.02	40.2 ± 0.2	0.052 ± 0.002	42.7 ± 0.3	0.071 ± 0.006	0.77 ± 0.02	0.15 ± 0.01	50 ± 20	0.94
DRM Empty 3:1										
2.9	63.5 ± 0.5	19.1 ± 0.3	6.0 ± 0.2	0.008 ± 0.001	12.2 ± 0.5	0.067 ± 0.004	0.49 ± 0.04	0.032 ± 0.004	240 ± 10	0.49
10	48.9 ± 0.9	10.4 ± 0.2	14.9 ± 0.3	0.005 ± 0.003	27.2 ± 0.7	0.057 ± 0.006	0.54 ± 0.05	0.04 ± 0.01	340 ± 20	0.55
17.5	42 ± 1	6.5 ± 0.2	19.4 ± 0.5	0.007 ± 0.004	33.3 ± 0.7	0.048 ± 0.007	0.39 ± 0.05	0.02 ± 0.01	300 ± 40	0.58
25	39.4 ± 0.3	4.8 ± 0.2	21.4 ± 0.3	0.012 ± 0.001	36.0 ± 0.6	0.051 ± 0.002	0.31 ± 0.03	0.018 ± 0.005	320 ± 30	0.60
32.5	38.5 ± 0.8	3.71 ± 0.08	22.9 ± 0.4	0.013 ± 0.002	36.8 ± 0.7	0.039 ± 0.005	0.20 ± 0.03	0.01 ± 0.01	230 ± 40	0.62
40	37.1 ± 0.7	2.93 ± 0.06	22.9 ± 0.5	0.014 ± 0.001	36.2 ± 0.7	0.038 ± 0.006	0.17 ± 0.03	0.014 ± 0.005	240 ± 20	0.63
55	35.3 ± 0.9	2.63 ± 0.08	23.8 ± 0.5	0.0114 ± 0.0007	37.1 ± 0.8	0.036 ± 0.005	0.16 ± 0.04	0.010 ± 0.005	300 ± 50	0.64
DRM Empty 1:3										
2.9	21.95 ± 0.03	61.5 ± 0.4	10.8 ± 0.3	0.0072 ± 0.0004	4.3 ± 0.1	0.284 ± 0.006	2.01 ± 0.03	0.62 ± 0.01	68 ± 3	2.49
10	14.5 ± 0.3	39 ± 1	29.4 ± 0.6	0.0088 ± 0.0004	12.5 ± 0.4	0.32 ± 0.02	3.85 ± 0.08	1.2 ± 0.3	40 ± 10	2.34
17.5	10.7 ± 0.4	27.7 ± 0.6	38.3 ± 0.8	0.009 ± 0.001	16.1 ± 0.5	0.26 ± 0.01	4.02 ± 0.09	1.43 ± 0.03	26 ± 5	2.37
25	7.5 ± 0.1	20.4 ± 0.5	45.0 ± 0.8	0.011 ± 0.001	18.6 ± 0.4	0.19 ± 0.01	3.69 ± 0.07	1.33 ± 0.05	54 ± 5	2.42
32.5	5.7 ± 0.5	17 ± 1	51 ± 3	0.02 ± 0.01	20.8 ± 0.5	0.16 ± 0.02	3.3 ± 0.1	1.16 ± 0.08	11 ± 2	2.44
40	4.8 ± 0.4	15 ± 1	51 ± 1	0.014 ± 0.001	20.2 ± 0.5	0.12 ± 0.01	3.0 ± 0.1	0.98 ± 0.06	23 ± 2	2.52
55	4.4 ± 0.2	14.1 ± 0.8	54 ± 1	0.018 ± 0.002	19.5 ± 0.4	0.096 ± 0.004	2.70 ± 0.04	0.83 ± 0.03	20 ± 10	2.74
70	4.0 ± 0.1	13.3 ± 0.2	56.1 ± 0.5	0.03 ± 0.002	18.2 ± 0.1	0.076 ± 0.005	2.54 ± 0.03	0.73 ± 0.05	68 ± 3	3.08

**Table D.7:** GC peak areas for different uncalibrated components for DRM, as a function of residence time, for the empty reactor with a CO<sub>2</sub>:CH<sub>4</sub> ratio of 1:1, the SiO<sub>2</sub>-packed reactor with 1:1 ratio, the empty reactor with 3:1 ratio, and the empty reactor with 1:3 ratio. All components are measured on the FID, except for propene (TCD), and rescaled per column as mentioned in the second row. These data are plotted in figure D.2. Continues on the next page.

Component	Propene (TCD)	C2	C3	Isobutane / Methanol	n-Butane	2-methylbutane / propanol / acetone	n-Pentane / Diethylether	I	2,2-Dimethyl butane / 1-propanol	
										x 1000
DRM Empty 1:1	τ (s)									
	2.9	30 ± 10	5700 ± 400	13400 ± 900	340 ± 20	4500 ± 300	380 ± 40	5000 ± 200	210 ± 10	710 ± 40
	10	40 ± 10	8050 ± 40	23000 ± 200	520 ± 20	6730 ± 60	566 ± 4	9000 ± 100	347 ± 5	1300 ± 60
	17.5	30 ± 10	7660 ± 50	22300 ± 400	450 ± 20	6000 ± 100	490 ± 5	8200 ± 200	292 ± 5	1240 ± 30
	25	30 ± 10	6700 ± 100	18800 ± 500	320 ± 50	4600 ± 200	410 ± 60	6000 ± 300	200 ± 20	860 ± 60
	32.5	42 ± 8	6020 ± 30	15190 ± 90	307 ± 6	3400 ± 20	500 ± 100	4470 ± 60	164 ± 3	695 ± 9
	40	10 ± 10	5320 ± 60	12900 ± 200	259 ± 7	2700 ± 60	310 ± 80	3400 ± 100	127 ± 4	510 ± 20
55	18 ± 9	4410 ± 40	9700 ± 100	210 ± 50	1860 ± 50	400 ± 200	2400 ± 80	95 ± 9	370 ± 70	
70	20 ± 10	4000 ± 50	8500 ± 300	150 ± 20	1540 ± 80	180 ± 30	1900 ± 200	70 ± 10	350 ± 40	
DRM SiO <sub>2</sub> 1:1	2.5	50 ± 20	6300 ± 500	11000 ± 1000	320 ± 40	3500 ± 500	260 ± 40	3500 ± 600	190 ± 20	600 ± 100
	10	40 ± 10	7170 ± 90	17100 ± 300	360 ± 40	4500 ± 100	342 ± 8	5500 ± 100	197 ± 5	700 ± 60
	17.5	20 ± 10	4800 ± 100	10900 ± 400	220 ± 20	2310 ± 90	184 ± 4	3000 ± 100	103 ± 3	370 ± 20
	25	20 ± 10	3630 ± 90	8400 ± 200	181 ± 5	1680 ± 60	160 ± 7	2310 ± 60	78 ± 2	307 ± 7
	32.5	20 ± 20	3140 ± 20	7580 ± 80	120 ± 10	1460 ± 10	137 ± 2	2060 ± 30	66 ± 3	220 ± 10
	40	13 ± 5	2900 ± 20	7100 ± 100	180 ± 50	1450 ± 70	180 ± 20	3000 ± 1000	100 ± 100	400 ± 200
	55	14 ± 8	2930 ± 9	7370 ± 90	90 ± 20	1430 ± 40	148 ± 2	2170 ± 80	59 ± 5	200 ± 10
DRM Empty 3:1	2.9	20 ± 10	1830 ± 40	1430 ± 60	140 ± 6	370 ± 20	69 ± 4	460 ± 30	97 ± 4	71 ± 9
	10	30 ± 20	1870 ± 10	1350 ± 30	90 ± 20	270 ± 10	63 ± 3	360 ± 30	71 ± 3	74 ± 8
	17.5	30 ± 10	1226 ± 9	740 ± 10	90 ± 20	163 ± 9	45 ± 1	210 ± 20	45 ± 2	50 ± 5
	25	40 ± 10	850 ± 40	460 ± 50	131 ± 5	96 ± 1	45 ± 7	200 ± 20	51 ± 8	46 ± 4
	32.5	20 ± 20	580 ± 10	270 ± 30	50 ± 10	83 ± 7	51 ± 2	140 ± 20	33 ± 8	40 ± 20
	40	30 ± 20	432 ± 3	207 ± 7	92 ± 5	73 ± 3	43 ± 7	150 ± 20	25 ± 3	55 ± 6
	55	30 ± 10	390 ± 20	180 ± 6	80 ± 20	65 ± 4	64 ± 7	130 ± 9	24 ± 3	67 ± 6
DRM Empty 1:3	2.9	70 ± 9	8600 ± 100	34900 ± 200	706 ± 3	12500 ± 100	823 ± 3	16600 ± 200	317 ± 6	2120 ± 20
	10	300 ± 400	16110 ± 40	77600 ± 800	1910 ± 40	29800 ± 400	2100 ± 30	52000 ± 1000	760 ± 30	6800 ± 200
	17.5	101 ± 9	16400 ± 200	83000 ± 1000	2100 ± 30	33000 ± 400	2340 ± 20	60800 ± 600	750 ± 50	8000 ± 100
	25	80 ± 20	14600 ± 200	74700 ± 700	1830 ± 20	29700 ± 200	2090 ± 30	53700 ± 500	690 ± 30	7490 ± 90
	32.5	80 ± 30	12700 ± 400	62000 ± 2000	1380 ± 70	24000 ± 1000	1600 ± 100	43000 ± 2000	520 ± 60	5800 ± 300
	40	60 ± 20	11800 ± 600	55000 ± 3000	1140 ± 90	20000 ± 2000	1400 ± 100	36000 ± 3000	470 ± 50	4700 ± 300
	55	63 ± 8	10300 ± 300	43100 ± 500	830 ± 40	14500 ± 200	1030 ± 40	24300 ± 300	326 ± 6	3200 ± 100
70	60 ± 20	9400 ± 100	36000 ± 800	540 ± 20	11100 ± 400	820 ± 70	17500 ± 700	210 ± 30	2200 ± 200	

## D.5 Raw product composition data of all experiments

Component	2-Methyl pentane		3-Methyl pentane		n-Hexane		2		3		Heptane(1) / 1-Butanol		Heptane(2) / Cyclohexane		Heptane(3)		
	t (s)	x 10	x 10	x 10	x 10	x 10	x 10	x 10	x 10	x 10	x 10	x 10	x 10	x 10	x 10	x 10	
DRM Empty 1:1	2.9	258 ± 9	2300 ± 300	138 ± 4	220 ± 30	1560 ± 30	350 ± 50	400 ± 20	384 ± 8								
	10	490 ± 20	3030 ± 20	240 ± 10	200 ± 30	2020 ± 30	320 ± 60	630 ± 40	630 ± 40								
	17.5	420 ± 40	2530 ± 50	220 ± 20	110 ± 40	1970 ± 40	210 ± 10	530 ± 60	560 ± 40								
	25	280 ± 10	1800 ± 70	150 ± 20	134 ± 4	407 ± 4	90 ± 10	370 ± 30	410 ± 30								
	32.5	162 ± 9	1290 ± 10	128 ± 5	98 ± 5	355 ± 5	80 ± 10	196 ± 9	265 ± 8								
	40	126 ± 6	1030 ± 30	97 ± 6	60 ± 10	370 ± 10	80 ± 10	160 ± 10	206 ± 8								
	55	89 ± 9	800 ± 100	60 ± 20	45 ± 7	1682 ± 7	60 ± 10	120 ± 20	140 ± 10								
70	117 ± 8	640 ± 30	60 ± 10				170 ± 70	190 ± 70									
DRM SiO <sub>2</sub> 1:1	2.5		1200 ± 400	103 ± 4	100 ± 20	460 ± 20	790 ± 20	180 ± 30	140 ± 40								
	10		1520 ± 20	140 ± 10	110 ± 20	790 ± 20	240 ± 40	240 ± 40	280 ± 20								
	17.5		690 ± 40	73 ± 8	49 ± 4	172 ± 4	67 ± 2	90 ± 20	108 ± 7								
	25		500 ± 10	67 ± 3	44 ± 3	142 ± 3		70 ± 10	81 ± 4								
	32.5		430 ± 10	58 ± 5	34 ± 3	211 ± 3		70 ± 20	65 ± 7								
	40		420 ± 20	90 ± 20	40 ± 8	473 ± 8		80 ± 30	74 ± 7								
	55		408 ± 4	65 ± 1	32 ± 3	870 ± 3		90 ± 30	80 ± 10								
DRM Empty 3:1	2.9	30 ± 6	240 ± 20	21 ± 3	25 ± 5	165 ± 5	40 ± 20	29 ± 8									
	10	27 ± 3	167 ± 9	17 ± 5	21 ± 4	204 ± 4		19 ± 8									
	17.5		70 ± 3		10 ± 1	113 ± 1											
	25		45 ± 6		10 ± 1	164 ± 1											
	32.5		32 ± 8														
	40		26 ± 6														
55		28 ± 3															
DRM Empty 1:3	2.9	1540 ± 20	3640 ± 20	390 ± 10	390 ± 20	2340 ± 20	820 ± 30	1530 ± 40	630 ± 20								
	10	5400 ± 100	8500 ± 200	1300 ± 100	1640 ± 90	5310 ± 90	2700 ± 100	6300 ± 100									
	17.5	6250 ± 80	9410 ± 50	1490 ± 70	1950 ± 30	5340 ± 30	3260 ± 20	7500 ± 100									
	25	5530 ± 70	8530 ± 90	1400 ± 100	1830 ± 60	4890 ± 60	3170 ± 50	6730 ± 40									
	32.5	3900 ± 200	6500 ± 300	1020 ± 90	1200 ± 100	3300 ± 100	2390 ± 50	3600 ± 300									
	40	3100 ± 300	5600 ± 400	900 ± 100	940 ± 40	3320 ± 40	2000 ± 100	2700 ± 300									
	55	1810 ± 40	4000 ± 100	600 ± 40	570 ± 50	1770 ± 50	1330 ± 90	1590 ± 80									
70	1170 ± 50	2900 ± 100	370 ± 20	320 ± 20	1550 ± 20	920 ± 50	990 ± 60										

**Table D.8:** Total mole equivalent of the FID peak areas, based on the number of C atoms per molecule (second column), and the individual shares of each component (third to last column), for the components formed during DRM as a function of residence time, for the empty reactor with a CO<sub>2</sub>:CH<sub>4</sub> ratio of 1:1, the SiO<sub>2</sub> packed reactor with 1:1 ratio, the empty reactor with 3:1 ratio, and the empty reactor with 1:3 ratio. Continues on the next page.

	t (s)	Mole equivalent area (x 1E4)	C2	C3	Isobutane	n-Butane	2-methyl butane	n-Pentane	2,2-Dimethyl butane
DRM Empty 1:1	2.9	36.38	0.78	0.12	0.02	0.03	0.02	0.003	0.003
	10	53.26	0.76	0.14	0.02	0.03	0.02	0.003	0.004
	17.5	50.44	0.76	0.15	0.02	0.03	0.02	0.003	0.004
	25	43.27	0.77	0.14	0.02	0.03	0.02	0.003	0.003
	32.5	38.38	0.78	0.13	0.02	0.02	0.03	0.002	0.003
	40	33.30	0.80	0.13	0.02	0.02	0.02	0.002	0.003
	55	27.31	0.81	0.12	0.02	0.02	0.03	0.002	0.002
70	24.27	0.83	0.12	0.02	0.02	0.02	0.002	0.002	
DRM SiO <sub>2</sub> 1:1	2.5	37.45	0.84	0.09	0.02	0.02	0.01	0.002	0.003
	10	44.85	0.80	0.13	0.02	0.03	0.02	0.002	0.003
	17.5	29.32	0.82	0.12	0.02	0.02	0.01	0.002	0.002
	25	22.33	0.81	0.12	0.02	0.02	0.01	0.002	0.002
	32.5	19.35	0.81	0.13	0.02	0.02	0.01	0.002	0.002
	40	18.26	0.79	0.13	0.02	0.02	0.02	0.003	0.004
	55	18.17	0.81	0.14	0.01	0.02	0.02	0.002	0.002
DRM Empty 3:1	2.9	10.28	0.89	0.05	0.03	0.01	0.01	0.001	0.001
	10	10.32	0.91	0.04	0.02	0.01	0.01	0.001	0.001
	17.5	6.75	0.91	0.04	0.03	0.01	0.01	0.001	0.001
	25	4.86	0.87	0.03	0.07	0.00	0.02	0.001	0.002
	32.5	3.23	0.89	0.03	0.04	0.01	0.03	0.001	0.002
	40	2.58	0.84	0.03	0.09	0.01	0.03	0.001	0.004
	55	2.38	0.82	0.03	0.08	0.01	0.05	0.001	0.005
DRM Empty 1:3	2.9	63.24	0.68	0.18	0.03	0.05	0.03	0.005	0.006
	10	128.81	0.63	0.20	0.04	0.06	0.03	0.008	0.009
	17.5	134.98	0.61	0.21	0.04	0.06	0.03	0.009	0.010
	25	120.49	0.61	0.21	0.04	0.06	0.03	0.009	0.010
	32.5	101.49	0.62	0.20	0.03	0.06	0.03	0.008	0.010
	40	91.80	0.64	0.20	0.03	0.05	0.03	0.008	0.009
	55	76.35	0.68	0.19	0.03	0.05	0.03	0.006	0.007
70	66.72	0.71	0.18	0.02	0.04	0.02	0.005	0.006	



	t (s)	Mole equivalent area (x 1E4)	2-Methyl pentane	3-Methyl pentane	n-Hexane	Heptane(1)	Heptane(2)	Heptane(3)
DRM Empty 1:1	2.9	36.38	0.0012	0.010	0.0006		0.0016	0.0015
	10	53.26	0.0015	0.009	0.0008	0.0009	0.0017	0.0017
	17.5	50.44	0.0014	0.008	0.0007	0.0009	0.0015	0.0016
	25	43.27	0.0011	0.007	0.0006	0.0007	0.0012	0.0013
	32.5	38.38	0.0007	0.006	0.0006	0.0003	0.0007	0.0010
	40	33.30	0.0006	0.005	0.0005	0.0003	0.0007	0.0009
	55	27.31	0.0005	0.005	0.0004	0.0004	0.0006	0.0008
70	24.27	0.0008	0.004	0.0004		0.0010	0.0011	
DRM SiO <sub>2</sub> 1:1	2.5	37.45	0.0010	0.005	0.0005		0.0007	0.0005
	10	44.85		0.006	0.0005	0.0002	0.0008	0.0009
	17.5	29.32		0.004	0.0004		0.0004	0.0005
	25	22.33		0.004	0.0005		0.0005	0.0005
	32.5	19.35		0.004	0.0005		0.0005	0.0005
	40	18.26		0.004	0.0009		0.0006	0.0006
	55	18.17		0.004	0.0006		0.0007	0.0006
DRM Empty 3:1	2.9	10.28	0.0005	0.004	0.0003		0.0006	0.0004
	10	10.32	0.0004	0.003	0.0003		0.0006	0.0003
	17.5	6.75		0.002				
	25	4.86	0.0003	0.002				
	32.5	3.23		0.002				
	40	2.58		0.002				
	55	2.38		0.002				
DRM Empty 1:3	2.9	63.24	0.0041	0.010	0.0010	0.0019	0.0034	0.0014
	10	128.81	0.0069	0.011	0.0016	0.0029	0.0069	
	17.5	134.98	0.0077	0.012	0.0018	0.0034	0.0079	
	25	120.49	0.0076	0.012	0.0020	0.0038	0.0080	
	32.5	101.49	0.0065	0.011	0.0017	0.0034	0.0051	0.0019
	40	91.80	0.0056	0.010	0.0016	0.0031	0.0042	0.0020
	55	76.35	0.0040	0.009	0.0013	0.0025	0.0030	0.0018
70	66.72	0.0029	0.007	0.0009	0.0020	0.0021	0.0016	

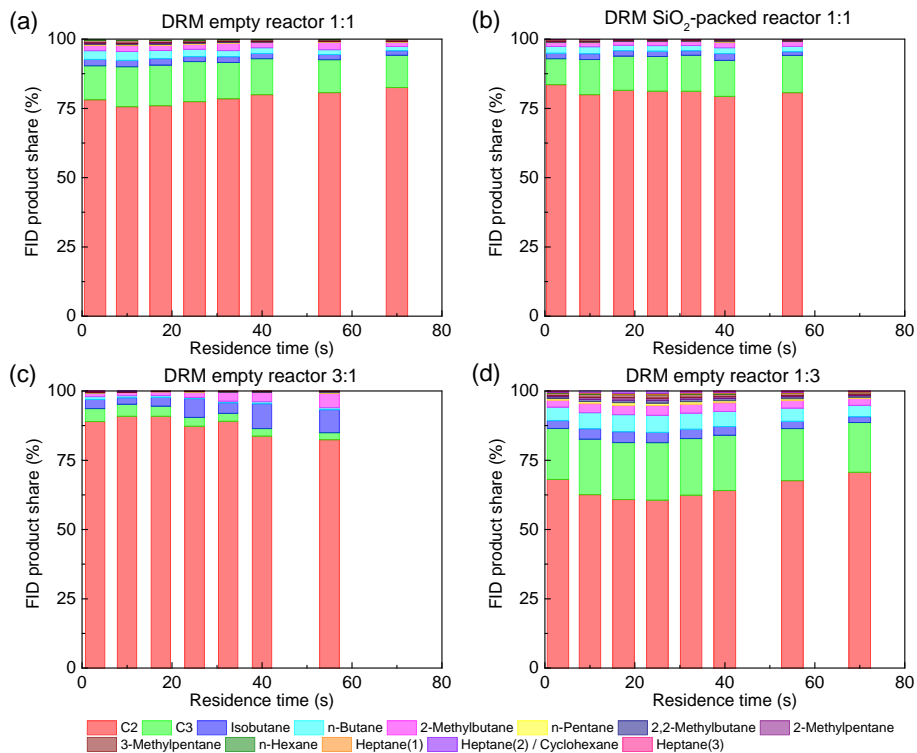


**Figure D.4:** Product shares based on the total mole equivalent FID peak area for DRM, plotted as stacked bars as a function of residence time, for (a) the empty reactor with a CO<sub>2</sub>:CH<sub>4</sub> ratio of 1:1, (b) the SiO<sub>2</sub>-packed reactor at 1:1 ratio, (c) the empty reactor at 3:1 ratio, and (d) the empty reactor at 1:3 ratio. The exact values of the product shares can be found in table D.6.



## D.6 Atom balances of all experiments

**Table D.9:** Atom balances for all gas mixtures and for both empty and SiO<sub>2</sub>-packed reactors (if applicable).

	CO <sub>2</sub>			DRM 3:1			DRM 1:1			DRM 1:3			CH <sub>4</sub>						
	t (s)	C (%)	O (%)	t (s)	C (%)	H (%)	O (%)	t (s)	C (%)	H (%)	O (%)	t (s)	C (%)	H (%)	O (%)	t (s)	C (%)	H (%)	
Empty	2.9	100.4	100.4	2.9	95.1	91.8	92.9	2.9	92.9	94.2	94.1	2.9	89.7	95.2	96.5	2.9	91.43	93.70	
	7.5	101.3	101.3	10	86.7	75.3	83.4	10	80.7	81.6	83.7	10	69.6	82.7	83.1	10	78.94	86.59	
	14.5	100.0	100.0	17.5	82.0	67.5	78.2	17.5	72.6	72.6	75.9	17.5	59.0	74.6	75.1	17.5	71.80	83.18	
	19.4	100.0	100.0	25	80.2	64.1	76.5	25	68.5	67.6	72.2	25	50.7	68.4	67.3	25	63.15	78.46	
	28.9	100.0	99.8	32.5	79.1	62.1	75.9	32.5	66.8	65.9	69.7	32.5	47.1	66.1	64.6	32.5	55.64	75.98	
	41.5	99.8	99.8	40	76.3	58.7	73.6	40	64.9	64.1	68.8	40	43.3	62.8	59.7	40	52.37	73.21	
	48.5	99.0	99.1	55	75.1	59.2	71.8	55	62.4	60.8	66.4	55	40.6	62.3	56.6	55	42.88	69.12	
	58.2	99.7	99.8	70	72.7	61.7	70	61.7	61.7	61.8	65.7	70	37.8	62.2	52.5	70	39.35	71.12	
	72.7	99.0	99.2																
	SiO <sub>2</sub>	2.6	100.7	100.8	2.5	90.3	91.6	92.4	2.5	90.3	91.6	92.4	2.5	89.88	91.79		2.5	89.88	91.79
10.2		100.5	100.5	10	89.7	92.3	91.0	10	89.7	92.3	91.0	10	89.73	92.65		10	89.73	92.65	
17.9		99.4	99.4	17.5	71.4	70.4	73.1	17.5	71.4	70.4	73.1	17.5	68.36	80.54		17.5	68.36	80.54	
25.5		98.8	98.8	25	64.7	61.4	65.9	25	64.7	61.4	65.9	25	50.39	69.29		25	50.39	69.29	
33.2		99.0	98.9	32.5	61.8	58.6	62.5	32.5	61.8	58.6	62.5	32.5	43.07	65.36		32.5	43.07	65.36	
40.8		98.2	98.2	40	61.1	57.3	61.4	40	61.1	57.3	61.4	40	42.30	69.87		40	42.30	69.87	
48.5		98.1	98.1	55	59.2	56.2	59.5	55	59.2	56.2	59.5	55	33.51	60.59		55	33.51	60.59	
56.1		97.6	97.7																
71.4		97.8	97.8																

## D.7 Applied voltage (or $E/N$ , or $T_e$ ) versus different gas mixing ratios and packing material.

Table D.10 shows the applied peak-to-peak voltage for the different gas mixing ratios investigated, and for both the empty and packed DBD reactor. Because we keep the discharge gap constant, the peak-to-peak voltage can be considered as a measure for the reduced electric field, and thus for the electron temperature. We see no clear correlation between this peak-to-peak voltage and the kinetic data derived in our study, for the different gas mixtures, only for the effect of packing. This indicates that besides the electron temperature, additional unknown factors will have an impact as well.

**Table D.10:** Comparison of the applied peak-to-peak voltage (a measure of the reduced electric field  $E/N$  and subsequent the electron temperature) versus the overall rate coefficients and PCE.

		CO <sub>2</sub>	DRM			CH <sub>4</sub>
		1:0	3:1	1:1	1:3	0:1
Empty	U <sub>pp</sub> (kV)	15.25 ± 0.08	15.74 ± 0.03	17.24 ± 0.07	18.1 ± 0.2	16.1 ± 0.2
	k (s <sup>-1</sup> )	0.120 ± 0.005	0.108 ± 0.004	0.088 ± 0.003	0.080 ± 0.002	0.041 ± 0.002
	Xe (%)	53.6 ± 0.8	60.5 ± 0.6	75.4 ± 0.6	83.0 ± 0.7	82 ± 2
SiO <sub>2</sub>	U <sub>pp</sub> (kV)	19.31 ± 0.09		18.9 ± 0.4		18.5 ± 0.5
	k (s <sup>-1</sup> )	0.111 ± 0.004		0.130 ± 0.005		0.074 ± 0.005
	Xe (%)	71.1 ± 0.8		84.3 ± 0.8		81 ± 2



# Appendix E

## Appendix of Chapter 6: Gas flow DRM

### E.1 Residence time distribution (RTD) simulations and measurements

#### E.1.1 Principle

Fluid flow through a reactor is rarely ideal, such as plug flow or mixed flow [19]. The geometry of the reactor, laminar or turbulent flow, diffusion, agitation, recirculation, stagnant regions, and shortcuts will influence the contact time in the reactor, resulting in a certain residence time distribution (RTD) instead of a fixed reaction time for all molecules. This RTD can be determined via a pulse experiment, i.e. adding a pulse of a tracer element to the inlet of the reactor, and recording the concentration of the tracer at the outlet as a function of time, giving us the age distribution curve, or E-curve. The shape of the E-curve can provide useful information about the flow in the reactor and can be used to calculate an average value for the residence time ( $\bar{t}$ ) according to:

$$\bar{t} = \frac{\int_0^{\infty} tC dt}{\int_0^{\infty} C dt} \cong \frac{\sum_i t_i C_i \Delta t_i}{\sum_i C_i \delta t_i} \quad (\text{E.1})$$

with  $C$  the trace concentration and  $t$  the time.

## **E.1.2 Highlights of the simulations**

### **E.1.2.1 Model**

CFD simulations were performed in COMSOL Multiphysics to determine a more theoretical RTD, in order to understand the changes seen in figure 6.6 of the main text. A combined ‘Laminar Flow’ model and ‘Transport of Diluted Species’ model was used to simulate the convection (stationary) and diffusion (time dependent), respectively. A simplified model of the reactor was used (see figure E.1(b and d)), to determine the exact RTD of the reaction volume and omit the extra pathways of the inlet and outlet, next to the complete 2D geometry of the reactor (see figure E.1(a and c)).



## E.1 Residence time distribution (RTD) simulations and measurements

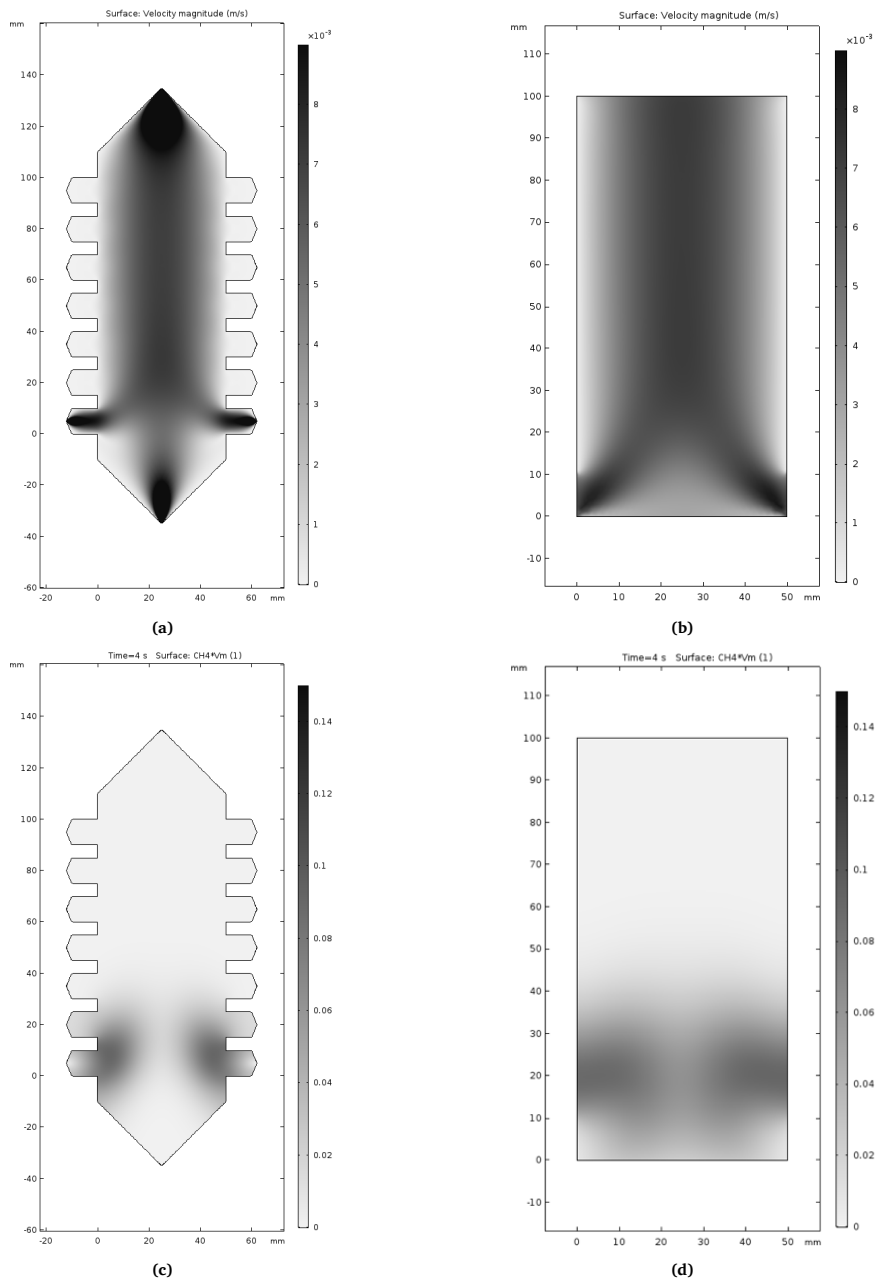
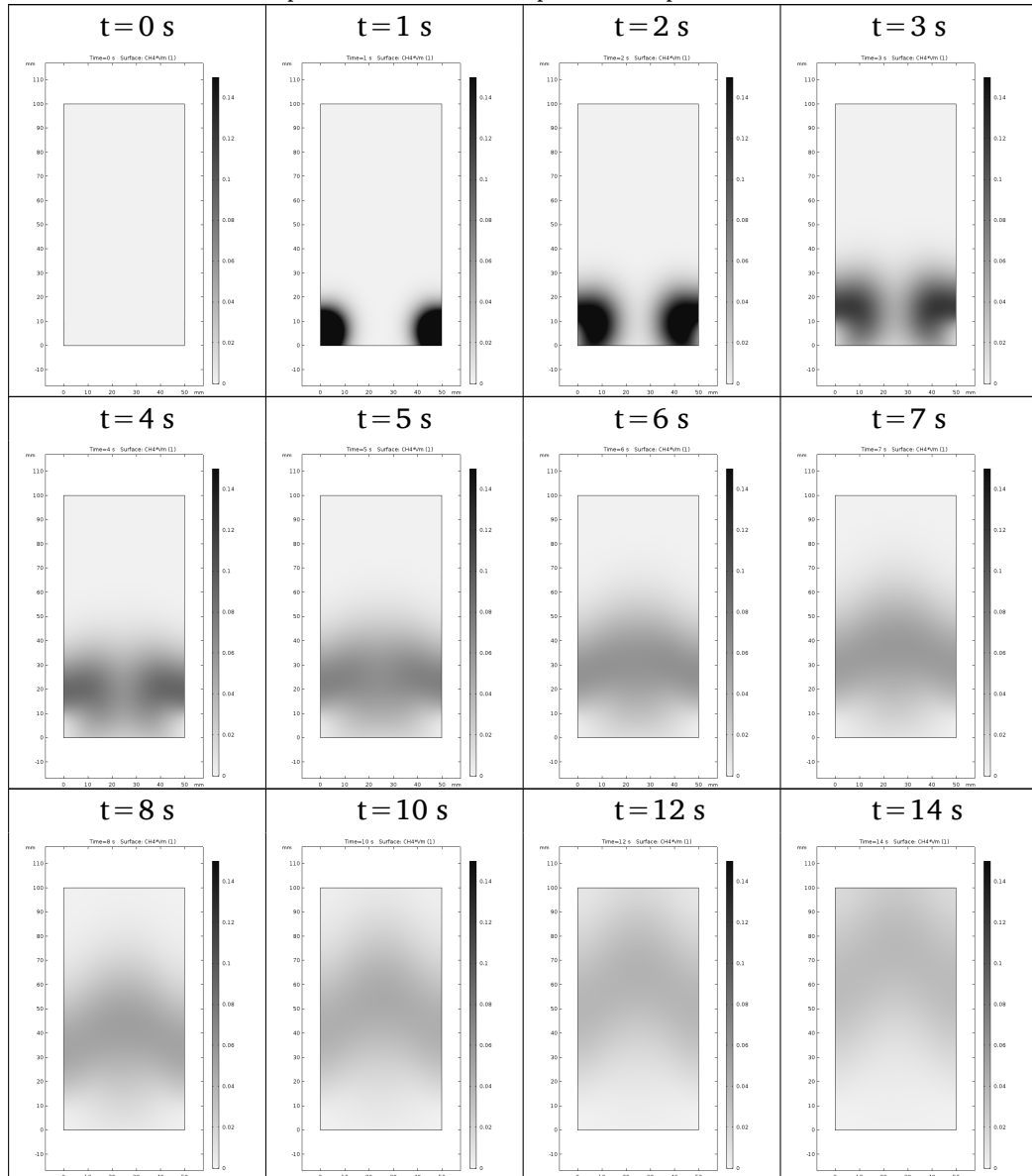


**Figure E.1:** (a and b) Velocity profile and (c and d) example of a concentration profile of CH<sub>4</sub>, (a and c) in the complete geometry of the reactor and (b and d) the simplified version.

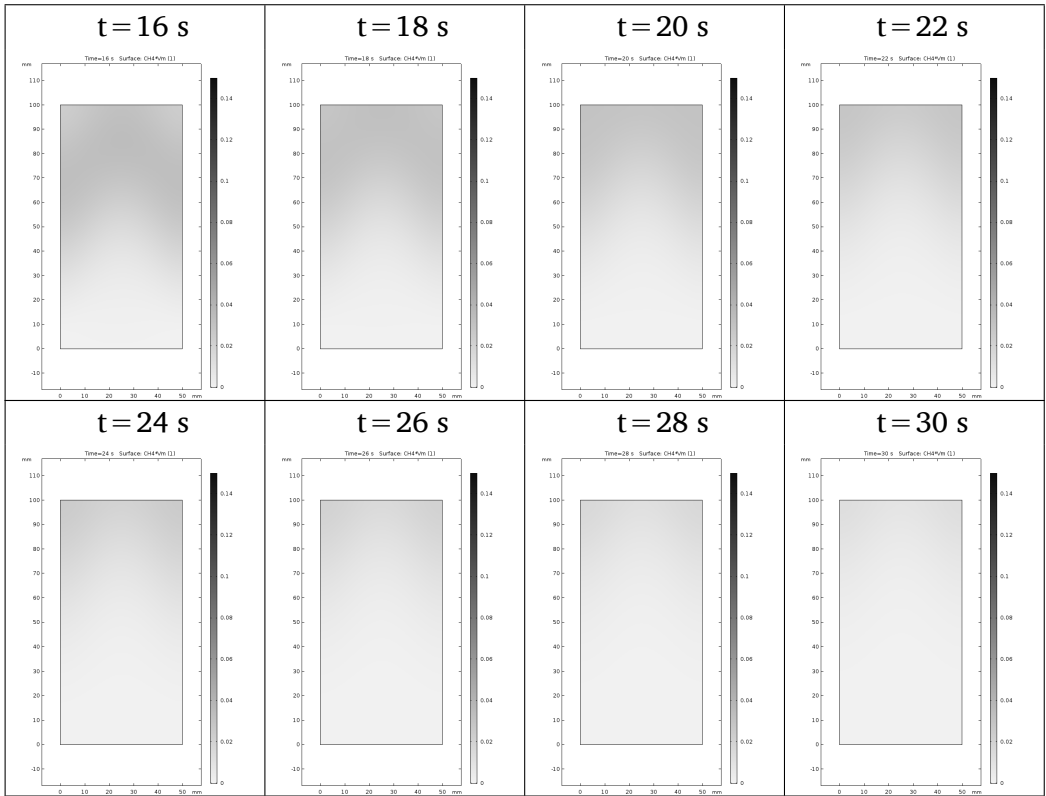
### E.1.2.2 Example of a RTD simulation

Table E.1 shows snapshots (with 1 second interval) of the RTD simulation from the separate addition configuration with CO<sub>2</sub> as the main gas and CH<sub>4</sub> added via entrance 1, see section 6.3.2.2 of the main text. The outlet concentration is measured at the upper border.

**Table E.1:** Snapshots at different time steps of an example RTD CFD simulation.



## E.1 Residence time distribution (RTD) simulations and measurements



### E.1.3 Results of the RTD study

#### E.1.3.1 Gradual addition

##### CFD results

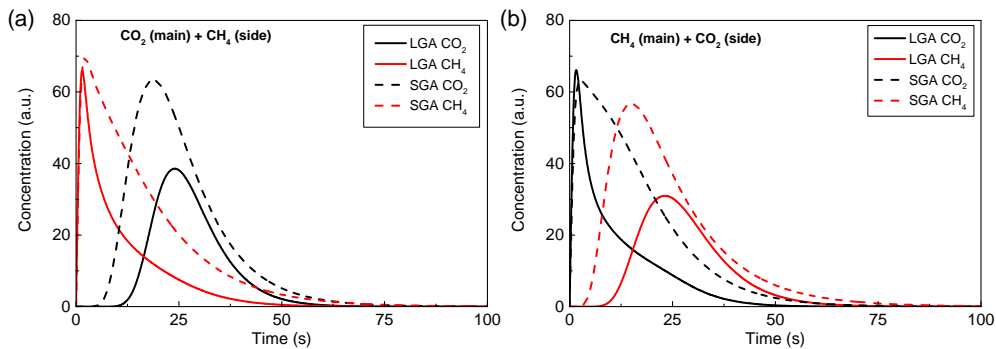


**Figure E.2:** Calculated RTD of CO<sub>2</sub> and CH<sub>4</sub> in the gradual addition configurations for (a) CO<sub>2</sub> as the main gas and (b) CH<sub>4</sub> as the main gas. The average calculated residence times can be found in table E.2.

## E.1.3.2 Separate addition

## CFD results

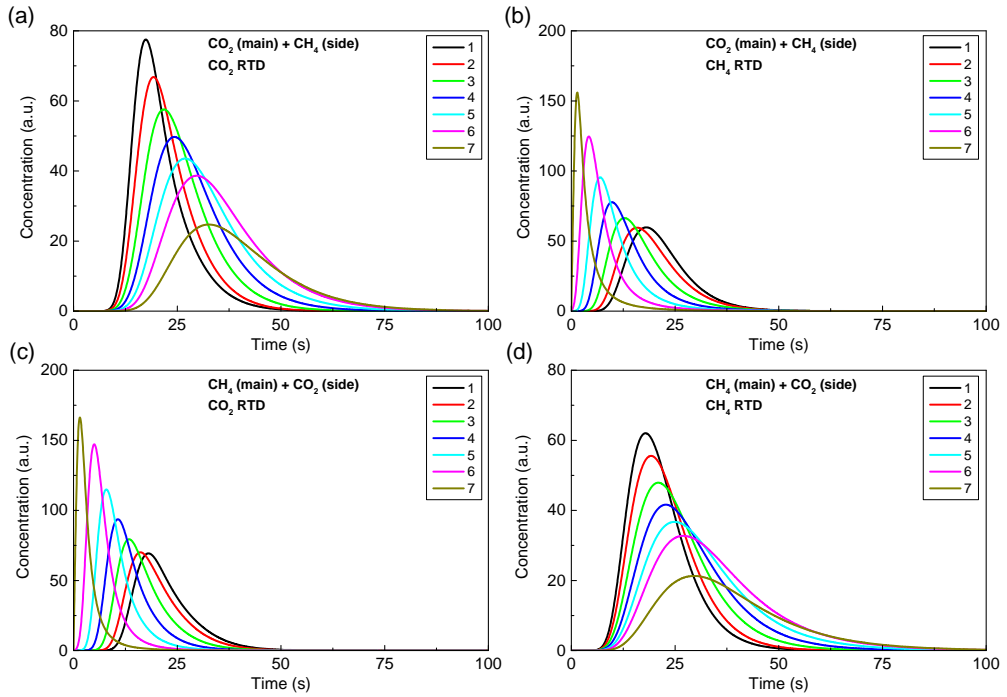


**Figure E.3:** Calculated RTD of (a and c)  $\text{CO}_2$  and (b and d)  $\text{CH}_4$  in the separate addition configurations, for (a and b)  $\text{CO}_2$  as the main gas and (c and d)  $\text{CH}_4$  as the main gas, plotted for the different inlet pairs. The average calculated residence times can be found in table E.2.

**Experimental results**

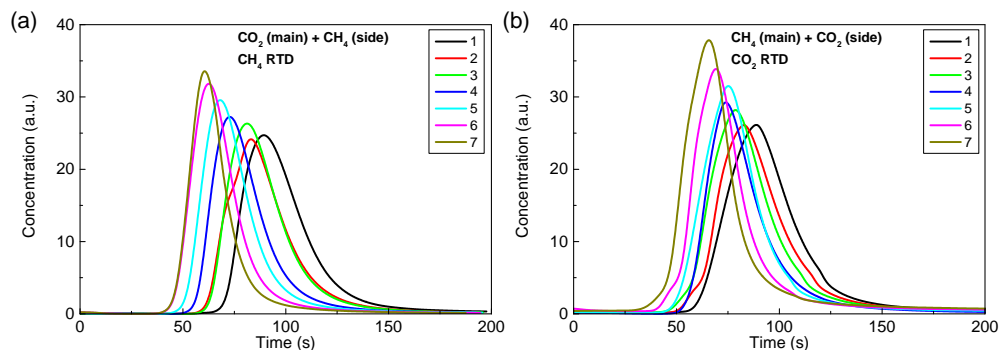


**Figure E.4:** Experimental RTD of the added gas in the separate addition configurations for (a) CO<sub>2</sub> as the main gas and (b) CH<sub>4</sub> as the main gas, plotted for the different inlet pairs. The average calculated residence times can be found in table E.2.

**E.1.3.3 Separate pre-activation**

**CFD results**

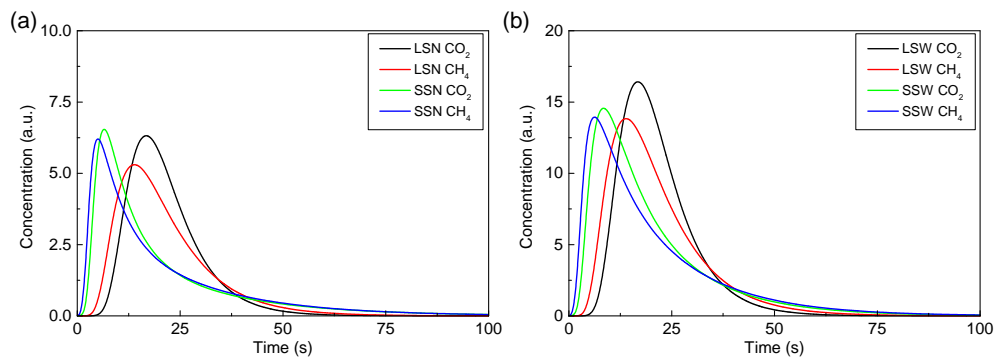


**Figure E.5:** Calculated RTD of CO<sub>2</sub> and CH<sub>4</sub> in the pre-activation configurations. The average calculated residence times can be found in table E.2.

E.1.4 Summary of the obtained RTD data

**Table E.2:** Calculated average residence times of the CFD simulations and experiments. Note that only the gradual addition cases were experimentally obtained due to their deviant behaviour in the main text of the manuscript. Also, only the added gas was pulsed in each case.

		Configuration	CFD		Experimental	
			$t_{CO_2}$ (s)	$t_{CH_4}$ (s)	$t_{CO_2}$ (s)	$t_{CH_4}$ (s)
Gradual addition	CO <sub>2</sub> main – CH <sub>4</sub> side	LGA	28.0	11.2		
		SGA	25.2	16.1		
		1	21.1	21.6		99.1
		2	22.9	19.9		90.9
		3	25.9	17.1		89.8
		4	29.0	14.0		81.5
		5	32.3	10.9		76.2
		6	35.7	7.7		69.5
	7	39.1	4.4		66.7	
Gradual addition	CH <sub>4</sub> main – CO <sub>2</sub> side	LGA	11.4	28.2		
		SGA	15.4	24.2		
		1	22.0	21.5	100.2	
		2	20.1	23.0	95.8	
		3	17.1	25.7	91.5	
		4	13.9	28.6	85.8	
		5	10.6	31.7	87.2	
		6	7.2	34.8	83.8	
	7	3.6	37.9	80.8		
Separate activation	LSN	21.5	21.3			
	LSW	21.5	21.3			
	SSN	20.0	20.0			
	SSW	19.9	19.9			





## **E.2 Raw data of figures 6.3 to 6.7**

**Table E.3:** Energy cost, i.e. the energy needed to convert one mole of reactant mixture, shown for all configurations.

	Configuration	X <sub>CO2</sub> (%)	X <sub>CH4</sub> (%)	X <sub>Total</sub> (%)	EC (kWh/mol)
One inlet – one outlet	L / 100 (i – iv)	12.9 ± 0.6	14.6 ± 0.7	13.7 ± 0.7	1.63 ± 0.04
	S	14.4 ± 0.5	15.5 ± 0.5	14.9 ± 0.5	1.50 ± 0.03
	75 (i)	13.2 ± 1.0	13.6 ± 0.9	13.4 ± 0.9	1.67 ± 0.10
	50 (i)	11.4 ± 0.8	14.4 ± 0.8	12.9 ± 0.8	1.7 ± 0.1
	25 (i)	10.4 ± 0.5	12 ± 1	11.2 ± 0.8	2.0 ± 0.1
	75 (ii)	9.1 ± 0.9	10 ± 2	10 ± 1	2.3 ± 0.2
	50 (ii)	6.5 ± 1.0	8 ± 1	7 ± 1	3.2 ± 0.4
	25 (ii)	2 ± 1	6 ± 1	4 ± 1	5.6 ± 0.6
	75 (iii)	9.5 ± 1.0	10 ± 1	10 ± 1	1.74 ± 0.08
	50 (iii)	4.6 ± 0.5	8 ± 1	6.1 ± 0.9	1.8 ± 0.2
	25 (iii)	4 ± 1	4 ± 2	4 ± 1	1.41 ± 0.09
	75 (iv)	15.2 ± 1.0	18 ± 2	16 ± 1	1.8 ± 0.1
	50 (iv)	20.1 ± 0.8	23.6 ± 1	21.9 ± 0.9	2.05 ± 0.01
	25 (iv)	26 ± 1	34.2 ± 0.8	30 ± 1	2.96 ± 0.09
CO <sub>2</sub> :CH <sub>4</sub> ratio	1:0	6 ± 2	-	6 ± 2	3.6 ± 0.9
	6:1	13 ± 1	24.5 ± 0.6	18.6 ± 0.9	1.5 ± 0.1
	3:1	14 ± 2	18 ± 3	16 ± 2	1.5 ± 0.2
	1:1	12.9 ± 0.6	14.6 ± 0.7	13.7 ± 0.7	1.63 ± 0.04
	1:3	8.6 ± 0.4	11.8 ± 0.4	10.2 ± 0.4	2.03 ± 0.05
	1:6	6.3 ± 0.5	9.8 ± 0.3	8.0 ± 0.4	2.42 ± 0.07
	0:1	-	7.3 ± 0.5	7.3 ± 0.5	3.1 ± 0.2
Residence time (s)	2.5	0.80 ± 0.07	2.8 ± 0.4	1.8 ± 0.3	1.5 ± 0.2
	10	6.7 ± 0.8	8 ± 4	7 ± 2	1.5 ± 0.4
	17.5	11 ± 1	13 ± 4	12 ± 3	1.5 ± 0.4
	25	13.4 ± 0.6	20 ± 3	17 ± 2	1.6 ± 0.2
	32.5	18 ± 1	24 ± 2	21 ± 1	1.66 ± 0.09
	40	21 ± 1	27 ± 3	24 ± 2	1.8 ± 0.1
	47.5	23.4 ± 0.8	31 ± 3	27 ± 2	1.9 ± 0.1
	55	22.9 ± 0.3	30 ± 2	27 ± 1	2.20 ± 0.09
	62.5	30.1 ± 0.6	37 ± 3	33 ± 2	2.0 ± 0.1
	70	31 ± 2	38 ± 3	35 ± 3	2.2 ± 0.1
Gradual addition CO <sub>2</sub> main – CH <sub>4</sub> side	LGA	12.6 ± 0.5	15.8 ± 0.2	14.2 ± 0.3	1.58 ± 0.02
	SGA	17 ± 1	21.0 ± 0.4	19.2 ± 0.8	1.17 ± 0.02
	1	12.4 ± 0.4	16.1 ± 0.4	14.2 ± 0.4	1.57 ± 0.02
	2	15 ± 1	16 ± 1	15 ± 1	1.47 ± 0.03
	3	14.5 ± 0.5	15.9 ± 0.4	15.2 ± 0.5	1.48 ± 0.04
	4	14.8 ± 0.5	15.5 ± 0.5	15.2 ± 0.5	1.48 ± 0.03
	5	15.5 ± 0.6	14.8 ± 0.1	15.1 ± 0.3	1.48 ± 0.01
	6	15.9 ± 0.7	13.4 ± 1.0	14.6 ± 0.9	1.53 ± 0.08
7	16.0 ± 0.4	12.9 ± 0.2	14.5 ± 0.3	1.549 ± 0.007	
Gradual addition CH <sub>4</sub> main – CO <sub>2</sub> side	LGA	15.6 ± 0.8	20.9 ± 0.7	18.3 ± 0.8	1.23 ± 0.05
	SGA	16 ± 1	21.5 ± 0.8	19 ± 1	1.21 ± 0.06
	1	15.5 ± 0.7	19.7 ± 0.6	17.6 ± 0.7	1.27 ± 0.05
	2	16 ± 0.5	20.5 ± 0.4	18.2 ± 0.4	1.23 ± 0.02
	3	16 ± 1	21 ± 2	18 ± 1	1.21 ± 0.08
	4	16.1 ± 0.6	20.1 ± 0.7	18.1 ± 0.6	1.23 ± 0.04
	5	16 ± 2	19 ± 2	17 ± 2	1.3 ± 0.1
	6	15.6 ± 0.8	20 ± 3	18 ± 2	1.26 ± 0.09
7	14.4 ± 0.8	19 ± 2	17 ± 1	1.34 ± 0.05	
Separate activation	LSN	11.9 ± 0.5	17.6 ± 0.6	14.7 ± 0.5	1.52 ± 0.02
	LSW	12.7 ± 0.6	16 ± 2	14 ± 1	1.6 ± 0.1
	SSN	15 ± 1	17 ± 2	16 ± 1	1.41 ± 0.07
	SSW	16.5 ± 0.5	19 ± 2	18 ± 1	1.26 ± 0.06

**Table E.4:** Measured concentration of different calibrated components after the DRM reaction for all configurations used and plotted in figures 6.3 to 6.7. All components are measured on the TCD with the H<sub>2</sub>:CO ratio shown in the last column.

Configuration	CO <sub>2</sub> (%)	CH <sub>4</sub> (%)	H <sub>2</sub> (%)	O <sub>2</sub> (%)	CO (%)	Ethene (%)	Ethane (%)	Propane (%)	Ethanol (ppm)	H <sub>2</sub> :CO
One Inlet - one outlet	L/100 (i-iv)	43.1 ± 0.2	41.3 ± 0.8	6.0 ± 0.6	0.04 ± 0.01	6.4 ± 0.2	0.092 ± 0.005	1.97 ± 0.04	66 ± 7	0.94
	S	44 ± 1	42 ± 1	6.4 ± 0.7	0.03 ± 0.01	7.2 ± 0.3	0.094 ± 0.005	1.03 ± 0.05	108 ± 7	0.90
	75 (i)	43.2 ± 0.8	42 ± 1	5.9 ± 0.6	0.03 ± 0.01	6.3 ± 0.3	0.086 ± 0.007	0.9 ± 0.07	94 ± 3	0.93
	50 (i)	44.1 ± 0.3	41.7 ± 0.7	5.7 ± 0.6	0.04 ± 0.01	5.9 ± 0.1	0.088 ± 0.006	0.91 ± 0.04	84 ± 6	0.97
	25 (i)	45.1 ± 0.2	43.2 ± 0.8	5.0 ± 0.6	0.03 ± 0.02	5.15 ± 0.09	0.077 ± 0.007	0.83 ± 0.04	83 ± 5	0.97
	75 (ii)	44.9 ± 0.2	45.5 ± 0.8	3.8 ± 0.2	0.006 ± 0.003	4.8 ± 0.3	0.069 ± 0.003	0.72 ± 0.02	90 ± 3	0.79
	50 (ii)	46.2 ± 0.6	46.8 ± 1	2.6 ± 0.2	0.006 ± 0.003	3.8 ± 0.2	0.053 ± 0.002	0.88 ± 0.02	85 ± 3	0.70
	25 (ii)	47.0 ± 0.3	49.0 ± 0.5	1.6 ± 0.2	0.002 ± 0.001	2.04 ± 0.05	0.0297 ± 0.0002	0.309 ± 0.008	46 ± 4	0.77
	75 (iii)	48.4 ± 0.5	46.9 ± 0.6	3.6 ± 0.1	0.0096 ± 0.0006	5.0 ± 0.1	0.093 ± 0.006	0.81 ± 0.05	140 ± 3	0.72
	50 (iii)	51.0 ± 0.1	48.1 ± 0.6	2.3 ± 0.4	0.010 ± 0.009	3.0 ± 0.4	0.085 ± 0.006	0.60 ± 0.04	108 ± 4	0.78
	25 (iii)	51.0 ± 0.4	49.0 ± 0.4	1.4 ± 0.2	0.0073 ± 0.0004	1.99 ± 0.08	0.086 ± 0.004	0.44 ± 0.03	72 ± 2	0.70
	75 (iv)	42.7 ± 0.7	40.6 ± 0.8	7.3 ± 0.7	0.03 ± 0.02	7.8 ± 0.2	0.089 ± 0.006	1.11 ± 0.05	140 ± 20	0.93
	50 (iv)	40 ± 1	37.2 ± 1.0	9.6 ± 0.7	0.04 ± 0.01	10.5 ± 0.3	0.088 ± 0.006	1.37 ± 0.04	111 ± 7	0.91
	25 (iv)	36.9 ± 0.8	31.9 ± 0.5	14 ± 1	0.03 ± 0.02	14.1 ± 0.4	0.080 ± 0.005	1.70 ± 0.06	124 ± 3	0.99
	1:0	91 ± 1	3.1 ± 0.8	6 ± 2	3.1 ± 0.8	6 ± 2	0.069 ± 0.002	0.20 ± 0.01	0.017 ± 0.001	31 ± 1
6:1	73.9 ± 0.5	10.4 ± 0.2	5.1 ± 0.6	0.04 ± 0.02	9.06 ± 0.10	0.096 ± 0.006	0.65 ± 0.04	0.11 ± 0.02	116 ± 6	0.74
3:1	64.0 ± 0.5	19.7 ± 0.3	5.6 ± 0.6	0.04 ± 0.02	8.8 ± 0.1	0.06 ± 0.006	0.46 ± 0.04	0.027 ± 0.003	25 ± 2	0.56
1:1	43.1 ± 0.2	41.3 ± 0.8	6.0 ± 0.6	0.04 ± 0.01	6.4 ± 0.2	0.094 ± 0.005	0.97 ± 0.04	0.16 ± 0.03	66 ± 7	0.94
1:3	22.6 ± 0.1	64 ± 1	6.1 ± 0.6	0.03 ± 0.02	3.13 ± 0.06	0.131 ± 0.007	1.31 ± 0.08	0.31 ± 0.04	64 ± 2	1.95
1:6	13.2 ± 0.4	75 ± 3	5.7 ± 0.7	0.03 ± 0.01	1.68 ± 0.07	0.15 ± 0.01	1.37 ± 0.05	0.35 ± 0.02	38 ± 6	3.40
0:1	90 ± 2	90 ± 2	5.0 ± 0.1	0.03 ± 0.01	1.68 ± 0.07	0.208 ± 0.008	1.57 ± 0.04	0.42 ± 0.02	59 ± 10	0.82
2:5	51.7 ± 0.4	48 ± 1	0.64 ± 0.02	0.0135 ± 0.0009	0.87 ± 0.02	0.069 ± 0.002	0.20 ± 0.01	0.017 ± 0.001	31 ± 1	0.74
10	48.8 ± 0.2	46 ± 1	2.68 ± 0.04	0.014 ± 0.001	3.61 ± 0.06	0.096 ± 0.006	0.65 ± 0.04	0.11 ± 0.02	116 ± 6	0.74
17.5	46.5 ± 0.4	43 ± 1	4.8 ± 0.1	0.013 ± 0.001	6.2 ± 0.2	0.094 ± 0.007	0.99 ± 0.06	0.15 ± 0.02	167 ± 9	0.77
25	44.6 ± 0.2	40.0 ± 0.8	6.6 ± 0.2	0.011 ± 0.003	8.4 ± 0.2	0.095 ± 0.006	1.24 ± 0.04	0.20 ± 0.01	160 ± 10	0.79
32.5	42.4 ± 0.3	37.8 ± 0.5	8.5 ± 0.2	0.016 ± 0.001	10.5 ± 0.3	0.096 ± 0.007	1.51 ± 0.06	0.26 ± 0.03	239 ± 9	0.81
40	40.9 ± 0.4	36.2 ± 0.7	9.9 ± 0.2	0.015 ± 0.002	12.1 ± 0.3	0.093 ± 0.008	1.6 ± 0.06	0.29 ± 0.03	219 ± 5	0.82
47.5	39.5 ± 0.2	34.5 ± 0.9	11.3 ± 0.2	0.013 ± 0.004	13.6 ± 0.5	0.095 ± 0.007	1.73 ± 0.05	0.33 ± 0.02	212 ± 2	0.83
55	40 ± 1	30 ± 4	11 ± 2	0.010 ± 0.004	13 ± 2	0.097 ± 0.006	1.83 ± 0.05	0.35 ± 0.02	262 ± 5	0.87
62.5	36.0 ± 0.2	31.5 ± 0.7	13.9 ± 0.4	0.025 ± 0.002	17 ± 2	0.089 ± 0.005	1.84 ± 0.04	0.35 ± 0.01	231 ± 5	0.81
70	35.4 ± 0.7	30.8 ± 0.7	14.9 ± 0.4	0.0525 ± 0.0009	17.4 ± 0.4	0.093 ± 0.006	1.87 ± 0.05	0.40 ± 0.02	268 ± 4	0.86
LGA	42.8 ± 0.2	41.0 ± 0.8	6.0 ± 0.6	0.04 ± 0.01	7.2 ± 0.2	0.076 ± 0.006	0.80 ± 0.04	0.12 ± 0.02	60 ± 6	0.83
SGA	41.2 ± 0.9	38.5 ± 0.9	8.6 ± 0.7	0.04 ± 0.02	9.0 ± 0.2	0.095 ± 0.006	1.21 ± 0.05	0.24 ± 0.02	120 ± 4	0.95
1	42.9 ± 0.8	41 ± 1	6.3 ± 0.6	0.04 ± 0.01	6.7 ± 0.2	0.092 ± 0.007	0.97 ± 0.06	0.16 ± 0.02	95 ± 6	0.94
2	43.3 ± 0.7	41.5 ± 0.9	6.7 ± 0.6	0.03 ± 0.01	7.2 ± 0.1	0.098 ± 0.004	1.04 ± 0.03	0.17 ± 0.02	87 ± 6	0.92
3	43.4 ± 0.2	41.5 ± 0.7	6.4 ± 0.6	0.03 ± 0.01	7.5 ± 0.2	0.091 ± 0.005	0.99 ± 0.04	0.16 ± 0.02	90 ± 6	0.86
4	43.2 ± 0.3	41.7 ± 0.7	6.4 ± 0.6	0.03 ± 0.01	7.6 ± 0.2	0.086 ± 0.006	0.88 ± 0.04	0.15 ± 0.03	83 ± 5	0.84
5	43.2 ± 0.2	42.0 ± 0.7	6.3 ± 0.6	0.04 ± 0.01	7.9 ± 0.2	0.079 ± 0.007	0.76 ± 0.04	0.10 ± 0.03	104 ± 9	0.80
6	43.0 ± 0.3	42.7 ± 0.8	5.8 ± 0.5	0.03 ± 0.01	8.1 ± 0.1	0.071 ± 0.006	0.57 ± 0.04	0.06 ± 0.01	52 ± 4	0.72
7	42.9 ± 0.2	43.0 ± 0.8	5.7 ± 0.6	0.03 ± 0.02	8.2 ± 0.2	0.068 ± 0.005	0.46 ± 0.04	0.046 ± 0.008	35 ± 3	0.69
LGA	42.1 ± 0.3	38.5 ± 0.7	8.3 ± 0.5	0.02 ± 0.01	8.2 ± 0.1	0.108 ± 0.007	1.36 ± 0.05	0.28 ± 0.03	128 ± 5	1.00
SGA	42.1 ± 0.8	38.2 ± 1.0	8.6 ± 0.6	0.04 ± 0.01	8.2 ± 0.2	0.098 ± 0.007	1.27 ± 0.04	0.28 ± 0.03	122 ± 4	1.05
1	42.6 ± 0.3	40.0 ± 0.7	7.7 ± 0.7	0.03 ± 0.02	8.3 ± 0.2	0.099 ± 0.007	1.19 ± 0.05	0.21 ± 0.03	118 ± 7	0.92
2	42.4 ± 0.6	40 ± 1	7.9 ± 0.6	0.03 ± 0.02	8.7 ± 0.2	0.099 ± 0.006	1.25 ± 0.06	0.23 ± 0.03	118 ± 5	0.91
3	42.3 ± 0.8	39.5 ± 0.7	8.2 ± 0.7	0.03 ± 0.02	8.6 ± 0.2	0.100 ± 0.007	1.26 ± 0.06	0.23 ± 0.02	132 ± 6	0.96
4	43.0 ± 0.3	39.8 ± 0.8	8.3 ± 0.6	0.04 ± 0.01	8.2 ± 0.2	0.101 ± 0.007	1.27 ± 0.06	0.26 ± 0.04	124 ± 6	1.01
5	43 ± 1	40.3 ± 0.8	8.0 ± 0.8	0.03 ± 0.02	7.7 ± 0.3	0.103 ± 0.006	1.24 ± 0.06	0.24 ± 0.04	114 ± 6	1.04
6	43.3 ± 0.9	40 ± 1	8.3 ± 0.7	0.04 ± 0.01	7.6 ± 0.2	0.106 ± 0.006	1.33 ± 0.04	0.28 ± 0.03	105 ± 5	1.09
7	43.7 ± 0.6	39.9 ± 0.9	7.8 ± 0.6	0.03 ± 0.02	7.17 ± 0.06	0.106 ± 0.007	1.32 ± 0.04	0.30 ± 0.03	108 ± 3	1.09
LSN	44.1 ± 0.2	40.9 ± 0.6	6.5 ± 0.7	0.02 ± 0.02	7.0 ± 0.2	0.084 ± 0.005	0.97 ± 0.05	0.16 ± 0.02	100 ± 10	0.89
LSW	43.6 ± 0.7	41.2 ± 0.9	6.2 ± 0.6	0.03 ± 0.01	7.0 ± 0.3	0.088 ± 0.007	0.98 ± 0.07	0.17 ± 0.02	109 ± 10	0.94
SSN	43.4 ± 0.7	40.8 ± 0.7	7.2 ± 0.7	0.04 ± 0.02	7.3 ± 0.1	0.093 ± 0.007	1.12 ± 0.08	0.20 ± 0.02	113 ± 3	1.00
SSW	42.2 ± 1.0	40.1 ± 0.8	8.3 ± 0.6	0.04 ± 0.01	8.1 ± 0.3	0.091 ± 0.004	1.17 ± 0.03	0.21 ± 0.02	136 ± 9	1.03

277  
Separate activation

**Table E.5:** GC peak areas for different uncalibrated components after the DRM reaction for all configurations used and plotted in figures 6.3 to 6.7. All components are measured on the FID, unless stated otherwise, and rescaled per column as stated in the second row. Continues on the next page.

Component	Propene (TCD)	C2	C3	Isobutane / Methanol	n-Butane	2-methylbutane / 2-propanol / acetone	n-Pentane / Diethylether	1	2,2-Dimethylbutane / 1-propanol	
	x 1000	x 100	x 10	x 10	x 10	x 10	x 10	x 1	x 10	
One inlet - one outlet	Configuration									
	L/100 (i-iv)									
	S	30 ± 10	4060 ± 50	7300 ± 200	1580 ± 60	2100 ± 80	1830 ± 70	290 ± 20	300 ± 40	
	26 ± 9	4300 ± 100	8400 ± 400	1980 ± 60	2300 ± 100	2130 ± 100	2130 ± 100	300 ± 10	500 ± 200	
	75 (i)	20 ± 10	3990 ± 50	7400 ± 200	1750 ± 20	2080 ± 60	1900 ± 50	1460 ± 50	300 ± 60	
	50 (ii)	29 ± 10	3850 ± 60	8000 ± 300	1800 ± 50	2160 ± 80	2020 ± 70	1400 ± 50	330 ± 90	
	25 (i)	20 ± 10	3550 ± 30	7600 ± 200	1750 ± 50	2000 ± 50	1970 ± 60	280 ± 4	450 ± 20	
	75 (ii)	16 ± 7	2800 ± 40	4800 ± 200	1280 ± 40	1360 ± 40	1270 ± 50	164 ± 7	300 ± 70	
	23 ± 8	1980 ± 50	2800 ± 200	950 ± 30	790 ± 70	105 ± 5	820 ± 40	110 ± 30	110 ± 30	
	12 ± 2	1150 ± 30	1800 ± 100	540 ± 40	530 ± 30	64 ± 5	490 ± 30	400 ± 30	40 ± 10	
	75 (iii)	30 ± 10	3130 ± 40	4580 ± 70	1580 ± 10	1330 ± 20	1350 ± 20	156 ± 3	230 ± 10	
	50 (iii)	19 ± 8	2420 ± 30	2900 ± 100	1140 ± 20	870 ± 30	910 ± 20	108 ± 7	380 ± 60	
	25 (iv)	17 ± 6	1580 ± 20	1470 ± 40	679 ± 8	470 ± 10	462 ± 9	52 ± 2	130 ± 20	
	75 (iv)	20 ± 10	4500 ± 500	9500 ± 500	2300 ± 100	2700 ± 200	2460 ± 70	360 ± 20	500 ± 100	
	50 (iv)	30 ± 10	5800 ± 40	14400 ± 400	3050 ± 50	4000 ± 100	3590 ± 90	550 ± 20	1000 ± 100	
	25 (iv)	40 ± 10	6910 ± 30	19800 ± 300	4300 ± 100	5900 ± 200	4900 ± 200	800 ± 20	1700 ± 100	
	1:0									
	6:1	42 ± 5	524 ± 10	189 ± 7	170 ± 10	70 ± 10	120 ± 20	260 ± 70	260 ± 70	
	3:1	30 ± 10	1550 ± 10	1180 ± 9	500 ± 20	297 ± 7	499 ± 6	790 ± 40	60 ± 10	
	1:1	30 ± 10	4060 ± 50	7300 ± 200	1580 ± 60	2100 ± 80	1830 ± 70	1500 ± 200	300 ± 40	
	1:3	30 ± 20	5970 ± 40	17000 ± 200	2670 ± 30	5860 ± 50	3230 ± 30	1650 ± 100	780 ± 10	
	1:6	30 ± 10	6490 ± 30	21000 ± 200	3240 ± 40	7480 ± 80	3770 ± 60	1450 ± 80	1050 ± 20	
	0:1	40 ± 10	6860 ± 40	24100 ± 200	3910 ± 60	9140 ± 60	4310 ± 20	1030 ± 9	1400 ± 40	
	CO <sub>2</sub> :CH <sub>4</sub> ratio	2.5	3 ± 1	820 ± 40	791 ± 2	369 ± 5	228 ± 2	245 ± 3	133 ± 7	
		10	30 ± 10	2700 ± 10	9950 ± 50	1300 ± 30	1170 ± 10	1110 ± 10	108 ± 4	260 ± 40
17.5		23 ± 10	4110 ± 30	7600 ± 100	2210 ± 60	2140 ± 30	2130 ± 30	229 ± 5	420 ± 30	
25		21 ± 9	5060 ± 20	10540 ± 90	2610 ± 90	2840 ± 30	2820 ± 30	315 ± 6	500 ± 100	
32.5		30 ± 20	6090 ± 50	14100 ± 200	3690 ± 10	3850 ± 40	4148 ± 7	477 ± 5	850 ± 20	
40		30 ± 20	6510 ± 40	15500 ± 100	3760 ± 20	4220 ± 40	4430 ± 20	521 ± 6	880 ± 20	
47.5		40 ± 10	6780 ± 10	16780 ± 20	3920 ± 20	4591 ± 5	4930 ± 10	591 ± 1	1020 ± 20	
55		30 ± 10	7280 ± 10	18300 ± 100	4370 ± 30	5030 ± 30	4910 ± 40	636 ± 5	1160 ± 20	
62.5		30 ± 10	7150 ± 30	18800 ± 200	4380 ± 50	5200 ± 60	5700 ± 50	698 ± 8	1340 ± 70	
70		40 ± 10	7384 ± 8	20000 ± 100	4740 ± 90	5630 ± 60	6700 ± 30	765 ± 5	1450 ± 30	
Gradual addition		LGA	20 ± 10	3430 ± 20	5200 ± 200	1270 ± 40	1370 ± 40	1460 ± 20	1430 ± 50	
		SGA	30 ± 10	5220 ± 10	12750 ± 90	2820 ± 20	3620 ± 30	3170 ± 20	2160 ± 50	880 ± 40
		1	30 ± 10	4240 ± 40	8100 ± 100	1780 ± 30	2320 ± 30	2020 ± 30	1680 ± 60	600 ± 200
		2	36 ± 10	4390 ± 30	8270 ± 70	1820 ± 40	2340 ± 20	2050 ± 20	1710 ± 50	300 ± 100
		3	30 ± 10	4210 ± 20	7600 ± 100	1750 ± 30	2090 ± 20	1930 ± 20	1620 ± 40	500 ± 100
	4	30 ± 10	3827 ± 7	6320 ± 40	1570 ± 40	1703 ± 7	1678 ± 9	1470 ± 40	211 ± 10	
	5	20 ± 10	3360 ± 80	4600 ± 100	1500 ± 100	1280 ± 40	1390 ± 30	1320 ± 60	103 ± 3	
Gradual addition	LGA	30 ± 10	5730 ± 40	15200 ± 200	3230 ± 40	4550 ± 50	3630 ± 50	2260 ± 90	930 ± 30	
	SGA	30 ± 10	5440 ± 90	14800 ± 400	3200 ± 100	4400 ± 100	3590 ± 100	2270 ± 90	1040 ± 50	
	1	30 ± 10	5060 ± 30	11220 ± 100	2490 ± 30	3160 ± 50	2760 ± 10	1910 ± 50	600 ± 100	
	2	30 ± 10	5310 ± 90	12000 ± 300	2600 ± 60	3420 ± 80	2940 ± 50	2080 ± 70	640 ± 30	
	3	30 ± 10	5480 ± 70	13000 ± 200	2840 ± 40	3730 ± 40	3170 ± 40	2130 ± 60	720 ± 30	
	4	30 ± 10	5440 ± 90	13600 ± 400	2900 ± 90	3960 ± 100	3250 ± 80	2200 ± 100	880 ± 50	
	5	30 ± 10	5300 ± 100	12900 ± 600	2700 ± 100	3800 ± 200	3150 ± 200	2100 ± 100	790 ± 80	
Separate activation	LGA	30 ± 10	5640 ± 60	14800 ± 300	3010 ± 60	4500 ± 100	3430 ± 80	2160 ± 50	1000 ± 100	
	SGA	40 ± 10	5600 ± 90	15200 ± 300	3110 ± 80	4640 ± 90	3470 ± 60	2090 ± 100	900 ± 200	
	LSN	16 ± 9	4240 ± 80	8600 ± 200	1960 ± 80	2380 ± 60	2150 ± 60	1520 ± 60	470 ± 30	
	LSW	30 ± 10	4190 ± 100	8300 ± 300	1950 ± 70	2310 ± 60	2100 ± 50	1530 ± 40	360 ± 90	
	SSN	30 ± 10	4700 ± 200	10300 ± 800	2300 ± 100	2900 ± 300	2500 ± 200	1700 ± 100	560 ± 70	
	SSW	20 ± 10	5000 ± 100	11700 ± 500	2680 ± 70	3400 ± 200	3000 ± 200	1980 ± 50	710 ± 40	

Component	2-Methyl pentane		3-Methyl pentane		n-Hexane		2		3		Heptane(1) / 1-Butanol		Heptane(2) / Cyclohexane		Heptane(3)	
	Configuration	x 10	x 10	x 10	x 10	x 10	x 10	x 10	x 10	x 10	x 10	x 10	x 10	x 10	x 10	x 10
One inlet - one outlet	L / 100 (i - iv)	130 ± 30	870 ± 50	100 ± 30	60 ± 20	300 ± 100	130 ± 50									
	S	190 ± 10	1020 ± 40	105 ± 4	69 ± 6	750 ± 90	270 ± 60									
	75 (i)	150 ± 20	910 ± 30	110 ± 10	80 ± 10	600 ± 300	180 ± 40									
	50 (i)	210 ± 20	920 ± 30	101 ± 9	60 ± 10	1400 ± 300	260 ± 30									
	25 (i)	168 ± 9	810 ± 30	100 ± 10	80 ± 10	340 ± 30	160 ± 20	73 ± 9								
	75 (ii)	135 ± 9	720 ± 30	90 ± 10	60 ± 10	870 ± 20	173 ± 10									
	50 (ii)	49 ± 6	420 ± 40	49 ± 6	30 ± 7	300 ± 100	90 ± 20									
	25 (ii)	24 ± 2	280 ± 20	280 ± 20	17 ± 3	49 ± 5	25 ± 3	9 ± 2								
	75 (iii)	780 ± 20	780 ± 20	41 ± 7	400 ± 100	110 ± 20	110 ± 20									
	50 (iii)	60 ± 5	530 ± 60	60 ± 10	40 ± 10	980 ± 80	80 ± 10									
	25 (iii)	290 ± 20	290 ± 20	17 ± 4	260 ± 30	39 ± 2	27 ± 6									
	75 (iv)	180 ± 20	1130 ± 40	142 ± 5	105 ± 6	370 ± 40	170 ± 20	68 ± 9								
	50 (iv)	380 ± 40	1610 ± 40	191 ± 7	170 ± 10	1200 ± 300	440 ± 60	320 ± 50								
25 (iv)	570 ± 30	1980 ± 70	220 ± 20	250 ± 50	1000 ± 100	410 ± 40	500 ± 50									
CO <sub>2</sub> :CH <sub>4</sub> ratio	1:0															
	6:1		60 ± 30			289 ± 8										
	3:1		230 ± 20		30 ± 10	270 ± 6										
	1:1		870 ± 50		100 ± 30	300 ± 100										
	1:3		1400 ± 20		230 ± 20	690 ± 40										
	1:6		730 ± 20		260 ± 30	240 ± 60										
	0:1		1020 ± 40		340 ± 30	380 ± 40										
	2:5		60 ± 6			110 ± 20										
	10		630 ± 10			31 ± 2										
	17.5		1100 ± 50			90 ± 30										
	25		1320 ± 40			84 ± 7										
	32.5		1800 ± 70			155 ± 8										
	40		1866 ± 8			140 ± 2										
47.5		372 ± 4			190 ± 10											
55		380 ± 10			225 ± 4											
62.5		430 ± 20			250 ± 10											
70		450 ± 20			270 ± 30											
Gradual addition	LGA	140 ± 10	700 ± 30	100 ± 20	60 ± 10	890 ± 90	170 ± 20									
	SGA	360 ± 10	1433 ± 8	160 ± 10	120 ± 20	1760 ± 60	430 ± 20									
	1	220 ± 20	1040 ± 30	150 ± 20	100 ± 20	1100 ± 200	270 ± 30									
	2	200 ± 20	1010 ± 20	140 ± 8	90 ± 8	1000 ± 100	250 ± 20									
	3	200 ± 20	950 ± 20	126 ± 6	69 ± 8	1500 ± 200	270 ± 20									
	4	180 ± 10	828 ± 7	113 ± 6	59 ± 9	1400 ± 100	240 ± 10									
	5	90 ± 20	600 ± 20	80 ± 10	34 ± 6	200 ± 100	80 ± 40									
Gradual addition	LGA	430 ± 20	1620 ± 30	200 ± 10	180 ± 20	780 ± 40	400 ± 20									
	SGA	470 ± 20	1580 ± 40	190 ± 20	180 ± 30	1200 ± 200	480 ± 40									
	1	280 ± 10	1310 ± 10	150 ± 10	100 ± 10	1400 ± 100	350 ± 40									
	2	300 ± 10	1370 ± 20	170 ± 10	130 ± 10	800 ± 200	170 ± 20									
	3	330 ± 10	1450 ± 20	190 ± 20	130 ± 10	800 ± 200	190 ± 20									
	4	390 ± 20	1500 ± 40	170 ± 20	140 ± 30	1600 ± 200	450 ± 30									
	5	350 ± 40	1410 ± 70	180 ± 20	140 ± 20	1100 ± 400	380 ± 60									
Separate activation	LGA	190 ± 10	1000 ± 30	105 ± 9	80 ± 10	600 ± 200	180 ± 30									
	LSW	190 ± 20	990 ± 10	120 ± 10	80 ± 20	1000 ± 600	80 ± 10									
	SSN	230 ± 30	1150 ± 90	140 ± 10	110 ± 10	470 ± 80	220 ± 50									
	SSW	270 ± 20	1270 ± 40	150 ± 20	130 ± 20	700 ± 100	190 ± 50									

**Table E.6:** Total mole equivalent FID peak area based on the number of C atoms per molecule (second column), and the individual shares of each component (third to last column), for the components formed during DRM for all configurations. Continues on the next page.

Configuration	Mole equivalent area (x 1E4)	C2	C3	Isobutane	n-Butane	2-methylbutane	n-Pentane	2,2-Dimethylbutane
One inlet - one outlet	L / 100 (i - iv)	24.32	0.83	0.10	0.02	0.02	0.0023	0.002
	S	26.35	0.82	0.11	0.02	0.02	0.0022	0.003
	75 (i)	24.09	0.83	0.10	0.02	0.02	0.0023	0.002
	50 (i)	23.70	0.81	0.11	0.02	0.02	0.0024	0.002
	25 (i)	21.96	0.81	0.12	0.02	0.02	0.0025	0.003
	75 (ii)	16.80	0.83	0.09	0.02	0.02	0.0019	0.003
	50 (ii)	11.57	0.86	0.08	0.02	0.02	0.0018	0.002
	25 (ii)	6.80	0.85	0.09	0.02	0.02	0.0019	0.001
	75 (iii)	18.43	0.85	0.08	0.02	0.02	0.0017	0.002
	50 (iii)	13.96	0.87	0.07	0.02	0.02	0.0015	0.005
	25 (iii)	8.84	0.89	0.06	0.02	0.01	0.0012	0.002
	75 (iv)	27.99	0.81	0.11	0.02	0.02	0.0026	0.003
	50 (iv)	37.04	0.78	0.13	0.02	0.03	0.0030	0.005
	25 (iv)	45.71	0.76	0.14	0.02	0.03	0.0035	0.006
	CO <sub>2</sub> :CH <sub>4</sub> ratio	1:0	2.80	0.94	0.02	0.02	0.01	0.0004
6:1		8.51	0.91	0.05	0.01	0.01	0.0013	0.001
3:1		24.32	0.83	0.10	0.02	0.02	0.0023	0.002
1:1		39.10	0.76	0.14	0.02	0.04	0.0037	0.003
1:3		43.82	0.74	0.16	0.02	0.04	0.0041	0.004
1:6		47.60	0.72	0.17	0.02	0.05	0.0043	0.005
0:1		4.59	0.90	0.06	0.02	0.01	0.0009	0.003
2:5		15.84	0.85	0.08	0.02	0.02	0.0014	0.003
10		24.97	0.82	0.10	0.02	0.02	0.0018	0.003
17.5		31.24	0.81	0.11	0.02	0.02	0.0020	0.003
25		38.58	0.79	0.12	0.02	0.02	0.0025	0.004
32.5		41.35	0.79	0.12	0.02	0.03	0.0025	0.004
40		43.49	0.78	0.13	0.02	0.03	0.0027	0.004
47.5		46.74	0.78	0.13	0.02	0.03	0.0027	0.004
55		46.56	0.77	0.13	0.02	0.03	0.0030	0.005
62.5	48.57	0.76	0.14	0.02	0.03	0.0031	0.005	
70	20.13	0.85	0.09	0.02	0.02	0.0021	0.002	
Gradual addition	LGA	33.24	0.78	0.13	0.02	0.03	0.0030	0.004
	SGA	25.80	0.82	0.10	0.02	0.02	0.0025	0.004
	1	26.56	0.83	0.10	0.02	0.02	0.0024	0.004
	2	25.33	0.83	0.10	0.02	0.02	0.0022	0.003
	3	22.69	0.84	0.09	0.02	0.02	0.0020	0.002
	4	19.55	0.86	0.08	0.02	0.02	0.0019	0.002
	5	14.72	0.89	0.06	0.02	0.01	0.0017	0.001
6	11.00	0.90	0.05	0.02	0.01	0.0017	0.001	
CO <sub>2</sub> main - CH <sub>4</sub> side	LGA	37.19	0.77	0.14	0.02	0.03	0.0034	0.004
	SGA	35.57	0.76	0.14	0.02	0.03	0.0035	0.005
	1	31.57	0.80	0.12	0.02	0.03	0.0026	0.003
	2	33.23	0.80	0.12	0.02	0.03	0.0028	0.003
	3	34.64	0.79	0.13	0.02	0.03	0.0029	0.003
	4	34.82	0.78	0.13	0.02	0.03	0.0031	0.004
	5	33.94	0.79	0.13	0.02	0.03	0.0030	0.004
CH <sub>4</sub> main - CO <sub>2</sub> side	6	36.49	0.77	0.14	0.02	0.03	0.0034	0.005
	7	36.53	0.77	0.14	0.02	0.03	0.0035	0.004
	LGA	26.00	0.82	0.11	0.02	0.02	0.0023	0.003
	SGA	25.57	0.82	0.11	0.02	0.02	0.0023	0.002
	1	29.24	0.80	0.12	0.02	0.03	0.0027	0.003
	2	31.59	0.79	0.12	0.02	0.03	0.0029	0.004
	3							
Separate activation	LSN							
	LSW							
	SSN							
SSW								

	Configuration	Mole equivalent area (x 1E4)	2-Methylpentane	3-Methylpentane	n-Hexane	Heptane(1)	Heptane(2)	Heptane(3)	
One Inlet - one outlet	L/100 (i-iv)	24.32	0.001	0.006	0.0007	0.0004	0.001	0.0008	
	S	26.35	0.001	0.006	0.0007	0.0004	0.001	0.0011	
	75 (i)	24.09	0.001	0.006	0.0008	0.0004	0.001	0.0009	
	50 (i)	23.70	0.001	0.006	0.0007	0.0004	0.001	0.0010	
	25 (i)	21.96	0.001	0.006	0.0008	0.0005	0.001	0.0006	
	75 (iii)	16.80	0.001	0.007	0.0009	0.0001	0.001	0.0013	
	50 (ii)	11.57	0.001	0.006	0.0007	0.0001	0.001	0.0010	
	25 (ii)	6.80	0.001	0.007	0.0005	0.0002	0.001	0.0008	
	75 (iii)	18.43	0.000	0.007	0.0005	0.0002	0.001	0.0008	
	50 (iii)	13.96	0.001	0.006	0.0007	0.0002	0.001	0.0008	
	25 (iii)	8.84	0.001	0.006	0.0007	0.0001	0.001	0.0007	
	75 (iv)	27.99	0.001	0.007	0.0008	0.0003	0.001	0.0007	
	50 (iv)	37.04	0.002	0.007	0.0009	0.0012	0.002	0.0011	
	25 (iv)	45.71	0.002	0.007	0.0008	0.0013	0.002	0.0007	
	CO <sub>2</sub> :CH <sub>4</sub> ratio	1:0	2.80		0.004		0.0076		0.0005
		6:1	8.51		0.004	0.0006		0.001	0.0008
1:1		24.32	0.001	0.006	0.0007	0.0004	0.001	0.0008	
1:3		39.10	0.002	0.006	0.0010	0.0012	0.002	0.0010	
1:6		43.82	0.003	0.005	0.0010	0.0016	0.002	0.0007	
0:1		47.60	0.004	0.004	0.0012	0.0022	0.003	0.0005	
2:5		4.59		0.002				0.0007	
10		15.84		0.007			0.001	0.0008	
17.5		24.97	0.001	0.007			0.001	0.0009	
25		31.24	0.001	0.008	0.0004	0.0010	0.001	0.0010	
Residence time (s)	32.5	38.58	0.001	0.008	0.0006	0.0009	0.001	0.0009	
	40	41.35	0.001	0.008	0.0006	0.0010	0.001	0.0010	
	47.5	43.49	0.001	0.008	0.0007	0.0010	0.001	0.0010	
	55	46.74	0.001	0.008	0.0006	0.0009	0.001	0.0009	
	62.5	46.56	0.002	0.008	0.0007	0.0012	0.002	0.0011	
	70	48.57	0.002	0.008	0.0007	0.0012	0.002	0.0010	
	Gradual addition	LGA	20.13	0.001	0.006	0.0008		0.001	0.0010
		SGA	33.24	0.002	0.007	0.0008		0.002	0.0011
		1	25.80	0.001	0.007	0.0009		0.001	0.0013
		2	26.56	0.001	0.006	0.0009		0.001	0.0011
3		25.33	0.001	0.006	0.0008		0.002	0.0013	
4		22.69	0.001	0.006	0.0008		0.001	0.0013	
5		19.55	0.001	0.005	0.0007		0.001	0.0006	
CO <sub>2</sub> main - CH <sub>4</sub> side	6	14.72	0.002	0.004	0.0008		0.001	0.0007	
	7	11.00	0.002	0.004	0.0010		0.001	0.0010	
	LGA	37.19	0.002	0.007	0.0009	0.0010	0.002	0.0010	
	SGA	35.57	0.002	0.007	0.0009	0.0014	0.002	0.0011	
	1	31.57	0.001	0.007	0.0008		0.002	0.0011	
	2	33.23	0.001	0.007	0.0009	0.0007	0.001	0.0010	
	3	34.64	0.002	0.007	0.0008	0.0008	0.001	0.0009	
CH <sub>4</sub> main - CO <sub>2</sub> side	4	34.82	0.002	0.007	0.0009	0.0013	0.002	0.0012	
	5	33.94	0.002	0.007	0.0009	0.0010	0.002	0.0011	
	6	36.49	0.002	0.007	0.0009	0.0013	0.002	0.0011	
	7	36.53	0.002	0.007	0.0009	0.0017	0.002	0.0013	
	LGA	26.00	0.001	0.006	0.0007	0.0005	0.001	0.0007	
	LSW	25.57	0.001	0.006	0.0008	0.0004	0.001	0.0009	
	SSN	29.24	0.001	0.007	0.0008	0.0007	0.001	0.0007	
Separate activation	SSW	31.59	0.001	0.007	0.0008	0.0008	0.001	0.0008	





# Appendix F

## Appendix of Chapter 7: Gas flow NH<sub>3</sub>

### F.1 Raw data of figure 7.1 to figure 7.5

**Table F.1:** Ammonia yield and energy cost, i.e. the energy needed to convert one mole of reactant mixture, shown for all configurations.

	Configuration	Yield (ppm)	EC (kWh/mol)
One inlet – one outlet	L / 100 (i – iv)	1610 ± 20	139 ± 2
	S	1580 ± 40	142 ± 4
	75 (i)	1500 ± 20	150 ± 2
	50 (i)	1244 ± 8	180 ± 1
	25 (i)	1059 ± 5	212 ± 1
	75 (ii)	1140 ± 10	197 ± 3
	50 (ii)	1010 ± 30	223 ± 8
	25 (ii)	820 ± 20	275 ± 6
	75 (iii)	933 ± 7	180 ± 2
	50 (iii)	750 ± 30	149 ± 9
	25 (iii)	396 ± 2	141 ± 1
	75 (iv)	1840 ± 20	163 ± 2
	50 (iv)	2280 ± 60	196 ± 6
25 (iv)	3710 ± 90	242 ± 7	
N <sub>2</sub> : H <sub>2</sub> ratio	1:0		
	6:1	510 ± 20	232 ± 9
	3:1	680 ± 10	173 ± 4
	1:1	1330 ± 30	89 ± 2
	1:3	1610 ± 20	73 ± 1
	1:6	1286 ± 10	91.5 ± 0.7
Residence time (s)	2.5	300 ± 6	116 ± 2
	10	905 ± 10	154 ± 2
	17.5	1400 ± 20	174 ± 3
	25	1840 ± 30	189 ± 3
	32.5	2180 ± 20	207 ± 2
	40	2450 ± 20	227 ± 2
	47.5	2670 ± 50	248 ± 4
	55	2870 ± 40	267 ± 3
	62.5	2980 ± 30	292 ± 3
	70	3110 ± 40	313 ± 4
Gradual addition N <sub>2</sub> main – H <sub>2</sub> side	LGA	1610 ± 40	139 ± 4
	SGA	1570 ± 60	143 ± 7
	1	1430 ± 40	157 ± 4
	2	1390 ± 20	161 ± 3
	3	1350 ± 30	166 ± 4
	4	1320 ± 30	170 ± 4
	5	1340 ± 20	167 ± 3
	6	1250 ± 10	179 ± 2
Gradual addition H <sub>2</sub> main – N <sub>2</sub> side	LGA	1396 ± 9	161 ± 1
	SGA	1349 ± 6	166.1 ± 0.9
	1	1449 ± 8	81.2 ± 0.5
	2	1410 ± 10	83.4 ± 0.7
	3	1390 ± 10	84.7 ± 0.8
	4	1350 ± 10	87 ± 1
	5	1270 ± 10	92.6 ± 1.0
	6	1312 ± 10	89.7 ± 0.8
Separate activation	LSN	1670 ± 50	134 ± 5
	LSW	1440 ± 10	156 ± 2
	SSN	1690 ± 60	133 ± 6
	SSW	1700 ± 20	132 ± 2





# Bibliography

- [1] IPCC, *Climate Change 2014 Synthesis Report Summary Chapter for Policymakers*. IPCC, 2014.
- [2] M. Brander, “Greenhouse Gases , CO<sub>2</sub> , CO<sub>2</sub>e , and Carbon : What Do All These Terms Mean?,” *Ecometrica*, no. August, p. 3, 2012.
- [3] H. Ritchie and M. Roser, “Co<sub>2</sub> and greenhouse gas emissions,” *Our World in Data*, 2017. <https://ourworldindata.org/co2-and-other-greenhouse-gas-emissions>.
- [4] European Comission, “A Clean Planet for all A European strategic long-term vision for a prosperous, modern, competitive and climate neutral economy,” tech. rep., European Comission, Brussels, 2018.
- [5] M. Appl, “Ammonia,” in *Ullmann’s Encyclopedia of Industrial Chemistry*, Weinheim, Germany: Wiley-VCH Verlag GmbH & Co. KGaA, dec 2006.
- [6] European Comission, *White paper on transport policy*. Brussels: European Comission, 2001.
- [7] S. Davis and R. Boundry, *Transportation energy Data book*. Oak Ridge: Oak Ridge National Laboratory, 38.1 ed., 2020.
- [8] R. Snoeckx and A. Bogaerts, “Plasma technology – a novel solution for CO<sub>2</sub> conversion?,” *Chem. Soc. Rev.*, vol. 46, pp. 5805–5863, 2017.
- [9] R. M. Cuéllar-Franca and A. Azapagic, “Carbon capture, storage and utilisation technologies: A critical analysis and comparison of their life cycle environmental impacts,” *Journal of CO<sub>2</sub> Utilization*, vol. 9, pp. 82–102, 2015.
- [10] H. Ritchie, “Renewable energy,” *Our World in Data*, 2017. <https://ourworldindata.org/renewable-energy>.
- [11] M. Pehl, A. Arvesen, F. Humpenöder, A. Popp, E. G. Hertwich, and G. Luderer, “Understanding future emissions from low-carbon power systems by integration of life-cycle assessment and integrated energy modelling,” *Nature Energy*, vol. 2, no. 12, pp. 939–945, 2017.

- [12] U. Fritsche, B. Berndes, A. Cowie, V. Dale, and K. Kline, “Sustainable energy options and implications for land use,” tech. rep., United Nations, 2017.
- [13] “Hidden consequences of intermittent electricity production.” <https://docs.wind-watch.org/Hidden-consequences-intermittent-electricity-production.html>. Accessed: 27/07/2020.
- [14] D. Rowe, S. Sayeef, and G. Platt, “Intermittency: It’s the Short-Term That Matters,” in *Future of Utilities Utilities of the Future*, pp. 129–150, Elsevier, 2016.
- [15] W. Zappa, M. Junginger, and M. van den Broek, “Is a 100% renewable European power system feasible by 2050?,” *Applied Energy*, vol. 233-234, no. November 2018, pp. 1027–1050, 2019.
- [16] California ISO, “Energy and environmental goals drive change,” *Technical Report*, p. 4, 2016.
- [17] J. Lazar, “Teaching the “ Duck ” to Fly,” *Regulatory Assistance Project, RAP*, no. January, 2014.
- [18] “Power prices go negative in germany, a positive for energy users.” <https://www.nytimes.com/2017/12/25/business/energy-environment/germany-electricity-negative-prices.html>. Accessed: 29/06/2020.
- [19] Y. Yang, S. Bremner, C. Menictas, and M. Kay, “Battery energy storage system size determination in renewable energy systems: A review,” *Renewable and Sustainable Energy Reviews*, vol. 91, no. January, pp. 109–125, 2018.
- [20] F. Díaz-González, A. Sumper, O. Gomis-Bellmunt, and R. Villafáfila-Robles, “A review of energy storage technologies for wind power applications,” *Renewable and Sustainable Energy Reviews*, vol. 16, no. 4, pp. 2154–2171, 2012.
- [21] X. Lim, “How to make the most of carbon dioxide,” *Nature*, vol. 526, no. 7575, p. 628, 2015.
- [22] “Lightning 14.07.2009 20-42-33.” [https://commons.wikimedia.org/wiki/File:Lightning\\_14.07.2009\\_20-42-33.JPG](https://commons.wikimedia.org/wiki/File:Lightning_14.07.2009_20-42-33.JPG). Accessed: 19/06/2020.
- [23] “Aurora in abisko near torneträsk.” [https://commons.wikimedia.org/wiki/File:Aurora\\_in\\_Abisko\\_near\\_Torneträsk.jpg](https://commons.wikimedia.org/wiki/File:Aurora_in_Abisko_near_Torneträsk.jpg). Accessed: 19/06/2020.

- 
- [24] “Lepecvd plasma.” [https://commons.wikimedia.org/wiki/File:LEPECVD\\_plasma.png](https://commons.wikimedia.org/wiki/File:LEPECVD_plasma.png). Accessed: 19/06/2020.
- [25] J. A. Bittencourt, *Fundamentals of Plasma Physics*. New York, NY: Springer New York, 2004.
- [26] A. Fridman, *Plasma Chemistry*, vol. №3. Cambridge: Cambridge University Press, 2008.
- [27] T. Kozák and A. Bogaerts, “Splitting of CO<sub>2</sub> by vibrational excitation in non-equilibrium plasmas: a reaction kinetics model,” *Plasma Sources Science and Technology*, vol. 23, no. 4, p. 045004, 2014.
- [28] R. Aerts, T. Martens, and A. Bogaerts, “Influence of vibrational states on CO<sub>2</sub> splitting by dielectric barrier discharges,” *The Journal of Physical Chemistry C*, vol. 116, pp. 23257–23273, nov 2012.
- [29] A. Bogaerts, E. Neyts, R. Gijbels, and J. van der Mullen, “Gas discharge plasmas and their applications,” *Spectrochimica Acta - Part B Atomic Spectroscopy*, vol. 57, no. 4, pp. 609–658, 2002.
- [30] F. Paschen, “Ueber die zum Funkenübergang in Luft, Wasserstoff und Kohlensäure bei verschiedenen Drucken erforderliche Potentialdifferenz,” *Annalen der Physik*, vol. 273, no. 5, pp. 69–96, 1889.
- [31] M. a. Lieberman and A. J. Lichtenberg, *Principles of Plasma Discharges and Materials Processing: Second Edition*. 2005.
- [32] G. Eigenberger and W. Ruppel, “Catalytic Fixed-Bed Reactors,” in *Ullmann’s Encyclopedia of Industrial Chemistry*, Weinheim, Germany: Wiley-VCH Verlag GmbH & Co. KGaA, jul 2012.
- [33] T. Nunnally, K. Gutsol, A. Rabinovich, A. Fridman, A. Gutsol, and A. Kemoun, “Dissociation of CO<sub>2</sub> in a low current gliding arc plasmatron,” *Journal of Physics D: Applied Physics*, vol. 44, no. 27, p. 274009, 2011.
- [34] G. Trenchev, A. Nikiforov, W. Wang, S. Kolev, and A. Bogaerts, “Atmospheric pressure glow discharge for CO<sub>2</sub> conversion: Model-based exploration of the optimum reactor configuration,” *Chemical Engineering Journal*, vol. 362, no. December 2018, pp. 830–841, 2019.
- [35] G. Trenchev, *Computational modeling of atmospheric DC discharges for CO<sub>2</sub> conversion*. PhD thesis, University of Antwerp, 2010.
- [36] M. S. Moss, K. Yanallah, R. W. K. Allen, and F. Pontiga, “An investigation of CO<sub>2</sub> splitting using nanosecond pulsed corona discharge: effect of argon

- addition on CO<sub>2</sub> conversion and energy efficiency,” *Plasma Sources Science and Technology*, vol. 26, p. 035009, feb 2017.
- [37] U. Kogelschatz, “Dielectric-barrier discharges: Their history, discharge physics, and industrial applications,” *Plasma Chemistry and Plasma Processing*, vol. 23, no. 1, pp. 1–46, 2003.
- [38] R. Aerts, W. Somers, and A. Bogaerts, “Carbon Dioxide Splitting in a Dielectric Barrier Discharge Plasma: A Combined Experimental and Computational Study,” *ChemSusChem*, vol. 8, no. 4, pp. 702–716, 2015.
- [39] A. Ozkan, A. Bogaerts, and F. Reniers, “Routes to increase the conversion and the energy efficiency in the splitting of CO<sub>2</sub> by a dielectric barrier discharge,” *Journal of Physics D: Applied Physics*, vol. 50, no. 8, p. 084004, 2017.
- [40] T. Manley, “The Electric Characteristics of the Ozonator Discharge,” *Transactions of the Electrochemical Society*, vol. 84, pp. 83–96, 1943.
- [41] F. J. J. Peeters and M. C. M. van de Sanden, “The influence of partial surface discharging on the electrical characterization of DBDs,” *Plasma Sources Science and Technology*, vol. 24, no. 1, p. 015016, 2014.
- [42] J. Van Durme, J. Dewulf, C. Leys, and H. Van Langenhove, “Combining non-thermal plasma with heterogeneous catalysis in waste gas treatment: A review,” *Applied Catalysis B: Environmental*, vol. 78, no. 3-4, pp. 324–333, 2008.
- [43] B. S. Patil, Q. Wang, V. Hessel, and J. Lang, “Plasma N<sub>2</sub>-fixation: 1900–2014,” *Catalysis Today*, vol. 256, pp. 49–66, 2015.
- [44] “Ozonia ozone system by suez water technologies and solutions.” <https://www.suezwatertechnologies.com/products/disinfection-oxidation/ozonia-ozone-systems>. Accessed: 19/06/2020.
- [45] U. Kogelschatz, “Applications of microplasmas and microreactor technology,” *Contributions to Plasma Physics*, vol. 47, no. 1-2, pp. 80–88, 2007.
- [46] Q. Wang, Y. Cheng, and Y. Jin, “Dry reforming of methane in an atmospheric pressure plasma fluidized bed with Ni/ $\gamma$ -Al<sub>2</sub>O<sub>3</sub> catalyst,” *Catalysis Today*, vol. 148, pp. 275–282, nov 2009.
- [47] T. Mizushima, K. Matsumoto, J. I. Sugoh, H. Ohkita, and N. Kakuta, “Tubular membrane-like catalyst for reactor with dielectric-barrier-



- discharge plasma and its performance in ammonia synthesis,” *Applied Catalysis A: General*, vol. 265, no. 1, pp. 53–59, 2004.
- [48] T. Mizushima, K. Matsumoto, H. Ohkita, and N. Kakuta, “Catalytic effects of metal-loaded membrane-like alumina tubes on ammonia synthesis in atmospheric pressure plasma by dielectric barrier discharge,” *Plasma Chemistry and Plasma Processing*, vol. 27, no. 1, pp. 1–11, 2007.
- [49] C. Subrahmanyam, M. Magureanu, a. Renken, and L. Kiwi-Minsker, “Catalytic abatement of volatile organic compounds assisted by non-thermal plasma. Part 1. A novel dielectric barrier discharge reactor containing catalytic electrode,” *Applied Catalysis B: Environmental*, vol. 65, no. 1-2, pp. 150–156, 2006.
- [50] S. Sato, K. Hensel, H. Hayashi, K. Takashima, and A. Mizuno, “Honeycomb discharge for diesel exhaust cleaning,” *Journal of Electrostatics*, vol. 67, no. 2-3, pp. 77–83, 2009.
- [51] S. Mori, N. Matsuura, L. L. Tun, and M. Suzuki, “Direct Synthesis of Carbon Nanotubes from Only CO<sub>2</sub> by a Hybrid Reactor of Dielectric Barrier Discharge and Solid Oxide Electrolyser Cell,” *Plasma Chemistry and Plasma Processing*, vol. 36, no. 1, pp. 231–239, 2016.
- [52] A. Huang, G. Xia, J. Wang, S. L. Suib, Y. Hayashi, and H. Matsumoto, “CO<sub>2</sub> reforming of CH<sub>4</sub> by atmospheric pressure AC discharge plasmas,” *Journal of Catalysis*, vol. 189, no. 2, pp. 349–359, 2000.
- [53] G. G. Xia, J. Y. Wang, A. Huang, S. L. Suib, Y. Hayashi, and H. Matsumoto, “A novel Y-type reactor for selective excitation of atmospheric pressure glow discharge plasma,” *Review of Scientific Instruments*, vol. 72, no. 2, pp. 1383–1390, 2001.
- [54] *Ullmann’s Encyclopedia of Industrial Chemistry*. Weinheim, Germany: Wiley, 7th ed., jun 2002.
- [55] A. Ozkan, T. Dufour, A. Bogaerts, and F. Reniers, “How do the barrier thickness and dielectric material influence the filamentary mode and CO<sub>2</sub> conversion in a flowing DBD?,” *Plasma Sources Science and Technology*, vol. 25, no. 4, 2016.
- [56] Y. Uytendhouwen, K. Bal, I. Michiels, E. Neyts, V. Meynen, P. Cool, and A. Bogaerts, “How process parameters and packing materials tune chemical equilibrium and kinetics in plasma-based CO<sub>2</sub> conversion,” *Chemical Engineering Journal*, vol. 372, pp. 1253–1264, sep 2019.

- [57] T. Wang, B. M. Sun, H. P. Xiao, J. Y. Zeng, E. P. Duan, J. Xin, and C. Li, "Effect of reactor structure in DBD for nonthermal plasma processing of NO in N<sub>2</sub> at ambient temperature," *Plasma Chemistry and Plasma Processing*, vol. 32, no. 6, pp. 1189–1201, 2012.
- [58] I. Michielsens, Y. Uytendhouwen, J. Pype, B. Michielsens, J. Mertens, F. Reniers, V. Meynen, and A. Bogaerts, "CO<sub>2</sub> dissociation in a packed bed DBD reactor: First steps towards a better understanding of plasma catalysis," *Chemical Engineering Journal*, vol. 326, pp. 477–488, 2017.
- [59] M. Bai, Z. Zhang, M. Bai, X. Bai, and H. Gao, "Synthesis of Ammonia Using CH<sub>4</sub>/N<sub>2</sub> Plasmas Based on Micro-Gap Discharge under Environmentally Friendly Condition," *Plasma Chemistry and Plasma Processing*, vol. 28, pp. 405–414, aug 2008.
- [60] K. Van Laer and A. Bogaerts, "Influence of gap size and dielectric constant of the packing material on the plasma behaviour in a packed bed DBD reactor: A fluid modelling study," *Plasma Processes and Polymers*, vol. 14, p. 1600129, apr 2017.
- [61] A. Ağiral, T. Nozaki, M. Nakase, S. Yuzawa, K. Okazaki, and J. G. E. Han Gardeniers, "Gas-to-liquids process using multi-phase flow, non-thermal plasma microreactor," *Chemical Engineering Journal*, vol. 167, no. 2-3, pp. 560–566, 2011.
- [62] E. C. Neyts and A. Bogaerts, "Understanding plasma catalysis through modelling and simulation—a review," *Journal of Physics D: Applied Physics*, vol. 47, p. 224010, 2014.
- [63] R. Snoeckx, A. Ozkan, F. Reniers, and A. Bogaerts, "The Quest for Value-Added Products from Carbon Dioxide and Water in a Dielectric Barrier Discharge: A Chemical Kinetics Study," *ChemSusChem*, vol. 10, no. 2, pp. 409–424, 2017.
- [64] K. Van Laer and A. Bogaerts, "Fluid modelling of a packed bed dielectric barrier discharge plasma reactor," *Plasma Sources Science and Technology*, vol. 25, no. 1, p. 15002, 2016.
- [65] W. Wang, H. H. Kim, K. Van Laer, and A. Bogaerts, "Streamer propagation in a packed bed plasma reactor for plasma catalysis applications," *Chemical Engineering Journal*, vol. 334, no. September 2017, pp. 2467–2479, 2018.
- [66] Y. R. Zhang, K. Van Laer, E. C. Neyts, and A. Bogaerts, "Can plasma be formed in catalyst pores? A modeling investigation," *Applied Catalysis B: Environmental*, vol. 185, pp. 56–67, 2016.

- 
- [67] E. C. Neyts, K. Ostrikov, M. K. Sunkara, and A. Bogaerts, "Plasma catalysis: Synergistic effects at the nanoscale," *Chemical Reviews*, vol. 115, no. 24, pp. 13408–13446, 2015.
- [68] X. Duan, Z. Hu, Y. Li, and B. Wang, "Effect of dielectric packing materials on the decomposition of carbon dioxide using DBD microplasma reactor," *AIChE Journal*, vol. 61, no. 3, pp. 898–903, 2015.
- [69] H.-H. Kim, "Nonthermal plasma processing for air-pollution control: A historical review, current issues, and future prospects," *Plasma Processes and Polymers*, vol. 1, pp. 91–110, sep 2004.
- [70] T. Butterworth, R. Elder, and R. Allen, "Effects of particle size on CO<sub>2</sub> reduction and discharge characteristics in a packed bed plasma reactor," *Chemical Engineering Journal*, vol. 293, pp. 55–67, 2016.
- [71] A. M. Vandenbroucke, R. Morent, N. De Geyter, and C. Leys, "Non-thermal plasmas for non-catalytic and catalytic VOC abatement," *Journal of Hazardous Materials*, vol. 195, no. August, pp. 30–54, 2011.
- [72] X. Tu and J. C. Whitehead, "Plasma-catalytic dry reforming of methane in an atmospheric dielectric barrier discharge: Understanding the synergistic effect at low temperature," *Applied Catalysis B: Environmental*, vol. 125, pp. 439–448, 2012.
- [73] S. Kameshima, K. Tamura, Y. Ishibashi, and T. Nozaki, "Pulsed dry methane reforming in plasma-enhanced catalytic reaction," *Catalysis Today*, vol. 256, no. Part 1, pp. 67–75, 2015.
- [74] D. Mei, X. Zhu, Y.-l. He, J. D. Yan, and X. Tu, "Plasma-assisted conversion of CO<sub>2</sub> in a dielectric barrier discharge reactor : understanding the effect of packing materials," *Plasma Sources Science and Technology*, vol. 24, p. 15011, 2015.
- [75] M. Kraus, B. Eliasson, U. Kogelschatz, and A. Wokaun, "CO<sub>2</sub> reforming of methane by the combination of dielectric-barrier discharges and catalysis," *Physical Chemistry and Chemical Physics*, vol. 3, pp. 294–300, 2001.
- [76] Y. F. Guo, D. Q. Ye, K. F. Chen, and J. C. He, "Toluene removal by a DBD-type plasma combined with metal oxides catalysts supported by nickel foam," *Catalysis Today*, vol. 126, no. 3-4 SPEC. ISS., pp. 328–337, 2007.
- [77] J. C. Whitehead, "Plasma – catalysis : the known knowns , the known unknowns and the unknown unknowns," *Journal of Physics D: Applied Physics*, vol. 49, no. 24, p. 243001, 2016.
-

- [78] I. Michiels, *Plasma catalysis: Study of packing materials on CO<sub>2</sub> reforming in a DBD reactor*. PhD thesis, University of Antwerp, 2019.
- [79] O. Levenspiel, *Chemical Reaction Engineering Third Edition*. 1999.
- [80] A. Zhou, D. Chen, B. Dai, C. Ma, P. Li, and F. Yu, "Direct decomposition of CO<sub>2</sub> using self-cooling dielectric barrier discharge plasma," *Greenhouse Gases: Science and Technology*, vol. 7, pp. 721–730, aug 2017.
- [81] Y. F. Zhang, L. S. Wei, X. Liang, H. Z. Deng, and M. Šimek, "Characteristics of the Discharge and Ozone Generation in Oxygen-Fed Coaxial DBD Using an Amplitude-Modulated AC Power Supply," *Plasma Chemistry and Plasma Processing*, vol. 38, no. 6, pp. 1199–1208, 2018.
- [82] H. L. Chen, H. M. Lee, S. H. Chen, Y. Chao, and M. B. Chang, "Review of plasma catalysis on hydrocarbon reforming for hydrogen production-Interaction, integration, and prospects," *Applied Catalysis B: Environmental*, vol. 85, no. 1-2, pp. 1–9, 2008.
- [83] J. C. Whitehead, "Plasma catalysis: A solution for environmental problems," *Pure and Applied Chemistry*, vol. 82, no. 6, pp. 1329–1336, 2010.
- [84] I. Michiels, Y. Uytendhouwen, A. Bogaerts, and V. Meynen, "Altering Conversion and Product Selectivity of Dry Reforming of Methane in a Dielectric Barrier Discharge by Changing the Dielectric Packing Material," *Catalysts*, vol. 9, p. 51, jan 2019.
- [85] Z. Machala, B. Tarabova, K. Hensel, E. Spetlikova, L. Sikurova, and P. Lukes, "Formation of ROS and RNS in water electro-sprayed through transient spark discharge in air and their bactericidal effects," *Plasma Processes and Polymers*, vol. 10, no. 7, pp. 649–659, 2013.
- [86] R. Snoeckx, R. Aerts, X. Tu, and A. Bogaerts, "Plasma-Based Dry Reforming: A Computational Study Ranging from the Nanoseconds to Seconds Time Scale," *The Journal of Physical Chemistry C*, vol. 117, pp. 4957–4970, mar 2013.
- [87] Y. N. Chun, Y. C. Yang, and K. Yoshikawa, "Hydrogen generation from biogas reforming using a gliding arc plasma-catalyst reformer," *Catalysis Today*, vol. 148, no. 3-4, pp. 283–289, 2009.
- [88] Z. A. Allah and J. C. Whitehead, "Plasma-catalytic dry reforming of methane in an atmospheric pressure AC gliding arc discharge," *Catalysis Today*, vol. 256, no. P1, pp. 76–79, 2015.

- 
- [89] S. Vepřek, "Statistical model of chemical reactions in nonisothermal low pressure plasma," *The Journal of Chemical Physics*, vol. 57, no. 2, pp. 952–959, 1972.
- [90] S. Vepřek and W. Peier, "Chemical equilibrium in nonisothermal low pressure plasma," *Chemical Physics*, vol. 2, no. 4, pp. 478–484, 1973.
- [91] J. J. Wagner and S. Vepřek, "Kinetic study of the heterogeneous Si/H system under low-pressure plasma conditions by means of mass spectrometry," *Plasma Chemistry and Plasma Processing*, vol. 2, no. 1, pp. 95–107, 1982.
- [92] Y. Uytendhouwen, S. Van Alphen, I. Michielsens, V. Meynen, P. Cool, and A. Bogaerts, "A packed-bed DBD micro plasma reactor for CO<sub>2</sub> dissociation: Does size matter?," *Chemical Engineering Journal*, vol. 348, pp. 557–568, 2018.
- [93] H. Sekiguchi, M. Ando, and H. Kojima, "Study of hydroxylation of benzene and toluene using a micro-DBD plasma reactor," *Journal of Physics D: Applied Physics*, vol. 38, no. 11, pp. 1722–1727, 2005.
- [94] J. Pype, B. Michielsens, E. M. Seftel, S. Mullens, and V. Meynen, "Development of alumina microspheres with controlled size and shape by vibrational droplet coagulation," *Journal of the European Ceramic Society*, vol. 37, no. 1, pp. 189–198, 2017.
- [95] S. Paulussen, B. Verheyde, X. Tu, C. De Bie, T. Martens, D. Petrovic, A. Bogaerts, and B. Sels, "Conversion of carbon dioxide to value-added chemicals in atmospheric pressure dielectric barrier discharges," *Plasma Sources Science and Technology*, vol. 19, no. 3, p. 034015, 2010.
- [96] N. Pinhão, A. Moura, J. B. Branco, and J. Neves, "Influence of gas expansion on process parameters in non-thermal plasma plug-flow reactors: A study applied to dry reforming of methane," *International Journal of Hydrogen Energy*, vol. 41, no. 22, pp. 9245–9255, 2016.
- [97] R. Snoeckx, S. Heijckers, K. Van Wesenbeeck, S. Lenaerts, and A. Bogaerts, "CO<sub>2</sub> conversion in a dielectric barrier discharge plasma: N<sub>2</sub> in the mix as a helping hand or problematic impurity?," *Energy Environ. Sci.*, vol. 9, no. 3, pp. 999–1011, 2016.
- [98] B. Wang, W. Yan, W. Ge, and X. Duan, "Kinetic model of the methane conversion into higher hydrocarbons with a dielectric barrier discharge microplasma reactor," *Chemical Engineering Journal*, vol. 234, pp. 354–360, dec 2013.

- [99] K. Van Laer and A. Bogaerts, "How bead size and dielectric constant affect the plasma behaviour in a packed bed plasma reactor: a modelling study," *Plasma Sources Science and Technology*, vol. 26, p. 085007, jul 2017.
- [100] T. Butterworth and R. W. K. Allen, "Plasma-catalyst interaction studied in a single pellet DBD reactor: Dielectric constant effect on plasma dynamics," *Plasma Sources Science and Technology*, vol. 26, no. 6, 2017.
- [101] Y. Uytendhouwen, V. Meynen, P. Cool, and A. Bogaerts, "The Potential Use of Core-Shell Structured Spheres in a Packed-Bed DBD Plasma Reactor for CO<sub>2</sub> Conversion," *Catalysts*, vol. 10, p. 530, may 2020.
- [102] Z. Roosta, A. Izadbakhsh, A. M. Sanati, and S. Osfoury, "Synthesis and evaluation of NiO@MCM-41 core-shell nanocomposite in the CO<sub>2</sub> reforming of methane," *Journal of Porous Materials*, vol. 25, no. 4, pp. 1135–1145, 2018.
- [103] J. Bao, J. He, Y. Zhang, Y. Yoneyama, and N. Tsubaki, "A core/shell catalyst produces a spatially confined effect and shape selectivity in a consecutive reaction," *Angewandte Chemie - International Edition*, vol. 47, no. 2, pp. 353–356, 2008.
- [104] C. J. Zhong and M. M. Maye, "Core-shell assembled nanoparticles as catalysts," *Advanced Materials*, vol. 13, no. 19, pp. 1507–1511, 2001.
- [105] S. H. Joo, J. Y. Park, C. K. Tsung, Y. Yamada, P. Yang, and G. A. Somorjai, "Thermally stable Pt/mesoporous silica core-shell nanocatalysts for high-temperature reactions," *Nature Materials*, vol. 8, no. 2, pp. 126–131, 2009.
- [106] L. Yu, C. Ni, S. M. Grist, C. Bayly, and K. C. Cheung, "Alginate core-shell beads for simplified three-dimensional tumor spheroid culture and drug screening," *Biomedical Microdevices*, vol. 17, no. 2, 2015.
- [107] R. A. Ramli, W. A. Laftah, and S. Hashim, "Core-shell polymers: A review," *RSC Advances*, vol. 3, no. 36, pp. 15543–15565, 2013.
- [108] Z. He, R. Tu, H. Katsui, and T. Goto, "Synthesis of SiC/SiO<sub>2</sub> core-shell powder by rotary chemical vapor deposition and its consolidation by spark plasma sintering," *Ceramics International*, vol. 39, no. 3, pp. 2605–2610, 2013.
- [109] X. H. Yang, H. T. Fu, K. Wong, X. C. Jiang, and A. B. Yu, "Hybrid Ag@TiO<sub>2</sub> core-shell nanostructures with highly enhanced photocatalytic performance," *Nanotechnology*, vol. 24, no. 41, 2013.

- 
- [110] W. Luc, C. Collins, S. Wang, H. Xin, K. He, Y. Kang, and F. Jiao, "Ag-sn bimetallic catalyst with a core-shell structure for CO<sub>2</sub> reduction," *Journal of the American Chemical Society*, vol. 139, no. 5, pp. 1885–1893, 2017.
- [111] L. Palugan, M. Cerea, L. Zema, A. Gazzaniga, and A. Maroni, "Coated pellets for oral colon delivery," *Journal of Drug Delivery Science and Technology*, vol. 25, no. February, pp. 1–15, 2015.
- [112] J. Varshosaz, J. Emami, N. Tavakoli, M. Minaiyan, N. Rahmani, and F. Dorkoosh, "Development and Evaluation of a Novel Pellet-Based Tablet System for Potential Colon Delivery of Budesonide," *Journal of Drug Delivery*, vol. 2012, no. April, pp. 1–7, 2012.
- [113] J. Y. Liu, X. X. Zhang, H. Y. Huang, B. J. Lee, J. H. Cui, and Q. R. Cao, "Esomeprazole magnesium enteric-coated pellet-based tablets with high acid tolerance and good compressibility," *Journal of Pharmaceutical Investigation*, vol. 48, no. 3, pp. 341–350, 2018.
- [114] N. Hampel, A. Bück, M. Peglow, and E. Tsotsas, "Continuous pellet coating in a Wurster fluidized bed process," *Chemical Engineering Science*, vol. 86, pp. 87–98, 2013.
- [115] X. Zheng, S. Tan, L. Dong, S. Li, and H. Chen, "LaNiO<sub>3</sub>@SiO<sub>2</sub> core-shell nano-particles for the dry reforming of CH<sub>4</sub> in the dielectric barrier discharge plasma," *International Journal of Hydrogen Energy*, vol. 39, no. 22, pp. 11360–11367, 2014.
- [116] X. Zheng, S. Tan, L. Dong, S. Li, and H. Chen, "Plasma-assisted catalytic dry reforming of methane: Highly catalytic performance of nickel ferrite nanoparticles embedded in silica," *Journal of Power Sources*, vol. 274, pp. 286–294, 2015.
- [117] J. Hong, M. Aramesh, O. Shimoni, D. H. Seo, S. Yick, A. Greig, C. Charles, S. Praver, and A. B. Murphy, "Plasma Catalytic Synthesis of Ammonia Using Functionalized-Carbon Coatings in an Atmospheric-Pressure Non-equilibrium Discharge," *Plasma Chemistry and Plasma Processing*, vol. 36, no. 4, pp. 917–940, 2016.
- [118] J. Lefevre, M. Gysen, S. Mullens, V. Meynen, and J. Van Noyen, "The benefit of design of support architectures for zeolite coated structured catalysts for methanol-to-olefin conversion," *Catalysis Today*, vol. 216, pp. 18–23, 2013.
- [119] J. Lefevre, L. Protasova, S. Mullens, and V. Meynen, "3D-printing of hierarchical porous ZSM-5: The importance of the binder system," *Materials and Design*, vol. 134, pp. 331–341, 2017.
-

- [120] J. Lefevre, S. Mullens, and V. Meynen, "The impact of formulation and 3D-printing on the catalytic properties of ZSM-5 zeolite," *Chemical Engineering Journal*, vol. 349, no. April, pp. 260–268, 2018.
- [121] Z. Vajglová, N. Kumar, P. Mäki-Arvela, K. Eränen, M. Peurla, L. Hupa, and D. Y. Murzin, "Effect of Binders on the Physicochemical and Catalytic Properties of Extrudate-Shaped Beta Zeolite Catalysts for Cyclization of Citronellal," *Organic Process Research and Development*, vol. 23, no. 11, pp. 2456–2463, 2019.
- [122] Q.-Z. Zhang, W.-Z. Wang, and A. Bogaerts, "Importance of surface charging during plasma streamer propagation in catalyst pores," *Plasma Sources Science and Technology*, vol. 27, p. 065009, jun 2018.
- [123] C. E. Stere, W. Adress, R. Burch, S. Chansai, A. Goguet, W. G. Graham, and C. Hardacre, "Probing a non-thermal plasma activated heterogeneously catalyzed reaction using in situ DRIFTS-MS," *ACS Catalysis*, vol. 5, no. 2, pp. 956–964, 2015.
- [124] E. K. Gibson, C. E. Stere, B. Curran-McAteer, W. Jones, G. Cibin, D. Gianolio, A. Goguet, P. P. Wells, C. R. A. Catlow, P. Collier, P. Hinde, and C. Hardacre, "Probing the Role of a Non-Thermal Plasma (NTP) in the Hybrid NTP Catalytic Oxidation of Methane," *Angewandte Chemie - International Edition*, vol. 56, no. 32, pp. 9351–9355, 2017.
- [125] F. Azzolina-Jury, "Novel boehmite transformation into  $\gamma$ -alumina and preparation of efficient nickel base alumina porous extrudates for plasma-assisted CO<sub>2</sub> methanation," *Journal of Industrial and Engineering Chemistry*, vol. 71, pp. 410–424, 2019.
- [126] F. Azzolina-Jury and F. Thibault-Starzyk, "Mechanism of Low Pressure Plasma-Assisted CO<sub>2</sub> Hydrogenation Over Ni-USY by Microsecond Time-resolved FTIR Spectroscopy," *Topics in Catalysis*, vol. 60, no. 19-20, pp. 1709–1721, 2017.
- [127] H.-H. Kim, Y. Teramoto, and A. Ogata, "Time-resolved imaging of positive pulsed corona-induced surface streamers on TiO and  $\gamma$ -Al<sub>2</sub>O<sub>3</sub> -supported Ag catalysts," *Journal of Physics D: Applied Physics*, vol. 49, p. 459501, nov 2016.
- [128] H. H. Kim, Y. Teramoto, A. Ogata, W. S. Kang, M. Hur, and Y. H. Song, "Negative surface streamers propagating on TiO<sub>2</sub> and  $\gamma$ -Al<sub>2</sub>O<sub>3</sub>-supported Ag catalysts: ICCD imaging and modeling study," *Journal of Physics D: Applied Physics*, vol. 51, no. 24, 2018.



- 
- [129] D. Mei, B. Ashford, Y. L. He, and X. Tu, "Plasma-catalytic reforming of biogas over supported Ni catalysts in a dielectric barrier discharge reactor: Effect of catalyst supports," *Plasma Processes and Polymers*, vol. 14, no. 6, 2017.
- [130] R. Snoeckx, Y. X. Zeng, X. Tu, and A. Bogaerts, "Plasma-based dry reforming: improving the conversion and energy efficiency in a dielectric barrier discharge," *RSC Adv.*, vol. 5, no. 38, pp. 29799–29808, 2015.
- [131] L. Wang, Y. Yi, C. Wu, H. Guo, and X. Tu, "One-step reforming of CO<sub>2</sub> and CH<sub>4</sub> into high-value liquid chemicals and fuels at room temperature by plasma-driven catalysis," *Angewandte Chemie - International Edition*, vol. 56, no. 44, pp. 13679–13683, 2017.
- [132] Q.-Z. Z. Zhang and A. Bogaerts, "Propagation of a plasma streamer in catalyst pores," *Plasma Sources Science and Technology*, vol. 27, p. 035009, mar 2018.
- [133] A. Berthelot and A. Bogaerts, "Modeling of CO<sub>2</sub> plasma: effect of uncertainties in the plasma chemistry," *Plasma Sources Science and Technology*, vol. 26, no. 11, p. 115002, 2017.
- [134] S. Kolev and A. Bogaerts, "A 2D model for a gliding arc discharge," *Plasma Sources Science and Technology*, vol. 24, p. 015025, dec 2014.
- [135] A. Berthelot and A. Bogaerts, "Modeling of CO<sub>2</sub> Splitting in a Microwave Plasma: How to Improve the Conversion and Energy Efficiency," *The Journal of Physical Chemistry C*, vol. 121, pp. 8236–8251, apr 2017.
- [136] A. Bogaerts, T. Kozák, K. van Laer, and R. Snoeckx, "Plasma-based conversion of CO<sub>2</sub> : current status and future challenges," *Faraday Discussions*, vol. 183, pp. 217–232, 2015.
- [137] Y. Uytendhouwen, K. Bal, E. Neyts, V. Meynen, P. Cool, and A. Bogaerts, "On the kinetics and equilibria of plasma-based dry reforming of methane," *Chemical Engineering Journal*, vol. 405, p. 126630, feb 2021.
- [138] C. De Bie, B. Verheyde, T. Martens, J. Van Dijk, S. Paulussen, and A. Bogaerts, "Fluid modeling of the conversion of methane into higher hydrocarbons in an atmospheric pressure dielectric barrier discharge," *Plasma Processes and Polymers*, vol. 8, no. 11, pp. 1033–1058, 2011.
- [139] C. Xu and X. Tu, "Plasma-assisted methane conversion in an atmospheric pressure dielectric barrier discharge reactor," *Journal of Energy Chemistry*, vol. 22, no. 3, pp. 420–425, 2013.
-

- [140] Y. Gao, S. Zhang, H. Sun, R. Wang, X. Tu, and T. Shao, "Highly efficient conversion of methane using microsecond and nanosecond pulsed spark discharges," *Applied Energy*, vol. 226, no. May, pp. 534–545, 2018.
- [141] Y. Yang, "Direct Non-oxidative Methane Conversion by Non-Thermal Plasma: Experimental Study," *Plasma Chemistry and Plasma Processing*, vol. 23, no. 2, pp. 283–296, 2003.
- [142] A. Indarto, "Hydrogen production from methane in a dielectric barrier discharge using oxide zinc and chromium as catalyst," *Journal of the Chinese Institute of Chemical Engineers*, vol. 39, no. 1, pp. 23–28, 2008.
- [143] W. C. Chung and M. B. Chang, "Review of catalysis and plasma performance on dry reforming of CH<sub>4</sub> and possible synergistic effects," *Renewable and Sustainable Energy Reviews*, vol. 62, pp. 13–31, 2016.
- [144] E. Cleiren, S. Heijkers, M. Ramakers, and A. Bogaerts, "Dry Reforming of Methane in a Gliding Arc Plasmatron: Towards a Better Understanding of the Plasma Chemistry," *ChemSusChem*, 2017.
- [145] A. Bogaerts, C. De Bie, R. Snoeckx, and T. Kozák, "Plasma based CO<sub>2</sub> and CH<sub>4</sub> conversion: A modeling perspective," *Plasma Processes and Polymers*, vol. 14, no. 6, 2017.
- [146] C. De Bie, J. Van Dijk, and A. Bogaerts, "The Dominant Pathways for the Conversion of Methane into Oxygenates and Syngas in an Atmospheric Pressure Dielectric Barrier Discharge," *Journal of Physical Chemistry C*, vol. 119, no. 39, pp. 22331–22350, 2015.
- [147] A. S. Morillo-Candas, C. Drag, J.-p. Booth, T. C. Dias, V. Guerra, and O. Guaitella, "Oxygen atom kinetics in CO<sub>2</sub> plasmas ignited in a DC glow discharge," *Plasma Sources Science and Technology*, vol. 28, p. 075010, jul 2019.
- [148] T. Kaneko, F. Derbyshire, E. Makino, D. Gray, M. Tamura, and K. Li, "Coal Liquefaction," in *Ullmann's Encyclopedia of Industrial Chemistry*, p. 96, Weinheim, Germany: Wiley-VCH Verlag GmbH & Co. KGaA, jul 2012.
- [149] Y. Uytendhouwen, J. Hereijgers, T. Breugelmans, P. Cool, and A. Bogaerts, "How gas flow design can influence the performance of a DBD plasma reactor for dry reforming of methane," *Chemical Engineering Journal*, vol. 405, p. 126618, feb 2021.
- [150] H. H. Kim, Y. Teramoto, A. Ogata, H. Takagi, and T. Nanba, "Atmospheric-pressure nonthermal plasma synthesis of ammonia over ruthenium catalysts," *Plasma Processes and Polymers*, vol. 14, no. 6, pp. 1–9, 2017.

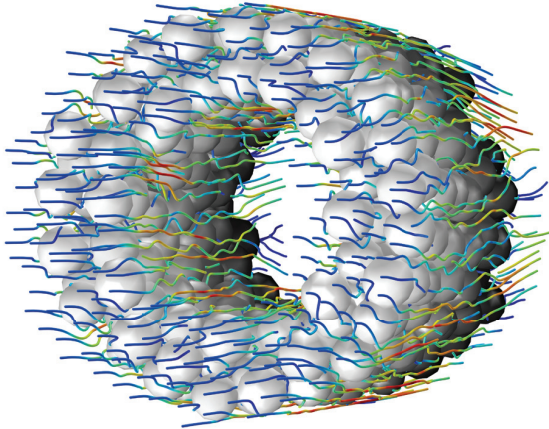
- 
- [151] M. D. Bai, X. Y. Bai, Z. T. Zhang, B. Mingdong, B. Xiyao, and Z. Zhitao, "Synthesis of ammonia in a strong electric field discharge at ambient pressure," *Plasma Chemistry and Plasma Processing*, vol. 20, no. 4, pp. 511–520, 2000.
- [152] M. Bai, Z. Zhang, X. Bai, M. Bai, and W. Ning, "Plasma Synthesis of Ammonia With a Microgap Dielectric Barrier Discharge at Ambient Pressure," *IEEE Transactions on Plasma Science*, vol. 31, no. 6 II, pp. 1285–1291, 2003.
- [153] P. Peng, Y. Li, Y. Cheng, S. Deng, P. Chen, and R. Ruan, "Atmospheric Pressure Ammonia Synthesis Using Non-thermal Plasma Assisted Catalysis," *Plasma Chemistry and Plasma Processing*, vol. 36, no. 5, pp. 1201–1210, 2016.
- [154] A. Ozkan, T. Dufour, G. Arnoult, P. De Keyzer, A. Bogaerts, and F. Reniers, "CO<sub>2</sub>-CH<sub>4</sub> conversion and syngas formation at atmospheric pressure using a multi-electrode dielectric barrier discharge," *Journal of CO<sub>2</sub> Utilization*, vol. 9, pp. 74–81, 2015.
- [155] A. Ozkan, T. Dufour, T. Silva, N. Britun, R. Snyders, F. Reniers, and A. Bogaerts, "DBD in burst mode: Solution for more efficient CO<sub>2</sub> conversion?," *Plasma Sources Science and Technology*, vol. 25, no. 5, 2016.
- [156] K. Li, J.-L. Liu, X.-S. Li, X. Zhu, and A.-M. Zhu, "Warm plasma catalytic reforming of biogas in a heat-insulated reactor: Dramatic energy efficiency and catalyst auto-reduction," *Chemical Engineering Journal*, vol. 288, pp. 671–679, mar 2016.
- [157] J. Slaets, M. Aghaei, S. Ceulemans, S. Van Alphen, and A. Bogaerts, "CO<sub>2</sub> and CH<sub>4</sub> conversion in "real" gas mixtures in a gliding arc plasmatron: how do N<sub>2</sub> and O<sub>2</sub> affect the performance?," *Green Chemistry*, vol. 22, no. 4, pp. 1366–1377, 2020.
- [158] G. J. van Rooij, D. C. M. van den Bekerom, N. den Harder, T. Minea, G. Berden, W. A. Bongers, R. Engeln, M. F. Graswinckel, E. Zoethout, and M. C. M. van de Sanden, "Taming microwave plasma to beat thermodynamics in CO<sub>2</sub> dissociation," *Faraday Discussions*, vol. 183, no. 4, pp. 233–248, 2015.
- [159] W. Bongers, H. Bouwmeester, B. Wolf, F. Peeters, S. Welzel, D. van den Bekerom, N. den Harder, A. Goede, M. Graswinckel, P. W. Groen, J. Kopecki, M. Leins, G. van Rooij, A. Schulz, M. Walker, and R. van de Sanden, "Plasma-driven dissociation of CO<sub>2</sub> for fuel synthesis," *Plasma Processes and Polymers*, vol. 14, p. 1600126, jun 2017.

- [160] N. den Harder, D. C. van den Bekerom, R. S. Al, M. F. Graswinckel, J. M. Palomares, F. J. Peeters, S. Ponduri, T. Minea, W. A. Bongers, M. C. van de Sanden, and G. J. van Rooij, "Homogeneous CO<sub>2</sub> conversion by microwave plasma: Wave propagation and diagnostics," *Plasma Processes and Polymers*, vol. 14, no. 6, pp. 1–24, 2017.
- [161] D. C. M. van den Bekerom, J. M. P. Linares, T. Verreycken, E. M. van Veldhuizen, S. Nijdam, G. Berden, W. A. Bongers, M. C. M. van de Sanden, and G. J. van Rooij, "The importance of thermal dissociation in CO<sub>2</sub> microwave discharges investigated by power pulsing and rotational Raman scattering," *Plasma Sources Science and Technology*, vol. 28, p. 055015, may 2019.
- [162] A. J. Wolf, T. W. H. Righart, F. J. J. Peeters, P. W. C. Groen, M. C. M. van de Sanden, and W. A. Bongers, "Characterization of CO<sub>2</sub> microwave plasma based on the phenomenon of skin-depth-limited contraction," *Plasma Sources Science and Technology*, vol. 28, p. 115022, nov 2019.
- [163] A. J. Wolf, T. W. H. Righart, F. J. J. Peeters, W. A. Bongers, and M. C. M. van de Sanden, "Implications of thermo-chemical instability on the contracted modes in CO<sub>2</sub> microwave plasmas," *Plasma Sources Science and Technology*, vol. 29, p. 025005, feb 2020.
- [164] D. C. M. van den Bekerom, A. van de Steeg, M. C. M. van de Sanden, and G. J. van Rooij, "Mode resolved heating dynamics in pulsed microwave CO<sub>2</sub> plasma from laser Raman scattering," *Journal of Physics D: Applied Physics*, vol. 53, p. 054002, jan 2020.
- [165] C. Montesano, S. Quercetti, L. M. Martini, G. Dilecce, and P. Tosi, "The effect of different pulse patterns on the plasma reduction of CO<sub>2</sub> for a nanosecond discharge," *Journal of CO<sub>2</sub> Utilization*, vol. 39, p. 101157, jul 2020.
- [166] G. Trenchev and A. Bogaerts, "Dual-vortex plasmatron: A novel plasma source for CO<sub>2</sub> conversion," *Journal of CO<sub>2</sub> Utilization*, vol. 39, p. 101152, jul 2020.
- [167] S. Heijkers and A. Bogaerts, "CO<sub>2</sub> Conversion in a Gliding Arc Plasmatron: Elucidating the Chemistry through Kinetic Modeling," *The Journal of Physical Chemistry C*, vol. 121, pp. 22644–22655, oct 2017.
- [168] V. Kotov and P. M. J. Koelman, "Plug flow reactor model of the plasma chemical conversion of CO<sub>2</sub>," *Plasma Sources Science and Technology*, vol. 28, p. 095002, sep 2019.

- 
- [169] A. Bogaerts, X. Tu, J. C. Whitehead, G. Centi, L. Lefferts, O. Guaitella, F. Azzolina-Jury, H.-H. Kim, A. B. Murphy, W. F. Schneider, T. Nozaki, J. C. Hicks, A. Rousseau, F. Thevenet, A. Khacef, and M. Carreon, "The 2020 plasma catalysis roadmap," *Journal of Physics D: Applied Physics*, vol. 53, p. 443001, oct 2020.
- [170] C. R. Wilke and C. Y. Lee, "Estimation of Diffusion Coefficients for Gases and Vapors," *Industrial & Engineering Chemistry*, vol. 47, no. 6, pp. 1253–1257, 1955.
- [171] G. Akay and K. Zhang, "Process intensification in ammonia synthesis using novel coassembled supported microporous catalysts promoted by nonthermal plasma," *Industrial and Engineering Chemistry Research*, vol. 56, no. 2, pp. 457–468, 2017.
- [172] P. Peng, P. Chen, C. Schiappacasse, N. Zhou, E. Anderson, D. Chen, J. Liu, Y. Cheng, R. Hatzenbeller, M. Addy, Y. Zhang, Y. Liu, and R. Ruan, "A review on the non-thermal plasma-assisted ammonia synthesis technologies," *Journal of Cleaner Production*, vol. 177, pp. 597–609, 2018.
- [173] P. Kaliyappan, A. Paulus, J. D'Haen, P. Samyn, K. Leyssens, Y. Uytendhouwen, S. Defossé, N. Hafezkhiani, A. Bogaerts, V. Meynen, K. Elen, A. Hardy, and M. K. Van Bael, "Probing the impact of material properties of core-shell SiO<sub>2</sub>@TiO<sub>2</sub> spheres on the plasma catalytic CO<sub>2</sub> dissociation using packed bed DBD plasma reactor," *Journal of CO<sub>2</sub> Utilization (Submitted)*, 2020.
- [174] S. Rana, Y. Uytendhouwen, A. Bogaerts, and V. Meynen, "A detailed study on the effect of calcination temperatures of gamma alumina on chemical equilibrium and kinetics in plasma-based DRM reaction," *In preparation*, 2020.







## Tuning the performance of a DBD plasma reactor for CO<sub>2</sub> reforming

**Yannick Uytendhouwen**

Combating the ever rising concentrations of greenhouse gases in the atmosphere, in particular CO<sub>2</sub> and CH<sub>4</sub>, is one of the biggest challenges of peoplekind in this century. Reducing emissions and developing innovative solutions for capturing and reusing the gases that are inevitably produced, are the tasks at hand for the next decades. However, novel technologies are required in order to convert these greenhouse gases in a sustainable and efficient way. Plasma technology could offer a viable solution, by directly targeting the molecules in reacting into value-added chemicals. Their quick on-and-off-switching capabilities by electrical energy, in combination with intermittent renewable energy sources, makes them a promising technology to directly convert CO<sub>2</sub> and CH<sub>4</sub> in a sustainable way.

Therefore, in this work, we studied the potential use of the DBD reactor for sustainable CO<sub>2</sub> and CH<sub>4</sub> conversion. We aimed to improve the reactor performance via different methods, and to develop a technique to gain more fundamental insight on how the kinetics in the reactor change on the macro scale when optimising the performance.